# Development of the two-fluid turbulence-resolving approach for sediment transport applications

Antoine Mathieu

Université Grenoble Alpes

# THÈSE

Pour obtenir le grade de

## DOCTEUR DE L'UNIVERSITÉ GRENOBLE ALPES

Spécialité : **Sciences de la Terre et de l'Univers et de l'Environnement**

Arrêtée ministériel : 25 mai 2016

Présentée par


## Antoine MATHIEU

Thèse dirigée par **Julien CHAUCHAT**
et co-encadrée par **Cyrille BONAMY**

préparée au sein du **Laboratoire des Écoulements Géophysiques et Industriels**
dans **l'École Doctorale Sciences de la Terre, de l'Environnement et des Planètes**


# Development of the two-fluid turbulence-resolving approach for sediment transport applications

# Développement de l'approche bi-fluide à turbulence résolue pour des applications de transport de sédiments

Thèse soutenue publiquement le **30 novembre 2021**
devant le jury composé de :

**Ivana VINKOVIC**
Université Claude Bernard Lyon 1 - LMFA, Rapporteur

**Pascal FEDE**
Université Toulouse 3 - IMFT, Rapporteur

**Guillaume BALARAC**
Grenoble INP - LEGI, Président

**Anne TANIÈRE**
Université de Lorraine - LEMTA, Examinatrice

**Thierry GARLAN**
SHOM, Examinateur

**Tian-Jian HSU**
University of Delaware - Center for Applied Coastal Research, Examinateur

**Cyrille BONAMY**
CNRS - LEGI, Co-Encadrant de thèse

**Julien CHAUCHAT**
Grenoble INP - LEGI, Directeur de thèse

# Avant-propos

*Cette thèse est rédigée en anglais mais un résumé des principaux résultats en français est proposé dans l'annexe A.*

# Foreword

*This thesis is written in english but a summary of the main results in french is proposed in appendix A.*

# Remerciements

Je tiens tout d'abord à exprimer ma reconnaissance envers les membres du jury d'avoir accepté de juger mon travail et plus particulièrement, Ivana Vinkovic et Pascal Fede d'avoir été rapporteurs.

Je souhaite ensuite remercier sincèrement Julien et Cyrille, qui ont su trouver le parfait équilibre d'encadrement en me laissant suffisamment de liberté et d'autonomie tout en sachant me guider, m'orienter et m'aider quand j'en avais besoin. Leur complémentarité a été un atout majeur pour mener à bien cette thèse. J'espère qu'ils ont eu autant de plaisir que moi à travailler sur les sujets passionnants que nous avons abordés. Je souhaite à tout jeune chercheur la chance de trouver des encadrants aussi disponibles, investis et passionnés.

Je tiens aussi à remercier toutes les personnes ayant participé de près ou de loin à cette thèse, notamment les contributeurs de sedFoam, les personnes travaillant sur les thématiques de transport de sédiments au LEGI et le groupe de Tian-Jian Hsu à l'université du Delaware. Les discussions lors de nos réunions de travail ont toujours été stimulantes, m'ont permis de mettre en perspective mes résultats et ont su accroître ma curiosité scientifique sur de nombreux sujets.

Plus généralement, je remercie les membres du LEGI, le service informatique, l'administration, les chercheurs et chercheuses avec qui nous avons pu avoir des discussions passionnantes ainsi que les doctorants et postdoctorants pour les moments passés ensemble.

Enfin, aucun mot ne serait assez fort pour exprimer la gratitude que j'ai envers ma famille et mes amis qui ont toujours été un soutien sans faille pendant ces années. Plus particulièrement pour Elia, il serait vain d'essayer de résumer ici en quelques lignes ma reconnaissance. Je n'aurais jamais assez d'une vie pour te remercier de tout ce que tu m'apportes.

# Table of Contents

# General introduction

In the coastal environment, in river beds, torrents or for material transport in ducts, sediment transport is present in many geophysical or industrial applications. Sediment transport corresponds to mobilization, erosion and deposition of a dispersed phase composed of solid particles in a liquid carrier phase. The generic notion of sediment transport contains a whole diversity of flows, processes and it involves a wide range of spatio-temporal scales. Size of particles, density ratio between the dispersed and carrier phases and flow regimes are one of the many ingredients at the origin of the wide variety of physical mechanisms involved in sediment transport.

In the context of geophysical flows, particles can be organic (micro-organisms, algae, ...) or mineral (sand, pebbles, ...). The latter are generally classified based on their size $d_p$ corresponding to their equivalent diameter. The classification following Wentworth (1922) [123] is presented in table 1.

| Sediment types | | $d_p$ $(mm)$ |
|---|---|---|
| Gravels | Boulders | $\geq 256$ |
| | Cobbles | $64-256$ |
| | Pebbles | $4-64$ |
| | Granules | $2-4$ |
| Sand | Very coarse sand | $1-2$ |
| | Coarse sand | $0.5-1$ |
| | Medium sand | $0.25-0.5$ |
| | Fine sand | $0.125-0.25$ |
| | Very fine sand | $0.0625-0.125$ |
| Silt | Coarse silt | $0.0312-0.0625$ |
| | Medium silt | $0.0156-0.0312$ |
| | Fine silt | $0.0078-0.0156$ |
| | Very fine silt | $0.00390625-0.0078$ |
| Clay | | $0.0001-0.00390625$ |
| Colloid | | $< 0.0001$ |

*Table 1: Mineral sediment classification following following Wentworth (1922) [123].*

Sediment size is crucial to determine the type of interactions occurring between the particles and the carrier phase and between the particles themselves. The smallest particles ($d_p < 0.06mm$), having very small fall velocities, are easily driven and maintained into suspension by the carrier phase turbulence. For such small particles, electrostatic forces between the particles are im-

portant and cohesive behavior such as flocculation can occur. The dynamics of larger particles ($d_p > 2mm$), having a very high fall velocity, are mainly influenced by gravity and they will be transported in the bedload regime (particles rolling or saltating on a still bed). In between these two extremes, sand is composed of particles having intermediate sizes. The particles are big enough for cohesive forces to be negligible and small enough to be driven either in the bedload or in the suspended load regime.

The bottom shear stress $\tau_b$ applied on the bed by a flowing fluid is often taken as the controlling parameter of sediment motion. The corresponding destabilizing force, proportional to $(u_\tau d_p)^2/\rho^f$ with $u_\tau = \sqrt{\tau_b/\rho^f}$ the bottom friction velocity and $\rho^f$ the fluid density can be compared to the stabilizing force proportional the buoyant weight of the particles $(\rho^s - \rho^f)gd_p^3$ with $\rho^s$ the particles density,and $g$ the acceleration of gravity to construct the Shields number

$$\theta = \frac{u_\tau^2}{(s-1)gd_p} \tag{1}$$

where $s = \rho^s/\rho^f$ the density ratio between the particles and the fluid. Particles start to move when the Shields number exceeds a threshold value. The critical Shields number $\theta_c$ for the initiation of motion is a function of the particle Reynolds number

$$Re_p = \frac{\|u^s - u^f\| d_p}{\nu^f} \tag{2}$$

with $u^s$ the particle velocity, $u^f$ the fluid velocity and $\nu^f$ the fluid kinematic viscosity. Typical values of the critical Shields number for sand is $\theta_c \approx 0.05$.

In the coastal environment, great ecological and economical issues related to sediment transport are at stake such as coastal erosion, silting phenomena or ecosystems modifications. In the case of sandy beaches, marine currents, tides and waves are the main mechanisms at the origin of sediment transport. During extreme meteorological events such as storms, waves and currents generated by strong winds can significantly impact the beach dynamics and its morphology.

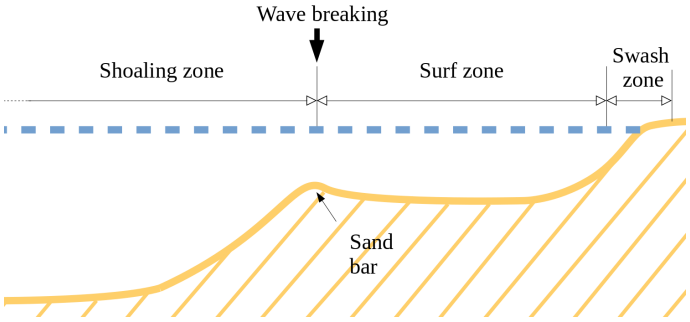


*Figure 1: Schematic representation of the cross-shore profile of a sandy beach.*

A sandy beach morphology is largely influenced by cross-shore hydrodynamic mechanisms and corresponding sediment transport [43, 116]. As illustrated in figure 1, the cross-shore profile of a beach is composed of different zones. Far away from the beach, waves can be considered as sinusoidal (top panel of figure 2). In the shoaling zone, under the effect of decreasing water depth, a combination of velocity and acceleration skewness develops resulting in a greater wave crest (middle panel of figure 2) and a steeper front (bottom panel of figure 2) respectively. Once the wave front is steep enough, waves break above the sand bar generating rollers that travel towards the shoreline through the surf zone. The zone where waves run ashore is called the swash zone. Depending on the cross-shore location, physical processes coming into play are different.

In the shoaling and swash zones, hydrodynamic forcing conditions are intense with strong orbital velocities. During the passage of waves, a whole layer of sediment having a typical thickness on the order of $10 - 60d_p$ [28] is transported in the sheet flow regime. In the surf zone,

where hydrodynamic forcing conditions are less intense, bed forms such as ripples may appear and sediment transport is dominated by sediment-laden vortices generated at the top of the bed forms during successive flow reversals [115]. During storms, intense hydrodynamic conditions are generalized to all the zones. Bed forms are washed away in the surf zone and sheet flow occurs everywhere across the beach profile.

Under the effects of currents and wave asymmetry, the flux of sediment during a wave cycle can be non zero leading to a net transport rate and beach morphological evolution. Knowing the direction and intensity of the net sediment transport rate for a given hydrodynamic condition in the different zones allows to predict the beach morphological evolution. Given the great amount of sand transported during sheet flow, it is of outmost importance to provide relations between sediment flux and hydrodynamic forcing for this flow regime. Furthermore, in the context of climate change, the frequency and intensity of extreme events are expected to increase. Therefore, predicting the beach morphology evolution for intense flow conditions is crucial for the development and protection of the coastal environment.

Sheet flow is characterized by multiple layers of sediment moving on top of the others by sliding, rolling or saltating. In this flow regime, transport is mainly located in a high sediment concentration layer close to the bed where interactions are dominated by friction and collisions between the particles. However, interactions between the particles and turbulence can also play a prominent role. Turbulent coherent structures of the fluid can pull the particles from the bed and drive them into suspension. The suspended sediment flux can contribute for a significant part of the total transport rate especially for fine sand that is more easily suspended.

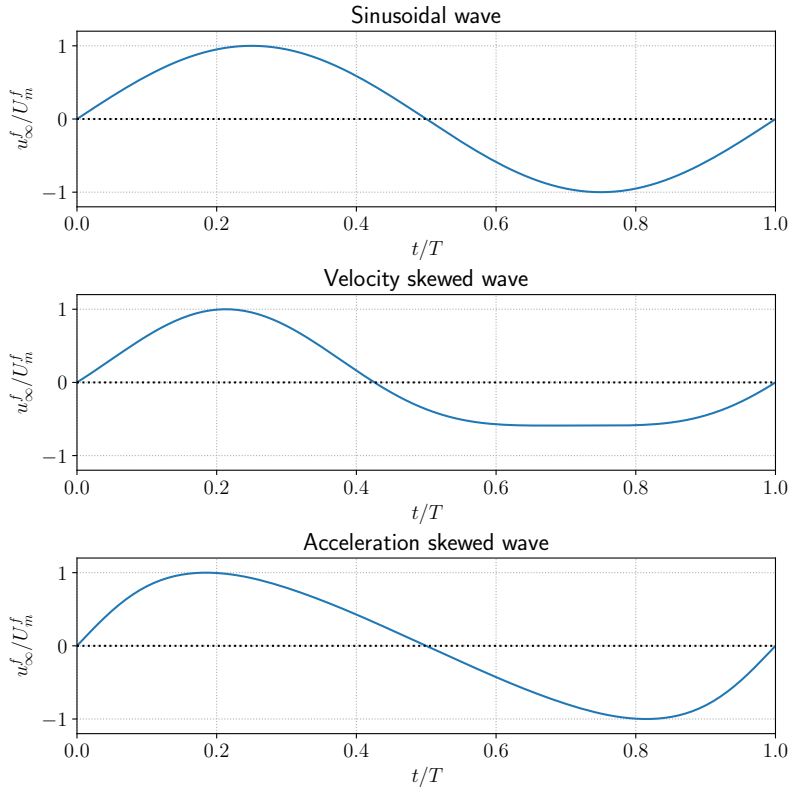


*Figure 2: Time series of free stream velocity $u^f_\infty$ made dimensionless by the maximum free stream velocity $U^f_m$ for a sinusoidal wave (top), a velocity skewed wave (middle) and an acceleration skewed wave (bottom) with $T$ the wave period.*

There is not only an effect of turbulence on the transport of particles but also an effect of the presence of the particles on the turbulence. Depending on flow conditions and particles parameters, the presence of the particles can modulate the surrounding fluid turbulence. Particles can

contribute to increase turbulence in their neighborhood because of wake effects [9] and attenuate it by density stratification [29] or drag induced dissipation [23]. Because of the complexity of the physical processes and the large range of spatio-temporal scales involved in turbulence-particles interactions, they remain not well known especially for finite-size particles (particles having a diameter larger than the smallest turbulent scales). Even if significant progress has been made, turbulence-particle interactions modeling remains an open question. The complex interplay between particles and turbulence and particles themselves is often called four-way coupling.

Given the importance of fine scale physical processes occurring in the bottom boundary layer on sediment transport, our ability to predict the evolution of the coastal environment at large scales relies on our ability to understand and model the fine scale interactions. In this context, this thesis aims at bringing a better characterization of fine scale physical processes involved in sand transport in the sheet flow regime under waves using high resolution numerical simulations. A turbulence-resolving Eulerian two-phase flow model is developed to reproduce experimental configurations of idealized sand transport conditions in the coastal environment. The numerical simulations conducted during this thesis help improving our understanding of the mechanisms occurring in the wave bottom boundary layer for intense flow conditions and provide a deeper insight into the modeling of turbulence-particle interactions.

In the first chapter, a literature review about turbulence-resolving two-phase flow models, their strength and limitations together with a review of the most recent advances in characterizing sediment transport in oscillatory boundary layers is presented to stress the motivations of this thesis. In the second chapter, the turbulence-resolving two-phase flow model sedFoam, its implementation and validation are described. In the third chapter, an analysis on the physical processes involved in oscillatory sheet flow for medium and fine sand is presented. In the fourth chapter, the effect of the wave shape on the net sediment transport rate is investigated. In the fifth chapter, a correction model to take into account finite-size effects is proposed and validated using dilute particle-laden unidirectional boundary layer flow configurations. Finally, conclusions are drawn and perspectives of this work are discussed.

# 1 State of the art and motivations

This chapter presents the state of the art concerning turbulence-resolving methodologies for sediment transport and the recent advances on the characterization of physical processes involved in sheet flow. The objective of this chapter is twofold. First, the contribution of turbulence-resolving methodologies to improve the physical understanding of particle-laden flows is discussed. Strength and limitations of the different approaches are highlighted based on their applicability to a given flow condition and their computational cost. Second, the current knowledge on coastal sand transport in sheet flow regime involving mono-dispersed sand particles based on both experimental and numerical studies is presented. More particularly, the emphasis is set on oscillatory flows and the effects of grain size and wave shape on sand transport.

## Contents

## 1.1 Turbulence-resolving methodologies for sediment transport applications

Our ability to predict the dynamics of the system as a whole relies on our understanding of the fine-scale physical processes such as particle–particle interactions or fluid–particle interactions. As a consequence, the development of modeling methodologies that account for the large number of scales and processes involved in sediment transport is a highly active topic among the sediment transport scientific community [120]. The modeling methodology has to be carefully chosen depending on the available computational resources, flow regime and turbulence-particle interaction regime [9].

In the next sections, different available turbulence-resolving modeling methodologies are presented together with their strength and limitations. Then, guidelines to find the "method of choice" for given flow and particle parameters are provided based on the regime maps proposed by Balachandar (2009) [9] and Finn & Li (2016) [39]. Eventually, recent development of fluid-particle interaction models are presented.

### 1.1.1 Fully resolved direct numerical simulation

Fully resolved direct numerical simulation (FR-DNS) is the most powerful tool to accurately predict physical processes occurring at the grain scale. All the relevant scales of the flow, the fluid-particle interface and, by extension, the fluid–particle interactions are explicitly resolved by solving the incompressible Navier-Stokes equations constituted of the mass and momentum equations

$$\frac{\partial u_i}{\partial x_i} = 0 \tag{1.1}$$

and

$$\frac{\partial \rho^f u_i}{\partial t} + \frac{\rho^f \partial u_i u_j}{\partial x_j} = \frac{\partial \sigma_{ij}}{\partial x_i} + f_i^v + \rho^f g_i + f_i^p \tag{1.2}$$

with $u_i = (u,v,w)^T$ the point velocity of the fluid, $x_i = (x,y,z)^T$ the position vector, $\sigma_{ij}$ the fluid stress tensor, $f_i^v$ the volume forces driving the flow and $f_i^p$ a force term ensuring no-slip boundary condition at the particle interface. Indices appearing twice in a single term implies summation of that term over the three spatial components following Einstein's repeated index notation.

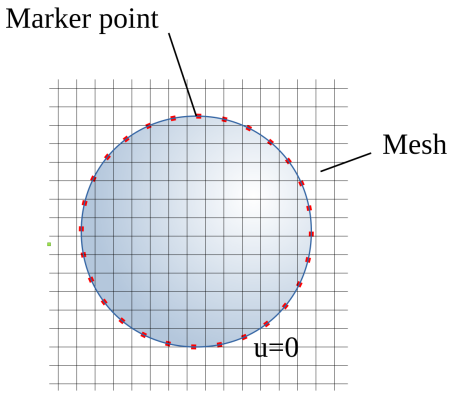


*Figure 1.1: Visual representation of marker points on the particle's surface and background computational mesh for fully resolved direct numerical simulations using immersed boundary method.*

The most popular method to represent the interface between the fluid and the particles for FR-DNS is the immersed boundary method (IBM) [120]. The particle's surface is discretized and tracked using marker points moving inside the fixed mesh (see figure 1.1). Unlike in conventional

methods using body-fitted grids like overset method [121], using IBM prevents the computational mesh to conform to the particle's shape [11, 111].

In sediment transport applications, particles experience multiple collisions and enduring contact especially when they interact with a deposited bed. Accurate description of particle-particle interactions is therefore required to take a full advantage of the predictive capabilities that particle resolved simulations can provide [120]. In FR-DNS applications involving large volume fraction for which particle-particle interactions become important, contacts between particles are usually modeled using discrete-elements method (DEM) based on the soft-sphere approach. The contact force between two particles is assumed to be the contribution of normal and tangential elastic and damping components and a tangential frictional component (see figure 1.2).

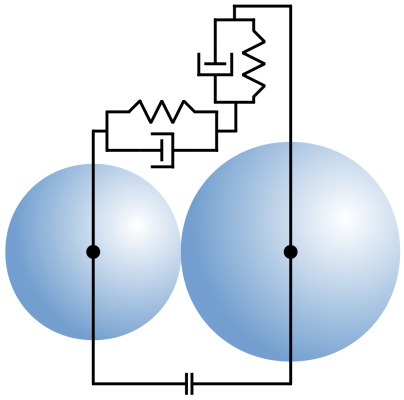

*Figure 1.2: Representation of the contact force modeling between two particles with DEM using the soft sphere approach.*

Eventually, the movement of each particle is computed by integrating the Euler-Newton equations for rigid body motion taking into account forces and torques induced by the fluid, gravity and solid contact between the particles.

Taking advantage of the resolved fluid-particle interactions, FR-DNS is the best method to study finite-size effects (*i.e.* particles larger than the Kolmogorov scale) [60, 128, 129] and the effect of the particle shape [5, 6, 35].

In coastal sediment transport applications, FR-DNS methodology provided significant insight into the mechanisms responsible for initiation of transport [69], ripple formation under steady and oscillatory flows [70, 103] or bed load transport [118]. Given the high resolution required to perform FR-DNS, the applicability of this methodology is limited because of computational costs. More details on the limitations of the FR-DNS methodology are provided in section 1.1.4.

### 1.1.2 Lagrangian point-particle methodology

In the Lagrangian point-particle (PP) methodology, particles are considered punctual. For this assumption to be valid, the grid size must be larger than the particle diameter [9] (see figure 1.3). As a consequence, the flow is not resolved at the particle scale and fluid particle interactions are modeled using empirical correlations. Compared with the FR-DNS methodology, PP methodology is less computationally expensive given the fact that requirements in term of flow resolution can be relaxed. Indeed, the equations can be filtered to perform large-eddy simulation (LES) and still provide quantitative results as long as the effects of unresolved turbulent scales are accurately modeled [9, 39].

Particle trajectories are obtained by integrating thr momentum conservation equation for each particle taking into account hydrodynamic forces and contact forces between the particles follow-

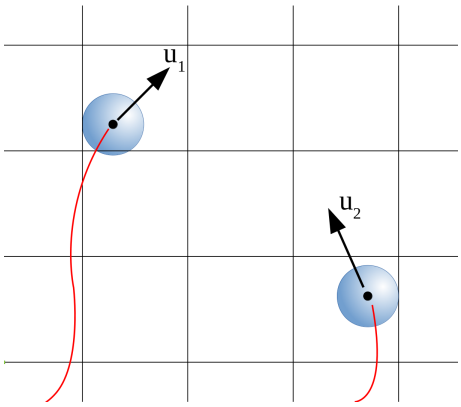


*Figure 1.3: Visual representation of two point-particles and their trajectories.*

ing

$$\rho^s V_p \frac{\partial u_p}{\partial t} = f_i^f + \sum_{q \neq p} f_i^{pq} + \rho^s V_p g_i + f_i^v \tag{1.3}$$

with $V_p$ and $u_p$ the volume and the velocity of particle $p$, $f_i^f$ the hydrodynamic force applied by the fluid on particle $p$ and $f_i^{pq}$ the forces applied by a particle $q$ on particle $p$.

For dilute systems, particle-particle interactions can be neglected. However, for typical sand transport applications, sediment volume fraction can become large. Similarly to FR-DNS, contacts between particles in the PP methodology can be modeled using DEM.

The key challenge to obtain a good representation of the flow using PP methodology is to accurately model $f_i^f$. The most common representation of fluid particle interactions contain the contribution of drag, lift, added mass and Basset history forces [44, 68]. The drag force, function of the relative velocity between the fluid and the particle and the time scale associated with the particle's inertia, acts as a relaxation term, lift forces take into account rotation effects and the non-uniform pressure distribution around the particles, added mass represents the effect of the relative acceleration between the fluid and the particle and Basset history force represents the effect of the time development of the boundary layer around the particle in a non-uniform flow.

Assumptions made to develop these interaction laws are either limited in term of Reynolds number or in term of flow uniformity. The problem intensifies when there is no more separation of scales with particles bigger than the smallest turbulent scale (finite-sized particles) [9]. There is no fundamental objection to model fluid-particle interactions for finite-size particles but complex mechanisms occurring at grain scale should be carefully integrated by taking into account unresolved turbulence-particle interactions using sub-particle models [39]. More details about ongoing development on interaction laws for PP methodology are given in section 1.1.5.

The PP methodology has successfully been applied to sediment transport applications such as particle sedimentation in a turbulent pipe flow [7], unidirectional steady flows [104] or ripples and sheet flow under waves [40]. Given the fact that the trajectories of each individual particles are tracked, the applicability of the PP methodology can be limited by the number of particles involved in the flow. More details on the limitations of the PP methodology are given in section 1.1.4.

### 1.1.3 Eulerian methodology

Other methodologies operate a total change of paradigm compared with the FR-DNS and PP methodology by no longer tracking the trajectories of each individual particles but by having an Eulerian representation of the dispersed phase. The two-phase system is represented by two inter-penetrating continua composed of the dispersed and carrier phase for which local and instantaneous concentrations and velocities are defined everywhere in the domain by performing a

spatial averaging operation (see figure 1.4). More details on the spatial averaging are provided in chapter 2.

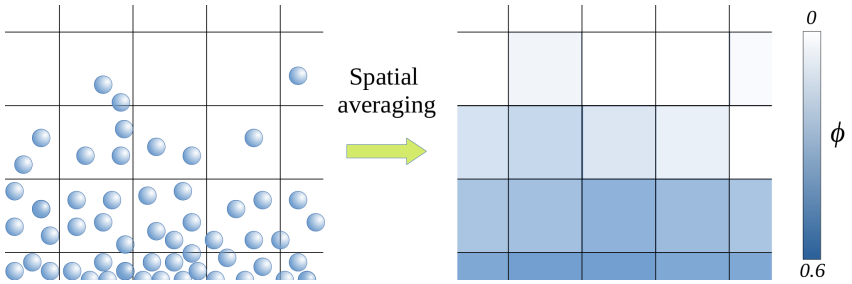


*Figure 1.4: Visual representation of spatial averaging operation for Eulerian representation of the dispersed phase with $\phi$ the volume fraction of particles.*

Depending on the turbulence-particle interaction regime and on the volume fraction, different level of complexity can be found in Eulerian models. For very small particles that perfectly follow the carrier phase, the local dispersed phase velocity is assumed to be equal to the local carrier phase velocity upon which is superimposed the particle settling velocity [39]. Making the so-called passive scalar assumption allows to simplify the numerical resolution of the problem. Compared with single-phase flow models, only one additional mass conservation equation (1.4) for the particles needs to be solved [9]

$$\frac{\partial \phi}{\partial t} + \frac{\partial}{\partial x_i}\left[\left(u_i^f + v_s \frac{g_i}{\|\boldsymbol{g}\|}\right)\phi\right] = \nu^\phi \frac{\partial \phi}{\partial x_i} \tag{1.4}$$

with $\phi$ the sediment concentration, $u_i^f$ the spatially-averaged fluid velocity, $v_s$ the particle fall velocity, $\|\boldsymbol{g}\|$ the norm of the acceleration of gravity and $\nu^\phi$ the sediment diffusion coefficient. This model can be extended by including a relaxation equation for the particle phase velocity to capture more accurately the velocity difference that can exist between the particles and the carrier phase [37]. Given the fact that the dispersed phase is assumed to be in equilibrium with the carrier phase, this modeling methodology will be referred to as equilibrium-Eulerian (EE) methodology in the following.

For increasing particle sizes and volume fraction, the particles do not exactly follow the carrier phase and the effect of particle-particle interactions can no longer be neglected. A more complex set of equations is required to represent the two-phase system including coupled mass and momentum equations for both the carrier and the dispersed phase together with an energy equation for the particles [9]. This modeling methodology will be referred to as the two-fluid (TF) methodology. The momentum exchange between the two phases is not resolved but modeled using spatially averaged contributions of the drag, added mass and lift forces. Concerning the Basset history force, given the fact that it is defined from a purely Lagrangian point of view and not from local and instantaneous flow variables, it would be very difficult if not impossible to obtain its average expression for the Eulerian formalism and should therefore be neglected. Derivation of the TF model and closure models are detailed in chapter 2.

Similarly to the PP methodology, the assumptions made to derive TF models comprise grid size larger than the particle diameter and scale separation. Equations can be filtered to perform LES as long as a appropriate sub-grid closures are provided. Furthermore, similarly to PP methodology, there is no fundamental objection for simulations involving finite-size particles as long as sub-particle interactions are modeled [39].

The EE methodology has been extensively used to study fine sediment transport in turbidity currents [16, 101] or oscillatory flows [24, 83, 84, 130]. TF methodology has mostly been used for gas-solid applications such as fluidized beds [1, 85]. The development of the turbulence-resolving TF methodology for sediment transport applications is more recent providing quantitative results

for simulations of unidirectional sheet flow [23] and qualitative results for oscillatory sheet flow configurations [21].

### 1.1.4 Method of choice

Depending on the flow regime and the number of particles involved, the appropriate turbulence-resolving modeling methodology to predict the evolution of a given two-phase system should be carefully chosen relative to the available computational resources and the turbulence-particle interaction regimes.

FR-DNS methodology is obviously the most relevant tool to provide statistical description of physical processes that can eventually be used as constitutive equations for larger scales sediment transport models [120]. However, this modeling methodology suffers from important limitations in term of flow regimes and number of particles because of the computational expense induced by the wide range of flow scales that needs to be resolved. Even with nowadays available computational power, typical configurations investigated using FR-DNS are still far away from the most energetic conditions present in the river or coastal environment. The most energetic oscillatory flow conditions investigated recently using FR-DNS by Mazzuoli *et al.* (2019) [70], Mazzuoli *et al.* (2020) [69] and Vittori *et al.* (2020) [118] corresponded to Shields numbers $\theta$ on the order of 0.5 whereas typical values of $\theta$ encountered in the coastal region can be up to ten times larger [81]. Configurations involving the presence of a deposited bed require modeling of a large number of particles. As the flow regime becomes more energetic, the transport layer thickness becomes larger and the number of moving particles that needs to be tracked increases drastically. The same limitation applies to the PP methodology. Even if the flow regime in term of Reynolds number can be relaxed by performing LES [9, 39], the greater number of moving particles for flow regimes increasing in intensity greatly limits the applicability of the PP methodology for the most energetic conditions encountered in the environment. As an example, the oscillatory sheet flow configuration from O'Donoghue & Wright (2004a) [81] involving medium sand with median diameter $d_{50} = 280\mu m$ has been successfully reproduced by Finn *et al.* (2016) [40] using a point-particle model. Despite the effort made to reduce the number of particles to be tracked in the numerical domain, their simulations involved 3.8 million particles. Compared with configurations simulated by Finn *et al.* (2016) [40], other configurations involving smaller particles subjected to a similar flow forcing, the Shields number, inversely proportional to $d_p$, will become even greater. As a consequence of the linear relation between the Shields number and the transport layer thickness made dimensionless by $d_p$ [109], the number of transported particles to be tracked would increase by several orders of magnitude making the computational cost of such simulations prohibitive.

Given the absence of limitations in term of number of particles using the Eulerian methodology, EE and TF models have a great advantage compared with Lagrangian methodologies to predict the evolution of sediment transport systems involving intense flow regimes and a large number of particles. However, the assumptions made to derive the EE and TF models are restrictive having for effect to narrow their range of applicability in term of turbulence-particle interaction regimes.

As pointed out in the descriptions of the modeling methodologies, the scale separation between the flow and the particles, the capacity of a particle to follow the carrier phase fluctuations and turbulence modulation induced by the particles come into play in the choice of a modeling methodology for a given two-phase system. More specifically, the important flow parameters orienting the choice of the modeling methodology are the size ratio $d_p/\eta$ with $\eta$ the length scale associated with the smallest turbulent flow scales (or Kolmogorov length scale), the stokes number $St = t_s/t_\eta$ with $t_s$ the particle response time and $t_\eta$ the time scale associated with the smallest turbulent flow scales (or Kolmogorov time scale), and the particle Reynolds number $Re_p$.

During the last four decades, many studies represented regime maps of turbulence-particle interactions using scaling laws based on these three parameters in order to provide guidelines to select the "method of choice" [9, 32–34]. More recently, Finn & Li (2016) [39] re-casted

Balachandar (2009) [9] scaling relations for sediment transport applications in terms of Shields parameter defined in equation (1) and Galileo number

$$Ga = \frac{\sqrt{(s-1)gd_p^3}}{\nu^f}. \tag{1.5}$$

Figure 1.5a illustrates this map for typical values of the density ratio in sediment transport application $s = 2.65$ with $\rho^s = 2650\ kg.m^{-3}$ for natural sediment particles and $\rho^f = 1000\ kg.m^{-3}$ for water. Lines of constant suspension numbers $v_s/u_\tau = 0.3$, 1 and 5 representing the ratio between a velocity scale associated with gravitational settling and a velocity scale associated with turbulent intensity are also represented on the regime map. The suspension number characterizes the capability of the carrier phase turbulence to suspend particles by representing the relative importance of bed load compared with suspended load. Decreasing suspension number corresponds to greater fraction of the suspended load in the total transport. For values significantly higher than unity, sediments are transported as bed-load only (no-suspension) while for values lower than 0.3 sediments are transported as wash-load and never settle to the bed. In between these two extreme values, bed load and suspended load coexist. The regime map is divided into five regions corresponding to different dominant turbulence-particle interactions.

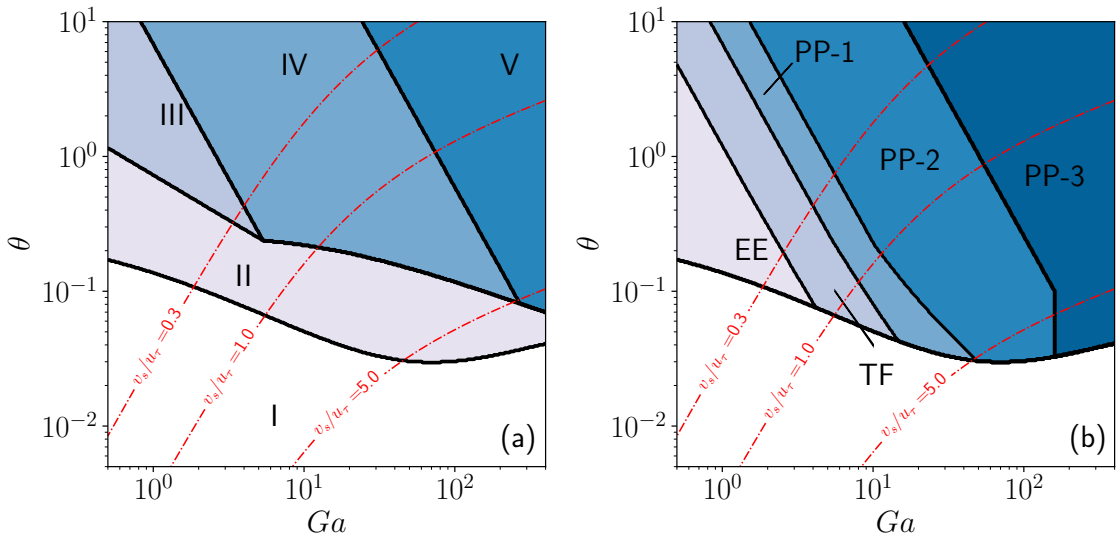


*Figure 1.5: Turbulence-particle interactions regime map (panel (a)) and method of choice (panel (b)) for sediment transport applications with $s = 2.65$ from Finn & Li (2016) [39].*

The first regime (regime I in panel (a) of figure 1.5) corresponds to values of the Shields parameter lower than the critical value for which particles are not moving. In regime II, gravitational settling dominates and the carrier phase turbulence is too weak to suspend the particles. In regime III, corresponding to rather fine particles and energetic flow conditions ($St < 1$ and high $\theta$) the upward turbulent sediment flux associated with Kolmogorov scale exceeds the gravitational settling flux to lead to the existence of a turbulent suspension. In this regime, the particles behave almost as passive tracers of the carrier phase velocity fluctuations. In regimes IV and V, the particle Stokes number is higher than unity $St > 1$ and the particles dynamics is primarily influenced by an inertial eddy scale having a time scale that matches the particle response time. The length scale associated with these eddies is denoted as $l^* = t_s^{3/2}\varepsilon^{1/2}$ with $\varepsilon$ the dissipation rate of turbulent kinetic energy (TKE). The difference between regime IV and V is the modulation of the carrier phase turbulence induced by the presence of particles. In regime IV, turbulence-particle interactions essentially lead to a net dissipation of TKE corresponding to particulate Reynolds number lower than a certain crit-

ical value ($Re_p < 400$). For higher values of $Re_p$, the particle wakes becomes oscillatory leading to a net production of turbulence (regime V).

In panel (b) of figure 1.5, the map for the "method of choice" suggested by Finn & Li (2016) [39] are presented for $s = 2.65$. For particles having a response time smaller than the Kolmogorov time scale ($St < 0.2$), there is no need to have a complex representation of the two-phase system. The action of individual particles does not affect the fluid turbulence, the time scales associated with the particles are smaller than the Kolmogorov time scale meaning that particles follow exactly the fluid motion. In that case, the use of EE methodology is greatly justified given the very low computational resources required to predict the evolution of the two-phase flow system. For higher Stokes numbers ($St > 0.2$) more sophisticated models such as TF models, PP models or FR-DNS models are required to take into account the couplings between the particles and the carrier phase turbulence.

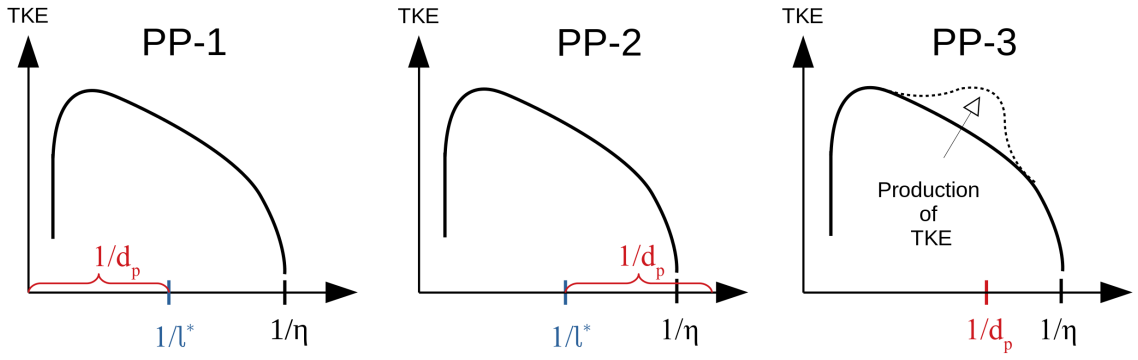


*Figure 1.6: Idealized TKE spectrum and flow scales in regions of the map PP-1 (left panel), PP-2 (middle panel) and PP-3 (left panel) from panel (b) of figure 1.5.*

According to Balachandar (2009) [9] and Finn & Li (2016) [39], for inertial particles, corresponding to $St > 1$, the PP approach is the method of choice. The region of the map for which $St > 1$ can be divided into three sub-regions depending on the regime of turbulence-particle interactions (see panel (b) of figure 1.5). In the PP-1 region, the grid size $\Delta$ should be smaller than the particle diameter to resolve $l^*$ and a sub-particle scale correction model is needed to accurately predict the particle dynamics (left panel of figure 1.6). In the PP-2 region, $l^*$ is greater than the particle diameter meaning that the particle relative velocity can be accurately predicted from the resolved flow scales because the grid size can be chosen such that $l^* > \Delta > d_p$, *i.e.* a separation of scale exists between the particle size and the most efficient eddy sizes for particles dynamics (middle panel of figure 1.6). Eventually, in the PP-3 region, the presence of particles leads to increase the production of turbulence and $Re_p > 400$ (right panel of figure 1.6). In this regime, either FR-DNS should be used or the PP methodology should incorporate additional models to account for the unresolved sub-particle scale turbulence production processes [39].

According to the authors, the TF approach is only suited in a narrow band of the regime map for $0.2 < St < 1$. Indeed for $St > 1$, the uniqueness of the Eulerian particle phase velocity field is not guaranteed [36]. In other words, for a given fluid phase velocity field, the particles can follow different paths (*i.e.* the particles velocity field is not unique) depending on the initial condition. Nevertheless, uniqueness of the particle phase velocity is not crucial considering time-averaged particle phase quantities (*e.g.* concentration, velocity) and assuming ergodicity. More precisely, time-averaged variables are issued from multiple realization of the flow and, therefore, multiple particles trajectories. However, similarly to the point-particle approach, for finite-sized particles, there is no clear separation of scales between the turbulent motions and the particle size and additional sub-particle scale correction models are required.

As a consequence of supposedly narrow range of applicability of the TF model compared with

the large number of scales involved in sand transport, the scientific community under-estimated the predictive capabilities of the TF model and preferred the PP methodology at its expense. However, parameter ranges provided by scaling analysis are not fixed and can even overlap [9, 39, 120]. Therefore, taking advantage of the opportunity to overcome the limitation in term of the number of particles to simulate intense flow configurations such as oscillatory sheet flow using the TF model is crucial.

However, fluid-particle interactions laws derived for idealized flow conditions should be improved to cover the widest range of flow and particle parameters using the TF model and further extend its range of applicability. The recent advances in fluid-particle interaction models are presented in the next section.

### 1.1.5 Toward the improvement of fluid-particle interaction modeling

Classical fluid-particle interaction laws based on a drag coefficient are derived for particles smaller than the Kolmogorov length scale in a non-uniform flow in the limit of small Reynolds numbers [44, 68]. This assumption is no longer valid for most sediment transport applications [120]. The Reynolds number dependency of the drag law is generally accounted for using empirical corrections obtained from either experiments or numerical simulations but taking into account finite-size effects is not trivial [120].

Experimental studies [86, 119, 126] provided evidence that finite-size particle dynamics is substantially affected by turbulent flow scales smaller than the particles compared with the case of particles smaller than the Kolmogorov length scale. It is therefore necessary to account for the inhomogeneity of the flow at the particle scale for the case of finite-size particles [48]. All the studies agreed on the facts that the variance of the acceleration probability density functions decreases for increasing particle size. These experimental observations have been further confirmed by numerical studies using FR-DNS or PP methodology [15, 48, 51, 119].

One way to recover some of the features of finite-size particle acceleration probability density function is to include the Faxén correction term in the fluid-particle interaction model. The Faxén correction term takes into account the non-homogeneity of the flow in the particle's neighborhood by including the integral of the flow velocity and acceleration over the surface and the volume of the particle respectively in the definition of the interaction forces. By means of approximations, Calzavarini *et al.* (2009) [15] successfully implemented the Faxén correction term and tried to reproduce acceleration statistics of finite-size particles from experimental configurations of Voth *et al.* (2002) [119] and Qureshi *et al.* (2007) [86]. They managed to recover some of the features of the particles acceleration such as the reduction of particle acceleration fluctuations and increase of acceleration time correlation for increasing particle size.

Defined from a purely Lagrangian point of view, implementing the Faxén correction term in the Eulerian framework appears to be a very challenging task. A more Eulerian friendly modeling approach to take into account finite-size effects would be more useful.

Gorokhovski & Zamansky (2018) [48] proposed a sub-grid closure for the PP methodology to account for the effect of unresolved turbulent flow scales in fluid-particle interactions for both small and finite-size particles. In their model, large scale contributions of the instantaneous particle acceleration is given by resolved flow scales and the effect of unresolved flow scales is taken into account by the addition of a random contribution modeled using a stochastic approach.

For particles larger than the Kolmogorov length scale, the effect of turbulent flow scales smaller than the particle is taken into account by replacing the fluid viscosity in the drag model by an effective viscosity at the scale of the particle defined as the sum of the fluid viscosity $\nu^f$ and the turbulent viscosity at the particle scale $\nu_p^t$. From mixing length hypothesis and Kolmogorov theory, Gorokhovski & Zamansky (2018) [48] showed that $\nu_p^t$ scales with the particle diameter $d_p$ and the local and instantaneous dissipation rate of TKE at the particle scale $\varepsilon_p$ following

$$\nu_p^t \sim \varepsilon_p^{1/3} d_p^{4/3}. \tag{1.6}$$

Rather than only acting as a temporal filter, the drag law now also acts as a spatial filter. Turbulent flow scales larger and smaller than the particle diameter will contribute differently to the particle dynamics.

While the use of the Faxén correction term is suitable for Lagrangian simulations, the methodology developed by Gorokhovski & Zamansky (2018) [48], taking into account finite-size effect through an effective viscosity at the particle scale included in the expression of the drag force, is more suitable for volume-averaged two-phase flow models such as the TF model. Indeed, the definition of turbulent viscosity at the scale of the particle can be function of the Eulerian flow variables.

## 1.2 Sand transport in the sheet flow regime

Classical sand transport applications in the coastal environment correspond to Galileo numbers on the order of $Ga \sim \mathcal{O}(1-100)$ and Shields numbers $\theta \sim \mathcal{O}(0-10)$ covering all the turbulence-particle interaction regimes discussed in section 1.1.4. Furthermore, for unsteady flows occurring in sediment transport configurations under waves for example, the Shields number is not constant throughout the wave period. As a consequence, a wide variety of turbulence-particle interaction regimes coexist at different moments or different locations resulting in complex transport mechanisms.

Given the importance of the sheet flow transport regime in the morphological evolution of sandy beaches, a lot of effort has been put into understanding the relations between intense flow conditions and the corresponding sand transport. In the last three decades, the conjunction of experimental and numerical investigation of sheet flow in unidirectional and oscillatory boundary layer, an idealization of the wave bottom boundary layer, provided significant insight into sand transport processes [97].

In this section, the knowledge acquired on sheet flow from experiments in flumes and oscillating water tunnels (OWTs) are first presented. Then, the insight provided by single phase flow models and turbulence-averaged two-phase flow models on the physical processes occurring in oscillatory sheet flow is discussed. Eventually, the limitations of the aforementioned models to accurately simulate oscillatory sheet flow are debated to introduce the motivations for performing turbulence-resolving two-phase flow simulations.

### 1.2.1 Investigation of sheet flow processes at the laboratory scale

#### Unidirectional sheet flow

In a first attempt to predict sand transport in the sheet flow regime as a function of macroscopic parameters of the flow and characterize underlying physical processes, unidirectional sheet flow experiments were performed. Whereas early experimental investigations mainly focused on relating the dimensionless streamwise sediment flux

$$Q^* = \frac{Q}{\sqrt{(s-1)gd_{50}^3}} \tag{1.7}$$

to the Shields number $\theta$ using power laws of the form $Q^* = m(\theta - \theta_c)^n$ [125], experiments from Sumer *et al.* (1996) [109] focused on the vertical structure of the flow. Detailed measurements of sediment concentration and flow velocity from dense to more dilute regions of the flow allowed to highlight features of the velocity profile in the near bed region and to characterize flow resistance and sheet flow layer thickness as a function of the Shields number. The authors showed

that the apparent roughness increases for increasing Shields number and that the dimensionless sheet flow layer thickness $\delta_s/d_{50}$ increases linearly with the Shields number. From figure 1.7, the dimensionless sheet flow layer thickness is well represented by the relation

$$\frac{\delta_s}{d_p} = 13\theta. \tag{1.8}$$

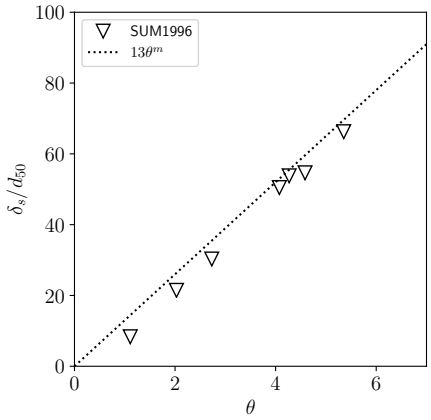


*Figure 1.7: Sheet flow layer thickness made dimensionless by the median diameter $\delta_s/d_{50}$ as a function of the Shields number $\theta$ from Sumer et al. (1996) [109].*

Considering the wide range of flow and particle parameters investigated by Sumer *et al.* (1996) [109], their experimental configurations have been extensively used as model validations [20, 76, 87]. However, velocity and concentration were not measured simultaneously.

Taking advantage of the collocated measurements of concentration and velocity that offer the acoustic concentration and velocity profiler (ACVP) [54], unidirectional sheet flow experiments from Revil-Baudard *et al.* (2016) [89] provided significant insight into turbulent processes occurring inside the sheet flow layer, especially the effect of the bed-level variability and the modification of the von Kármán parameter in the expression of the logarithmic velocity profile. This experimental configuration has been reproduced numerically using a TF model for LES by Cheng *et al.* (2018) [23]. The numerical study from Cheng *et al.* (2018) [23] is the first reported use of the turbulence-resolving TF model for sediment transport applications. Comparison between average Reynolds stress, velocity and concentration profiles from experiments and simulations using the TF model with three different resolutions are presented in figure 1.8.

Overall, the agreement between numerical simulation and experimental measurements is satisfactory. However, sediment suspension is under-estimated by the TF model in the upper section of the flow with a significant grid size dependency.

The LES model used by Cheng *et al.* (2018) [23] integrates a sub-grid closure model for fluid-particle interactions developed by Ozel *et al.* (2013) [85] for fluidized bed applications. The sub-grid model takes into account the effect of unresolved mesoscale structures formed by preferential concentration of particles in the momentum exchange term between the two phases. Considering that typical length scale associated with the mesoscale structures is on the order of 10 to 100 particle diameters [1] and that the resolution of the simulations presented in Cheng *et al.* (2018) [23] is on the order of the particle diameter or smaller, mesoscale structures are resolved and the use of the sub-grid closure for fluid-particle interactions is not ideal. From concentration profiles given by simulations without the use of the sub-grid model (not shown), particle suspension is even more under-estimated.

In the sheet flow configuration investigated by Revil-Baudard *et al.* (2016) [89] and Cheng *et al.* (2018) [23], particles are bigger than the Kolmogorov scale. Finite-size effect probably play

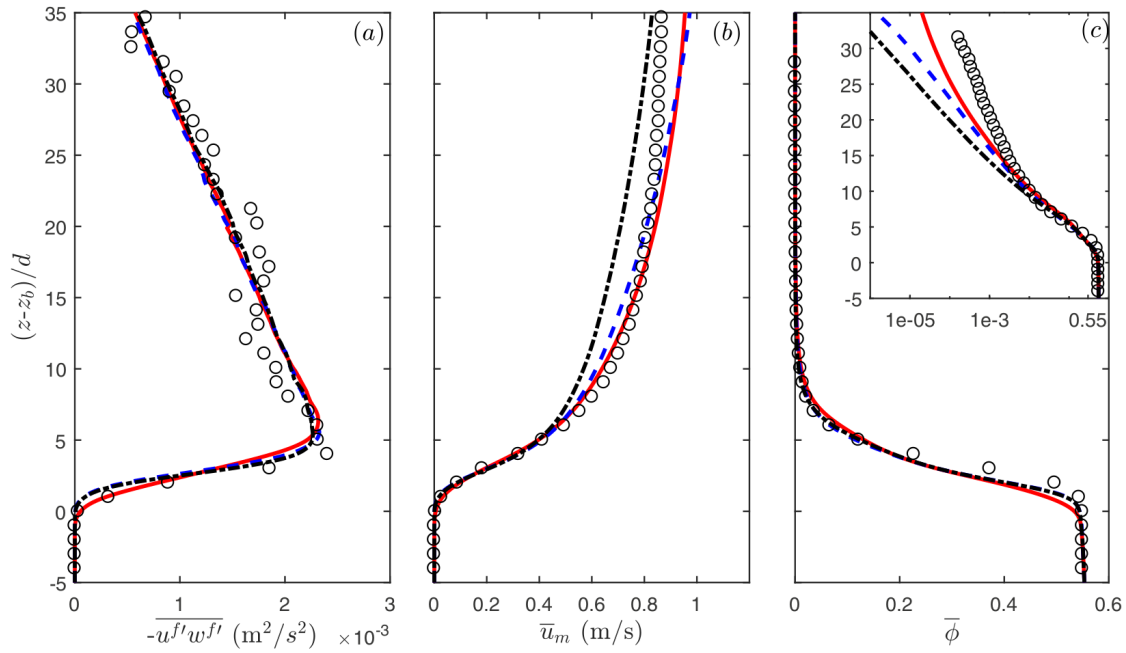


*Figure 1.8: Profiles of averaged Reynolds stress in panel (a), velocity in panel (b) and concentration in panel (c) from experiments (symbols) and numerical simulations using the TF model with a coarse resolution (dash dotted black line), a medium resolution (dashed line) and a fine resolution (solid line) from Cheng et al. (2018) [23]. In this figure, $z$ is the vertical coordinate, $z_b$ is the bed level, $d$ is the particle diameter, $\overline{\cdot}$ is the ensemble averaging operator, $u^{f'}$ and $w^{f'}$ are the streamwise and spanwise fluid velocity fluctuations, $u_m$ is the streamwise mixture velocity and $\phi$ the sediment concentration.*

an important role and shall be modeled to accurately predict the vertical distribution of particles.

Even if the investigation of unidirectional sheet flow helps providing relations between sand transport rate and macroscopic flow parameters, investigation of oscillatory sheet flow configurations, more representative of the wave bottom boundary layer is necessary to be able to predict morphological evolution in the coastal environment.

### Oscillatory sheet flow

Performing experiments in OWTs allows to reproduce idealized near-shore sediment transport configurations in a controlled way. In OWTs, a piston is located at one end of the tunnel and the other end is open to the atmosphere (see figure 1.9). The back and forth motion of the piston allows to mimic the time dependent pressure gradient induced by the free surface oscillations.

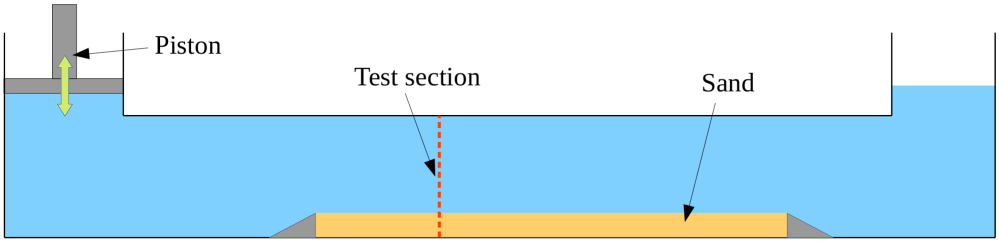


*Figure 1.9: Schematic representation of an oscillating water tunnel (OWT).*

Water tunnel experiments allows to provide important data to derive empirical descriptions of the physical processes and to develop and test numerical models [81]. Indeed, they offer the advantage to be easily reproduced numerically because of the absence of a free surface. However, compared with real waves, free surface effects such as progressive wave streaming and spatial non-uniformity of the flow in the direction of the wave propagation are not reproduced in OWTs [28]. Nevertheless, flows generated in water tunnels remain a good approximation of flows occurring under real waves [82].

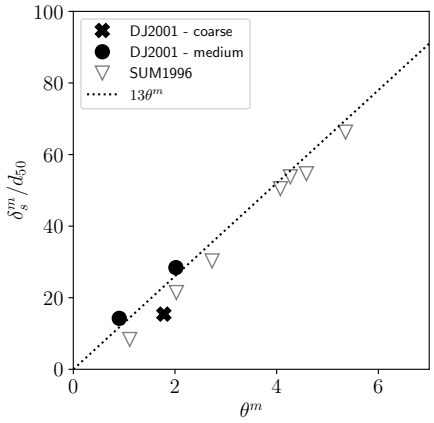


*Figure 1.10: Maximum sheet flow layer thickness made dimensionless by the median diameter $\delta_s^m/d_{50}$ as a function of the maximum Shields number $\theta^m$ from Dohmen-Janssen et al. (2001) [29] ans Sumer et al. (1996) [109].*

From comparative experiments performed in an OWT and a wave flume, Dohmen-Janssen & Hanes (2002) [28] showed that the behavior of oscillatory sheet flow is the same between the two experimental facilities for a given wave condition. However, vertical contributions of the orbital

velocity present under progressive waves are suppressed in a water tunnel having for effect to slightly decrease the vertical diffusion of particles into the flow.

Time dependent concentration measurements in OWTs experiments allowed to describe the behavior of the sheet flow transport layer. Experiments involving medium sand of median diameter $d_{50} = 210\ \mu m$ under velocity skewed and sinusoidal flow forcing typical from the near shore environment with maximum free stream velocity $U^f_{max} \sim \mathcal{O}(0.5 - 1.5\ m.s^{-1})$ and wave period $T \sim \mathcal{O}(6-9\ s)$ from Ribberink & Al-Salem (1995) [92] and Dohmen-Janssen & Hanes (2002) [28] showed that the sheet flow layer thickness $\delta_s$ has a typical size of 10 to 60 particle diameter. In their definition, $\delta_s$ is calculated as the difference between the erosion depth $\delta_e$ corresponding to the bed level at which the fluid velocity goes back to zero and the bed level at which the sediment concentration is equal to $\phi = 8\%$ corresponding to location where inter-particle collisions become less dominant.

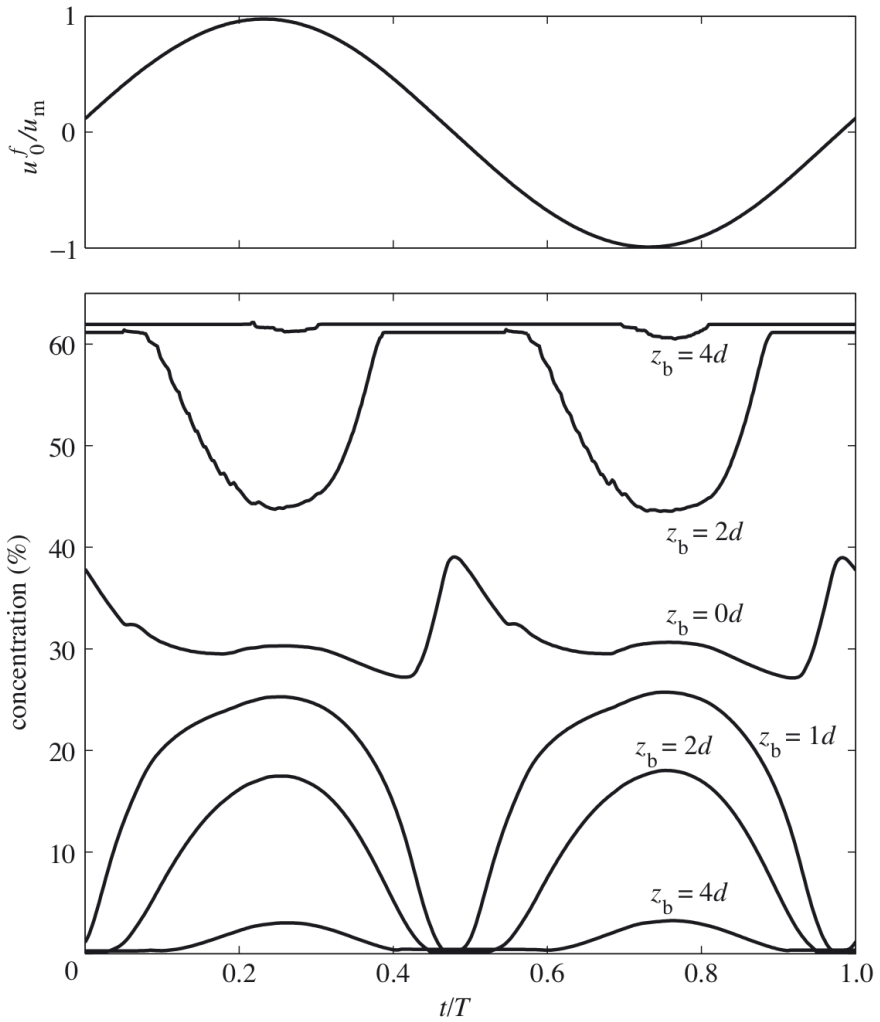


*Figure 1.11: Time series of sediment concentration in percent at different elevations (denoted $z_b$ as a fraction of the particle diameter d in this figure) in the pick-up layer (positions $z_b = 2d$ and $z_b = 4d$ under the initial bed level), in upper sheet flow layer (positions $z_b = 1d$, $z_b = 2d$ and $z_b = 4d$ above the initial bed level) and at initial bed level (position $z_b = 0d$) in the bottom panel compared with the free stream velocity as a fraction of its maximum value ($u_0^f/u_m$ in this figure) in the top panel taken from Hsu et al. (2004) [53].*

Furthermore, the authors stressed the fact that the dimensionless maximum sheet flow layer

thickness $\delta_m^s/d_{50}$ increases linearly with the maximum Shields number $\theta^m$. Similarly to the steady sheet flow configurations from Sumer *et al.* (1996) [109], Dohmen-Janssen *et al.* (2001) [29] showed that the dimensionless maximum sheet flow layer thickness for configurations involving medium and coarse sand is well represented by expression (1.8) (see figure 1.10) .

In other words, for the flow and particle parameters investigated in their experiments, the evolution of the sheet flow layer thickness during the wave can be represented as a succession of quasi-steady states.

In more details, Ribberink & Al-Salem (1995) [92] and Dohmen-Janssen & Hanes (2002) [28] highlighted the existence of three layers in the sediment concentration profile. In the lower part of the sheet flow layer called the pick-up layer, successive erosion and deposition phases occur during acceleration and deceleration phases of the wave respectively. In the upper part of the sheet flow layer, concentration increases during acceleration phases and decreases during deceleration phases. Above the sheet flow layer, the suspension layer is characterized by dilute particles driven into suspension by the carrier phase turbulence. Typical time series of sediment concentration in the pick-up layer and upper sheet flow layer for oscillatory sheet flow configurations involving medium or coarse sand are compared with the free stream velocity in figure 1.11.

In the upper sheet flow layer, concentration is in phase with the free stream velocity. Between the pick-up layer and the upper sheet flow layer, concentration is in opposition of phase because of the vertical exchange of sediment between the two layers during acceleration and deceleration phases of the waves. From observations made by Ribberink & Al-Salem (1995) [92], at the top part of the sheet flow layer (bottom of the suspension layer), the maximum concentration corresponds to the moment of highest orbital velocity. The higher up in the suspension layer, the larger the phase shift between concentration and flow velocity becomes.

Visually, this evolution of the concentration profile can be represented as a clockwise rotation of the concentration profile around an almost constant concentration "pivot" during flow acceleration resulting in a decrease in concentration in the pick-up layer and an increase in the upper sheet flow layer layer and an anticlockwise rotation resulting in an increase of the concentration of the pick-up layer and a decrease in the upper layer as sediments settle back to the bed during flow deceleration [81] (see figure 1.12).

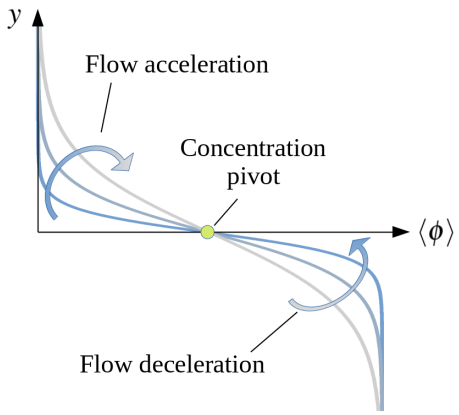


*Figure 1.12: Schematic representation of the concentration profile rotating clockwise during flow acceleration and anti-clockwise during flow deceleration around the concentration pivot (drawn from O'Donoghue & Wright (2004a) [81]).*

From their experiments involving similar flow forcing compared with Ribberink & Al-Salem (1995) [92] and Dohmen-Janssen & Hanes (2002) [28] and different type of sand, O'Donoghue & Wright (2004a) [81] provided quantitative description of intra-wave sediment concentration profiles. Based on their observations the concentration profile can be well characterized by the erosion depth $\delta_e(t)$ and a reference concentration $\phi_0$ at a reference bed level $y_0$ taken at the top of

the pick-up layer where concentration is relatively constant following the power law

$$\langle \phi \rangle (y,t) = \frac{(y_0 - \delta_e(t))^{\alpha_\phi}}{(y_0 - \delta_e(t))^{\alpha_\phi} + \left(\frac{1}{\phi_0} - 1\right)(y - \delta_e(t))} \tag{1.9}$$

with $\langle \cdot \rangle$ the phase averaging operator, $\alpha_\phi$ an empirical coefficient and $y$ the vertical space coordinates.

For more severe wave conditions (greater maximum free stream velocity or shorter period), the effect of the pressure gradient can become dominant at flow reversal resulting in a totally different sheet flow layer behavior. Experimental studies from Zala-Fores and Sleath (1998) [131] and Sleath (1999) [107] revealed the existence of a bed failure and formation of a plug flow under strong flow acceleration. For pressure gradient higher to a certain threshold, the bed loses its yield strength and sediments move as a single block like a plug. As flow velocity increases, a shear layer develops having for effect to erode the plug and the sheet flow layer recovers classical characteristics but with a much larger thickness.

To characterize the flow acceleration, a dimensionless parameter called the Sleath parameter $Sl = U^f_{max}\omega/(s-1)g$ with $\omega = 2\pi/T$ the angular frequency has been introduced by Sleath (1999) [107]. Based on a force balance analysis, Sleath (1999) [107] found the threshold value for plug formation to be $Sl > 0.3$ but field measurements highlighted the occurrence of plug flow for values of Sleath parameter as low as $Sl = 0.1 - 0.2$ [41]. The threshold for plug flow can be modified by (i) the compaction of the sediment bed [107] and (ii) the Shields number [22, 41]. On the one hand, the lesser the sediment is compacted, the lower the yield strength of the bed and the lower the pressure gradient is necessary to generate the plug flow. On the other hand, the higher the Shields number is, the deeper the mobile sediment layer is during flow acceleration, the looser the sediment bed becomes at the next flow reversal having for effect to alter the yield strength of the sediment bed.

Experimental studies also provided information of the sediment flux and velocities inside the sheet flow layer. From velocity measurements, Dohmen-Janssen *et al.* (2001) [29] pointed out the fact that the apparent bed roughness is increased by the presence of the sheet flow layer with a roughness length scale on the order of the sheet flow layer thickness. Similarly to observations made for steady sheet flow by Sumer *et al.* (1996) [109], greater flow resistance is observed for increasing sheet flow layer thickness due to inter-particles and turbulence-particle interactions, especially turbulence attenuation due to stable density stratification.

Flux measurements performed by O'Donoghue & Wright (2004b) [82] confirmed the observation made by Dohmen-Janssen & Hanes (2002) [28] that given the strong velocities and concentration close to the bed, most of the transport happen in the sheet flow layer. For sinusoidal waves, the net flux generated during a full wave cycle is zero. Indeed, the onshore directed sediment flux generated during the first half of the wave is balanced by the offshore-oriented sand flux generated during the second half of the wave because of flow symmetry. However, when flow asymmetry comes into play, the sediment flux generated during the first and the second half of the wave do not balance each other and a net sediment flux is observed. Given the fact that the cross-shore morphological evolution of a beach is controlled by the net sediment flux generated under waves, the effect of wave shape on oscillatory sheet flow has been intensively investigated.

For experimental configurations involving medium and coarse sand under velocity skewed waves, Ribberink & Al-Salem (1995) [92], O'Donoghue & Wright (2004b) [82] and Dohmen-Janssen *et al.* (2002) [30] observed a net onshore-oriented sand flux. As a result of the higher amplitude of the flow forcing during the wave crest (see middle panel of figure 2 in the general introduction), the amount of sediment transported onshore is greater than the amount of sediment transported offshore during wave trough. However, Ribberink & Al-Salem (1995) [92] noticed a small offshore sand flux in the upper section of the suspension layer due to phase-lag effects. For

these particle and flow conditions, contributions of the flux from phase-lag effects are not strong enough to generate a net offshore-oriented sand flux.

Acceleration skewed waves are symmetric (see bottom panel of figure 2 in the general introduction) but an onshore-oriented net flux in the direction of the strongest acceleration is observed [93, 105, 112]. As a consequence of a stronger acceleration during wave crest, the amount of sediment transported onshore is larger compared with the amount of sediment transported during wave trough. The net sand flux increases for increasing acceleration asymmetry. The quantity of sand transported under acceleration skewed waves is comparable to the one transported under velocity skewed waves for comparable free stream velocity amplitude and flow period demonstrating the importance of acceleration skewness in oscillatory flows [112].

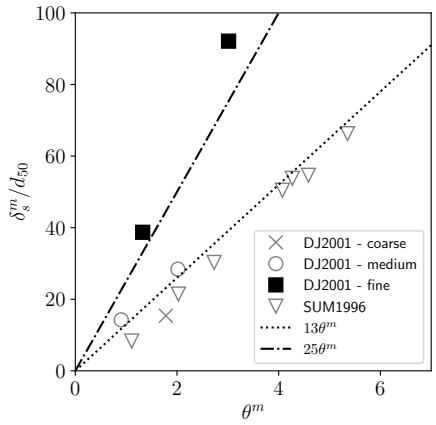


*Figure 1.13: Maximum sheet flow layer thickness made dimensionless by the median diameter $\delta_s^m/d_{50}$ as a function of the maximum Shields number $\theta^m$ from Dohmen-Janssen et al. (2001) [29] and Sumer et al. (1996) [109].*

One of the factor playing a major role in the behavior of the sheet flow layer and net sediment flux under velocity or acceleration skewed waves is the size of the particles. According to Dohmen-Janssen & Hanes (2002) [28], for medium sand of diameter $d_{50} > 200\mu m$, the sediment bed response to changes of the velocity is very quick because the sheet flow layer is relatively thin close to the bed. O'Donoghue & Wright (2004a) [81] also found that the time evolution of the erosion depth for medium and coarse sand can directly be related to the instantaneous Shields parameter. However, empirical models to determine the erosion depth becomes less accurate for decreasing grain sizes [81]. Dohmen-Janssen *et al.* (2001) [29] showed that erosion depth and sheet flow layer thickness were greater for fine sand. This result is in contradiction with previous observations suggesting that erosion depth and sheet flow layer thickness were independent of the grain size. Indeed, dimensionless erosion depth and sheet flow layer thickness $\delta_e/d_{50}$ and $\delta_s/d_{50}$ increase linearly with the Shields parameter. The particle diameter being at the denominator in the expression of the Shields parameter (1), the sheet flow layer thickness and the erosion depth only scale as the square of the bottom friction velocity and are independent of the particle diameter for a given flow condition. As visible on figure 1.13, the maximum sheet flow layer thickness for fine sand is well represented by the expression

$$\frac{\delta_s^m}{d_{50}} = 25\theta^m \tag{1.10}$$

used in the practical sand transport model proposed by van der A *et al.* (2013) [114] for fine sand. According to Dohmen-Janssen *et al.* (2001) [29], the sheet flow layer thickness and erosion depth dependence on the grain size indicates that fine sand is transported in a different flow regime compared with medium and coarse sand.

Dohmen-Janssen *et al.* (2002) [30] showed that the net sediment flux generated under velocity skewed waves can be significantly reduced due to the increasing importance of the offshore sand flux contribution consequence of the phase-lag between the velocity and the concentration. Indeed, for fine sand, the sediment flux is not confined to a region immediately close to the bed as for medium and coarse sand [82]. In the experimental configurations involving fine sand under velocity skewed waves from O'Donoghue & Wright (2004b) [82], phase-lag effects are so large that the net sediment flux changes sign and becomes offshore-oriented. This process probably plays a role in the change of direction of sand bars migration that is directed onshore during low-energy periods and offshore during storms.

To characterize phase-lag effects, Dohmen-Janssen *et al.* (2002) [30] introduced the phase-lag parameter $p = \delta_s \omega / v_s$ relating the time needed for a particle to settle through the sheet flow layer thickness during the wave period at its terminal settling velocity. From Dohmen-Janssen *et al.* (2002) [30] observations, phase-lag effects are particularly present for $p > 0.5$.

Based on the definition of the phase-lag parameter, the occurrence of phase-lag effects is not directly related to particle size but on the relations between the particle settling velocity, the sheet flow layer thickness and the wave period. For example, phase-lag effects can happen for medium sand if the period of the wave is very short or if the sheet flow layer thickness is sufficiently large [30]. However, for a given wave condition, phase-lag effects increase for decreasing particle size (decreasing fall velocity).

Contrary to velocity skewed waves, experiments performed by van der A *et al.* (2010) [112] showed that phase-lag effects contribute to increase the onshore-oriented net flux for acceleration skewed waves. The net sediment flux generated in configurations involving fine sand will be greater than the one generated in configuration involving medium sand for a given condition.

The effect of grain size on the behavior of the sheet flow layer and the net transport rate under velocity or acceleration skewed waves from experiments remain mainly qualitative. To further characterize the physical processes associated with the effect of the wave shape and the size of the particles on the sheet flow layer dynamics, detailed high resolution measurements of concentration, velocity and turbulent statistics are required. However, measurements in the near bed are very difficult, even in laboratory experiments [92].

In this context, the development of turbulence-averaged numerical models can significantly contribute to improve our understanding of the physical processes occurring in oscillatory sheet flow. Indeed, they can be set up much more easily than an experiment campaign and therefore cover a wider range of flow and particle parameters for a lesser effort.

### 1.2.2 Turbulence-averaged numerical modeling of sheet flow

Two modeling methodologies are available to perform turbulence-averaged simulations of sheet flow: the conventional single phase flow and the two-phase flow approaches.

In the conventional approach, a distinction is made between sediment transported as bed load and suspended load (left panel of figure 1.14). In the upper section of the flow, Reynolds averaged mass and momentum equations for the fluid phase are solved together with the advection-diffusion equation (1.4) for sediment to ensure mass conservation and describe the evolution of suspended load. The sediment flux transported as bed load $q_s$ in the lower section of the transport layer is empirically related to the bottom shear stress computed using the single phase model. Sediment exchange between the lower and upper sections of the transport layer is modeled using empirical relations for erosion of the sediment bed. Bed elevation $y_b$ is calculated by solving the Exner equation

$$\rho^s \phi \frac{\partial y_b}{\partial t} + \frac{\partial q_s}{\partial x} = D - E \tag{1.11}$$

with $D$ and $E$ the erosion and deposition fluxes.

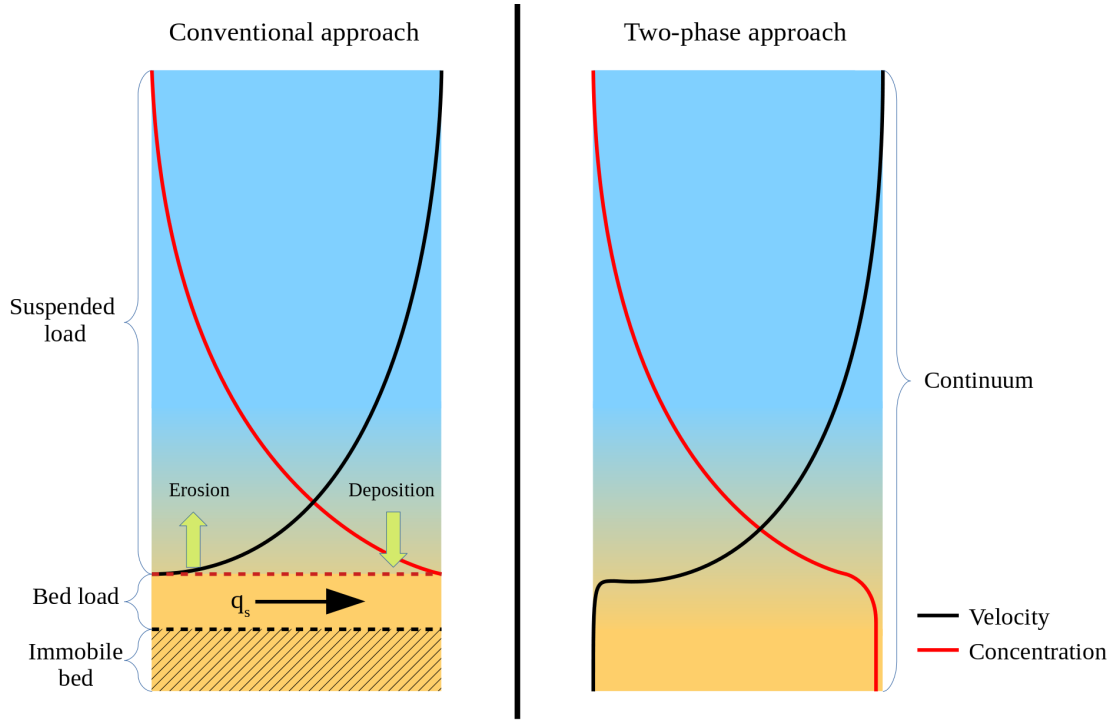


*Figure 1.14: Schematic representation of the conventional and the two-phase modeling approaches.*

In early conventional models, the evolution of sediment transport forced by an oscillatory free stream velocity was assumed to be a succession of quasi-steady states. In other words, sand transport rate is modeled as a function of the time-dependent velocity or the bed shear stress assuming quasi-steady approximation [92]. Processes such as pick-up and settling are assumed to occur at a time scale much smaller than the wave period [92].

According to Dohmen-Janssen *et al.* (2002) [30], models based on the quasi-steady approximation accurately predict net sediment flux for phase-lag parameter up to $p = 0.5$. For $p > 0.5$ the net sediment flux is always over-estimated.

The development of semi-unsteady model integrating phase-lag effects in an empirical manner allowed to improve the net sand transport prediction but significant differences still persist between predictions and measurements. The high degree of empiricism in the conventional modeling approach does not allow to cover a wide range of flow and particle parameters without any significant model coefficient tuning. Integrating more physics in the modeling methodology such as in the two-phase flow approach should help overcome this strong limitation.

The two-phase flow approach corresponds to the turbulence-averaged version of the TF model presented in section 1.1.3. Contrary to single phase flow models, continuity and momentum equations for both the dispersed and the carrier phases are solved. To avoid correlations between the concentration and the fluid and solid phase velocities $u_i^f$ and $u_i^s$ respectively in the two-phase flow equations, Favre averaged fluid and solid phase velocities are introduced:

$$\langle u_i^f \rangle_F = \frac{\langle (1-\phi) u_i^f \rangle}{\langle 1-\phi \rangle}, \quad \langle u_i^s \rangle_F = \frac{\langle \phi u_i^f \rangle}{\langle \phi \rangle} \qquad (1.12a,b)$$

with $\langle \cdot \rangle_F$ the Favre averaging operator and $\langle \cdot \rangle$ representing either the ensemble averaging operator for steady flows or the phase averaging operator for oscillatory flows.

Applying the ensemble averaging operator to the two-phase flow equations presented in chapter 2 and expressing the terms in term of Favre averaged variables gives the turbulence averaged

mass and momentum conservation equations for fluid and solid phases:

$$\frac{\partial\langle 1-\phi\rangle}{\partial t}+\frac{\partial\langle 1-\phi\rangle\langle u_i^f\rangle_F}{\partial x_i}=0, \tag{1.13}$$

$$\frac{\partial\langle \phi\rangle}{\partial t}+\frac{\partial\langle \phi\rangle\langle u_i^s\rangle_F}{\partial x_i}=0, \tag{1.14}$$

$$\begin{aligned}\frac{\partial\rho^f\langle 1-\phi\rangle\langle u_i^f\rangle_F}{\partial t}+\frac{\partial\rho^f\langle 1-\phi\rangle\langle u_i^f\rangle_F\langle u_j^f\rangle_F}{\partial x_j}&=-\langle 1-\phi\rangle\frac{\partial\langle P^f\rangle}{\partial x_i}+\frac{\partial}{\partial x_j}\left(T_{ij}^f+R_{ij}^f\right)\\&+\langle 1-\phi\rangle\rho^f g_i+\langle 1-\phi\rangle f_i^v-\langle\phi\rangle\langle 1-\phi\rangle K\left[\langle u_i^f\rangle_F-\langle u_i^s\rangle_F\right]\\&+\langle 1-\phi\rangle\frac{\nu_t^f}{S_c}\frac{\partial\langle\phi\rangle}{\partial x_i},\end{aligned} \tag{1.15}$$

$$\begin{aligned}\frac{\partial\rho^s\langle\phi\rangle\langle u_i^s\rangle_F}{\partial t}+\frac{\partial\rho^s\langle\phi\rangle\langle u_i^s\rangle_F\langle u_j^s\rangle_F}{\partial x_j}&=-\langle\phi\rangle\frac{\partial\langle P^f\rangle}{\partial x_i}-\frac{\partial\langle P^s\rangle}{\partial x_i}+\frac{\partial}{\partial x_j}(T_{ij}^s+R_{ij}^s)+\langle\phi\rangle\rho^f g_i\\&+\langle\phi\rangle f_i^v+\langle\phi\rangle\langle 1-\phi\rangle K\left[\langle u_i^f\rangle_F-\langle u_i^s\rangle_F\right]-\langle 1-\phi\rangle\frac{\nu_t^f}{S_c}\frac{\partial\langle\phi\rangle}{\partial x_i},\end{aligned} \tag{1.16}$$

with $\langle P^f\rangle$ and $\langle P^s\rangle$ the averaged fluid and solid phase pressures, $T_{ij}^f$ and $T_{ij}^s$ the fluid and solid phase viscous stress tensors, $R_{ij}^f$ and $R_{ij}^s$ the fluid and solid phase Reynolds stress tensor, $K$ the drag parameter, $\nu_t^f$ the eddy viscosity and $S_c$ the Schmidt number representing the ratio between the turbulent momentum diffusivity or eddy viscosity and the sediment mass diffusivity.

The two-phase flow equations are very similar to the single-phase Navier-Stokes equations with the addition of coupling terms. The last two terms of equations (1.15) and (1.16) represent the momentum exchange between the two phases. The first term represents the drag force between the fluid and the particle function of the drag parameter and the relative velocity between the two phases and the second term represents the upward diffusion of particles due to turbulence function of the eddy viscosity, the Schmidt number and the concentration gradient. Accurate predictions using the two-phase flow model rely on an accurate modeling of the fluid phase eddy viscosity $\nu_t^f$ by a turbulence model and solid phase pressure $\langle P^s\rangle$ and shear stress tensor $T_{ij}^s$ to take into account the rheological behavior of the dispersed phase induced by particle-particle interactions. The solid phase Reynolds stress tensor $R_{ij}^s$ is usually neglected but new models are developed to take into account the solid phase turbulence [47].

As a consequence of the continuum vision of the fluid and the solid phases, there is no distinction between bed load and suspended load. A description of the velocity and concentration profiles is provided from the immobile bed to the top of the domain (right panel of figure 1.14). Compared with conventional models, the degree of empiricism in the two-phase flow approach is significantly reduced. The physical basis upon which two-phase flow models are developed should improve sediment transport predictions.

Dong et Zhang (2002) [31] proposed a turbulence-averaged two-phase flow model capable of capturing erosion and transport processes in the sheet flow layer. Their work is the first attempt to predict time series of the concentration in the pick-up layer. The amplitude of the time variation of the concentration is slightly under-estimated compared with experiments. For smaller particles, the model fails to reproduce concentration peaks observed experimentally at flow reversal.

The early modeling approach proposed by Hsu *et al.* (2004) [53] who implemented the turbulent diffusion term in the momentum equation and introduced a two-equation turbulence model for two-phase flow based on the single phase $k-\varepsilon$, allowed to quantitatively predict time-evolution of the concentration profile for configurations involving large inertial particles for which effects

of the fluid are of minor importance. Using the same model, Hsu & Hanes (2004) [52] recovered the net onshore sediment flux for velocity and acceleration skewed waves. Furthermore, horizontal momentum balance revealed that collisional forces compensate the drag contribution having for effect to increase the relative contribution of the pressure gradient in the sediment dynamics. Numerical experiments showed that sediment bed failure is a direct consequence of strong horizontal pressure gradients corresponding to strong flow acceleration confirming the findings of Sleath (1999) [107]. Similarly to Ribberink & Al-Salem (1995) [92] and Dohmen-Janssen & Hanes (2002) [28], they showed that sediment transport can directly be related to the bed shear stress for such flow and particle parameters.

Liu and Sato (2006) [64] also studied the effect of wave shape with a turbulence-averaged two-phase flow model but this time for different particle sizes. The model failed to reproduce unsteady effects for fine sand and the net sediment flux was under-estimated. Considering that for fine sand, the particles inertia is no longer dominant, the discrepancy observed for smaller particles can be related to missing features of the effect of the fluid phase on the particles in the model such as turbulence-particle interactions.

Significant progress has been made by Amoudry *et al.* (2008) [2] and Amoudry (2014) [4] to improve the two-phase model from Hsu *et al.* (2004) [53]. First, the inclusion of an additional fluid-particle interactions in the two-phase $k-\varepsilon$ turbulence model by Amoudry *et al.* (2008) [2] allowed to improve sediment transport under waves even if some discrepancies still remain in the concentration time series. Second, based on the observation that the turbulence model remains dominant for accurate velocity and concentration profile predictions [3], Amoudry (2014) [4] proposed a two-phase flow version of the $k-\omega$ turbulence model. From the simulations, the $k-\varepsilon$ model provide better results but the differences between the two models are small. For both models, the suspension of fine particles at flow reversal is under-estimated suggesting that some of the physics behind oscillatory sheet flow involving fine sand is still missing in the two-phase flow model. Nevertheless, more than just a turbulence model, Amoudry (2014) [4] introduced a systematic methodology to adapt single phase flow turbulence models to the two-phase flow formalism.

More recently, Cheng *et al.* (2017) [22] used a turbulence-averaged two-phase flow model to study the formation of plug flow and particularly the dependence in term of Sleath and Shields number. They confirmed the field observations that plug flow occurs for threshold values of the Sleath number much smaller for larger Shields numbers. It should be noted that the model results are strongly sensitive to the closure coefficients associated with turbulence-particle interactions [22].

Even if significant insight into mechanisms involved in oscillatory sheet flow has been provided, the promises of the two-phase flow model to overcome the limitations of the conventional approach is not completely fulfilled considering that simulations results are not very accurate and still extremely sensitive to the model coefficients for fine sand [62].

## 1.3 Motivations

Our understanding of the physical processes involved in sediment transport at small scale is an important step toward developing predictive tools for large scale applications. This is especially the case for physical processes occurring in sediment transport under intense flow forcing such as oscillatory sheet flow. Indeed, the prediction of the cross-shore morphological evolution of a beach depends on the accurate modeling of sand transport under a given wave forcing.

Experimental configurations of idealized oscillatory sheet flow occurring in the near shore environment reproduced in OWTs allowed to provide both quantitative and qualitative description

of the sheet flow layer involving medium and coarse sand. When unsteady effects induced by the phase-lag between the flow velocity and sediment concentration are small, the evolution of the sheet flow layer is composed of a succession of quasi-static events meaning that sand transport can directly be related to the instantaneous mean flow quantities such as the near bed velocity and the Shields parameter.

For smaller particles in similar wave conditions, unsteady effects become dominant and the behavior of the transport layer changes drastically. The sheet flow layer increases having for effect to significantly affect the flow by modifying the apparent bed roughness and the turbulence modulation due to density stratification for example.

Understanding physical processes at the origin of unsteady effects is extremely important considering that phase-lag significantly affects the net sand flux generated under velocity and acceleration skewed waves. For velocity skewed waves, phase-lag effects induce a reduction of the net onshore sediment flux. It can even change sign and become offshore-oriented when unsteady effects are dominant. For acceleration skewed waves, phase-lag effects induce greater onshore directed sediment flux compared with configurations where phase-lag effects are absent. To this day, the origin of unsteady effects is not well understood. The effect of phase-lag is taken into account in large scale morphological models through empirical closures and model predictions show a significant variability.

Unfortunately, turbulence-averaged numerical models, supposed to provide a deeper insight into grain-scale processes involved in oscillatory sheet flow, show limited predictive capabilities when it comes to oscillatory sheet flow involving fine sand. Simulations results are extremely sensitive to the turbulence-particle interaction closure models and need to be fine tuned to cover a wide range of flow and particle parameters highlighting our misunderstanding of the underlying physical processes.

Provide empirical relations to tune model coefficients in order to match measurements is equivalent to blindly integrate the missing physics. A more efficient way of improving the models predictive capabilities is to provide more physically based parameterizations for turbulence-averaged models. To do so, turbulence-resolving two-phase flow methodologies represent a great opportunity to investigate the fine scale processes involved in sediment transport such as turbulence-particle and particle-particle interactions.

The choice of modeling methodology has to be carefully chosen based on the flow regime and available computational resources. For intense flow conditions such as oscillatory sheet flow involving fine sand for example, the significant number of particles interacting in the transport layer would make the computational cost of such simulations using FR-DNS or PP methodologies prohibitive. In this context, the development of Eulerian modeling methodologies for which there is no limitations in terms of number of particles is needed.

Simplifying assumptions made to derive the EE modeling methodologies are too restrictive to represent the fluid-particle interactions occurring in sand transport under an intense flow forcing. Therefore, the TF methodology appears to be the only viable option to simulate such configurations. However, considering the wide range of flow and particle parameters involved in typical sand transport applications typical of the coastal environment, the modeling methodology should be able to accurately predict particles' dynamics for multiple turbulence-particle interaction regimes occurring at different moments or different locations. As a consequence, the applicability of the TF model should be extended to cover a wider range of turbulence-particle interaction regimes.

# 2

# Turbulence-resolving two-fluid model

In this chapter, the Eulerian two-phase flow (or two-fluid) model sedFoam used in this thesis is presented. First, the governing equations are derived using the detailed averaging procedure and closure models. Then, Favre filtered two-phase flow equations and their numerical implementation are presented. Eventually, the model is validated using numerical and experimental data of two boundary layer flows: one unidirectional and one oscillatory.

## Contents

## 2.1 Eulerian two-phase flow equations

The Eulerian two-phase flow equations of the two-fluid model can be derived by performing ensemble or spatial averaging of the local and instantaneous mass and momentum equations of the fluid and dispersed particles over the mixture. On the one hand, the ensemble averaging procedure used to derive the two-phase flow equations presented in Zhang & Prosperetti (1997) [132] consists of averaging the equations at each point of space over an ensemble of macroscopically equivalent systems. On the other hand the spatial averaging procedure proposed by Jackson (2000) [55] consists of a local spatial average of a given quantity over the volume occupied by the fluid or the particles. Both procedures eventually lead to the same set of equations and only the spatial averaging methodology proposed by Jackson (2000) [55] will be detailed in the thesis.

### 2.1.1 Derivation of the two-phase flow equations

To derive the two-phase flow equations, spatial averaging operators are applied on the mass and momentum conservation equations of the fluid and on the momentum conservation equation of a single particle. The averaging operators and their properties are presented in the following section and are eventually used for the derivation of the two-phase flow equations.

#### Averaging operators

The spatial average value $\langle \psi \rangle_S(x_i,t)$ of a quantity of interest $\psi$ in the control volume V at position $\boldsymbol{x} = (x,y,z)^T$ and time $t$ is defined by the following expression:

$$\langle \psi \rangle_S(x_i,t) = \int_V \psi(y_i,t) G(|x_i - y_i|) dV \tag{2.1}$$

with $G(|x_i - y_i|)$ a weighting function given by:

$$G(|x_i - y_i|) = \begin{cases} \dfrac{3}{4\pi L_G^3} & \text{for} \quad |x_i - y_i| \leq L_G \\ 0 & \text{for} \quad |x_i - y_i| > L_G \end{cases} \tag{2.2}$$

associating the spatial averaging operator with a given length scale $L_G$. In order to have a clear separation of scales to obtain phase averaged quantities, $L_G$ has to be smaller than the macroscopic length scale of interest and greater than the particle diameter.

For dispersed particles in a fluid, the particle volume fraction $\phi$ and the void fraction (or volume occupied by the fluid) $1-\phi$ at location $x_i$ are obtained by integrating the weighting function $G$ over the volume occupied by the particles and the fluid respectively following the expressions

$$\phi(x_i,t) = \sum_p \int_{V_p} G(|x_i - y_i|) dV \tag{2.3}$$

$$(1-\phi)(x_i,t) = \int_{V_f} G(|x_i - y_i|) dV \tag{2.4}$$

with $V_p$ the volume occupied by a single particle $p$ and $V_f$ the volume occupied by the fluid. Similarly, for a quantity of interest $\psi$, the corresponding solid phase and fluid phase averaged quantities $\langle \psi \rangle_S^s$ and $\langle \psi \rangle_S^f$ at location $x_i$ (written $\psi^s$ and $\psi^f$ for simplicity) are given by

$$\psi^s(x_i,t) = \frac{1}{\phi} \sum_p \int_{V_p} \psi(y_i,t) G(|x_i - y_i|) dV \tag{2.5}$$

$$\psi^f(x_i,t) = \frac{1}{1-\phi} \int_{V_f} \psi(y_i,t) G(|x_i - y_i|) dV. \tag{2.6}$$

The averaging operators do not commute with the partial differential operators but, using Leibniz rule, we can write the following expressions:

$$\left(\frac{\partial \psi}{\partial t}\right)^s (x_i,t) = \frac{1}{\phi}\left(\frac{\partial \phi \psi^s}{\partial t} - \frac{\partial}{\partial x_k}\sum_p \psi^s u_k^p V_p G(|x_i - y_i|)\right) \tag{2.7}$$

$$\left(\frac{\partial \psi}{\partial x_i}\right)^f (x_i,t) = \frac{1}{1-\phi}\left(\frac{\partial (1-\phi)\psi^f}{\partial x_k} - \sum_p \int_{S_p} \psi(y_i) n_k(y_i) G(|x_i - y_i|) dS\right) \tag{2.8}$$

$$\left(\frac{\partial \psi}{\partial t}\right)^f (x_i,t) = \frac{1}{1-\phi}\left(\frac{\partial (1-\phi)\psi^f}{\partial t} + \sum_p \int_{S_p} \psi(y_i) n_k(y_i) u_k(y_i) G(|x_i - y_i|) dS\right) \tag{2.9}$$

with $u_k^p$ the velocity of particle $p$, $S_p$ the surface of particle $p$ and $n_k$ the outward unit vector normal to the particle surface.

### Two-phase mass and momentum equations

To derive the constitutive equations of the two-phase flow model, the spatial averaging operators defined in section 2.1.1 are applied to the equations of motion of the fluid and the particles. Starting with the mass conservation equation for an incompressible fluid, $\partial u_i/\partial x_i = 0$, using equations (2.8) and (2.9) gives the mass conservation equation for the fluid phase:

$$\frac{\partial (1-\phi)}{\partial t} + \frac{\partial (1-\phi) u_i^f}{\partial x_i} = 0. \tag{2.10}$$

Knowing that the mixture is incompressible, substracting equation (2.10) from the mass conservation equation of the mixture $\partial u_i^m/\partial x_i = 0$ with $u_i^m = (\phi u_i^s + (1-\phi)u_i^f)$ the mixture velocity we obtain the solid phase mass conservation equation:

$$\frac{\partial \phi}{\partial t} + \frac{\partial \phi u_i^s}{\partial x_i} = 0. \tag{2.11}$$

Taking the momentum conservation equations of the fluid and a particle $p$

$$\frac{\partial \rho^f u_i}{\partial t} + \frac{\partial \rho^f u_i u_j}{\partial x_j} = \frac{\partial \sigma_{ij}}{\partial x_i} + \rho^f g_i + f_i^v, \tag{2.12}$$

$$\rho^s V_p \frac{\partial u_i^p}{\partial t} = \int_{S_p} \sigma_{ij} n_k(y_i) dS + \sum_{q \neq p} f_i^{pq} + \rho^s V_p g_i + f_i^v, \tag{2.13}$$

with $\sigma_{ij}$ the fluid stress tensor, $f_i^v$ the external volume force driving the flow and $f^{pq}$ the force exerted by a particle $q$ on particle $p$ and applying the averaging operators gives the fluid and solid phase momentum conservation equations:

$$\frac{\partial \rho^f (1-\phi) u_i^f}{\partial t} + \frac{\partial \rho^f (1-\phi) u_i^f u_j^f}{\partial x_j} = \frac{\partial (1-\phi)\sigma_{ij}^f}{\partial x_j} - \sum_p \int_{S_p} \sigma_{ij}(y_i) n_k(y_i) G(|x_i - y_i|) dS + (1-\phi)\rho^f g_i + (1-\phi) f_i^v, \tag{2.14}$$

$$\frac{\partial \rho^s \phi u_i^s}{\partial t} + \frac{\partial \rho^s \phi u_i^s u_j^s}{\partial x_j} = \sum_p G(|x_i - y_p|)\left[\int_{S_p} \sigma_{ij} n_k dS + \sum_{q \neq p} f^{pq}\right] + \rho^s \phi g_i + \phi f_i^v. \tag{2.15}$$

Using Newton's third law and Taylor series expansions of the weighting function $G$ (more details in Jackson (2000) [55]) allows to decompose the second term of the right-hand-side (R.H.S.) of equation (2.14) and the first term of the R.H.S. of equation (2.15) into the average force applied

by the fluid on the particles $M_i$ and a stress related term to eventually give the final form of the fluid and solid momentum conservation equations

$$\frac{\partial \rho^f (1-\phi) u_i^f}{\partial t} + \frac{\partial \rho^f (1-\phi) u_i^f u_j^f}{\partial x_j} = \frac{\partial \Sigma_{ij}^f}{\partial x_j} - M_i + (1-\phi)\rho^f g_i + (1-\phi) f_i^v, \tag{2.16}$$

$$\frac{\partial \rho^s \phi u_i^s}{\partial t} + \frac{\partial \rho^s \phi u_i^s u_j^s}{\partial x_j} = \frac{\partial \Sigma_{ij}^s}{\partial x_j} + M_i + \rho^s \phi g_i + \phi f_i^v, \tag{2.17}$$

with $\Sigma_{ij}^f$ and $\Sigma_{ij}^s$ the fluid and solid phase effective stress tensor respectively.

### 2.1.2 Closure models for the effective stress tensors

The effective fluid and solid phase stress tensors are decomposed into normal and shear stress respectively following $\Sigma_{ij}^f = -P^f \delta_{ij} + T_{ij}^f$ and $\Sigma_{ij}^s = -P^s \delta_{ij} + T_{ij}^s$ with $P^f$ and $P^s$ the fluid and solid pressures, $\delta_{ij}$ the Kronecker symbol and $T_{ij}^f$ and $T_{ij}^s$ the fluid and solid shear stress tensors defined by

$$T_{ij}^f = \rho^f (1-\phi) \nu^f \left( \frac{\partial u_i^f}{\partial x_j} + \frac{\partial u_j^f}{\partial x_i} - \frac{2}{3} \frac{\partial u_k^f}{\partial x_k} \delta_{ij} \right), \tag{2.18}$$

$$T_{ij}^s = \rho^s \phi \nu^s \left( \frac{\partial u_i^s}{\partial x_j} + \frac{\partial u_j^s}{\partial x_i} - \frac{2}{3} \frac{\partial u_k^s}{\partial x_k} \delta_{ij} \right), \tag{2.19}$$

with $\nu^f$ and $\nu^s$ the fluid and solid viscosities respectively. The fluid is considered Newtonian with a constant viscosity but the solid phase pressure and viscosity taking into account friction, collisions and kinetic effects in the granular flow are modeled using the kinetic theory for granular flows presented in the next section.

#### Kinetic Theory for granular flows

In the kinetic theory of granular flows, an analogy is made between the behavior of a granular flow for moderate to low volume fraction and the behavior of molecules in a gas. It is extended to tackle high volume fraction for which friction between the particles is dominant by the inclusion a frictional model. The solid phase pressure $P^s$ and shear stress tensor $T_{ij}^s$ are given by $P^s = P^c + P^{fr}$ and $\nu^s = \nu^c + \nu^{fr}$ with $P^c$ and $\nu^c$ the granular pressure and viscosity due to collisions and kinetic effects, $P^{fr}$ and $\nu^{fr}$ the granular pressure and viscosity due to friction between the particles. The frictional granular pressure is modeled following Johnson and Jackson (1987) [58]

$$P^{fr} = \begin{cases} 0, & \text{for} \quad \phi < \phi^{fr} \\ 0.05 \dfrac{(\phi - \phi^{fr})^3}{(\phi^m - \phi)^5} & \text{for} \quad \phi > \phi^{fr} \end{cases} \tag{2.20}$$

where $\phi^{fr} = 0.57$ is the minimum volume fraction for which friction occurs and $\phi^m = 0.635$ the maximum volume fraction. To define the frictional viscosity, shear and normal stresses are related to the friction angle $\theta^{fr}$ (32° for sand particles) following Schaeffer (1987) [102]

$$\nu^{fr} = \frac{P^{fr} sin(\theta^{fr})}{\rho^s \sqrt{\|\boldsymbol{S}^s\|^2 + S_{small}^2}} \tag{2.21}$$

with $\|\boldsymbol{S}^s\| = \sqrt{S_{ij}^s S_{ij}^s}$ the norm of the resolved solid phase strain rate tensor $\boldsymbol{S}^s$ and $S_{small} = 1 \times 10^{-4} s^{-1}$ a regularization parameter.

The filtered granular pressure $P^c$ and viscosity $\nu^c$ induced by collisions and kinetic effects are given by

$$P^c = \rho^s \phi \left[1 + 2(1+e)\phi g_0\right]\Theta - \rho^s \lambda \frac{\partial u_k^s}{\partial x_k} \tag{2.22}$$

and

$$\nu^c = d_p \frac{5\sqrt{\pi}}{96}(\nu_k^* + \nu_c^* + \nu_b^*)\sqrt{\Theta} \tag{2.23}$$

with $\lambda$, $\nu_k^*$, $\nu_c^*$ and $\nu_b^*$ the compressible, kinetic, collisional and bulk viscosity contributions following

$$\lambda = \frac{4}{3}\phi^2 \rho^s d_p g_0 (1+e)\sqrt{\frac{\Theta}{\pi}}, \tag{2.24}$$

$$\nu_k^* = \frac{48/(5\sqrt{\pi})\phi - 2/5(1+e)(1-3e)\phi g_0}{(1-1/4(1-e)^2 - 5/24(1-e^2))g_0}, \tag{2.25}$$

$$\nu_c^* = \frac{4}{5}(1-e)\phi g_0 \nu_k^*, \tag{2.26}$$

$$\nu_b^* = \frac{384}{25\pi}(1-e)\phi^2 g_0, \tag{2.27}$$

where $e$ is the restitution coefficient for binary collisions (0.8 for sand particles), $\Theta$ is the filtered granular temperature representing the pseudo-thermal kinetic energy associated with the uncorrelated random motions of the particles and

$$g_0 = \frac{2-\phi}{2(1-\phi)^3} + \frac{2.71\phi^2}{(\phi^b - \phi)^{3/2}} \tag{2.28}$$

is the radial distribution function adapted for sand particles. Compared with the definition proposed by Chassagne *et al.* (submitted) [18], the radial distribution function does not diverges for $\phi = \phi^m$ but for a smaller value $\phi = \phi^b = 0.612$ with $\phi^b$ the effective maximum concentration in the bed. The fact that a radial distribution function diverging for a slightly smaller value of the volume fraction provide better results can be explained by the increased frictional contact for real sediment compared with the smooth spherical spheres used in the discrete element method simulations of Chassagne *et al.* (submitted) [18].

The filtered granular temperature $\Theta$ is obtained by solving the following transport equation:

$$\frac{3}{2}\left[\frac{\partial \phi \rho^s \Theta}{\partial t} + \frac{\partial \phi \rho^s u_i^s \Theta}{\partial x_j}\right] = \Pi_R + \Pi_q + J_{int} - \gamma. \tag{2.29}$$

Here $\Pi_R$ is the production of granular temperature given by

$$\Pi_R = \left(-P^c \delta_{ij} + \rho^s \phi \nu^c S_{ij}^s\right)\frac{\partial u_i^s}{\partial x_j}, \tag{2.30}$$

$\Pi_q$ the divergence of the granular temperature flux analogous to the Fourier's law of conduction is given by

$$\Pi_q = \frac{\partial}{\partial x_i}\left[-\kappa_\Theta \frac{\partial \Theta}{\partial x_j}\right], \tag{2.31}$$

where $\kappa_\Theta$ is the conductivity of the granular temperature calculated following

$$\kappa_\Theta = \rho^s d_p \frac{225\sqrt{\pi}}{1152}(\kappa_k^* + \kappa_c^* + \kappa_b^*)\sqrt{\Theta}, \tag{2.32}$$

with $\kappa_k^*$, $\kappa_c^*$ and $\kappa_b^*$ kinetic, collisional and bulk conductivity contributions given by

$$\kappa_k^* = \frac{2[576/(225\sqrt{\pi})\phi + 3/5(1+e)^2(2e-1)\phi g_0]}{(1-7/16(1-e))(1+e)g_0}, \tag{2.33}$$

$$\kappa_c^* = \frac{6}{5}(1+e)\phi g_0 \kappa_k^*, \tag{2.34}$$

and

$$\kappa_b^* = \frac{2304}{225\pi}(1+e)\phi^2 g_0, \tag{2.35}$$

$\gamma$ is the dissipation rate of granular temperature given by

$$\gamma = 3(1-e_{eff}^2)\phi^2 \rho^s g_0 \Theta \left[\frac{4}{d_p}\sqrt{\frac{\Theta}{\pi}} - \frac{\partial u_j^s}{\partial x_j}\right], \tag{2.36}$$

with $e_{eff} = e - 3/2\mu^p exp(-3\mu^p)$ the effective restitution coefficient for dissipation taking into account the effect of friction through the friction coefficient $\mu^p$ (0.4 for sand particles).

Eventually, $J_{int}$ the fluid-particle interaction term representing the dissipation of granular temperature due to drag is given by

$$J_{int} = -3\frac{\rho^s \phi}{t_s}\Theta \tag{2.37}$$

with $t_s$ the response time of the particle defined in section 2.1.3.

### 2.1.3 Closure models for the momentum exchange term

The momentum exchange term $M_i$ between the two phases is composed of buoyancy, drag, lift and added mass forces $B_i$, $D_i$, $L_i$ and $A_i$ respectively following the expression:

$$M_i = B_i + D_i + L_i + A_i \quad \text{with} \quad \begin{cases} B_i = -\phi \dfrac{\partial P^f}{\partial x_i} \\ D_i = \dfrac{\rho^s \phi}{t_s}\left(u_i^f - u_i^s\right) \\ L_i = \phi(1-\phi)C_l \rho^m \|u_i^f - u_i^s\| \varepsilon_{ijk} \dfrac{\partial u_k^m}{\partial x_j} \\ A_i = \phi(1-\phi)C_a \rho^f \left[\dfrac{\partial u_i^f}{\partial t} + \dfrac{\partial u_i^f u_j^f}{\partial x_j} - \left(\dfrac{\partial u_i^s}{\partial t} + \dfrac{\partial u_i^s u_j^s}{\partial x_j}\right)\right] \end{cases} \tag{2.38}$$

where $C_l = 0.5$ and $C_a = 0.5$ are the lift and added mass coefficients, $\varepsilon_{ijk}$ the Levi-Civita symbol and $t_s$ is the particle response time following the drag law proposed by Ding & Gidaspow (1990) [27] gathering the model of Ergun (1952) [100] for high concentrations ($\phi > 0.2$) and the model of Wen & Yu (1966) [122] for low concentrations ($\phi < 0.2$) following

$$t_s = \begin{cases} \rho^s \left(\dfrac{150\phi \nu^f \rho^f}{(1-\phi)d_p^2} + \dfrac{1.75\rho^f \|u_i^f - u_i^s\|}{d_p}\right)^{-1}, & \phi > 0.2 \\ \dfrac{4}{3}\dfrac{\rho^s}{\rho^f}\dfrac{d_p}{C_D\|u_i^f - u_i^s\|}(1-\phi)^{1.65}, & \phi < 0.2 \end{cases} \tag{2.39}$$

with $C_D$ the drag coefficient given by

$$C_D = \frac{24}{Re_p}\left(1 + 0.15 Re_p^{0.687}\right) \tag{2.40}$$

and the particle Reynolds number $Re_p$ expressed as

$$Re_p = \frac{(1-\phi)d_p\|u_i^f - u_i^s\|}{\nu^f}. \tag{2.41}$$

## 2.2 Favre filtered Eulerian two-phase flow equations

To perform LES with a two-phase flow model, a separation between the large turbulent flow scales, low frequency, and the small ones, high frequency, is operated by a filter (operator $\bar{\cdot}$). In analogy with compressible flows, a change of variable called Favre filtering is used to obtain filtered two-phase flow equations. Any variable $\psi(x_i,t)$ can be decomposed into the sum $\psi(x_i,t) = \tilde{\psi}(x_i,t) + \psi''(x_i,t)$ with $\tilde{\psi}(x_i,t)$ the resolved Favre filtered part and $\psi''(x_i,t)$ the unresolved sub-grid part. Favre-filtered fluid and solid velocities, $\tilde{u}_i^f$ and $\tilde{u}_i^s$, are defined as follows:

$$\tilde{u}_i^f = \frac{\overline{(1-\phi)u_i^f}}{(1-\bar{\phi})}, \quad \tilde{u}_i^s = \frac{\overline{\phi u_i^s}}{\bar{\phi}}, \tag{2.42a,b}$$

with $u_i^{f''} = u_i^f - \tilde{u}_i^f$ and $u_i^{s''} = u_i^s - \tilde{u}_i^s$ the sub-grid scale velocity fluctuations.

Applying the filtering operator to the mass and momentum equations (2.10), (2.11), (2.16), (2.17) and the granular temperature equation (2.29) gives the following filtered two-phase flow equations:

$$\frac{\partial(1-\bar{\phi})}{\partial t} + \frac{\partial(1-\bar{\phi})\tilde{u}_i^f}{\partial x_i} = 0, \tag{2.43}$$

$$\frac{\partial\bar{\phi}}{\partial t} + \frac{\partial\bar{\phi}\tilde{u}_i^s}{\partial x_i} = 0, \tag{2.44}$$

$$\begin{aligned}\frac{\partial\rho^f(1-\bar{\phi})\tilde{u}_i^f}{\partial t} + \frac{\partial\rho^f(1-\bar{\phi})\tilde{u}_i^f\tilde{u}_j^f}{\partial x_j} &= -(1-\bar{\phi})\frac{\partial\bar{P}^f}{\partial x_i} + \frac{\partial}{\partial x_j}\left(\tilde{T}_{ij}^f + \sigma_{ij}^{f,sgs}\right) - \bar{I}_i \\ &+\rho^f(1-\bar{\phi})g_i + (1-\phi)f_i^v - I_i^{sgs} + \Phi_i^{f,sgs},\end{aligned} \tag{2.45}$$

$$\begin{aligned}\frac{\partial\rho^s\bar{\phi}\tilde{u}_i^s}{\partial t} + \frac{\partial\rho^s\bar{\phi}\tilde{u}_i^s\tilde{u}_j^s}{\partial x_j} &= -\bar{\phi}\frac{\partial\bar{P}^f}{\partial x_i} - \frac{\partial\bar{P}^s}{\partial x_i} + \frac{\partial}{\partial x_j}\left(\tilde{T}_{ij}^s + \sigma_{ij}^{s,sgs}\right) + \bar{I}_i + \rho^s\bar{\phi}g_i \\ &+\phi f_i^v + I_i^{sgs} + \Phi_i^{s,sgs},\end{aligned} \tag{2.46}$$

$$\frac{3}{2}\left[\frac{\partial\bar{\phi}\rho^s\bar{\Theta}}{\partial t} + \frac{\partial\bar{\phi}\rho^s\tilde{u}_i^s\bar{\Theta}}{\partial x_j}\right] = \tilde{\Pi}_R + \tilde{\Pi}_q + \tilde{J}_{int} - \tilde{\gamma} + \Phi_\Theta^{sgs}. \tag{2.47}$$

where $\bar{I}_i = \bar{M}_i - \bar{B}_i$ is the momentum exchange term without the buoyancy term, $\sigma_{ij}^{f,sgs}$ and $\sigma_{ij}^{s,sgs}$ are the fluid and solid sub-grid scale stress tensors coming from the filtering of the non-linear advection terms, $I^{sgs}$ the sub-grid term coming from the filtering of the momentum exchange term, $\Phi_i^{f,sgs}$ and $\Phi_i^{s,sgs}$ are the fluid and solid sub-grid scale contributions coming from the filtering of pressure terms and effective stress tensors and $\Phi_\Theta^{sgs}$ the sub-grid term coming from the filtering of the terms of the granular temperature transport equation [85]. The effective stress tensors $\tilde{T}_{ij}^f$ and $\tilde{T}_{ij}^s$, the solid phase pressure $\bar{P}^s$, the momentum exchange term $\bar{I}_i$, and the terms of the granular temperature equation are given by their respective expressions in section 2.1 but are expressed in term of filtered variables. The particle-interaction term is modified to take into account the balance between the dissipation of granular temperature due to drag and the production due to the sub-grid fluid pseudo-thermal kinetic energy $\Theta^f$ following:

$$\tilde{J}_{int} = -3\frac{\rho^s\bar{\phi}}{\tilde{t}_s}(\bar{\Theta} - \bar{\Theta}^f). \tag{2.48}$$

This formulation is similar to the interaction term presented in Fox (2014) [42] but transcripted in the LES formalism with the difference that, the fluid pseudo-thermal kinetic energy is confounded with the sub-grid TKE. It is given by $\Theta^f = \frac{2}{3}\tilde{k}_{sgs}^f$, with the sub-grid fluid TKE $\tilde{k}_{sgs}^f =$

$(C_1^f/C_\varepsilon)^{2/3}\|\tilde{\boldsymbol{S}}^f\|$, where $C_\varepsilon$ is an empirical constant of the order of unity coming from the Kolmogorov theory [127] taken to be $C_\varepsilon = 1.048$ in recent studies [8, 19, 95] and $C_1^f$ a coefficient determined using a sub-grid scale model detailed in the next section.

### 2.2.1 Sub-grid scale modeling

The fluid and solid sub-grid stress tensors $\sigma_{ij}^{f,sgs} = \rho^f(1-\bar{\phi})(\widetilde{u_i^f u_j^f} - \tilde{u}_i^f\tilde{u}_j^f)$ and $\sigma_{ij}^{s,sgs} = \rho^s\bar{\phi}(\widetilde{u_i^s u_j^s} - \tilde{u}_i^s\tilde{u}_j^s)$ are modeled using the dynamic Lagrangian procedure proposed by Meneveau *et al.* (1996) [72]. The most common way to model the sub-grid stress is to use the Smagorinsky model,

$$\sigma_{ij}^{a,sgs} = 2\rho^a\overline{\phi}^a\Delta^2\|\tilde{\boldsymbol{S}}^a\|\left(C_1^a\tilde{S}_{ij}^a - \frac{1}{3}C_2^a\tilde{S}_{kk}^a\delta_{ij}\right), \tag{2.49}$$

with the superscript $a = f,s$ denoting either the fluid or solid phase, and $C_1^a$ and $C_2^a$ the model coefficients and $\Delta$ the filter width. To adjust the model coefficients, the dynamic procedure proposed by Meneveau *et al.* (1996) [72] samples the turbulent stress from the smallest resolved scales and extrapolates to determine the turbulent stress associated with unresolved turbulent flow scales below $\Delta$.

The starting point to determine the first coefficient $C_1^a$ is the algebraic identity

$$\mathscr{L}_{ij}^a = \mathscr{T}_{ij}^a - \tau_{ij}^a, \tag{2.50}$$

relating the turbulent stress associated to two different filter widths $\Delta$ and $\hat{\Delta} = 2\Delta$ with

$$\mathscr{L}_{ij}^a = \widehat{\tilde{u}_i^a\tilde{u}_j^a} - \widehat{\tilde{u}_i^a}\widehat{\tilde{u}_j^a}, \qquad \mathscr{T}_{ij}^a = \widehat{\widetilde{u_i^a u_j^a}} - \widehat{\tilde{u}_i^a}\widehat{\tilde{u}_j^a} \quad \text{and} \quad \tau_{ij}^a = \widehat{\widetilde{u_i^a u_j^a}} - \widehat{\tilde{u}_i^a\tilde{u}_j^a} \tag{2.51}$$

where the operator $\widehat{\cdot}$ represents filtering at scale $\hat{\Delta}$.

The Smagorinsky model is used to model the turbulent stress $\tau_{ij}^a$ at scale $\Delta$ and $\mathscr{T}_{ij}^a$ at scale $2\Delta$ following:

$$\tau_{ij}^a = -2C_1^a\Delta^2\|\tilde{\boldsymbol{S}}^a\|\tilde{S}_{ij}^a, \tag{2.52}$$

$$\mathscr{T}_{ij}^a = -2C_1^a(2\Delta)^2\|\widehat{\tilde{\boldsymbol{S}}^a}\|\widehat{\tilde{S}_{ij}^a}. \tag{2.53}$$

Replacing expressions (2.52) and (2.53) in the identity (2.50) and minimizing the mean square error between the resolved identity and the Smagorinsky model leads to the expression for the coefficient $C_1^a$,

$$C_1^a = \frac{\mathscr{F}_{LM}^a}{\mathscr{F}_{MM}^a}, \tag{2.54}$$

with $\mathscr{F}_{LM}^a$ and $\mathscr{F}_{MM}^a$ the products $\mathscr{L}_{ij}^a\mathscr{M}_{ij}^a$ and $\mathscr{M}_{ij}^a\mathscr{M}_{ij}^a$ with $\mathscr{M}_{ij}^a = 2\Delta^2\left[\widehat{\|\tilde{\boldsymbol{S}}^a\|\tilde{S}_{ij}^a} - 4\|\widehat{\tilde{\boldsymbol{S}}^a}\|\widehat{\tilde{S}^a}_{ij}\right]$ averaged over streamlines following the expressions:

$$\mathscr{F}_{LM}^a = \int_{-\infty}^{t}\mathscr{L}_{ij}^a\mathscr{M}_{ij}^a(z(t'),t')W(t-t')dt', \tag{2.55}$$

$$\mathscr{F}_{MM}^a = \int_{-\infty}^{t}\mathscr{M}_{ij}^a\mathscr{M}_{ij}^a(z(t'),t')W(t-t')dt'. \tag{2.56}$$

The kernel $W(t-t')$ is used to control the relative importance of the events around time $t$ with those of earlier times. The exponential form $W(t-t') = T^{-1}e^{-(t-t')/T}$, with $T = \frac{3\Delta}{2}(\mathscr{F}_{LM}^a\mathscr{F}_{MM}^a)^{-\frac{1}{8}}$, makes the integrals (2.55) and (2.56) solutions of the transport equations

$$\frac{\partial\overline{\phi}^a\mathscr{F}_{LM}^a}{\partial t} + \frac{\partial\overline{\phi}^a\tilde{u}_j^a\mathscr{F}_{LM}^a}{\partial x_i} = \frac{2}{3\Delta}(\mathscr{F}_{LM}^a\mathscr{F}_{MM}^a)^{\frac{1}{8}}(\mathscr{L}_{ij}^a\mathscr{M}_{ij}^a - \mathscr{F}_{LM}^a), \tag{2.57}$$

and

$$\frac{\partial \rho^a \overline{\phi}^a \mathscr{F}^a_{MM}}{\partial t} + \frac{\partial \rho^a \overline{\phi}^a \tilde{u}^a_j \mathscr{F}^a_{MM}}{\partial x_i} = \frac{2}{3\Delta}(\mathscr{F}^a_{LM}\mathscr{F}^a_{MM})^{\frac{1}{8}}(\mathscr{M}^a_{ij}\mathscr{M}^a_{ij} - \mathscr{F}^a_{MM}). \tag{2.58}$$

To compute the second model coefficient $C^a_2$, a similar procedure is used. Using the following identity for the spherical part of the sub-grid scale shear stress tensor:

$$\mathscr{L}^{*,a} = \mathscr{T}^{*,a} - \tau^{*,a}. \tag{2.59}$$

Here

$$\mathscr{L}^{*,a} = \frac{1}{3}tr(\widehat{\tilde{u}^a_i\tilde{u}^a_j} - \widehat{\tilde{u}}^a_i\widehat{\tilde{u}}^a_j), \qquad \mathscr{T}^{*,a} = \frac{1}{3}tr(\widehat{\widetilde{u^a_i u^a_j}} - \widehat{\tilde{u}}^a_i\widehat{\tilde{u}}^a_j) \quad \text{and} \quad \tau^{*,a} = \frac{1}{3}tr(\widehat{\widetilde{u^a_i u^a_j}} - \widehat{\tilde{u}^a_i\tilde{u}^a_j}), \tag{2.60}$$

modeled following

$$\tau^{*,a} = -\frac{2}{3}C^a_2\Delta^2\|\tilde{\boldsymbol{S}}^a\|\tilde{S}^a_{kk}\delta_{ij}, \tag{2.61}$$

$$\mathscr{T}^{*,a} = -\frac{2}{3}C^a_2(2\Delta)^2\|\widehat{\tilde{\boldsymbol{S}}^a}\|\widehat{\tilde{S}^a_{kk}}\delta_{ij}. \tag{2.62}$$

Minimizing the mean square error between the resolved identity and the Smagorinsky model leads to the expression for the coefficient $C^a_2$,

$$C^a_2 = \frac{\langle \mathscr{L}^{*,a}\rangle_C}{\langle \mathscr{M}^{*,a}\mathscr{M}^{*,a}\rangle_C}, \tag{2.63}$$

with $\mathscr{M}^{*,a} = -\frac{2}{3}\Delta^2\left[\|\widetilde{\tilde{\boldsymbol{S}}^a}\|\widetilde{\tilde{S}^a_{kk}}\delta_{ij} - 4\|\widehat{\tilde{\boldsymbol{S}}^a}\|\widehat{\tilde{S}^a}_{kk}\delta_{ij}\right]$ and operator $\langle\cdot\rangle_C$ representing average over the cell faces.

The main difference between this modeling methodology and the dynamic procedure proposed by Germano *et al.* (1992) [45] and Lilly (1992) [63] used in Cheng *et al.* (2018) [23] is that model coefficients are averaged over streamlines and not plane-averaged over homogeneous flow directions. The dynamic Lagrangian procedure has the advantage of getting rid of the necessity to have homogeneous directions and of preserving a certain locality in space making it applicable to more complex-geometries and inhomogeneous flows in future research [72].

The other Eulerian-Eulerian sub-grid contributions resulting from the filtering of the pressure, stress, momentum exchange terms and terms in the granular temperature equation represented by $\Phi^{f,sgs}_i$, $\Phi^{s,sgs}_i$, $I^{sgs}_i$ and $\Phi^{sgs}_\Theta$ are taking into account the effect of unresolved particles clusters and streamers having length scales smaller than the filter width $\Delta$ [1]. Cheng *et al.* (2018) [23] modeled the sub-grid momentum exchange term $I^{sgs}_i$ using a drift velocity model proposed by Ozel *et al.* (2013) [85] but since the typical size of the smallest mesoscale structures is on the order of 10 to 100 particle diameters [1], the sub-grid terms taking into account these effects should vanish for filter sizes on the order of the particle size. This has been confirmed by Ozel et al. (2013) [85] who quantitatively reported the relative importance of sub-grid terms by explicitly filtering two-phase Eulerian-Eulerian DNS results for different filter sizes. In all the simulations presented in this paper, $\Delta$ is always on the order of the particle size or slightly smaller and therefore, the sub-grid contributions $\Phi^{f,sgs}_i$, $\Phi^{s,sgs}_i$, $I^{sgs}_i$ and $\Phi^{sgs}_\Theta$ can be considered as negligible.

## 2.3 Energy transfers, mean field and turbulent kinetic energy budgets

To better understand the role of the different terms of the two-phase flow model in the LES framework, a schematic representation of the energy transfers between the mean resolved fluid

and solid phase kinetic energies $\tilde{K}^f = \langle \tilde{u}_i^f \tilde{u}_i^f \rangle_F / 2$ and $\tilde{K}^s = \langle \tilde{u}_i^s \tilde{u}_i^s \rangle_F / 2$, the correlated sub-grid fluid and solid phase kinetic energies $\tilde{k}_{sgs}^f = \langle \tilde{u}_i^{f''} \tilde{u}_i^{f''} \rangle_F / 2$ and $\tilde{k}_{sgs}^s = \langle \tilde{u}_i^{s''} \tilde{u}_i^{s''} \rangle_F / 2$ and the fluid and solid pseudo-thermal kinetic energies $\bar{\Theta}^f$ and $\bar{\Theta}$ is presented in figure 2.1 with $\varepsilon^f$ the fluid phase sub-grid dissipation of TKE.

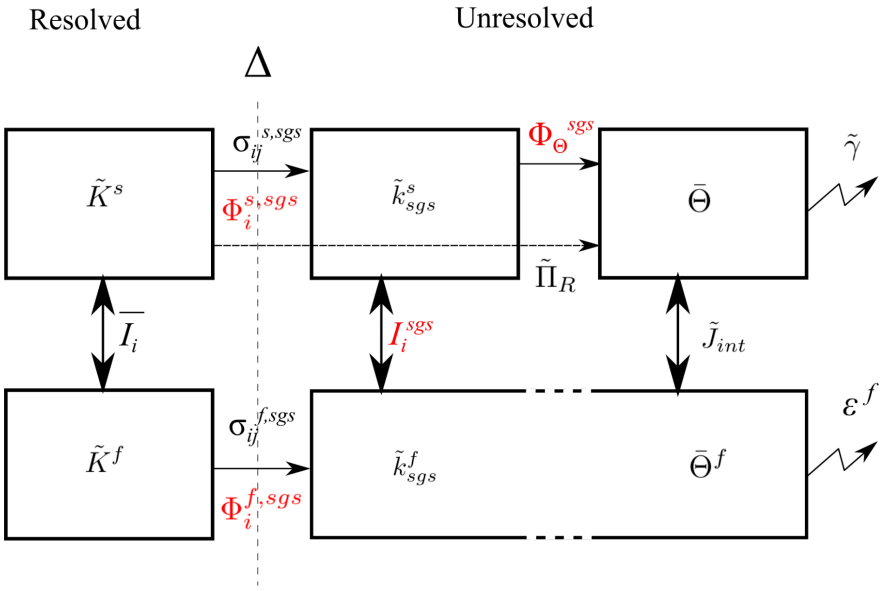


*Figure 2.1: Schematic representation of the energy transfers between fluid and solid resolved, unresolved, correlated and uncorrelated scales of the flow with $\tilde{K}^f$ and $\tilde{K}^s$ the resolved fluid and solid TKE, $\tilde{k}_{sgs}^f$ and $\tilde{k}_{sgs}^s$ the fluid and solid sub-grid TKE, $\bar{\Theta}^f$ the fluid pseudo-thermal kinetic energy and $\bar{\Theta}$ the granular temperature. Terms in red are neglected because the grid size $\Delta$ is of the order of the particles diameter $d_p$ [1, 85]*

To further study energy transfers between resolved flow scales, taking the filtered momentum equation of the fluid phase (2.45), multiplying it by the fluid velocity and rearranging the equation gives a transport equation of the mean resolved kinetic energy:

$$\underbrace{\frac{\partial (1-\langle\bar{\phi}\rangle)\tilde{K}^f}{\partial t}}_{\text{rate of change}} + \underbrace{\frac{\partial (1-\langle\bar{\phi}\rangle)\langle \tilde{u}_j^f \tilde{u}_i^f \tilde{u}_i^f/2\rangle_F}{\partial x_j}}_{II\ \text{convection}} = \underbrace{-\left\langle \tilde{u}_i^f \frac{(1-\bar{\phi})}{\rho^f}\frac{\partial \bar{P}^f}{\partial x_i}\right\rangle}_{\text{pressure contribution}} + \underbrace{\left\langle \frac{\partial \tilde{u}_i^f \tilde{T}_{ij}^f}{\partial x_j}\right\rangle}_{\text{viscous diffusion}} - \underbrace{\left\langle \tilde{T}_{ij}^f \frac{\partial \tilde{u}_i^f}{\partial x_j}\right\rangle}_{\text{viscous dissipation}}$$

$$\underbrace{-\langle \tilde{u}_i^f \bar{I}_i\rangle}_{\text{coupling contribution}} \underbrace{+(1-\langle\bar{\phi}\rangle)\langle \tilde{u}_i^f\rangle_F g_i}_{\text{gravity contribution}} + \underbrace{\left\langle \frac{\partial \tilde{u}_i^f \sigma_{ij}^{f,sgs}}{\partial x_j}\right\rangle}_{\text{sub-grid diffusion}} \underbrace{-\left\langle \sigma_{ij}^{f,sgs}\frac{\partial \tilde{u}_i^f}{\partial x_j}\right\rangle}_{\text{sub-grid dissipation}} + \underbrace{\left\langle \tilde{u}_i^f (\Phi_i^{f,sgs} + I_i^{sgs})\right\rangle}_{\text{other sub-grid contributions}}. \tag{2.64}$$

Symmetrically, the same equation can be constructed for the solid phase.

The mean kinetic energy can be decomposed into the sum of the mean field kinetic energy $\langle \tilde{K}^f \rangle_F = \langle \tilde{u}_i^f \rangle_F \langle \tilde{u}_i^f \rangle_F / 2$ and the turbulent kinetic energy $\tilde{k}^f = \langle \tilde{u}_i^{f'} \tilde{u}_i^{f'} \rangle_F / 2$ with $\tilde{u}_i^{f'}$ the resolved fluid velocity fluctuations. Making the decomposition of the mean kinetic energy in equation

(2.64) allows to extract the transport equations of the mean field and the turbulent kinetic energy:

$$\underbrace{\frac{\partial(1-\langle\overline{\phi}\rangle)\langle\tilde{K}^f\rangle_F}{\partial t}}_{\substack{\text{rate}\\ \text{of change}}}+\underbrace{\frac{\partial(1-\langle\overline{\phi}\rangle)\langle\tilde{u}_j^f\rangle_F\langle\tilde{K}^f\rangle_F}{\partial x_j}}_{\text{convection}}=\underbrace{-\langle\tilde{u}_i^f\rangle_F\left\langle\frac{(1-\overline{\phi})}{\rho^f}\frac{\partial\overline{P}^f}{\partial x_i}\right\rangle}_{\substack{\text{pressure}\\ \text{contribution}}}+\underbrace{\left\langle\frac{\partial\langle\tilde{u}_i^f\rangle_F\tilde{T}_{ij}^f}{\partial x_j}\right\rangle}_{\substack{\text{viscous}\\ \text{diffusion}}}$$
$$\underbrace{-\left\langle\tilde{T}_{ij}^f\frac{\partial\langle\tilde{u}_i^f\rangle_F}{\partial x_j}\right\rangle}_{\substack{\text{viscous}\\ \text{dissipation}}}\underbrace{-\langle\tilde{u}_i^f\rangle_F\frac{\partial(1-\langle\overline{\phi}\rangle)\langle\tilde{u}_j^{f'}\tilde{u}_i^{f'}\rangle_F}{\partial x_j}}_{\substack{\text{Reynolds-like}\\ \text{contribution}}}\underbrace{-\langle\tilde{u}_i^f\rangle_F\langle\overline{I}_i\rangle}_{\substack{\text{coupling}\\ \text{contribution}}}\underbrace{+(1-\langle\overline{\phi}\rangle)\langle\tilde{u}_i^f\rangle_F g_i}_{\substack{\text{gravity}\\ \text{contribution}}} \tag{2.65}$$
$$\underbrace{+\left\langle\frac{\partial\langle\tilde{u}_i^f\rangle_F\sigma_{ij}^{f,sgs}}{\partial x_j}\right\rangle}_{\substack{\text{sub-grid}\\ \text{diffusion}}}\underbrace{-\left\langle\sigma_{ij}^{f,sgs}\frac{\partial\langle\tilde{u}_i^f\rangle_F}{\partial x_j}\right\rangle}_{\substack{\text{sub-grid}\\ \text{dissipation}}}\underbrace{+\langle\tilde{u}_i^f\rangle_F\left\langle(\Phi_i^{f,sgs}+I_i^{sgs})\right\rangle}_{\substack{\text{other}\\ \text{sub-grid}\\ \text{contributions}}}$$

$$\underbrace{\frac{\partial(1-\langle\overline{\phi}\rangle)\tilde{k}^f}{\partial t}}_{\substack{\text{rate}\\ \text{of change}}}+\underbrace{\frac{\partial(1-\langle\overline{\phi}\rangle)\langle\tilde{u}_j^f\rangle_F\tilde{k}^f}{\partial x_j}}_{\text{convection}}=\underbrace{-(1-\langle\overline{\phi}\rangle)\langle\tilde{u}_j^{f'}\tilde{u}_i^{f'}\rangle_F\frac{\partial\langle\tilde{u}_i^f\rangle_F}{\partial x_j}}_{\text{production}}\underbrace{-\left\langle\tilde{u}_i^{f'}\frac{(1-\overline{\phi})}{\rho^f}\frac{\partial\overline{P}^f}{\partial x_i}\right\rangle}_{\substack{\text{pressure}\\ \text{contribution}}}$$
$$\underbrace{+\left\langle\frac{\partial\tilde{u}_i^{f'}\tilde{T}_{ij}^f}{\partial x_j}\right\rangle}_{\substack{\text{viscous}\\ \text{diffusion}}}\underbrace{-\left\langle\tilde{T}_{ij}^f\frac{\partial\tilde{u}_i^{f'}}{\partial x_j}\right\rangle}_{\substack{\text{viscous}\\ \text{dissipation}}}\underbrace{-\frac{\partial(1-\langle\overline{\phi}\rangle)\langle\tilde{u}_j^{f'}\tilde{u}_i^{f'}\tilde{u}_i^{f'}\rangle_F/2}{\partial x_j}}_{\substack{\text{turbulent}\\ \text{transport}}}\underbrace{-\left\langle\tilde{u}_i^{f'}\overline{I}_i\right\rangle}_{\substack{\text{coupling}\\ \text{contribution}}}$$
$$\underbrace{+\left\langle\frac{\partial\tilde{u}_i^{f'}\sigma_{ij}^{f,sgs}}{\partial x_j}\right\rangle}_{\substack{\text{sub-grid}\\ \text{diffusion}}}\underbrace{-\left\langle\sigma_{ij}^{f,sgs}\frac{\partial\tilde{u}_i^{f'}}{\partial x_j}\right\rangle}_{\substack{\text{sub-grid}\\ \text{dissipation}}}\underbrace{+\left\langle\tilde{u}_i^{f'}(\Phi_i^{f,sgs}+I_i^{sgs})\right\rangle}_{\substack{\text{other}\\ \text{sub-grid}\\ \text{contributions}}} \tag{2.66}$$

More details on the derivation of the kinetic energy equations are given in appendix B.

## 2.4 Numerical implementation

The present model is adapted from the turbulence-averaged two-phase flow solver sedFoam (https://github.com/sedFoam/sedFoam) [20, 22]. It is implemented in the open-source computational fluid dynamics toolbox OpenFoam [56] and solves the Eulerian-Eulerian two-phase flow mass and momentum equations using a finite volume method and a pressure-implicit with splitting of operators (PISO) algorithm for velocity-pressure coupling [99].

First, the solid mass conservation equation (2.11) is solved using the MULES (Multidimensional Universal Limiter for Explicit Solution) solver [66] to ensure boundedness of the solution. Then, the momentum exchange term, turbulence models coefficients and particle phase stress are updated. To solve for the coupled pressure and velocities, the fluid phase momentum equation

(2.45) written in vector form (taking only the drag force into account for simplicity) is rearranged and divided by $\rho^f(1-\bar{\phi})$ as follows

$$\frac{\partial \tilde{\mathbf{u}}^f}{\partial t} + \nabla\cdot(\tilde{\mathbf{u}}^f\tilde{\mathbf{u}}^f) - (\nabla\cdot\tilde{\mathbf{u}}^f)\tilde{\mathbf{u}}^f = -\frac{1}{\rho^f}\nabla\bar{P}^{f*} - \frac{\bar{\phi}K}{\rho^f}(\tilde{\mathbf{u}}^f - \tilde{\mathbf{u}}^s) + \frac{\mathbf{f}^v}{\rho^f} + \frac{1}{(1-\bar{\phi})}\nabla\cdot(\tilde{\mathbf{T}}^f + \sigma^{f,sgs}) \tag{2.67}$$

with $\bar{P}^{f*} = \bar{P}^f - \rho^f g y$ the reduced pressure and $K = \rho^s/\tilde{t}^s(1-\bar{\phi})$ the drag coefficient. The last term of the right hand side (R.H.S.) of equation (2.67) can be expended as follows

$$\frac{1}{(1-\bar{\phi})}\nabla\cdot(\tilde{\mathbf{T}}^f + \sigma^{f,sgs}) = \frac{1}{(1-\bar{\phi})}\nabla\cdot\left[\nu^f_{Eff}\left(\nabla\tilde{\mathbf{u}}^f + \nabla\tilde{\mathbf{u}}^{fT}\right) - \frac{2}{3}\nu^f_{sp}\nabla\cdot\tilde{\mathbf{u}}^f\right]$$
$$= \nabla\cdot\left(\nu^f_{Eff}\nabla\tilde{\mathbf{u}}^f\right) + \nu^f_{Eff}\frac{\nabla(1-\bar{\phi})}{(1-\bar{\phi})}\nabla\tilde{\mathbf{u}}^f + \frac{1}{(1-\bar{\phi})}\nabla\cdot\left[(1-\bar{\phi})\,\nu^f_{Eff}\nabla\tilde{\mathbf{u}}^{fT} - \frac{2}{3}\nu^f_{sp}\nabla\cdot\tilde{\mathbf{u}}^f\right]. \tag{2.68}$$

with $\nu^f_{sp} = \nu^f + 2C_2^f\Delta^2\|\tilde{\boldsymbol{S}}^f\|$ and $\nu^f_{Eff} = \nu^f + 2C_1^f\Delta^2\|\tilde{\boldsymbol{S}}^f\|$ the effective viscosities of the spherical and deviatoric parts of the stress tensor respectively taking into account sub-grid contributions.

The first two terms of equation (2.68), are treated implicitly whereas the last two terms are treated explicitly. Substituting this decomposition of the stress tensors in equation (2.67) gives

$$\frac{\partial \tilde{\mathbf{u}}^f}{\partial t} + \nabla\cdot(\tilde{\mathbf{u}}^f\tilde{\mathbf{u}}^f) - (\nabla\cdot\tilde{\mathbf{u}}^f)\tilde{\mathbf{u}}^f - \nabla\cdot\left(\nu^f_{Eff}\nabla\tilde{\mathbf{u}}^f\right) - \nu^f_{Eff}\frac{\nabla(1-\bar{\phi})}{(1-\bar{\phi})}\nabla\tilde{\mathbf{u}}^f + \frac{\bar{\phi}K}{\rho^f}\tilde{\mathbf{u}}^f = -\frac{1}{\rho^f}\nabla\bar{P}^{f*}$$
$$+\frac{\bar{\phi}K}{\rho^f}\tilde{\mathbf{u}}^s + \frac{\mathbf{f}^v}{\rho^f} + \frac{1}{(1-\bar{\phi})}\nabla\cdot\left[(1-\bar{\phi})\,\nu^f_{Eff}\nabla\tilde{\mathbf{u}}^{fT} - \frac{2}{3}\nu^f_{sp}\nabla\cdot\tilde{\mathbf{u}}^f\right] \tag{2.69}$$

In (2.69), all the terms on the left hand side (L.H.S) are treated implicitly and all the terms on the R.H.S. are treated explicitly. In the matrix form, equation (2.69) gives:

$$\mathbf{A}^f\cdot\tilde{\mathbf{u}}^f = \mathbf{H}^f + \mathbf{R}^f + \frac{\bar{\phi}K}{\rho^f}\tilde{\mathbf{u}}^s - \frac{1}{\rho^f}\nabla\bar{P}^{f*} \tag{2.70}$$

with $\mathbf{A}^f$ and $\mathbf{H}^f$ the matrices composed of the diagonal and off-diagonal terms of the algebraic system associated with equation (2.69) respectively and $\mathbf{R}^f$ the matrix composed with explicit terms.

Following the same methodology, the solid phase momentum equation can be decomposed following:

$$\frac{\partial \tilde{\mathbf{u}}^s}{\partial t} + \nabla\cdot(\tilde{\mathbf{u}}^s\tilde{\mathbf{u}}^s) - (\nabla\cdot\tilde{\mathbf{u}}^s)\tilde{\mathbf{u}}^s - \frac{1}{\bar{\phi}}\nabla\cdot\left(\nu^{fr}\nabla\tilde{\mathbf{u}}^s\right) - \nabla\cdot\left(\nu^s_{Eff}\nabla\tilde{\mathbf{u}}^s\right) - \nu^s_{Eff}\frac{\nabla\bar{\phi}}{\bar{\phi}}\nabla\tilde{\mathbf{u}}^s + \frac{(1-\bar{\phi})K}{\rho^s}\tilde{\mathbf{u}}^s$$
$$= -\frac{1}{\rho^s}\nabla\bar{P}^{f*} - \frac{1}{\bar{\phi}\rho^s}\nabla p^s + \frac{(1-\bar{\phi})K}{\rho^s}\tilde{\mathbf{u}}^f + \frac{\mathbf{f}^v}{\rho^s} + \mathbf{g}\left(1-\frac{\rho^f}{\rho^s}\right) + \frac{1}{\bar{\phi}}\nabla\cdot\left[(\bar{\phi}\nu^s_{Eff} + \nu^{fr})\nabla\tilde{\mathbf{u}}^{sT}\right] \tag{2.71}$$
$$-\frac{1}{\bar{\phi}}\nabla\cdot\left[\frac{2}{3}(\bar{\phi}\nu^s_{sp} + \nu^{fr})\nabla\cdot\tilde{\mathbf{u}}^s\right].$$

with $\nu^s_{sp} = \nu^c + 2C_2^s\Delta^2\|\tilde{\boldsymbol{S}}^s\|$ and $\nu^s_{Eff} = \nu^c + 2C_1^s\Delta^2\|\tilde{\boldsymbol{S}}^s\|$ the effective viscosities for the spherical and deviatoric parts of the stress tensor respectively taking into account sub-grid, collisional and kinetic effects. Written in matrix form, equation (2.72) gives:

$$\mathbf{A}^s\cdot\tilde{\mathbf{u}}^s = \mathbf{H}^s + \mathbf{R}^s + \frac{(1-\bar{\phi})K}{\rho^s}\tilde{\mathbf{u}}^f - \frac{1}{\rho^f}\nabla\bar{P}^{f*} \tag{2.72}$$

with $\mathbf{A}^s$ and $\mathbf{H}^s$ composed of the diagonal and off-diagonal terms and $\mathbf{R}^s$ composed with explicit terms.

### 2.4.1 Velocity-pressure algorithm

The PISO algorithm is used to solve fluid and particle velocities with the Rhie & Chow (1983) [90] method to ensure pressure-velocity coupling and avoid oscillations in the pressure field [99]

**Step 1:** Velocity predictor at the cell centers

First, the intermediate velocities $\tilde{\mathbf{u}}^{s*}$,$\tilde{\mathbf{u}}^{f*}$ are computed using the corresponding momentum equations (equations without the pressure gradient term and the explicit terms):

$$\begin{aligned} \tilde{\mathbf{u}}^{s*} &= \left[\mathbf{A}^s\right]^{-1}\mathbf{H}^s, \\ \tilde{\mathbf{u}}^{f*} &= \left[\mathbf{A}^f\right]^{-1}\mathbf{H}^f, \end{aligned} \tag{2.73}$$

where $\left[\mathbf{A}^s\right]^{-1}$ and $\left[\mathbf{A}^f\right]^{-1}$ represent the inverse matrices of $\mathbf{A}^s$ and $\mathbf{A}^f$, respectively. Given that $\mathbf{A}^s$ and $\mathbf{A}^f$ are diagonal, computation of $\left[\mathbf{A}^s\right]^{-1}$ and $\left[\mathbf{A}^f\right]^{-1}$ is rather straightforward. These intermediate velocities do not satisfy the mass conservation equations (2.10) and (2.11) and should be corrected.

**Step 2:** Velocity fluxes at the cell faces

The R.H.S. of equations (2.70) and (2.72) are computed at the cell faces (operator $\cdot|_f$):

$$\Phi^s_R = \left[\mathbf{A}^s|_f\right]^{-1}\mathbf{R}^a|_f \quad \text{and} \quad \Phi^f_R = \left[\mathbf{A}^f|_f\right]^{-1}\mathbf{R}^f|_f \tag{2.74}$$

and the velocity flux associated with the predictor step is interpolated at the cell faces:

$$\Phi^s_U = \left(\left[\mathbf{A}^s\right]^{-1}\mathbf{H}^s\right)\Big|_f \quad \text{and} \quad \Phi^f_U = \left(\left[\mathbf{A}^f\right]^{-1}\mathbf{H}^f\right)\Big|_f \tag{2.75}$$

Introducing the notation:

$$AK^s = \left(\left[\mathbf{A}^s\right]^{-1}(1-\bar{\phi})K/\rho^s\right)\Big|_f \quad \text{and} \quad AK^f = \left(\left[\mathbf{A}^f\right]^{-1}\bar{\phi}K/\rho^f\right)\Big|_f \tag{2.76}$$

one can write the volume averaged velocity flux at the cell faces as:

$$\Phi^* = \bar{\phi}|_f\left[\Phi^s_U + \Phi^s_R + AK^s\Phi^f\right] + (1-\bar{\phi})|_f\left[\Phi^f_U + \Phi^f_R + AK^f\Phi^s\right] \tag{2.77}$$

where $\Phi^s = \mathbf{u}^s|_f.\mathbf{n}|_f S_f$ and $\Phi^f = \mathbf{u}^f|_f.\mathbf{n}|_f S_f$ denote the fluid and particle phases velocity fluxes at the previous iteration or time step and at the cell faces, respectively, and $S_f$ is the cell face area. At this stage, the drag force is partially treated explicitly for the mixture flux $\Phi^*$.

**Step 3:** Velocity corrector at the cell faces

Writing the semi-discrete velocity equation including the pressure gradient term leads to the following equations:

$$\Phi^{s**} = \Phi^s_U + \Phi^s_R + AK^s\big|_f\Phi^{f**} - \frac{\nabla^\perp P^{f*}|_f}{\rho^s\mathbf{A}^s|_f} \tag{2.78}$$

$$\Phi^{f**} = \Phi^f_U + \Phi^f_R + AK^f\big|_f\Phi^{s**} - \frac{\nabla^\perp P^{f*}|_f}{\rho^f\mathbf{A}^f|_f} \tag{2.79}$$

Taking the divergence of the volume averaged mixture velocity and imposing the incompressibility constraint, $\nabla\cdot\tilde{\mathbf{U}}^{m**} = \nabla\cdot(\bar{\phi}\tilde{\mathbf{u}}^{s**} + (1-\bar{\phi})\tilde{\mathbf{u}}^{f**}) = 0$, one can built the pressure equation as

a function of the predicted velocity or predicted face fluxes:

$$\int_V \nabla\cdot\left[\left(\frac{\bar{\phi}}{\rho^s}\left[\mathbf{A}^s\right]^{-1}+\frac{(1-\bar{\phi})}{\rho^f}\left[\mathbf{A}^f\right]^{-1}\right)\nabla P^{f*}\right]dV=\int_V \nabla\cdot\tilde{\mathbf{U}}^{m*}dV \tag{2.80}$$

$$\text{or}\quad \oint_S\left(\frac{\bar{\phi}|_f}{\rho^s}\left[\mathbf{A}^s\right]^{-1}|_f+\frac{(1-\bar{\phi})|_f}{\rho^f}\left[\mathbf{A}^f\right]^{-1}|_f\right)\nabla^\perp P^{f*}|_f\,\mathbf{n}|_f\,dS=\oint_S\tilde{\mathbf{U}}^{m*}|_f\,\mathbf{n}|_f\,dS. \tag{2.81}$$

Using Gauss theorem, one can write the following expression:

$$\int_V\nabla\cdot\left[\bar{\phi}\tilde{\mathbf{u}}^{s**}+(1-\bar{\phi})\mathbf{u}^{f**}\right]dV=\oint_S\left[\bar{\phi}|_f\tilde{\mathbf{u}}^{s**}|_f+(1-\bar{\phi})|_f\tilde{\mathbf{u}}^{f**}|_f\right]\cdot\mathbf{n}\,dS=0. \tag{2.82}$$

At the discrete level, this equation is written as:

$$\sum_f\left[\bar{\phi}|_f\Phi^{s**}+(1-\bar{\phi})|_f\Phi^{f**}\right]=0. \tag{2.83}$$

Substituting the velocity corrector equations (2.78) and (2.79) into the previous equation, the Poisson equation for the pressure reads:

$$\sum_f\left(\frac{\bar{\phi}|_f}{\rho^s}\left[\mathbf{A}^s\right]^{-1}|_f+\frac{(1-\bar{\phi})|_f}{\rho^f}\left[\mathbf{A}^f\right]^{-1}|_f\right)\nabla^\perp P^{f*}|_f\,\mathbf{n}|_f\,S_f=\sum_f\Phi^*. \tag{2.84}$$

This equation leads to a matrix system written at the cell faces. The resulting algebraic system is usually solved using a multi-grid solver (GAMG). The resulting pressure field $P^{f*}$ is used for the correction step in which the mixture velocity face flux is corrected using equations (2.78) and (2.79):

$$\Phi^{**}=\Phi^*-\sum_f\nabla^\perp P^{f*}|_f S_f \tag{2.85}$$

and the fluid and particle phase face fluxes are corrected accordingly

$$\Phi^s_c=\Phi^s_U+\Phi^s_R-\frac{\nabla^\perp P^{f*}|_f}{\rho^s\mathbf{A}^s|_f} \tag{2.86}$$

$$\Phi^f_c=\Phi^f_U+\Phi^f_R-\frac{\nabla^\perp P^{f*}|_f}{\rho^f\mathbf{A}^f|_f} \tag{2.87}$$

in which the explicit drag contributions coming from the other phase are still missing. We can rewrite the corrected fluxes for each phase as:

$$\Phi^{s**}=\Phi^s_c+AK^s\Phi^{s**} \tag{2.88}$$

$$\Phi^{f**}=\Phi^f_c+AK^f\Phi^{f**} \tag{2.89}$$

and the face flux associated with the relative velocity as:

$$\Phi^{r**}=\Phi^{s**}-\Phi^{f**}=\Phi^s_c+AK^s(\Phi^f_c+AK^f\Phi^{s**})-\left[\Phi^f_c+AK^f(\Phi^s_c+AK^s\Phi^{f**})\right] \tag{2.90}$$

$$\Phi^{r**}=\Phi^s_c+AK^s\Phi^f_c-\left[\Phi^f_c+AK^f\Phi^s_c\right]+AK^sAK^f\left[\Phi^{s**}-\Phi^{f**}\right] \tag{2.91}$$

$$(1-AK^sAK^f)\Phi^{r**}=\Phi^s_c+AK^s\Phi^f_c-\left[\Phi^f_c+AK^f\Phi^s_c\right] \tag{2.92}$$

$$\Phi^{r**}=\frac{1}{1-AK^sAK^f}\left\{\Phi^s_c+AK^s\Phi^f_c-\left[\Phi^f_c+AK^f\Phi^s_c\right]\right\} \tag{2.93}$$

This new expression for the relative flux allows to treat the drag force almost implicitly. This operation is made to stabilize the coupling between the two momentum equations and allows for higher time steps with regard to the particle response time.

The predicted fluxes for each phase is then obtained from the mixture flux plus a correction coming from the relative flux. Let's write the mixture velocity and relative velocity expression:

$$\Phi^{**} = \bar{\phi}|_f \Phi^{s**} + (1-\bar{\phi})|_f \Phi^{f**} \quad \text{and} \quad \Phi^{r**} = \Phi^{s**} - \Phi^{f**} \tag{2.94}$$

from which we can deduce the following relationships:

$$\Phi^{s} = \Phi^{**} + (1-\bar{\phi})|_f \Phi^{r**} \quad \text{and} \quad \Phi^{f} = \Phi^{**} - \bar{\phi}|_f \Phi^{r**} \tag{2.95}$$

The same type of procedure is applied for the reconstruction of the velocities at the cell centers.

### 2.4.2 Summary of the solution procedure

The numerical solution procedure for the proposed two-phase flow model is outlined as follow:

1. Solve for sediment concentration $\bar{\phi}$, i.e., Eq. (2.11);
2. Update the drag parameter $K$;
3. Solve for the turbulence closure, update $C_1^f$, $C_2^f$, $C_1^s$, $C_2^s$;
4. Solve for the particle phase stress;
5. PISO-loop, solving velocity-pressure coupling for $N$ loops:
   (a) Construct the coefficient matrix $\mathbf{A}^s$, $\mathbf{A}^f$, $\mathbf{H}^s$ and $\mathbf{H}^f$ using Eqn (2.72) and (2.70).
   (b) update the other explicit source terms $\mathbf{R}^s$ and $\mathbf{R}^f$.
   (c) Calculate $\tilde{\mathbf{u}}^{s*}$,$\tilde{\mathbf{u}}^{f*}$ using equations (2.73) without fluid pressure gradient term;
   (d) Construct and solve the pressure Eq. (2.84);
   (e) Correct fluid and particle velocities after solving pressure and update fluxes Eqns (2.85)-(2.95);
   (f) go to (a-e) if the number of loops is smaller than $N$ (no tolerance criteria).
6. Advance to the next time step

## 2.5 Model validation

Two academic configurations of sedimentation and laminar bed load used to validate the Reynolds average model from Chauchat *et al.* (2017) [20] have been successfully reproduced using the two-phase flow model (not shown). The good agreement between numerical and analytical results allows to validate the implementation of the coupling between the two phases and the stress terms. In order to further validate the TF model and measure its the predictive capabilities, two turbulent clear water configurations (*i.e.* without particles) are reproduced numerically. The first one is a unidirectional turbulent boundary layer flow for which both experimental and numerical data are available and the second one is an oscillatory boundary layer in the transitionally turbulent regime for which experimental data is available for comparison. All the simulations presented in this thesis are performed using the GRICAD infrastructure and the GENCI infrastructure under the allocations A0060107567, A0080107567 and A0100107567.

### 2.5.1 Unidirectional boundary layer flow

The clear water configuration from Kiger & Pan (2002) [61] consists of a closed unidirectional channel flow with Reynolds number $Re_\tau = u_\tau h/\nu^f = 560$ based on the wall-friction velocity $u_\tau = 2.8 \times 10^{-2}\ m.s^{-1}$ and channel half height $h = 0.02\ m$. The flow parameters are presented in table 2.1.

| $U_b\ (m.s^{-1})$ | $h\ (m)$ | $u_\tau\ (m.s^{-1})$ | $Re_\tau$ |
|---|---|---|---|
| 0.51 | 0.02 | $2.8 \times 10^{-2}$ | 560 |

*Table 2.1: Flow parameters of the clear water configuration from Kiger & Pan (2002) [61].*

The numerical domain is a bi-periodic rectangular box (figure 2.2) with cyclic boundary conditions in $x$ and $z$ directions and no slip boundary condition at the top and bottom boundaries for the velocities. The gradient of any other quantities is set to zero at the walls. The flow is driven by the volume force $f_i^v$ dynamically adjusted at each time step in order to match the experimental bulk velocity $U_b = 0.51\ m.s^{-1}$. The mesh is composed of $314 \times 220 \times 160$ elements corresponding to a total of $11,105,280$ cells. The span-wise and stream-wise resolution is constant with $\Delta_x^+ \approx \Delta_z^+ \approx 11$ wall units ($+$ symbol for a given variable $\psi$ reads $\psi^+ = \psi u_\tau/\nu^f$). The mesh is stretched along the $y$-axis with $\Delta_y^+ \approx 1$ at the wall and $\Delta_y^+ \approx 6$ at the centerline. The time step is fixed to $\Delta t = 10^{-4}\ s$ to ensure a maximum Courant-Friedrichs-Lewy number (CFL) lower than 0.3 for stability reasons. In a recent publication, Montecchia *et al.* (2019) [73] performed a sensitivity analysis to the CFL number (CFL=0.1, 0.2 and 0.3) and the results did not show strong sensitivities. Numerical parameters are presented in table 2.2

| Mesh | Number of cells | $\Delta_x^+$ | $\Delta_z^+$ | $\Delta_y^+$ (wall) | $\Delta t\ (s)$ |
|---|---|---|---|---|---|
| $314 \times 220 \times 160$ | $11,105,280$ | 11 | 11 | 1 | $10^{-4}$ |

*Table 2.2: Numerical parameters of the clear water configuration from Kiger & Pan (2002) [61].*

All the simulations involving unidirectional flows presented in this thesis have a fully developed turbulent boundary layer flow for initial condition obtained from a preliminary simulation initialized with a perturbed velocity field following the methodology proposed by De Villiers (2006) [25] implemented in OpenFoam (https://github.com/wyldckat/perturbU). A first run is conducted to let the turbulence develop until the wall friction velocity and the integral of the total flow kinetic energy have reached a steady-state. This corresponds to approximately $200T_b$ with $T_b = h/U_b$ the non-dimensional bulk timescale of the flow. Then, a second run is performed to compute turbulence statistics and Favre-averaged quantities over a duration of $200T_b$. The Favre-averaging procedure is represented by the operator $\langle\cdot\rangle_F$ (details can be found in appendix C). In clear water flow conditions, Favre-averaging is equivalent to ensemble-averaging denoted as $\langle\cdot\rangle$. In the remaining of the manuscript, the operators $\langle\cdot\rangle_F$ and $\langle\cdot\rangle$ are used to denote Favre averaging and ensemble averaging for configurations involving an unidirectional flow and Favre phase averaging and classical phase averaging for configurations involving an oscillatory flow.

Second-order centered scheme is used for advection terms for which high frequency filtering of the oscillations induced by second-order discretization is performed by introducing a small amount of upwind scheme (*filteredLinear2V* in OpenFoam), a backward scheme is used for temporal integration (*backward* in OpenFoam) and gradients are calculated using a second order centered scheme (*linear* in OpenFoam).

Similarly to what has been done by Kiger & Pan (2002) [61], the average profiles obtained experimentally and numerically are compared to the profiles from the DNS of Moser *et al.* (1999) [74] with $Re_\tau = 590$. Since the Reynolds number in the configuration from Kiger & Pan (2002) [61] is close to the DNS, it is reasonable to compare the profiles between the two configurations.

The averaged velocity profiles, Reynolds stress and root-mean-square (r.m.s) of the stream-wise velocity fluctuations $\tilde{u}^{f'}_{rms}$ and wall normal velocity fluctuations $\tilde{v}^{f'}_{rms}$ are presented in figure 2.3 in wall units. In the simulations, the friction velocity is calculated based on the time-averaged stream-wise volume force following $u_\tau = \sqrt{h\langle f^v \rangle}$.

The computed wall-friction Reynolds number is equal to $Re_\tau = 544$ ($u_\tau = 2.72 \times 10^{-2}\ m.s^{-1}$) which corresponds to an error below 3% compared with the experiments.

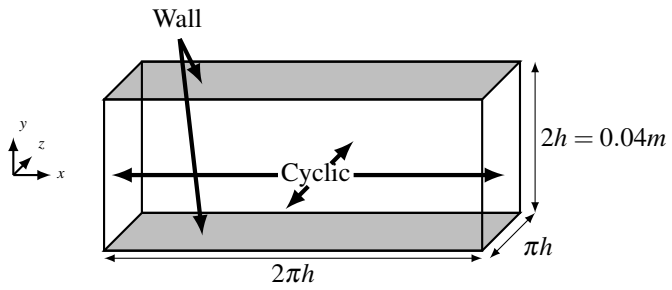


*Figure 2.2: Sketch of the geometry and boundary conditions of the numerical domain for the simulation of the clear water configuration from Kiger & Pan (2002) [61].*

The present clear water simulation produces profiles of averaged velocity and turbulence statistics that agree very well with the DNS and experimental data. However, especially for the Reynolds stress, some discrepancies between experimental measurements and the simulations appear near the wall. Kiger & Pan (2002) [61] stated that their measurements can be considered highly reliable in the outer log layer with less than 5% error for $y^+ > 50$ and up to 25% variability for $y^+ < 50$.

The present results shows the good predictive capabilities of the TF model for single phase unidirectional flows.

### 2.5.2 Oscillatory boundary layer

The clear water experimental configuration from Jensen *et al.* (1989) [57] is reproduced using the two-phase flow model. The configuration investigated corresponds to the test number 8 of Jensen *et al.* (1989) [57] with a smooth bottom boundary and a Reynolds number $Re = aU^f_m/\nu^f = 1.6 \times 10^6$ based on the maximum free stream velocity $U^f_m = 1.02m.s^{-1}$, the fluid viscosity $\nu^f = 1 \times 10^{-6} m^2.s^{-1}$ and the orbital excursion length $a = U^f_m/\omega = 1.58m$. The free stream velocity is sinusoidal with a period $T = 9.72s$. The Reynolds number based on the Stokes-layer thickness $\delta = \sqrt{2\nu^f/\omega} = 1.76 \times 10^{-3} m$ with $\omega = 2\pi/T$ the pulsation of the flow is equal to $Re_\delta = U^f_m \delta/\nu^f = 1790$ and the maximum friction velocity is $u^m_\tau = 0.047m.s^{-1}$. The hydrodynamic parameters are presented in table 2.3.

| $T\ (s)$ | $U^f_m\ (m.s^{-1})$ | $a\ (m)$ | $\delta_s\ (m)$ | $u^m_\tau\ (m.s^{-1})$ | $Re$ | $Re_\delta$ |
|---|---|---|---|---|---|---|
| 9.72 | 1.02 | 1.58 | $1.76 \times 10^{-3}$ | 0.047 | $1.6 \times 10^6$ | 1790 |

*Table 2.3: Hydrodynamical parameters of the clear water configurations from Jensen et al. (1989) [57].*

The numerical domain is a box of dimensions $80\delta \times 50\delta \times 40\delta$. Mesh dimensions and boundary conditions are represented on figure 2.4. A symmetry boundary condition is applied at the top boundary, a wall boundary condition is applied at the bottom boundary and cyclic boundary conditions are applied for the boundaries coincident the planes orthogonal to the $x$-axis and $z$-axis. The same scheme as in section 2.5.1 are used.

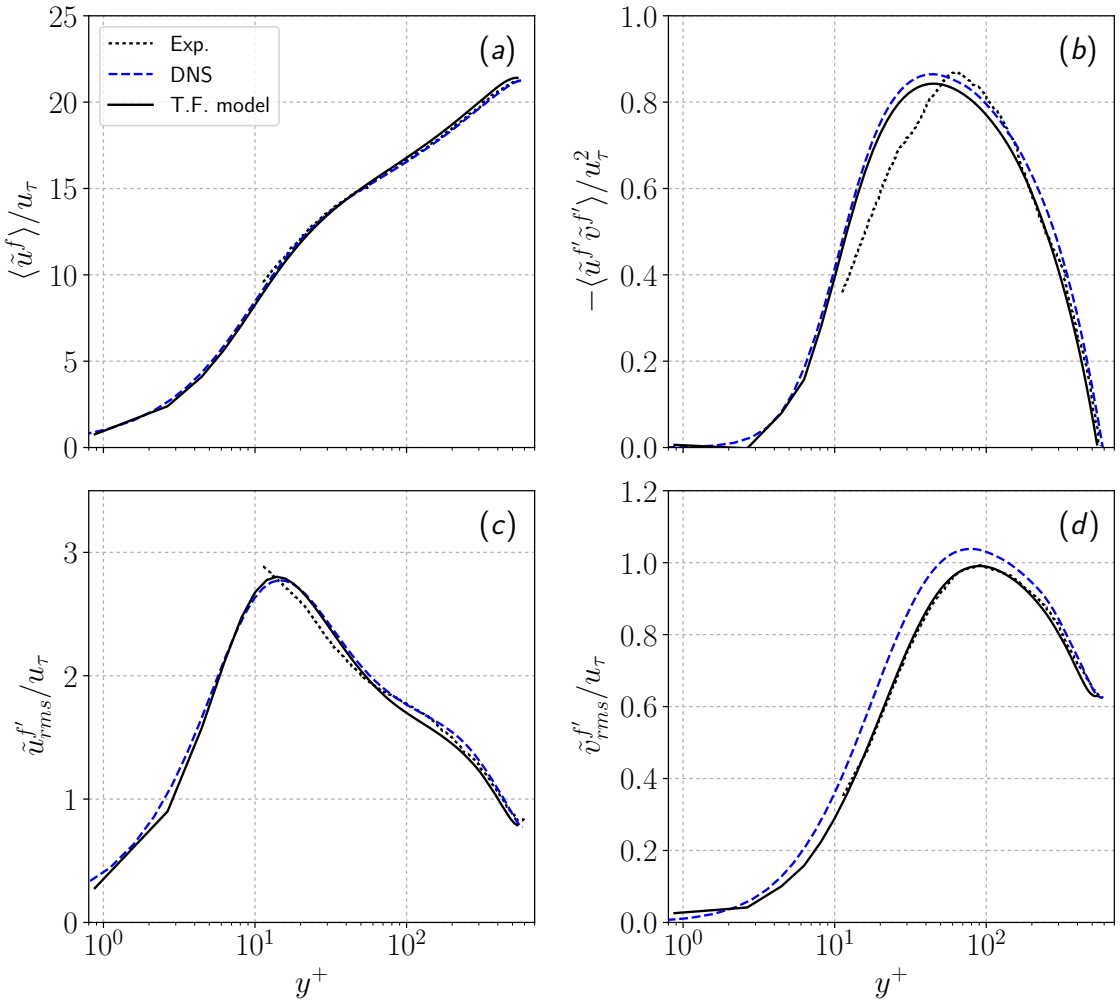


*Figure 2.3: Average profiles of velocity in $(a)$, Reynolds stress in $(b)$, r.m.s of stream-wise velocity fluctuations in $(c)$ and r.m.s of wall-normal velocity fluctuations in $(d)$ from the two-fluid model (T.F. model) compared with the numerical results from Moser et al. (1999) [74] (DNS) and experimental data from Kiger & Pan (2002) [61] (Exp.).*

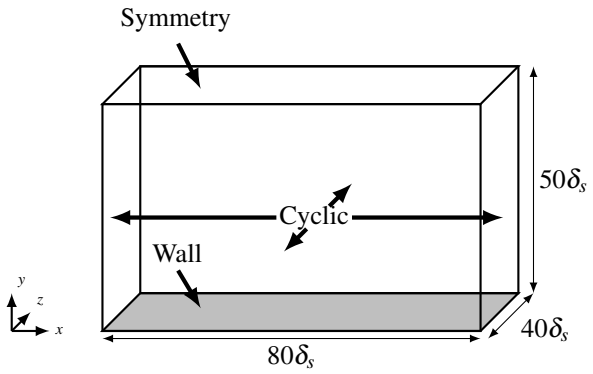


*Figure 2.4: Sketch of the geometry and boundary conditions of the numerical domain for the simulation of the clear water configuration from Jensen et al. (1989) [57].*

The mesh is decomposed into $60 \times 60 \times 55$ elements for a total of $198,000$ cells with a non-uniform grid size distribution along the $y$-axis. Cells sizes expands from the bottom wall toward the top boundary with an expansion ratio of 1.0135 giving a size ratio between the smallest and largest cells equal to 5.8446. The dimensionless grid spacing based on the maximum friction velocity is $\Delta x^+ = \Delta x u_\tau^m / \nu^f = 110$, $\Delta z^+ = 60$ and dimensionless cell size at the wall is $\Delta y^+_{wall} = 25$. Typical mesh resolution to resolve the laminar sub-layer impose a mesh requirement of $\Delta y^+_{wall} < 4$. However, accurate prediction of the flow hydrodynamics is obtained without resolving the laminar sub-layer and without any near-wall treatment. The time step is calculated to ensure a CFL below 0.3. Numerical parameters are presented in table 2.4.

| Mesh | Number of cells | $\Delta_x^+$ | $\Delta_z^+$ | $\Delta_y^+$ (wall) | $\Delta t$ |
|---|---|---|---|---|---|
| $60 \times 60 \times 55$ | $198,000$ | 110 | 60 | 25 | Adaptative ($CFL < 0.3$) |

*Table 2.4: Numerical parameters of the clear water configurations from Jensen et al. (1989) [57].*

The volume force driving the flow in the $x$-direction given by

$$f_i^v = \left( -\rho^f \frac{\partial u_\infty^f}{\partial t},\ 0\ ,\ 0 \right) = \left( -\rho^f U_m^f \omega cos(\omega t),\ 0\ ,\ 0 \right) \tag{2.96}$$

with $u_\infty^f = U_m^f sin(\omega t)$ the free-stream velocity.

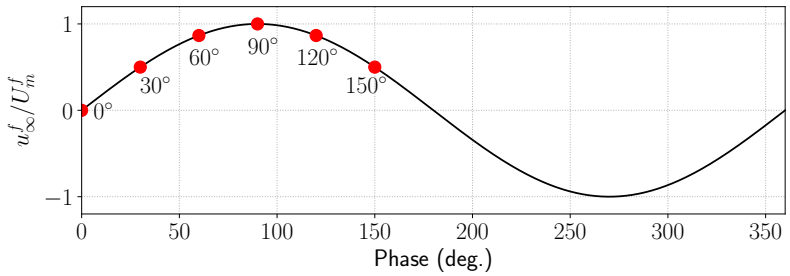


*Figure 2.5: Time series of the free stream velocity with indications on the wave phases for which intra-wave profiles are shown in the remaining of the manuscript.*

For the oscillatory flow simulations presented in this manuscript, four period are simulated to let the oscillating boundary layer develop and average profiles are calculated on the subsequent

four periods. A double average procedure (phase averaging operator $\langle\cdot\rangle$ for oscillatory flow with corresponding fluctuation $\cdot'$) is performed to increase statistical convergence. Indeed, the quantity of interest at a given moment of the wave period is averaged over the four periods and then, a spatial average is performed over the homogeneous directions of the flow ($x$- and $z$-directions) to obtain intra-wave one-dimensional vertical profiles.

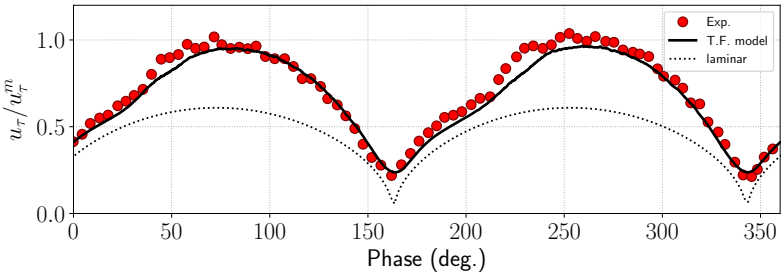


*Figure 2.6: Phase averaged friction velocity as a fraction of the experimental maximum friction velocity predicted by the two-fluid model (T.F. model) compared with experimental results of the clear water configuration from Jensen et al. (1989) [57] (Exp.) and analytical solution for the laminar case (laminar)*

.

Given that the wave forcing is symmetrical, intra-wave profiles from sinusoidal oscillatory flow configurations shown in the manuscript are presented only for the first half of the wave period (between 0° and 180°). For a given configuration, the figures are composed of six panels showing profiles at 0°, 30°, 60°, 90°, 120° and 150° (see figure 2.5).

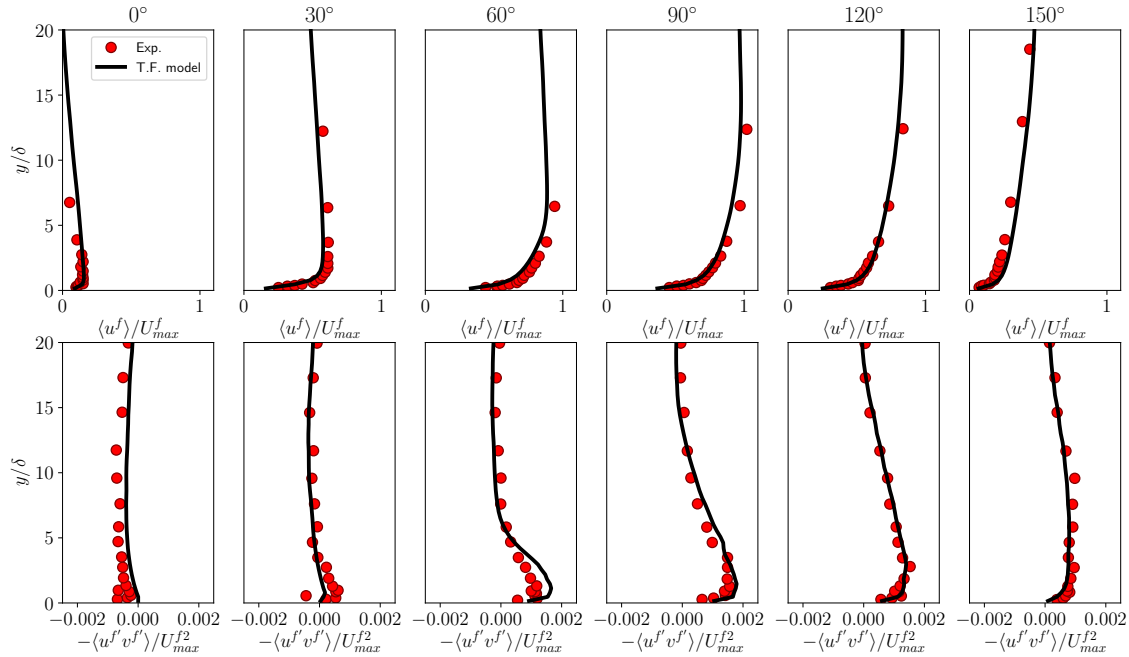


*Figure 2.7: Phase averaged velocity as a fraction of the maximum velocity (top) and phase averaged Reynolds stress as a fraction of the maximum velocity squared (bottom) predicted by the two-fluid model (T.F. model) compared with experimental results of the clear water configuration from Jensen et al. (1989) [57] (Exp.).*

The time evolution of the bottom friction velocity predicted by the T.F. model is compared

to experimental data and analytical solution for the laminar case in figure 2.6. The agreement is almost perfect between experiments and the simulation. It can also be noticed that the transition to turbulence occurring at around 20° and 200° characterized by an increase of the bottom shear stress compared with the laminar solution is accurately reproduced by the numerical model.

Velocity and shear stress profiles predicted by the TF model at different moments of the wave period are compared to experimental data in figure 2.7. Given that the wave forcing is symmetrical, only profiles in the first half of the wave period are presented (between 0° and 180°). Overall, the agreement between the TF model and the experimental data is quantitative over the wave period.

Eventually, the accurate prediction of the unidirectional boundary layer flow and oscillatory flow hydrodynamics allows to validate the implementation and numerical configuration of the model. These results give confidence in the model and allow us to perform particle-laden simulations in the next chapters.

# 3

# Two-phase flow simulations of oscillatory sheet flows subject to a sinusoidal flow forcing

*In this chapter, two phase flow simulations of oscillatory sheet flow configurations involving medium and fine sand subject to a sinusoidal flow forcing using the turbulence-resolving two-fluid model are presented. Detailed analysis of concentration profiles, flow hydrodynamics, turbulent statistics and vertical mass balance allowed to confirm that unsteady effects, namely phase-lag effect and enhanced boundary layer thickness for fine sand are not only due to the small settling velocity of the particles relative to the wave period. The occurrence and intensity of unsteady effects is also affected by a complex interplay between bed instabilities, strong solid phase Reynolds stress and turbulence attenuation caused by the presence of the particles.*

## Contents

## 3.1 Introduction

Considering the limitations in term of experimental capabilities and accurate representation of oscillatory sheet flow by turbulence-averaged model, the turbulence-resolving two-fluid model is applied to oscillatory sheet flow configurations subject to a sinusoidal flow forcing. The main objective is to study the mechanisms responsible for the observed significant differences between the behavior of medium and fine sand in oscillatory sheet flows. We hypothesize that the commonly recognized phase-lag effect is not only due to the small settling velocity of fine sand but is directly related to the enhanced transport layer thickness due to instabilities in the transitionally turbulent flow and turbulence attenuation by the presence of sediment.

In this chapter, the experimental configurations from O'Donoghue & Wright (2004a) [81] involving sinusoidal waves are reproduced numerically. Two types of sand are used: medium sand of diameter $d_p = 280\mu m$ (configuration M512) and fine sand of diameter $d_p = 150\mu m$ (configuration F512) with density $\rho^s = 2650 kg.m^{-3}$. For both configurations the flow conditions are the same with a sinusoidal flow forcing of period $T = 5s$ and maximum free stream velocity $U_m^f = 1.5 m.s^{-1}$. For this wave condition, the Stokes-layer thickness is $\delta = 1.26 \times 10^{-3} m$ and the maximum excursion length is $a = 1.19m$ giving Reynolds number based on theses quantities $Re = U_m^f a/\nu^f = 1.8 \times 10^6$ and $Re_\delta = U_m^f \delta/\nu^f = 1890$ respectively. Following the methodology used in O'Donoghue & Wright (2004a) [81], the friction velocity is calculated using the formula from Wilson *et al.* (1995) [124] giving $u_\tau^m = 0.112 m.s^{-1}$. This maximum friction velocity corresponds to a maximum Shields number $\theta^m = 2.75$ for medium sand and $\theta^m = 5.16$ for fine sand. For both configurations the Sleath parameter is equal to $Sl = 0.116$. The flow and particles parameters are summarized in table 3.1.

| Parameters | M512 | F512 |
|---|---|---|
| $T\ (s)$ | 5 | 5 |
| $U_m^f\ (m.s^{-1})$ | 1.5 | 1.5 |
| $d_p\ (\mu m)$ | 280 | 150 |
| $\rho^s\ (kg.m^{-3})$ | 2650 | 2650 |
| $v_s\ (m.s^{-1})$ | $3.96 \times 10^{-2}$ | $1.59 \times 10^{-2}$ |
| $a\ (m)$ | 1.19 | 1.19 |
| $\nu^f\ (m^2.s^{-1})$ | $1 \times 10^{-6}$ | $1 \times 10^{-6}$ |
| $\delta\ (m)$ | $1.26 \times 10^{-3}$ | $1.26 \times 10^{-3}$ |
| $u_\tau^m\ (m.s^{-1})$ | 0.112 | 0.112 |
| $Re$ | $1.8 \times 10^6$ | $1.8 \times 10^6$ |
| $Re_\delta$ | 1890 | 1890 |
| $\theta^m$ | 2.75 | 5.16 |
| $Sl$ | 0.116 | 0.116 |

*Table 3.1: Flow and particle parameters of the sheet flow configurations from O'Donoghue & Wright (2004a) [81] involving medium sand (M512) and fine sand (F512).*

## 3.2 Numerical configuration

For the sheet flow configuration, the numerical domain is a box of dimensions $160\delta \times 100\delta \times 40\delta$. Compared with the clear water configuration presented in section 2.5.2, the domain is two times larger in the $x$-direction because of bed instabilities susceptible to have length scales larger than $40\delta$. Mesh dimensions and boundary conditions are presented in figure 2.4. A symmetry boundary condition is applied at the top boundary, a wall boundary condition is applied at the bottom and cyclic boundary conditions are applied for the boundaries coincident with planes orthogonal to the $x$-axis and $z$-axis. The same numerical schemes as for the clear water configuration presented in section 2.5.2 configuration are used. The volume force driving the flow is given by expression (2.96).

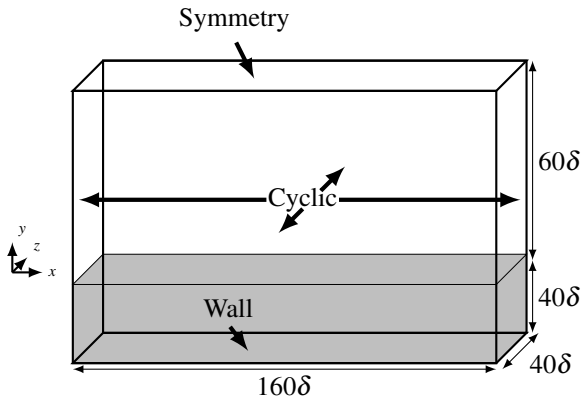


*Figure 3.1: Sketch of the geometry and boundary conditions of the numerical domain for the simulation of the sheet flow configurations from O'Donoghue & Wright (2004a) [81].*

The mesh is decomposed into $200 \times 260 \times 92$ elements for a total of $4,784,000$ cells. The dimensionless grid spacing in the $x$-direction and $z$-direction is $\Delta x^+ = 110$, $\Delta z^+ = 60$. The mesh is decomposed into three different regions in the vertical direction. Taking $h_s$ the height of the deposited sediment bed initialized by a power law, from the bottom to $y = h_s - 24\delta$, the region is decomposed into 20 cells using a non-uniform length distribution to have smaller cells with $\Delta y^+ = 25$ toward the top of the deposited sediment. The mesh region from $y = h_s - 24\delta$ to $y = h_s - 8\delta$ is decomposed into 132 cells of constant grid spacing $\Delta y^+ = 25$ and eventually, the mesh region from $y = h_s + 8\delta$ to the top boundary is decomposed into 108 elements with a non-uniform grid spacing and smallest cells having a length of $\Delta y^+ = 25$. Compared with the smooth wall configuration presented in section 2.5.2, velocity gradients in the bottom boundary layer are expected to be smoother in the oscillatory sheet flow configurations. The mesh resolution should therefore be sufficient to reproduce the boundary layer hydrodynamics considering that accurate prediction of the velocity and Reynolds stress profiles are obtained for similar grid resolution in the clear water configuration from section 2.5.2. The mesh resolution in the near bed region corresponds to grid sizes $\Delta x \approx 3.5 d_p$, $\Delta z \approx 1.9 d_p$ and $\Delta y \approx 0.8 d_p$ for configuration M512 and $\Delta x \approx 6.5 d_p$, $\Delta z \approx 3.5 d_p$ and $\Delta y \approx 1.5 d_p$ for configuration F512 ensuring the condition $\Delta \sim O(d_p)$. From flow initialization to the computation of phase averaged variables, numerical calculation last for about one week on 168 cores (n nodes) for a total of approximatively $29,000$ core-hours.

The pressure gradient driving the flow is given by equation (2.96) and the same averaging procedure is performed as in section 2.5.2.

## 3.3 Results

In this section, the results composed of intra-wave information on the concentration and velocities are presented. The main objective is to shed light on the physical difference of behavior between medium and fine sand for a given wave condition before exposing the underlying processes in the next section.

### 3.3.1 Time evolution of the solid phase concentration

Phase averaged concentration profiles are represented at different moment of the wave period in figures 3.2 for configurations M512 (top) and F512 (bottom). As for the results presented in section 2.5.2, profiles are shown only for the first half of the wave period because of the wave symmetry.

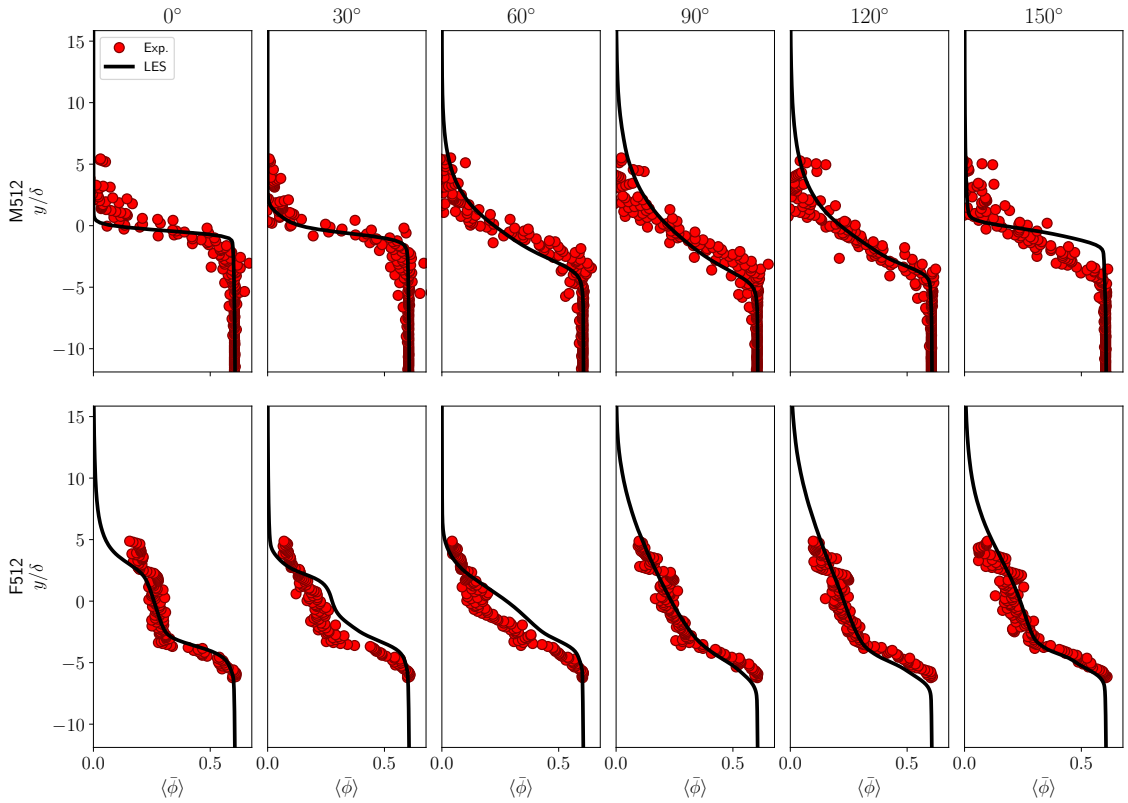


*Figure 3.2: Phase averaged concentration profiles from configurations M512 (top) and F512 (bottom) predicted by the two-phase flow model (LES) compared with experimental data from O'Donoghue & Wright (2004a) [81] (Exp.).*

As a consequence of the experimental uncertainty to determine the zero bed level, experimental concentration profiles might need to be shifted to align measured and numerically modeled maximum erosion depths. For configuration M512, concentration profiles do not need to be shifted. For configuration F512, concentration profiles are shifted downward by a distance of $1.5\delta$. Once the shift is determined, it is never changed for the rest of the comparison for that specific case.

For both configurations, the agreement with experimental data is very good throughout the wave period. The only discrepancy that can be observed for the simulation of configuration M512 is at 150° where the sediment concentration is overestimated in the lower part (pick-up layer) and underestimated in the upper part (suspension layer) of the concentration profile. This feature

suggests that the sediments settle too quickly to the bed during flow deceleration compared with the experimental observations.

For configuration M512, the evolution of the concentration profile across the wave period follows the well documented description proposed by O'Donoghue & Wright (2004a) [81]. A clockwise rotation of the concentration profile around an almost constant concentration "pivot" is observed during flow acceleration resulting in a decrease in concentration in the pick-up layer and increase in the suspension layer. During flow deceleration, an anticlockwise rotation results in an increase of the concentration of the pick-up layer and a decrease in the suspension layer as sediments settle back to the bed (see figure 1.12).

However, for configuration F512, the behavior of the sediment concentration profile shape is very different. Around flow peak (60°, 90° and 120°), the concentration profile shows a linear shape with a change of slope at around $\langle\bar{\phi}\rangle = 0.3$. During flow deceleration, the slope of the upper part of the concentration profile becomes steeper and the formation of a concentration plateau can start to be observed at late stage of deceleration (150°). At flow reversal, the concentration in the plateau is evident at $y/\delta = 3$ with a nearly depth uniform concentration at $\langle\bar{\phi}\rangle = 0.3$ between $y/\delta = -3$ to 3. The plateau is subsequently eroded during flow acceleration (30° and 60°). Although both cases are driven by the same oscillatory flow, we can notice at least qualitatively a significantly larger transport layer thickness of a peak value of $15\delta$ for configuration F512, which is two times larger than that of configuration M512. The significantly larger transport layer thickness and small settling velocity of fine sand both contribute to its unique features observed here and we will investigate in more detail in the remaining of this chapter.

### 3.3.2 Velocity profiles

The profiles of Favre phase-averaged velocities $\langle\tilde{u}_i^f\rangle_F = \langle(1-\bar{\phi})\tilde{u}_i^f\rangle/(1-\langle\bar{\phi}\rangle)$ and $\langle\tilde{u}_i^s\rangle_F = \langle\bar{\phi}\tilde{u}_i^s\rangle/\langle\bar{\phi}\rangle$ from configurations M512 and F512 are presented in figure 3.3.

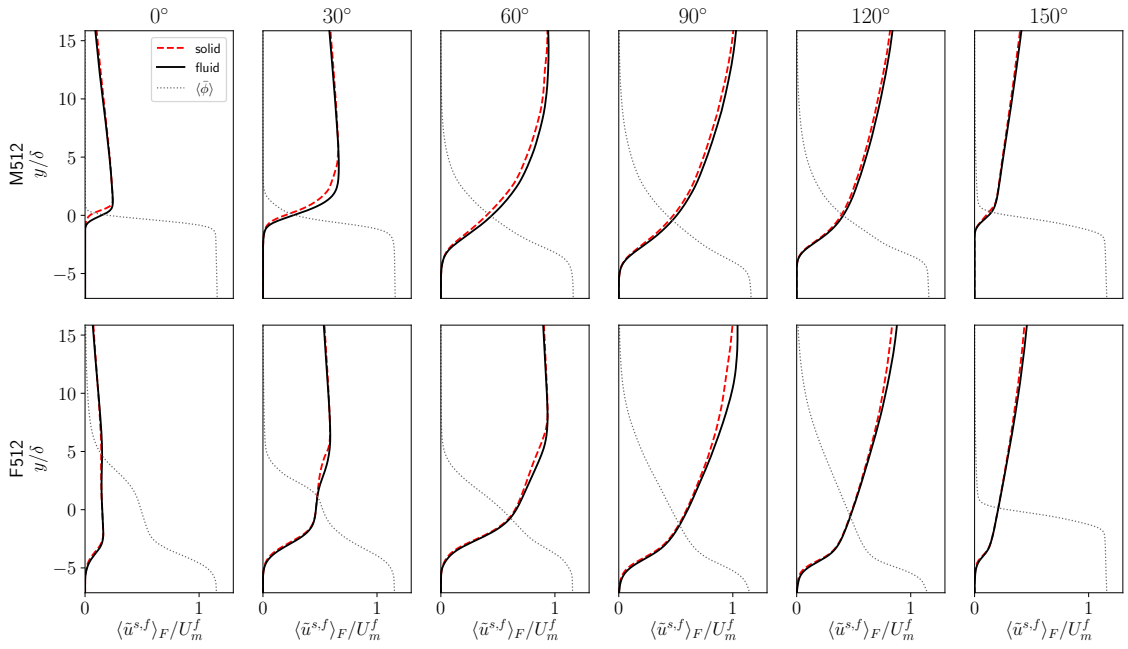


*Figure 3.3: Favre averaged fluid and solid velocity profiles predicted by the two-phase flow model as a fraction of the maximum velocity from configurations M512 (top) and F512 (bottom).*

For both configurations, the fluid and solid velocity profiles are superimposed during flow deceleration and flow reversal. However, during flow acceleration, the solid velocity slightly lags

the fluid velocity. At early stages of flow acceleration, this velocity lag is located near the bed and moves upward as the flow accelerates.

The velocity profiles in configuration M512 show expected behavior of the oscillatory boundary layer. However, for configuration F512, the velocity profiles show significant differences. The velocity profiles are affected by the concentration plateau (0°, 30° and 60°). At early stages of flow acceleration, the boundary layer is decomposed into two different layers of almost constant velocity. This behavior is very similar to the plug flow described by Zala-Flores & Sleath (1998) [131] and Sleath (1999) [107] but the mechanism is different. The threshold of plug flow can be modified by (i) the compaction of the sediment bed [107] and (ii) the Shields number [22, 41]. On the one hand, the yield strength decrease for lower bed compaction. As a consequence, smaller pressure gradient is necessary to generate the plug flow. On the other hand, the mobile sediment bed is larger during flow acceleration for higher Shields number. The sediment bed is looser at flow reversal having for effect to alter its yield strength. For configuration F512, the concentration at flow reversal in the plateau is too low for a yield strength to develop between the plateau and the immobile sediment bed. Therefore, under the action of the pressure gradient, the sediment plateau "slides" almost freely over the sediment bed for values of the Sleath number as low as $Sl = 0.116$.

The hydrodynamic is further investigated by comparing the different shear stress contributions from both phases.

### 3.3.3 Shear stress profiles

Profiles of Reynolds stresses for fluid and solid phases

$$R^f_{xy} = \rho^f (1 - \langle\bar{\phi}\rangle)\langle\tilde{u}^{f'}\tilde{v}^{f'}\rangle, \quad R^s_{xy} = \rho^s\langle\bar{\phi}\rangle\langle\tilde{u}^{s'}\tilde{v}^{s'}\rangle, \tag{3.1a,b}$$

and profiles of shear stress resulting from particle friction and collisions

$$\tau^{fr}_{xy} = \left\langle \rho^s\bar{\phi}\nu^{fr}\left(\frac{\partial\tilde{u}^s}{\partial y} + \frac{\partial\tilde{v}^s}{\partial x}\right)\right\rangle, \quad \tau^c_{xy} = \left\langle \rho^s\bar{\phi}\nu^c\left(\frac{\partial\tilde{u}^s}{\partial y} + \frac{\partial\tilde{v}^s}{\partial x}\right)\right\rangle, \tag{3.1a,b}$$

are presented in figure 3.4.

For both configurations, shear stress is dominated by friction in the sediment bed, collisions at the bottom of the transport layer and Reynolds stresses in upper section of the flow. The contribution of the shear stress resulting from collisions is almost zero at flow reversal, increases during the acceleration phase of the flow to reach its maximum before flow peak and decreases afterwards. As expected due to the greater particle's inertia for medium sand, the relative contribution of the collisional shear stress is greater for configuration M512 compared with configuration F512.

The time evolution of the fluid phase Reynolds stress profiles from configuration M512 shows the classical features of a rough oscillatory boundary layer. The relative contributions of the Reynolds stresses from fluid and solid phase are similar at the top of the transport layer. As the sediment concentration decreases, the solid phase contribution decreases and the fluid Reynolds stress dominates. Furthermore, around flow reversal, particles are deposited and the solid phase contribution to the Reynolds stress vanishes.

For configuration F512, the development of the fluid Reynolds stresses is inhibited by the formation of the plateau around flow reversal suggesting a strong modulation of turbulence by the particles. Turbulence modulation and formation of a concentration plateau shows similarities with the two layer structure separated by a lutocline well known for fine sediment transport [83, 101]. However, the mechanism at play is fundamentally different. As observed by Ozdemir *et al.* (2010) [83], the two layer structure with an almost homogeneous concentration profile in lower region of the flow followed by a rapid decrease of the concentration is the result of turbulence attenuation in the upper layer and strong mixing in the lower layer. For configuration F512, turbulence is damped everywhere in the flow meaning that the concentration plateau is not a consequence of

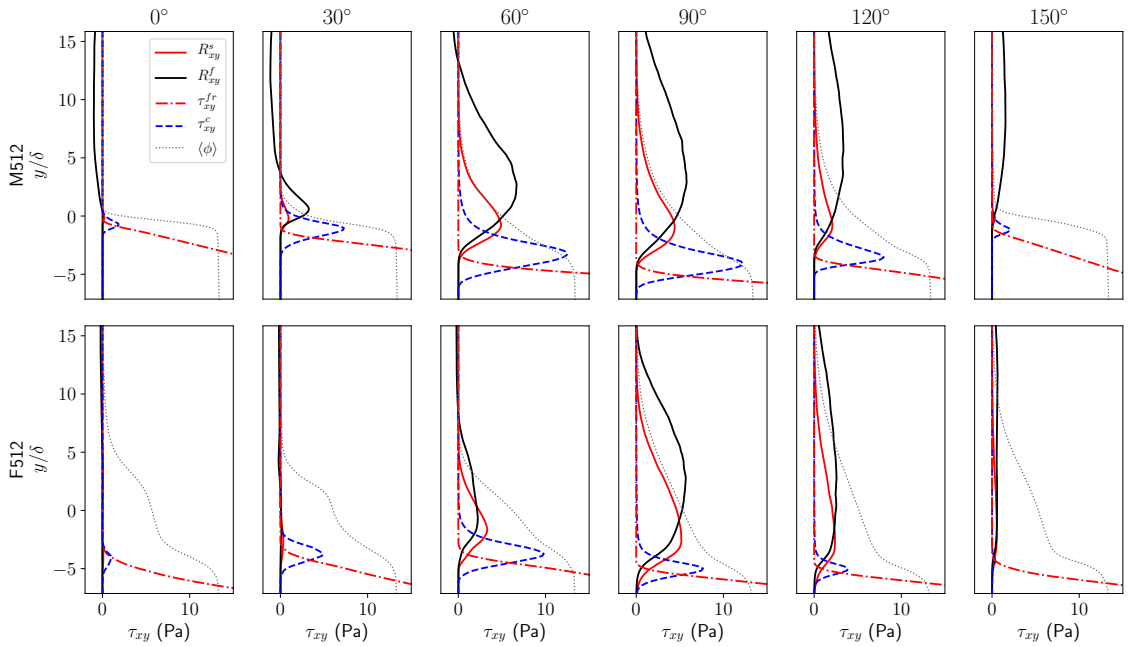


*Figure 3.4: Solid and fluid Reynolds shear stress profiles $R^s_{xy}$ and $R^f_{xy}$ respectively, shear stress resulting from particles friction $\tau^{fr}_{xy}$ and shear stress resulting from particles collisions $\tau^c_{xy}$ from configurations M512 (top) and F512 (bottom)*

strong vertical mixing of sediment. The formation of the concentration plateau is further discussed in section 3.4.2.

Compared with configuration M512, Reynolds stresses in configuration F512 penetrate deeper into the bed, the solid phase contribution dominates in the lower part of the transport layer and is present much higher in the flow. The great importance of solid phase Reynolds stress, usually considered negligible, contributes to explain the limitations of turbulence-averaged models in term of predictive capabilities for fine sand. Due to a greater contribution of the solid phase Reynolds stress relative to fluid phase Reynolds stress to the horizontal momentum budget, what can be called "solid phase turbulence" plays a key role during the acceleration phase of the wave for configuration F512. As a consequence, mixing and boundary layer's inertia are increased. Transport layer becomes thicker and it takes more time for the boundary layer to adapt to the evolving flow conditions resulting in the emergence of phase-lag effect.

### 3.3.4 Sheet flow layer thickness and streamwise sediment flux

An important feature of oscillatory sheet flows is the sheet flow layer thickness $\delta_s$. The sheet flow layer thickness is defined as the distance between the erosion depth and the elevation where the phase average concentration is equal to $\langle\bar{\phi}\rangle = 0.08$. It is rather straightforward to get the upper limit of the sheet flow layer thickness but the definition of the erosion depth is subject to discussion. For Dohmen-Janssen *et al.* (2001) [29], the erosion depth is defined as the still bed level for which the velocity returns back to zero whereas for O'Donoghue & Wright (2004a) [81], the erosion depth is obtained by fitting the power law to the concentration profile. The later definition can hardly be applied to the fine sand configuration given that the concentration profile can not be reproduced using a power-law. Therefore, the method of Dohmen-Janssen *et al.* (2001) [29] is used to define the erosion depth for both configurations. According to O'Donoghue & Wright (2004a) [81] for medium sand, the two definitions should give similar estimates of the erosion depth.

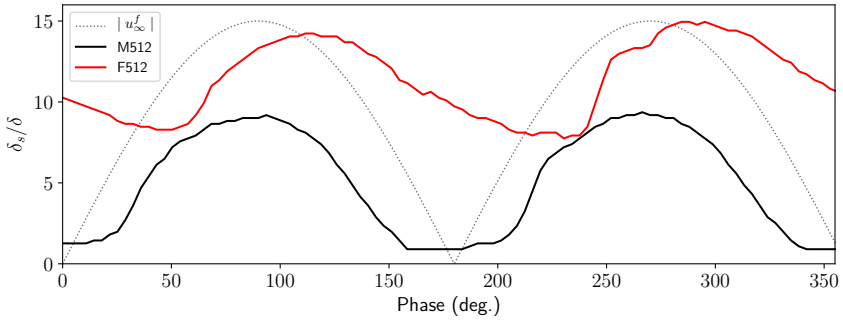


*Figure 3.5: Time series of the sheet flow layer thickness $\delta_s$ made dimensionless by the Stokes layer thickness $\delta$ from the sheet flow configurations M512 and F512.*

The time series of the sheet flow layer thickness made dimensionless by the Stokes layer thickness from configurations M512 and F512 are compared with the free stream velocity in figure 3.5. The sheet flow layer thickness is perfectly in phase with the free stream velocity for configuration M512. The sheet flow layer thickness is constant close to zero at flow reversal, start to grow at around 25°, reaches a maximum $\delta_s^m/\delta \approx 9$ at the maximum free stream velocity and decreases at almost the same rate as it grew during flow acceleration to reach a constant value around 25° before the next flow reversal. For configuration F512, the time series of $\delta_s$ is not in phase with the free stream velocity. The sheet flow layer thickness suddenly increases at around 55°, reaches a peak $\delta_s^m/\delta \approx 14$ at around 110° and then decreases slowly to reach a value of $\delta_s/\delta \approx 8$ before growing again at around 55° after the next flow reversal. Whereas the time series of the sheet flow layer thickness shows a symmetrical behavior in its growth and decrease for configuration M512, the ratio between growth phase and decrease phase for configuration F512 is lower than 0.5.

Most importantly, for the same hydrodynamic forcing between the two configurations, sheet flow layer thickness in configuration F512 is much greater than the sheet flow layer thickness in configuration M512 throughout the wave phase confirming the importance of unsteady effects in configuration F512.

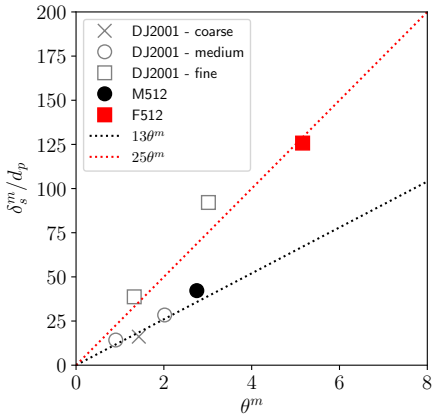


*Figure 3.6: Maximum sheet flow layer thickness made dimensionless by the particle diameter $\delta_s^m/d_p$ as a function of the maximum Shields number $\theta^m$ for configuration F512 and M512 compared with experimental measurements involving coarse, medium and fine sand from Dohmen-Janssen et al. (2001) [29].*

The maximum sheet flow layer thickness $\delta_s^m$ made dimensionless by the particle parameter as a function of the maximum Shields number for both configurations is presented in figure 3.6.

The dimensionless maximum sheet flow layer thickness for configuration M512 scales very well with measurements from Dohmen-Janssen *et al.* (2001) [29] involving medium and coarse sand. In the absence of unsteady effects, dimensionless maximum sheet flow layer thickness increases linearly with the Shields number with $\delta_s^m/d_p = 13\theta^m$ [29]. For configurations involving fine sand, the slope of the relation between $\delta_s^m/d_p$ and $\theta^m$ becomes steeper as a consequence of unsteady effects. Experimental measurements from Dohmen-Janssen *et al.* (2001) [29] involving fine sand and configuration F512 are well represented by the relation $\delta_s^m/d_p = 25\theta^m$ used in the practical sand transport model proposed by [114] for fine sand.

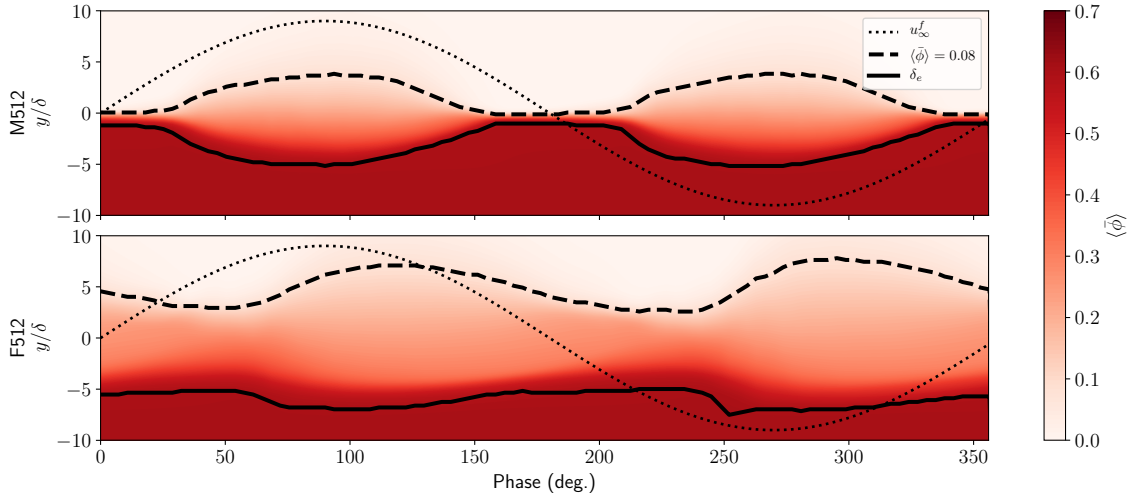


*Figure 3.7: Color map representing the time evolution of the solid phase concentration, time series of the erosion depth $\delta_e$ and the top of the sheet flow layer corresponding to concentration $\langle\bar{\phi}\rangle = 0.08$ from the sheet flow configurations M512 and F512.*

To supplement the study of the behavior of the sheet flow layer thickness, a color map representing the time evolution of the sediment concentration with the erosion depth $\delta_e$ and the line of iso-concentration $\langle\bar{\phi}\rangle = 0.08$ for both configuration are presented in figure 3.7. Compared with the time series presented in figure 3.5, this figure allows to describe the sheet flow layer thickness evolution in time by differentiating its upper and lower boundaries intra-wave dynamics. For configuration M512, there is a symmetry between the erosion depth and the line of iso-concentration $\langle\bar{\phi}\rangle = 0.08$ with respect to the still bed level $y = 0$. However, for configuration F512 the erosion depth is almost constant throughout the wave period. The successive shrinking and enlargement of the sheet flow layer thickness is mostly due to the variation of its upper limit. Compared with configuration M512, given that the erosion depth is almost constant for configuration F512, the amount of sediment in the transport layer is of lower variability throughout the wave period.

The time series of $q_x$ the streamwise depth-integrated sediment flux calculated as

$$q_x = \int_{-\infty}^{\infty} \langle \bar{\phi}\tilde{u}^s \rangle dy \tag{3.2}$$

are plotted in figure 3.8 for configurations F512 and M512. Similarly to the sheet flow layer thickness, the sediment flux is perfectly in phase with the free stream velocity for configuration M512. However, the temporal variability of sediment flux is more complex F512. There is a significant phase shift between the sediment flux and the free stream velocity. Sediment flux leads the velocity at flow reversal and lags it at flow peak. Furthermore, a sudden increase of the streamwise sediment flux can be observed corresponding to the sheet flow layer increase at around 55° and 235°. The two-fluid simulations reveal the strong non-linear interactions between turbulence and particles dynamics that lead to the increase of sediment transport.

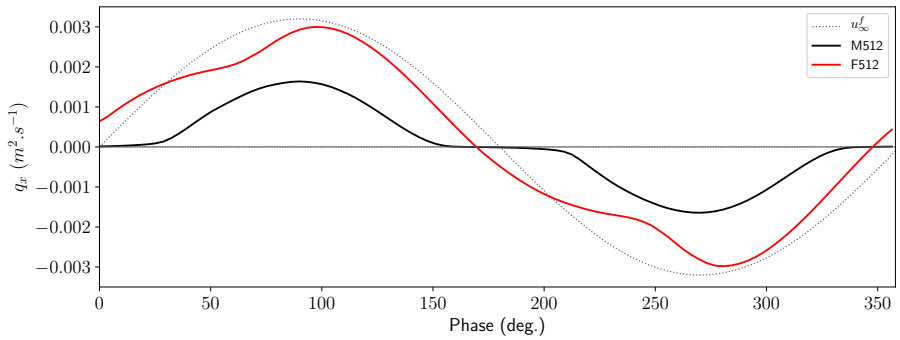


*Figure 3.8: Times series of $q_x$ the streamwise depth-integrated sediment fluxes and the respective bed load contributions.*

To better understand the difference of behavior between the two configurations, snapshots of the simulations showing the fluid phase coherent turbulent structures and surfaces of instantaneous concentration $\bar{\phi} = 0.5$ and $\bar{\phi} = 0.08$ at flow reversal (0°), during flow acceleration (21° and 58°) and at flow peak (90°) are presented in figure 3.9. At flow reversal, medium sand has completely settled to the bed and turbulent structures are visible whereas fine sand is still in suspension in the total absence of turbulence due to its low settling velocity and larger sheet flow layer thickness. At early stage of flow acceleration, small amplitude two-dimensional shear instabilities start to develop at the bottom in the form of small ripples on the surface of concentration $\bar{\phi} = 0.5$ at 21° in figure 3.9 for configuration M512 and rapidly transition to three-dimensional turbulent perturbation of the sediment bed. For configuration F512, turbulence starts to develop during flow acceleration and two-dimensional shear instabilities of larger amplitude in the form of breaking billows are visible on the surface of concentration $\bar{\phi} = 0.5$ at 58° in figure 3.9. These instabilities are visible at the bottom but the top of the sheet flow layer exhibits three-dimensional turbulent flow structures. Strong instabilities have for effect to increase vertical mixing of the sediment and significantly increase the sheet flow layer thickness. Eventually, the two-dimensional instabilities transition to turbulence. For both configurations, boundary layers are fully turbulent at flow peak.

To better understand turbulence modulation induced by the particles and enhanced mixing for configuration F512, the time evolution of resolved TKE in the oscillatory boundary layer is investigated in the next section.

## 3.4 Discussion

In this section, the physical mechanisms responsible for the differences of behavior observed in section 3.3 are discussed. First, the modulation of turbulence due to the presence of the particles is presented and its effect on the mass balance between downward settling and upward turbulent fluxes is analyzed.

### 3.4.1 Turbulence modulation induced by the particles

As suggested by Dohmen-Janssen *et al.* (2001) [29], an important feature of the difference of behavior can come from turbulence modulation by the particles. Compared with experiments, numerical simulation has the advantage to provide a better insight into turbulence statistics such as the time-evolution of TKE in the oscillatory boundary layer. The spatio-temporal evolution of

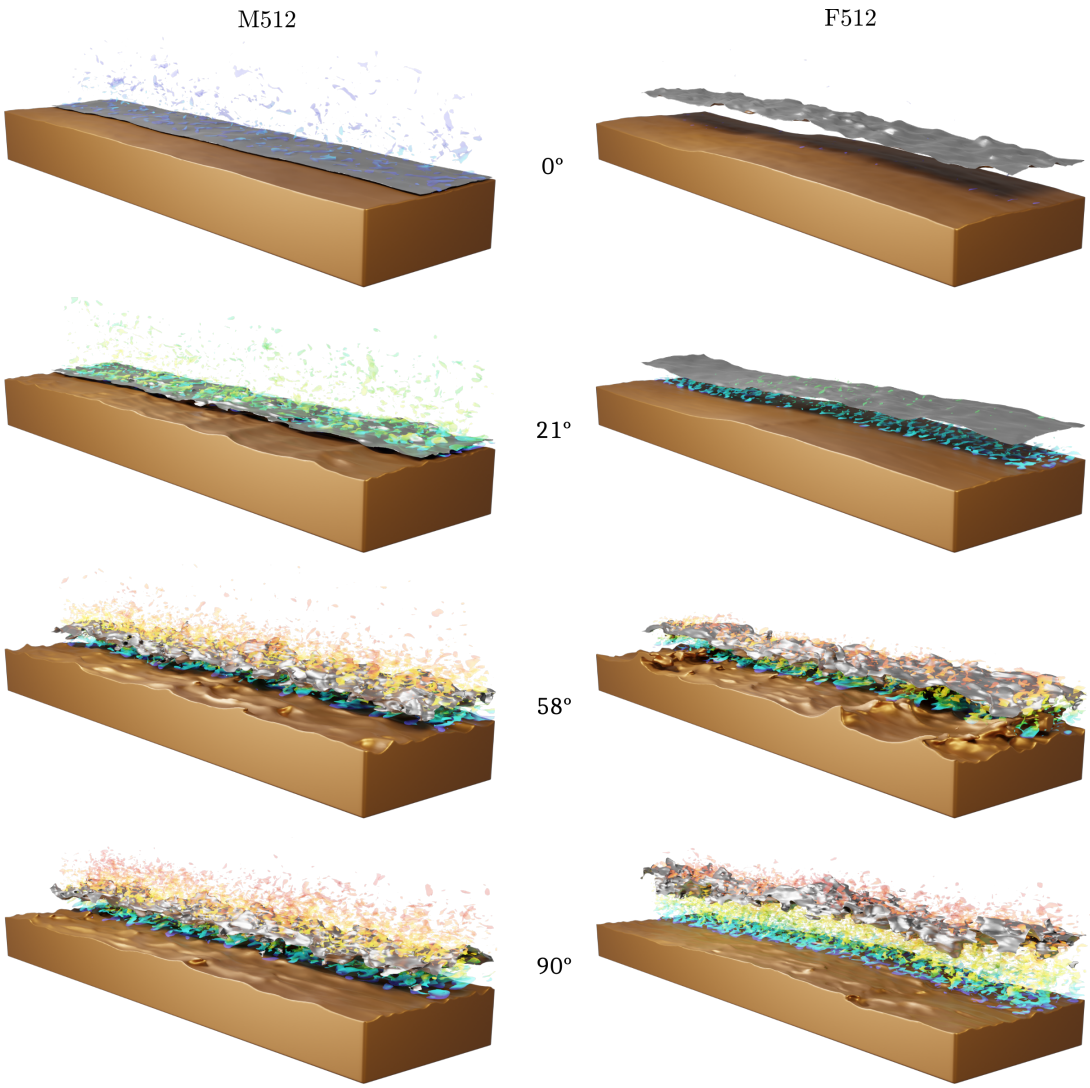


*Figure 3.9: Snapshots of the configurations M512 (left panels) and F512 (right panels) at* $0^\circ$, $21^\circ$, $58^\circ$ *and* $90^\circ$ *with surfaces of concentration* $\bar{\phi} = 0.5$ *(brown),* $\bar{\phi} = 0.08$ *(silver) and fluid turbulent coherent structures colored by the fluid velocity.*

resolved TKE during the wave period is presented in figure 3.10 for both configurations. Turbulence generation during flow acceleration and decay during flow deceleration behaves completely differently between configuration M512 and F512.

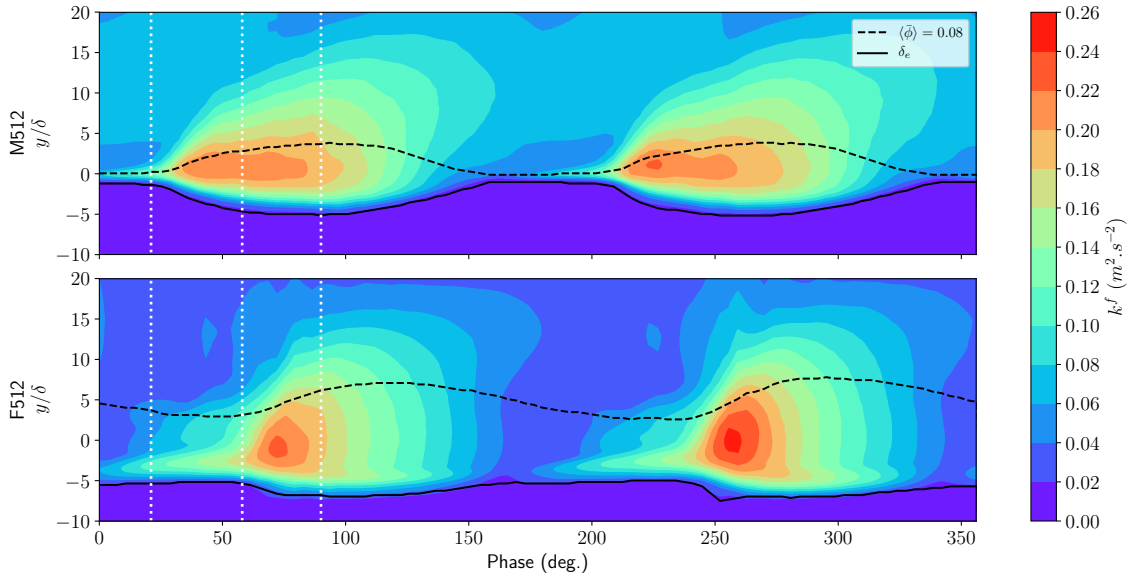


*Figure 3.10: Color map of the resolved fluid TKE from configurations M512 (top) and F512 (bottom) with white lines representing the moment where snapshots from figures 3.9 were taken.*

For configuration M512, the boundary layer remains fully turbulent throughout the wave period. Turbulence is generated due to strong shear close to the bed at early stage of the wave period, then a sudden increase of TKE is observed corresponding to appearance of the two-dimensional instabilities and the increase of the sheet flow layer thickness at around 20°. TKE reaches its maximum just before flow peak and eventually decays during flow deceleration resulting in the deposition of particles without re-laminarization of the flow.

For configuration F512, the mechanisms of turbulence production and dissipation inside the sheet flow layer thickness are a bit more complicated. As for configuration M512, TKE starts to increase at the top of the immobile bed at early stages of flow acceleration but, TKE is also produced at the top of the sheet flow layer. These production zones correspond to the high velocity shear rate regions of the flow located at the top and bottom of the concentration plateau as can be seen in figure 3.3. Similarly to configuration M512, the appearance of the two-dimensional shear instabilities corresponds to a sudden spread of the TKE. The top and bottom shear layers eventually meet and the resulting shear layer thickness increases as the sheet flow layer thickness increases.

The maximum TKE is larger for configuration F512 compared with M512 traducing the enhanced vertical mixing of fine sand. However, turbulence is dissipated much more rapidly with an almost complete re-laminarization of the boundary layer near flow reversal.

In that case, stratification induced by the particles in suspension in the concentration plateau near flow reversal has a stabilizing effect. Usually, this behavior is observed for very fine sediment with very low fall velocity [83] but, under such energetic conditions, the same phenomenon occurs given the significant quantity of sediment maintained into suspension during flow reversal. To quantify the stabilizing effect of density stratification, the vertical profiles of the Richardson number defined as

$$Ri = \frac{g}{\rho^m} \frac{|\partial \rho^m / \partial y|}{(\partial u^f / \partial y)^2} \tag{3.3}$$

with $\rho^m = \phi\rho^s + (1-\phi)\rho^f$ the mixture density are plotted in figure 3.11. The Richardson number

represents the ratio between turbulence attenuation induced by density stratification and turbulence production due to shear. From stability analysis, it is generally assumed that density stratification stabilizing forces dominate for $Ri > 0.25$.

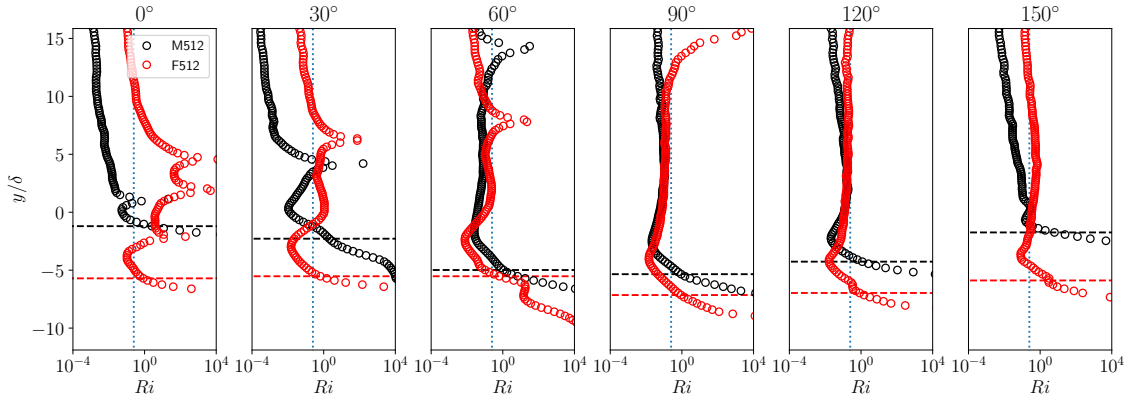


*Figure 3.11: Vertical profiles of Richardson number for configurations M512 and F512. Dotted line corresponds to $Ri = 0.25$ and dashed lines corresponds to the erosion depths.*

For both configurations, the Richardson number is below the threshold value of 0.25 over the still bed during the latest stage of flow acceleration, flow peak and early stage of flow reversal. However, the Richardson number becomes greater than 0.25 at latest stage of flow deceleration and at flow reversal for configuration F512. When shear becomes weaker during flow deceleration, the density gradient generated by the presence of the particles in the water column strongly attenuates the turbulence. Stabilizing forces induced by flow stratification predominates over turbulence production and the flow becomes laminar at flow reversal.

Density stratification may not be the only mechanism responsible for turbulence attenuation. For sand particles, drag-induced turbulence dissipation can also contribute to the reduction of the surrounding turbulence [23]. The analysis of detailed TKE budget in the future would allow to better identify and quantify the relative contributions of the mechanisms at the origin of turbulence modulation by the particles in the oscillatory boundary layer.

The modulation of turbulence has not only an effect on the hydrodynamics but also vertical mixing of the particles. Mechanisms of erosion and deposition are affected by the differences in the behavior of the turbulent boundary layer between the two configurations.

### 3.4.2 Vertical fluxes

Taking the phase average of the sediment mass conservation equation (2.44) gives the following expression:

$$\frac{\partial \langle \bar{\phi} \rangle}{\partial t} + \frac{\partial \langle \bar{\phi} \tilde{v}^s \rangle}{\partial y} = 0. \tag{3.4}$$

The time evolution of the concentration profile is controlled by the divergence of the vertical sand flux. This net sand flux can be decomposed into two components:

$$\langle \bar{\phi} \tilde{v}^s \rangle = \langle \bar{\phi} \rangle \langle \tilde{v}^s \rangle + \langle \phi' \tilde{v}^{s'} \rangle, \tag{3.5}$$

with the former being the averaged settling flux defined as the product of the average concentration and vertical velocity and the latter being the correlation between concentration and vertical velocity fluctuations, which is called the average Reynolds flux. The Reynolds flux represents the upward sediment flux generated by turbulence. The net flux can be either dominated by the settling or the Reynolds flux but both of them coexist at the same time throughout the wave period.

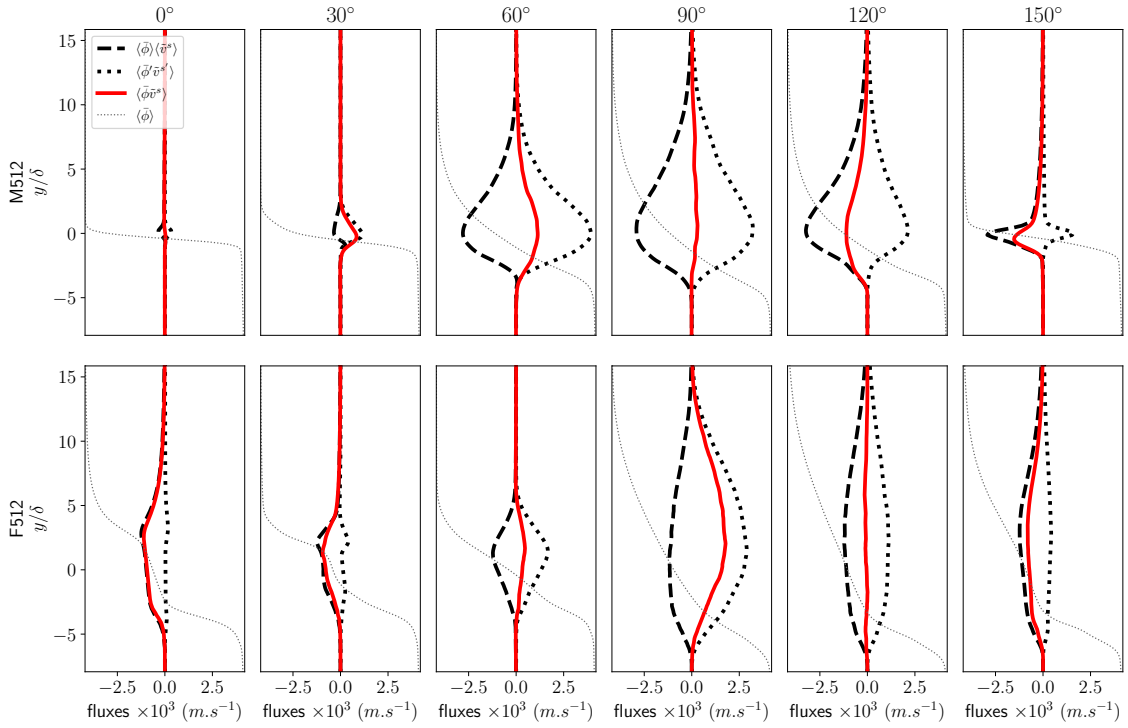


*Figure 3.12: Vertical fluxes at different moments of the wave period from the sheet flow configurations M512 (top) and F512 (bottom).*

The net, settling and Reynolds fluxes for both configurations are presented at different moment of the wave period in figure 3.12. For configuration M512, sand is completely deposited at flow reversal resulting in a zero vertical flux. During flow acceleration, the net sand flux is dominated by the upward Reynolds flux. Particles are picked-up from the bed by the fluid phase turbulent flow structures. At flow peak, a similar behavior compared with steady particle-laden boundary layer flows is observed. There is an equilibrium between upward Reynolds and downward settling fluxes meaning that the amount of particles eroded by turbulent flow structures equals the number of particles falling back to the bed. Eventually, during flow deceleration, the net flux is dominated by settling but a significant contribution to the net sand flux from upward Reynolds flux remains.

For configuration F512, the time evolution of the net vertical sand flux is more complex. Under the effect of instabilities during flow acceleration, solid phase Reynolds stress become large (see figure 3.4) and vertical mixing is enhanced. As a result, the net sediment flux is still dominated by Reynolds flux at flow peak. Compared with configuration M512, there is no equilibrium between settling and Reynolds fluxes. Settling and Reynolds fluxes are balanced at 150° and the net sediment flux becomes settling dominated during latest stage of flow deceleration. As a result of turbulence attenuation due to stable stratification, Reynolds flux is almost zero around flow reversal. During this phase, the net sediment flux is almost exclusively controlled by the free fall of the particles. This analysis represents the first observation of phase-lag effect on the vertical mass budget of sediments.

For configuration M512, the position of the maximum net sand flux corresponds approximately to the position of the inflection point of the concentration profile. In that case, the divergence of the flux is zero at the location of the inflection point. During flow acceleration, particles are picked-up from the bed and transits from the bottom to higher section of the flow with a maximum flux at the inflection point and vice versa during flow deceleration. This behavior results in a concentration profile pivoting around the inflection point during successive acceleration and deceleration phases following the classical description provided by O'Donoghue & Wright (2004a) [81]. However,

for configuration F512, the maximum sediment flux is located much higher in the flow when the flux is settling dominated around flow reversal. Particles settle faster in upper sections of the flow, the sediment concentration saturates as the particle fall velocity decreases due to hindered settling induced by neighboring particles toward the bed and the concentration plateau forms. Eventually, as the concentration becomes constant in the plateau, so does the net vertical flux and the divergence of the flux inside the plateau becomes zero. As a consequence, particles settling at a higher rate from upper section of the flow transit at a constant rate through the plateau of constant concentration before settling back to the bed. The formation of the concentration is therefore the direct consequence of the coupling between the shape of the concentration profile and hindered settling, not the consequence of a turbulent mechanism as observed for fine sediment by Ozdemir *et al.* (2010) [83] for fine sediment.

Indeed, the formation of concentration plateaus in sedimentation theory has already been observed and extensively investigated both analytically and numerically [12–14]. Finding solutions for the vertical sediment mass balance in sedimentation theory amounts to solving a Riemann problem where shocks and expansion waves can form. The formation of the concentration plateau at flow reversal in configuration F512 can directly be related to a sedimentation shock forming at the top of the transport layer and an expansion wave eventually leading to a constant concentration inside the plateau.

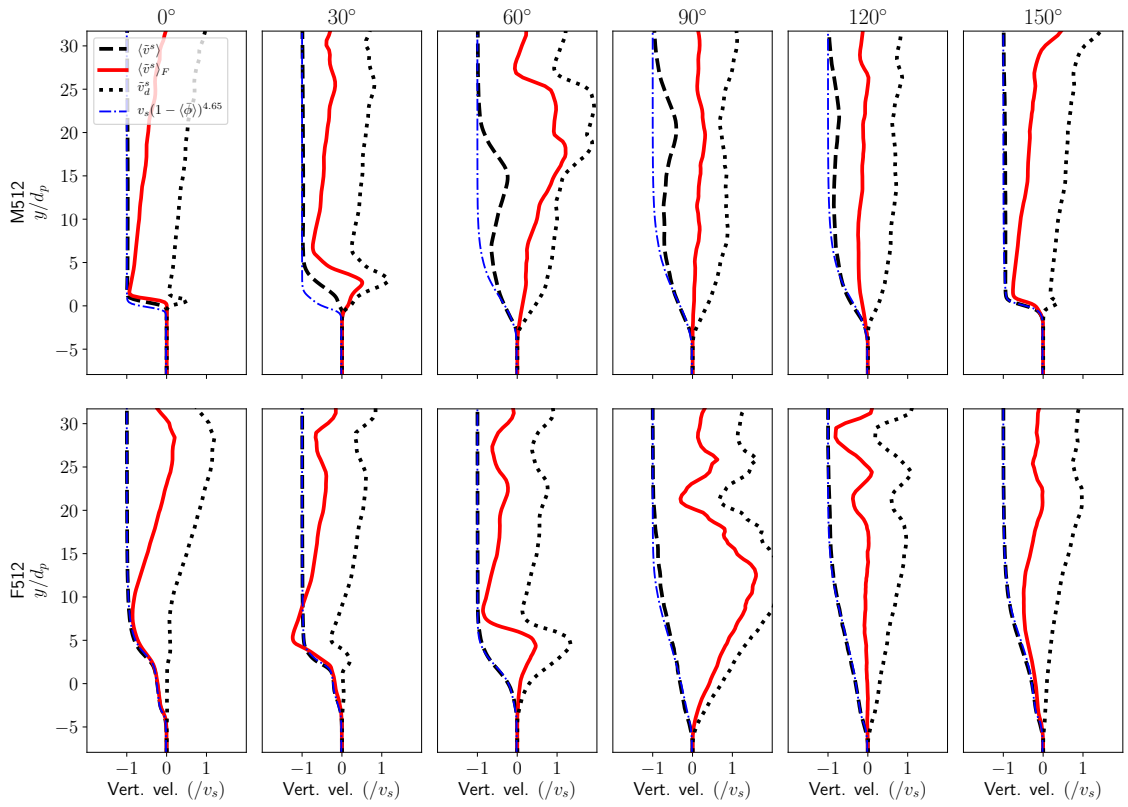


*Figure 3.13: Favre averaged vertical velocity, averaged settling velocity and drift velocity profiles as a fraction of the settling velocity $v_s$ at different moments of the wave period from the sheet flow configurations M512 (top) and F512 (bottom) compared with the empirical expression of the hindered settling velocity from Richardson & Zaki (1997) [94].*

The Reynolds flux contribution for configuration M512 during flow deceleration has for effect to decrease the net sediment flux in the upper section of the flow and shift the maximum net flux toward the concentration profile inflection point. If the Reynolds flux contribution was zero (*i.e.* if

the net flux was exclusively dominated by settling), the maximum net flux would be located higher in the flow and the formation of a concentration plateau would be expected.

More than the sediment fluxes, quantities of interest in the prospect of modeling oscillatory sheet flow are the vertical velocities. Taking the decomposition of the net sediment flux 3.5 and dividing it with the average sediment concentration $\langle\bar{\phi}\rangle$ allows to recover the vertical Favre averaged solid velocity

$$\langle\tilde{v}^s\rangle_F = \langle\tilde{v}^s\rangle + \tilde{v}^s_d \tag{3.6}$$

decomposed into the sum of an average settling velocity $\langle\tilde{v}^s\rangle$ and a vertical drift velocity $\tilde{v}^s_d = \langle\phi'\tilde{v}^{s'}\rangle/\langle\bar{\phi}\rangle$.

As for the fluxes in figure 3.12, the different contributions of the vertical particle velocities are plotted in figure 3.13.

For configuration F512, the mean particle settling velocity is well represented by the empirical expression of the hindered settling velocity proposed by Richardson & Zaki (1997) [94] $\langle v^s\rangle = v_s(1-\langle\bar{\phi}\rangle)^{4.65}$ throughout the wave period. However, for medium sand, a significant reduction of the effective particle settling velocity can be observed. The location where this settling velocity reduction occurs is moving upward as flow accelerates. The settling velocity reduction corresponds to location where Reynolds stress changes sign (figure 3.4). In this flow region, complex interactions between the particles and turbulent structures generated at flow reversal such as loitering [80], non linear drag effects [71] or vortex trapping [79] may cause settling retardation. However, this settling velocity reduction occurs at location where the concentration and the net vertical flux are very low and do not significantly impact the time evolution of the concentration profile.

Overall, the average settling velocity is well reproduced by the hindrance function. The dependence of the settling velocity on the sediment concentration is already easily implemented in traditional drag formulations. The modeling effort should therefore be directed toward reproducing the turbulence-particle interactions represented by the drift velocity to accurately predict the vertical balance between settling and Reynolds fluxes for these flow conditions.

## 3.5 Conclusion

The turbulence-resolving Eulerian two-fluid model sedFoam has been successfully applied to oscillatory sheet flow configurations involving fine and medium sand under a symmetrical flow forcing (configurations F512 and M512 from O'Donoghue & Wright (2004a) [81] respectively). Quantitative predictions of concentration profiles are obtained demonstrating the predictive capabilities of the two-fluid LES model. However, small discrepancies can be observed for the configuration involving medium sand. Sediments settle too quickly to the bed during flow deceleration leading to sharper concentration profile in the near bed region compared with the experimental observations. As observed in the regime map presented in figure 1.5, for larger particles, more complex turbulence-particle interaction regimes occur and physical processes such as finite-size effects may become dominant. In that case, modifications of the fluid-particle interaction term, susceptible to affect the vertical distribution of sediment, are required [39].

Nevertheless, the good quality of the model results allows us to validate the use the two-fluid model. It is remarkable that the turbulence-resolving two-phase flow model reproduces the differences of behavior observed between medium and fine sand whereas turbulence-averaged models require an almost systematic tuning of empirical model coefficients for turbulence-particle interactions. These important results demonstrate the two-fluid model explicitly resolves these interactions and can be used to study in details the mass balance and turbulent statistics to explain

the differences observed experimentally.

For oscillatory sheet flow involving medium sand, the evolution of the concentration profile across the wave period follows the well documented description proposed by O'Donoghue & Wright (2004a) [81] with a clockwise (resp. anti-clockwise) rotation of the concentration profile during flow acceleration (resp. deceleration) around a "pivot" of constant concentration. From the analysis of the two-fluid model results, this can be explained by a competition between downward settling flux and upward Reynolds flux. This behavior is the result of a maximum vertical net flux coinciding with the inflexion point of the concentration profile during most of the wave period. The sheet flow layer thickness, the erosion depth and the horizontal sediment flux are perfectly in phase with the free stream velocity suggesting that the sediment bed response to changes of the near bed velocity is very quick. This observation confirms that the evolution of the sheet flow layer is quasi-steady. In the streamwise direction, velocity and Reynolds stress profiles show the well known behavior of the turbulent oscillatory boundary layer.

For fine sand, unsteady effects are present resulting in a completely different behavior of the flow. As a result of instabilities observed during flow acceleration, the solid phase Reynolds stress becomes large and the sheet flow layer thickness is significantly increased throughout the wave period. Consequently, a large mass of sediment is transported in the boundary layer therefore increasing the sheet flow layer's inertia. The response of the sediment bed is no longer in phase with the free stream velocity. During the deceleration phase, the presence of suspended particles induces stable stratification that strongly damp turbulence and leads to almost vanishing vertical Reynolds fluxes. The boundary layer transition toward a laminar behavior and the sediment dynamics is increasingly dominated by gravitational settling. Compared with medium sand, the maximum vertical net flux is located higher in the flow leading to the formation of the concentration plateau due to non-linear behavior in the mass balance. Time evolution of the concentration can no longer be represented by the classical description provided by O'Donoghue & Wright (2004a) [81] using a power law. The concentration plateau slides almost freely above the immobile bed with a constant velocity profile showing similarities with the plug flows observed by Sleath (1999) [107] at lower concentration.

Compared with medium sand, the solid phase turbulence plays a greater role in oscillatory sheet flow. Usually not taken into account in turbulence-averaged models, it contributes to explain their limited predictive capabilities for configurations involving fine sand. Unsteady effects are the results of a chain of causes and consequences including shear instabilities that increase vertical mixing of sediment, strong solid phase Reynolds stress, increased boundary layer inertia, stable stratification, turbulence damping and hindered settling. An equilibrium between all these mechanisms establishes during the wave period controlling the vertical mass balance of sediment and phase-lag effects.

Eventually, accurately predict the time evolution of the concentration profile depends on a reliable modeling of the competition between the downward settling and the upward Reynolds fluxes. Simulation results using the two-fluid model show that the mean settling velocity can be well reproduced using empirical formulation taking into account hindered settling. Future research should therefore be focused on an accurate modeling of the drift velocity induced by turbulence-particle interactions.

# 4

# Effect of the wave shape on the net sediment transport rate

*In this chapter, the effect of wave shape on sediment transport in the sheet flow regime is investigated with a focus set on the grain size dependency and phase-lag effects. The imprint of unsteady effects on streamwise sediment transport and the behavior of the oscillatory boundary layer are discussed based on the time evolution of the streamwise sediment flux, the instantaneous Shields number, the transport layer thickness and the turbulent kinetic energy. The relation between onshore and offshore transport rate and their corresponding effective Shields number reveals that the sediment load transported during a given wave phase can not be determined from a power law using the same parameterization for medium and fine sand. Furthermore, the maximum sheet flow layer thickness used in the parameterization of phase-lag effects in the sand transport formula does not follow the classical scaling laws. Eventually, suggestions regarding phase-lag effects modeling based on the vertical sediment mass balance are provided.*

## Contents

## 4.1 Introduction

After a first validation on oscillatory sheet flow under symmetric waves in chapter 3, the two-fluid model is applied to study wave shape effects. Indeed, unsteady effects can have a significant impact on the wave averaged net flux generated under asymmetric or skewed waves. Providing detailed information on the effect of the wave shape using the two-fluid model is valuable considering that the wave averaged net flux controls the cross shore morphological evolution of sandy beaches.

Four experimental configurations from O'Donoghue & Wright (2004a) [81] and van der A *et al.* (2010) [112] are reproduced numerically to investigate the effect of the wave shape on sand transport and grain size dependency with a focus on phase-lag effects.

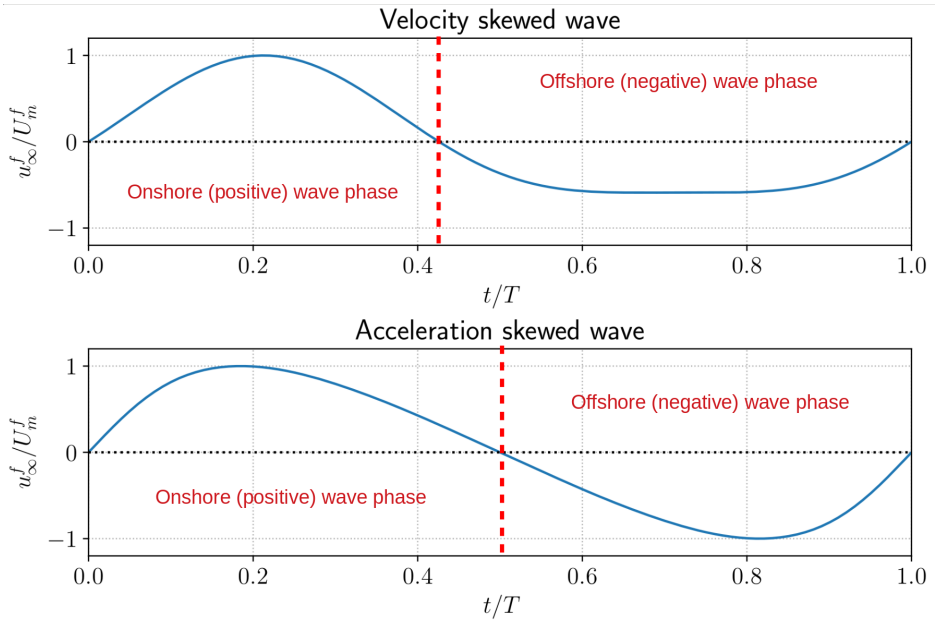


*Figure 4.1: Time series of free stream velocity $u^f_\infty$ made dimensionless by the maximum free stream velocity $U^f_m$ for a velocity skewed wave corresponding to the flow forcing in configurations M5010 and F5010 (top pannel) and an acceleration skewed wave corresponding to the flow forcing in configurations S706015m and S706015f (bottom pannel).*

The effect of velocity skewness is investigated by simulating configuration M5010 involving medium sand with diameter $d_p = 280\mu m$ and configuration F5010 involving fine sand with diameter $d_p = 150\mu m$ from O'Donoghue & Wright (2004a) [81]. Compared with the configurations investigated in chapter 3, only the shape of the waves changes. The wave period and maximum free stream velocity are the same with $T = 5\ s$ and $U^f_m = 1.5\ m.s^{-1}$ but the flow asymmetry is equal to $a^f = U^f_m/(U^f_m - u^f_m) = 0.63$ with $u^f_m$ the maximum off-shore velocity compared with $a^f = 0.5$ for sinusoidal waves (top pannel of figure 4.1). The Stokes boundary layer thickness $\delta$, maximum excursion length $a$ and estimates of the maximum friction velocity $u^m_\tau$ being only function of the wave period and maximum free stream velocity, remain unchanged compared with the corresponding values for sinusoidal waves giving $\delta = 1.26 \times 10^{-3} m$, $a = 1.19m$ and $u^m_\tau = 0.112m.s{-}1$. The corresponding Reynolds numbers based on $a$ and $\delta$ remains also unchanged with $Re = U^f_m a/\nu^f = 1.8 \times 10^6$ and $Re_\delta = U^f_m \delta/\nu^f = 1890$ respectively.

To study the effect of acceleration skewness, configuration S706015m involving medium sand with diameter $d_p = 270\mu m$ and configuration S706015f involving fine sand with diameter $d_p = 150\mu m$ from van der A *et al.* (2010) [112] are reproduced numerically. For both configurations, hydrodynamic conditions are the same with acceleration skewed waves of period $T = 6s$ and maximum free stream velocity $U^f_m = 1.3m.s^{-1}$ (bottom pannel of figure 4.1). The corresponding

| Parameters | M5010 | F5010 | S706015m | S706015f |
|---|---|---|---|---|
| $T\ (s)$ | 5 | 5 | 6 | 6 |
| $U^f_{max}\ (m.s^{-1})$ | 1.5 | 1.5 | 1.3 | 1.3 |
| $d_p\ (\mu m)$ | 280 | 150 | 270 | 150 |
| $\rho^s\ (kg.m^{-3})$ | 2650 | 2650 | 2650 | 2650 |
| $a\ (m)$ | 1.19 | 1.19 | 1.24 | 1.24 |
| $\nu^f\ (m^2.s^{-1})$ | $1\times10^{-6}$ | $1\times10^{-6}$ | $1\times10^{-6}$ | $1\times10^{-6}$ |
| $\delta\ (m)$ | $1.26\times10^{-3}$ | $1.26\times10^{-3}$ | $1.38\times10^{-3}$ | $1.38\times10^{-3}$ |
| $u^m_\tau\ (m.s^{-1})$ | 0.112 | 0.112 | 0.091 | 0.091 |
| $Re$ | $1.8\times10^6$ | $1.8\times10^6$ | $1.6\times10^6$ | $1.6\times10^6$ |
| $Re_\delta$ | 1890 | 1890 | 1794 | 1794 |

*Table 4.1: Flow and particle parameters of configurations M5010 and F5010 from O'Donoghue & Wright (2004a) [81] and configurations S706015m and S706015f from van der A et al. (2010) [112].*

Stokes layer thickness, maximum excursion length and estimated maximum friction velocity are $\delta = 1.38\times10^{-3}m$, $a = 1.24m$ and $u^m_\tau = 0.091m.s^{-1}$. Reynolds numbers based on $a$ and $\delta$ have similar values compared with the other configurations with $Re = 1.6\times10^6$ and $Re_\delta = 1794$.

Flow and particle parameters for the configurations M5010, F5010, S706015m and S706015f are listed in table 4.1. For simplicity, velocity skewed and acceleration skewed flow forcing are referred to as skewed and asymmetric wave respectively in the remaining of the manuscript.

## 4.2 Numerical configuration

The numerical domain dimensions, mesh decomposition and discretization schemes used to simulate the four three-dimensional configurations are the same as presented in section 3.2 for sinusoidal waves. However, the skewed and asymmetric waves configurations differ by the expression of the free stream velocity in the volume force driving the flow $f^v_x = -\rho^f \partial u^f_\infty/\partial t$.

For skewed waves, the expression of the free stream velocity is given by a second order stokes wave:

$$u^f_\infty(t) = u_1 sin\left[\omega(t-t_0)\right] - u_2 cos\left[2\omega(t-t_0)\right] \tag{4.1}$$

with $u_1 = 1.2m.s^{-1}$, $u_2 = 0.31m.s^{-1}$ and $t_0 = 0.185s$ chosen to obtain $U^f_m = 1.5m.s^{-1}$, $a^f = 0.63$ and $u^f_\infty(0) = 0$. For asymmetric waves, the free stream velocity is given by

$$u^f_\infty(t) = \alpha_u u^f_m \sum_{n=1}^{6} \frac{(2\beta-1)^{n-1} sin(n\omega t)}{n} \tag{4.2}$$

with $\beta = 0.7$ the skewness factor and $\alpha_u = 0.9725$ a coefficient adjusted to recover the maximum free stream velocity.

From now on, the flow quantities can not be monitored only during one half of the wave period as for sinusoidal waves presented in chapter 3 but during the positive onshore-oriented

and negative offshore-oriented phases of the wave cycle denoted as wave crest and wave trough respectively.

## 4.3 Results

In this section, comparison between measured and predicted net sediment fluxes are first presented. Then, intra-wave processes are investigated to provide more insight into the relations between flow forcing, turbulence and transport rate.

### 4.3.1 Wave averaged sediment flux

One of the major difference between oscillatory sheet flow involving a symmetric forcing and asymmetric and skewed waves is the occurrence of a net sediment flux in the streamwise direction $Q$ calculated following

$$Q = \frac{1}{T}\int_0^T q_x dt \tag{4.3}$$

with $q_x$ the depth integrated streamwise sediment flux per unit width given by equation (3.2). The comparison between the measured and the predicted net sand fluxes using the two-fluid model is presented in table 4.2.

| Configuration | Measured $Q$ $(\times 10^{-6} m^2.s^{-1})$ | Predicted $Q$ $(\times 10^{-6} m^2.s^{-1})$ | Ratio |
|---|---|---|---|
| $M5010$ | 53 | 139 | 2.6 |
| $F5010$ | $-128$ | $-140$ | 1.1 |
| $S706015m$ | 41.24 | 58.89 | 1.4 |
| $S706015f$ | 100.22 | 131.16 | 1.3 |

*Table 4.2: Comparison between measured and predicted net sediment fluxes Q for configurations F5010, M5010, S706015f and S706015m with their ratio.*

Similarly to experimental observations, for configurations S706015m and S706015f, the two-fluid model predicts a positive sand flux corresponding to a net onshore sand transport. Furthermore, the predicted net flux is close to the experimental measurements within a factor 1.4 for configuration S706015m and 1.3 for configuration S706015f. For configuration M5010, the net sediment flux is also positive but over-estimated by a factor 2.6 compared with the measurements. For configuration F5010, the change of sign of the net sand flux, signature of phase-lag effects, is well captured by the two-fluid flow model with a good prediction within a factor 1.1 compared with experimental measurements.

Taking into account the complexity of the mechanisms occurring in sediment transport under waves, difficulties to conduct experiments in a well controlled way and experimental measurements uncertainties, a prediction of the net transport rate is generally considered accurate within a factor two compared with the experiments [114]. The comparison between predicted and measured net sand fluxes presented in figure 4.2 shows that the predictions from the two-fluid model can be considered very good for configurations F5010, S706015f and S706015m. For configuration M5010, the agreement is only qualitative. However, on the one hand, prediction of the net

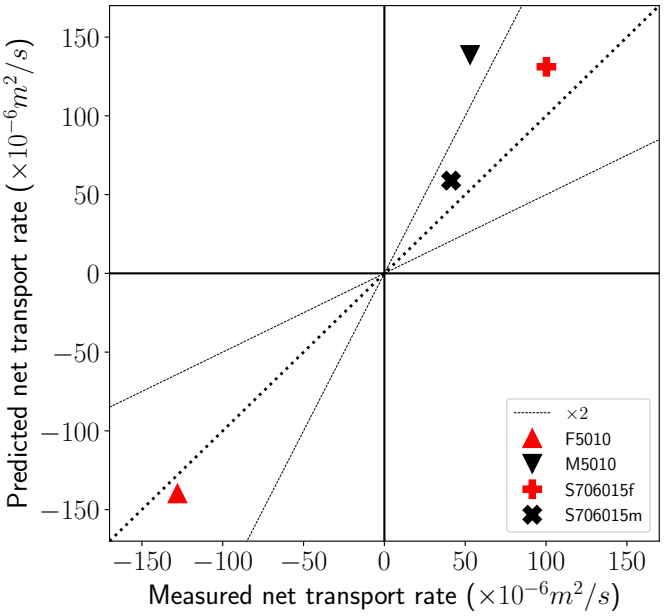


*Figure 4.2: Comparison between measured and predicted wave averaged sediment flux for configurations F5010, M5010, S706015f and S706015m.*

sand flux for configuration M5010 is close to the typical limit to be considered as acceptable. On the other hand, to study the effect of the wave shape and phase-lag, the most important feature is to be able to reproduce the behavior of the oscillatory boundary layer. In that case, the two-fluid model accurately predicts the mechanisms at the origin of the change of sign of the net sediment flux between configurations involving medium and fine sand subject to the same flow forcing.

### 4.3.2 Effect of velocity skewness

To better understand phase-lag effects associated with skewed waves, time series of intra-wave depth integrated streamwise sediment fluxes per unit width $q_x$ for configurations M5010 and F5010 are presented in figure 4.3. For configuration M5010, sediment flux is almost zero around both offshore/onshore and onshore/offshore flow reversals. Flow forcing is not strong enough to mobilize sediment at the early stages of the flow acceleration. Maximum onshore and offshore streamwise sediment fluxes are coincident with maximum onshore and offshore maximum free stream velocities with a stronger maximum onshore-oriented sediment flux. The amount of sediment transported offshore during the wave trough does not compensate the amount of sediment transported onshore during the shorter wave crest leading to a positive net sand flux.

For configuration F5010, streamwise sediment flux does not return back to zero throughout the wave period. In other words, there are still particles transported during successive flow reversals. As a consequence of unsteady effects, there is a significant phase shift between sediment flux and free stream velocity. As for configuration M5010, maximum onshore sediment flux is larger but the duration of the offshore oriented sediment flux is longer. The amount of sediment transported offshore over a longer period now exceeds the amount of sediment transported onshore having for effect to generate a net offshore-oriented (negative) flux.

In conventional approaches, sediment flux is parameterized based on the instantaneous Shields number $\theta$. To assess the validity of this hypothesis, the time series of the Shields number predicted by the two-fluid model calculated based on the maximum value of the fluid Reynolds stress inside the sheet flow layer for configurations M5010 and F5010 are presented in figure 4.4. Time series of the sediment flux are perfectly in phase with time series of the Shields number for configuration

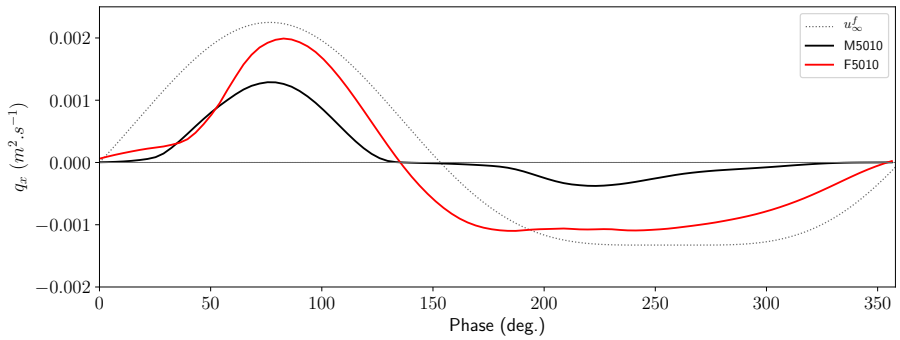


*Figure 4.3: Times series of $q_x$ the streamwise depth-integrated sediment fluxes for configurations M5010 and F5010.*

M5010. In other words, the bed response is fully correlated with the flow forcing represented by the dimensionless shear stress at the bottom. For configuration F5010, the maximum flux and maximum Shields number occur during wave crest but the time evolution of the sediment flux can not be represented by the instantaneous Shields number. The maximum Shields number during wave crest at 50° corresponds to the sudden increase of the streamwise flux but it reaches its maximum value around 30° later. On the contrary, the maximum offshore sediment flux occurs before the maximum Shields number during wave trough.

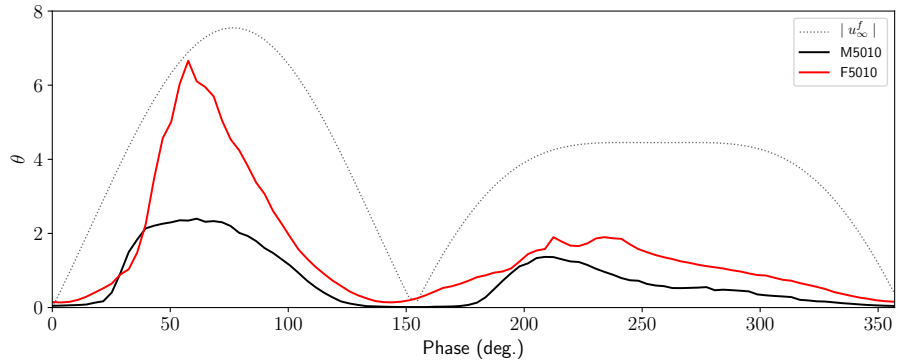


*Figure 4.4: Time series of the Shields number for configurations M5010 and F5010.*

As for sheet flow configurations subjected to a symmetrical flow forcing presented in chapter 3, for configuration M5010 involving medium sand, the sheet flow layer thickness represented in figure 4.5 is almost zero around both flow reversals. Sediment flux is in phase with the time evolution of the sheet flow layer thickness and the instantaneous Shields number. For configuration F5010, sheet flow layer thickness is never zero meaning that sediment are transported throughout the wave period. The sand flux is no longer in phase with the thickness of the transport layer. Whereas the increase of the onshore oriented sediment flux corresponds very well to the sheet flow layer thickness increase, the maximum offshore oriented sediment flux occurs when the sheet flow layer thickness is minimum. The flow changes direction while still carrying particles in suspension having for effect to generate a strong offshore flux that is not correlated with the instantaneous Shields number. There is a significant delay between the flow condition and the response of the transport layer.

To highlight the vertical distribution of the streamwise sediment flux over the wave period, a color map of the flux density $\langle \bar{\phi}\tilde{u}^s \rangle$ for both configurations M5010 ans F5010 are presented in figure 4.6 together with the erosion depth and the top of the sheet flow layer. For configuration

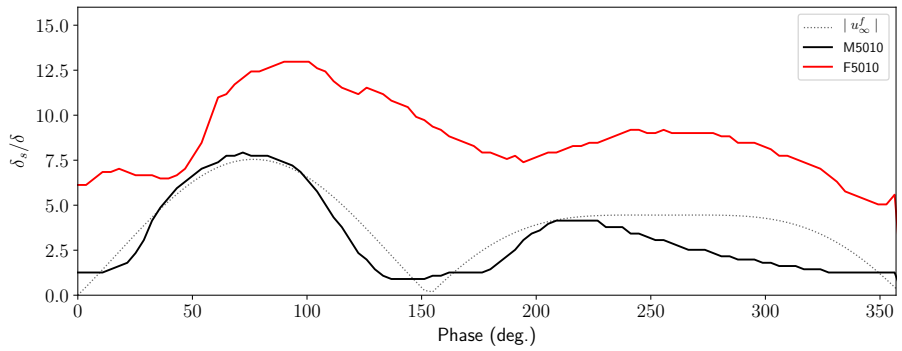


*Figure 4.5: Time series of the sheet flow layer thickness made dimensionless by the Stokes layer thickness for configurations M5010 and F5010.*

M5010, there is a symmetry between erosion depth and the top of the sheet flow layer showing the well known behavior of the concentration profile discussed in chapter 3. For configuration F5010, as the erosion depth shows a low variability, the evolution of the sheet flow layer thickness is mostly the consequence of the displacement of the top boundary. As the maximum offshore sediment flux corresponds to the minimum sheet flow layer thickness, sand is transported as a fast moving layer very close to the bed at around 190°.

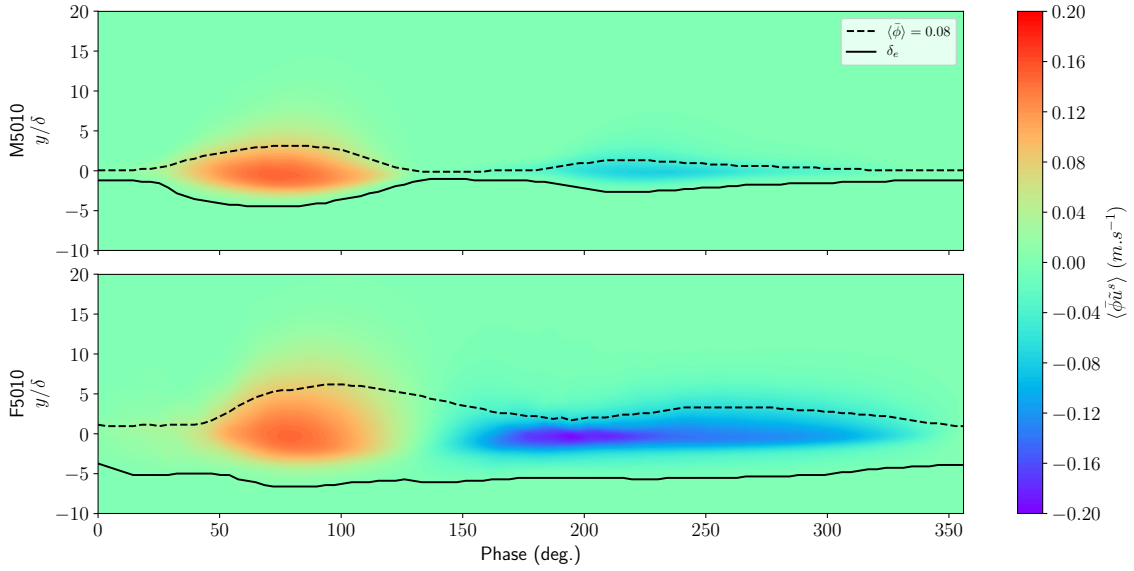


*Figure 4.6: Color map of the phase averaged sand flux from configurations M5010 (top) and F5010 (bottom).*

From the color map of TKE presented in figure 4.7 for both configurations F5010 and M5010, the same mechanisms described in section 3.4.1 occur. Due to flow instabilities during acceleration phase of the flow, larger maximum TKE values are observed for configuration involving fine sand. Furthermore, compared with configuration M5010, turbulence is attenuated as a result of increased sheet flow layer thickness and sediment concentration.

As a summary, for configuration M5010, the transport layer responds almost instantaneously to the flow forcing represented by the Shields number. Particles are eroded during flow acceleration and have sufficient time to settle back to the bed during flow reversal. Stronger flow velocities during wave crest generate larger bottom shear stress resulting in larger sediment flux compared

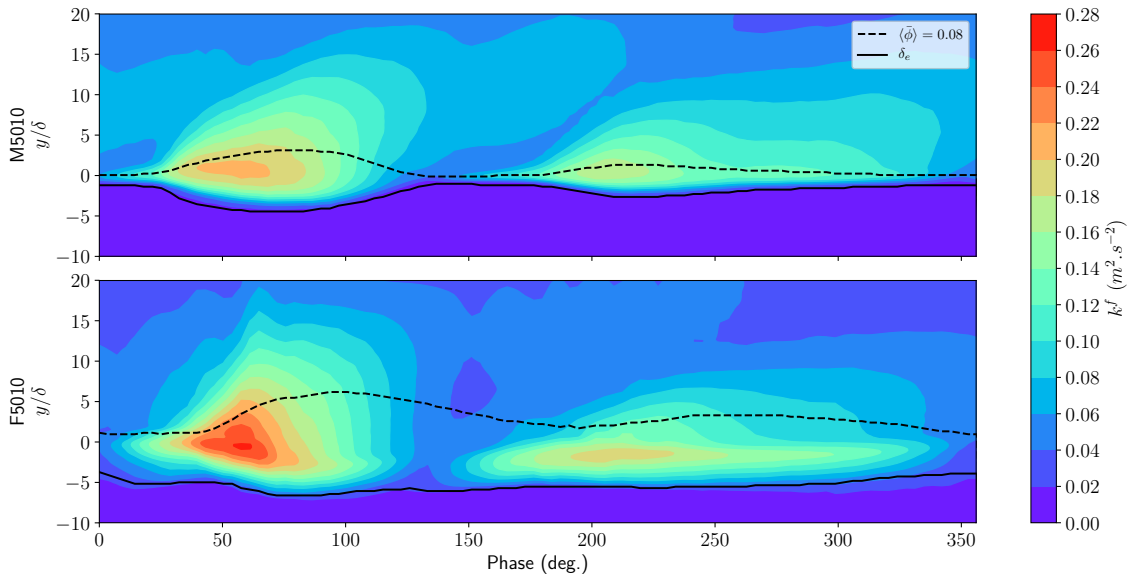


*Figure 4.7: Color map of the TKE from configurations M5010 (top) and F5010 (bottom).*

with the wave trough. Even if the duration of the wave trough is longer than the duration of the wave crest, the average offshore oriented sediment flux during wave trough is smaller than the onshore-oriented average sediment flux during wave crest resulting in a net onshore-oriented flux. For configuration F5010, a large quantity of sediment is transported during wave crest that do not have time to settle back to the bed before the flow reversal. As a result, when the flow changes direction, sediments are still settling from the previous wave phase are transported as a fast moving layer close to the bed. The same behavior is observed at the off-onshore flow reversal but to a lesser extent. As a consequence, the large amount of sediment eroded from the bed during the wave crest is still suspended during flow reversal and contributes to increase the average offshore sediment flux during the wave trough generating a net offshore-oriented flux.

### 4.3.3 Acceleration skewness effect

The same analysis is performed for oscillatory sheet flow under asymmetric waves. Time series of depth integrated streamwise sediment flux for configurations S706015m and S706015f are presented in figure 4.8.

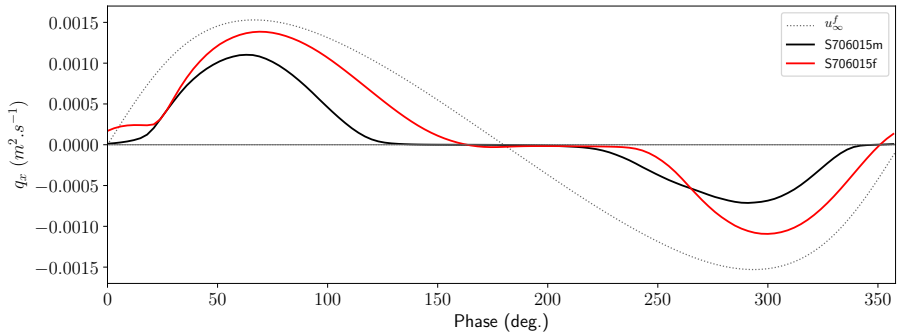


*Figure 4.8: Times series of $q_x$ the streamwise depth-integrated sediment fluxes for configurations S706015m and S706015f .*

As for configurations M512 investigated in chapter 3 and configuration M5010, streamwise flux for configuration S706015m is zero during both flow reversal and their maximum onshore an offshore values are in phase with the free stream velocity. The sediment flux is almost symmetrical but under the effect of strong acceleration during wave crest, the amount of sediment transported onshore is greater than the amount of sediment transported offshore resulting in a net onshore-oriented sand flux. For configuration S706015f, streamwise sediment flux is also more important during the wave crest and returns back to zero only at onshore/offshore flow reversal. Whereas phase-lag effects are stronger during on-offshore flow reversal for fine sand subject to a velocity skewed flow forcing, under acceleration skewed waves, phase-lag effects are dominant at off-onshore flow reversal and absent at on-offshore flow reversal. Because of the longer deceleration phase during the wave crest, sediments have sufficient time to settle back to the bed but not during the shorter deceleration phase of the wave trough. As a consequence, particles still in suspension at off-onshore flow reversal are transported onshore resulting in a greater onshore-oriented sand flux for fine sand.

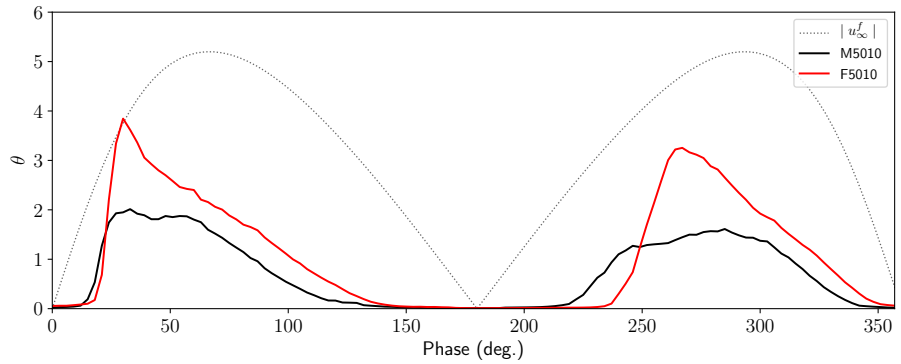


*Figure 4.9: Time series of the Shields number for configurations S706015m and S706015f.*

Even if the shape of the time series of streamwise sand flux look similar, the time series of Shields number presented in figure 4.9 highlight a significant difference of behavior between configurations S706015m and S706015f. For configuration S706015m, the Shields number increases suddenly at around 20° under the effect of strong acceleration during the wave crest, it reaches a maximum and then decreases more gently because of the longer duration of the deceleration phase. During the wave trough, the Shields number increases more slowly than during the wave crest and decreases more quickly during the deceleration phase. The acceleration asymmetry of the free stream velocity has a direct effect on the bottom shear stress evolution.

For configuration S706015f, similarly to the observations made for configuration S706015m, during the wave crest, the Shields number suddenly increases at around 20° and decreases gently during the deceleration phase. However, during the acceleration phase of the wave trough, a similar behavior as during the wave crest is observed with a sudden increase of the Shields number before decreasing more gently. The flow asymmetry in configuration S706015f is no longer as clearly visible on the bottom shear stress as it is for configuration S706015m. As for configurations involving skewed waves, the sand flux can be well parameterized by the instantaneous Shields number for configuration S706015m involving medium sand but not for configuration S706015f involving fine sand. However in this case, the difference of behavior can not be explained by phase-lag effects considering that they do not play a role around the on-offshore flow reversal. This feature further confirms the observations made in chapter 3 that other mechanisms than phase lag are responsible for increased sheet flow layer thickness.

As a result of greater Shields number during the wave crest, the sheet flow layer thicknesses is greater compared with their corresponding values during wave trough for both configurations (see figure 4.10). As expected, for configuration S706015m, the sheet flow layer thickness is

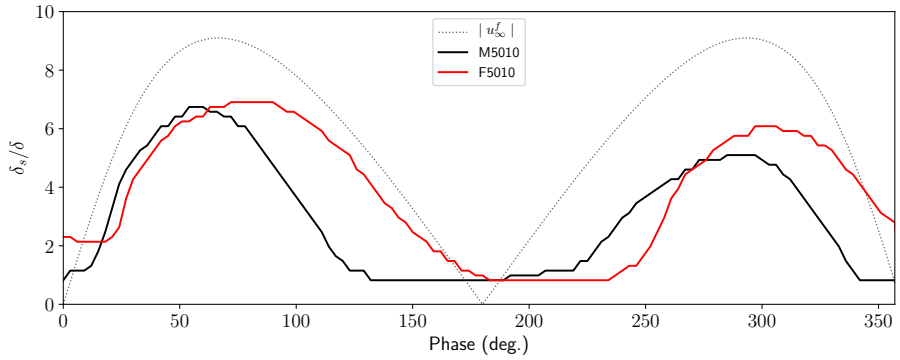


*Figure 4.10: Time series of the sheet flow layer thickness made dimensionless by the Stokes layer thickness for configurations S706015m and S706015f.*

almost zero during both flow reversals and the sediment flux is in phase with the time evolution of the sheet flow layer thickness. For configuration S706015f, sheet flow layer thickness is almost zero around onshore/offshore flow reversal but not at off-onshore flow reversal. Particles still in suspension during off-onshore flow reversal are transported during wave crest.

From the time series of the erosion depth and upper limit of the sheet flow layer thickness presented in section 4.11, similarly to configuration M5010, there is a symmetry between erosion and suspension for configuration S706015m during the wave crest and the wave trough. For configuration S706015f, this symmetry exists during wave trough but, as a consequence of phase-lag effects, the erosion depth shows a lower variability during wave crest. Furthermore, from the color map of the sediment flux in the bottom panel of figure 4.11, sediment are transported as a thin layer close to the bed during off-onshore flow reversal.

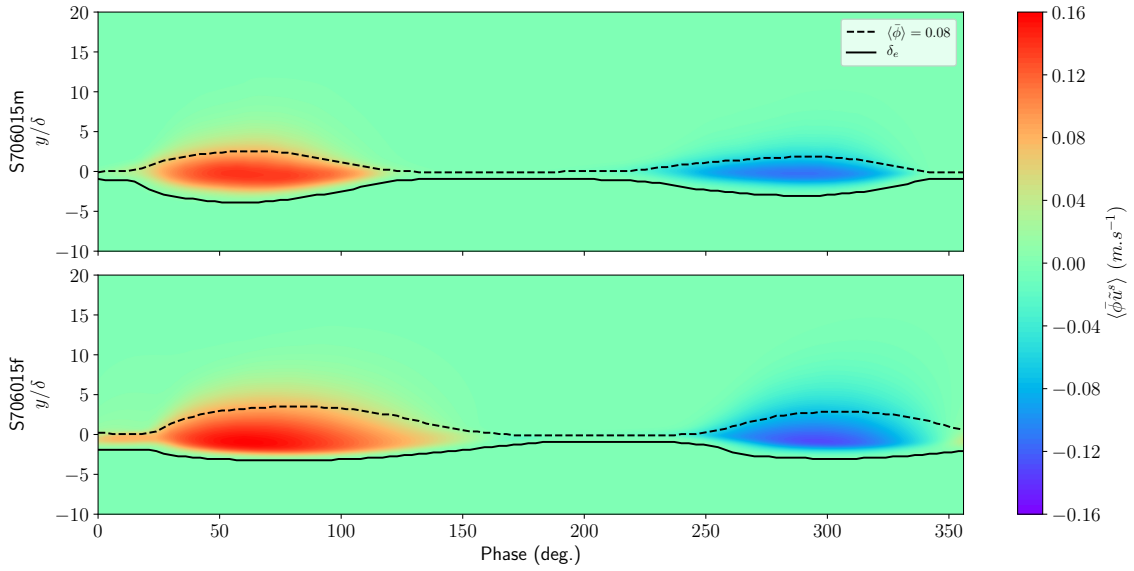


*Figure 4.11: Color map of the phase averaged sand flux from configurations S706015m (top) and S706015f (bottom).*

From the color maps of TKE for configurations S706015m and S706015f presented in figure 4.12, maximum values of the TKE during wave crest are larger for both configurations as a result of greater flow acceleration. Similarly to the other configurations investigated in this manuscript, maximum TKE is larger for the configuration involving fine sand as a consequence of flow in-

stability. Furthermore, the color maps of TKE show some differences between configurations S706015m and S706015f at both flow reversals suggesting that turbulence is strongly modulated by the particles. Increased TKE is also observed during the acceleration phase of the wave trough even if phase-lag effect are absent. Whereas turbulence intensity increases gently during the acceleration phase of the wave trough for configuration S706015m, the almost laminar behavior of the oscillatory boundary layer during the early stage of flow acceleration of the wave trough for configuration S706015f has for effect to delay the initiation of turbulence and to suddenly generate strong instabilities. These instabilities enhance the vertical mixing of sediment and the sheet flow layer thickness further increases.

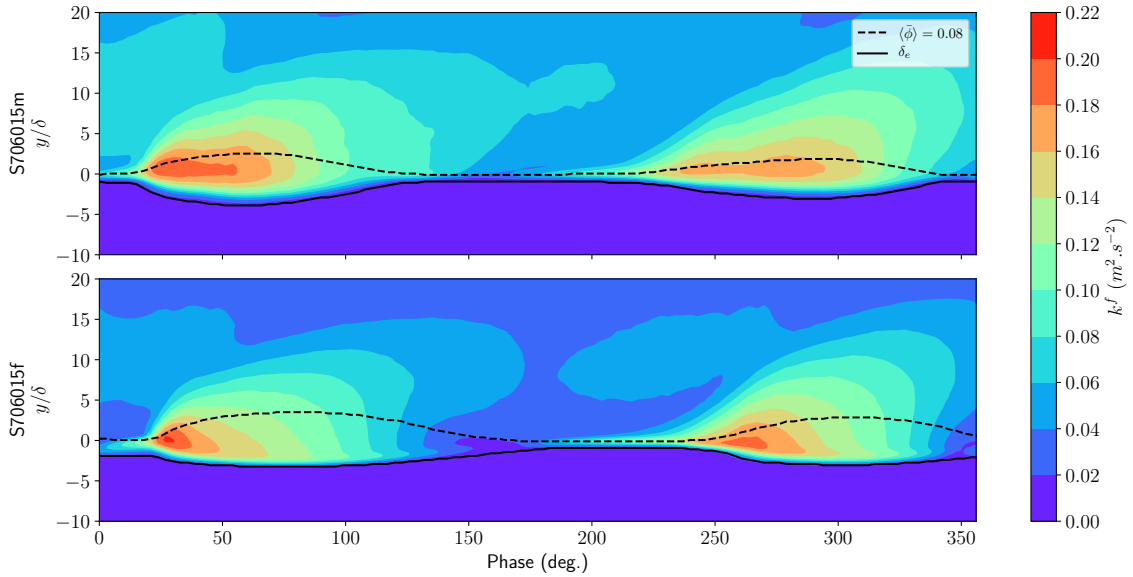


*Figure 4.12: Color map of the TKE from configurations S706015m (top) and S706015f (bottom).*

Under asymmetric waves, larger bottom shear stress resulting from stronger flow acceleration during wave crest has for effect to induce a net onshore-oriented sand flux. The net flux is further increased by the phase-lag effects when particles extracted from the bed during the wave trough do not have time to settle during the short deceleration phase and are transported during wave trough. This phenomenon is amplified by the complex interplay between turbulence attenuation induced by the particles and flow instabilities having for effect to increase vertical mixing of particles.

## 4.4 Discussion

Under asymmetric and skewed waves, unsteady effects highlighted in chapter 3 are also present for configurations involving fine sand. Compared with configurations involving medium sand, the time evolution of the vertical distribution of fine sand is the result of bed instabilities visible in figues 4.7 and 4.12 showing higher peaks of TKE and turbulence damping around flow reversal visible in figures 4.13 and 4.14 with a Richardson number $Ri > 0.25$ in the transport layer.

Compared with sinusoidal waves, the importance of streamwise sediment flux is crucial to determine the net transport rate during a wave cycle. In this section, the role of unsteady effects on the balance between onshore and offshore oriented sand flux is discussed. Then, suggestions regarding phase-lag effects modeling based on the vertical sediment mass balance are provided.

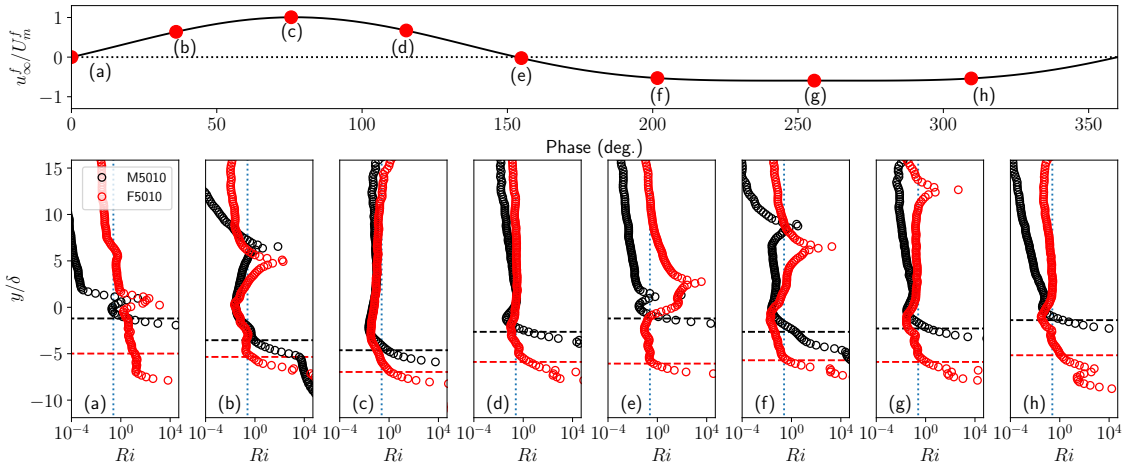


*Figure 4.13: Vertical profiles of Richardson number for configurations M5010 and F5010. Dotted line corresponds to $Ri = 0.25$ and dashed lines corresponds to the erosion depths.*

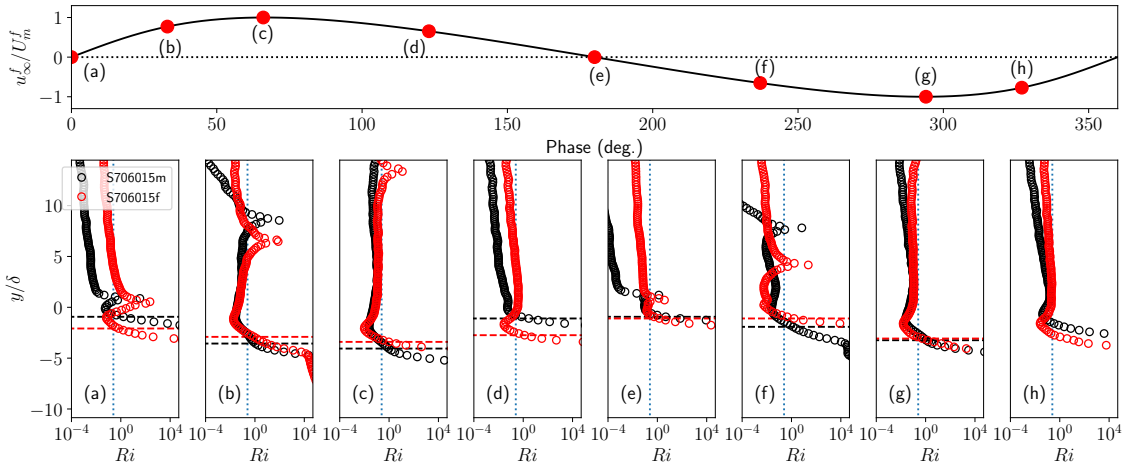


*Figure 4.14: Vertical profiles of Richardson number for configurations S706015m and S706015f. Dotted line corresponds to $Ri = 0.25$ and dashed lines corresponds to the erosion depths.*

### 4.4.1 Unsteady effects and streamwise sand transport rates

Typical expressions to predict sediment transport as a function hydrodynamic forcing are power laws relating the dimensionless transport rate to the Shields number. Under waves, the transport rate and Shields number are decomposed into an onshore and offshore components during wave crest and wave trough. The onshore and offshore components of the dimensionless transport rate $Q^*_+$ and $Q^*_-$ are given by:

$$Q^*_+ = \frac{1}{T_+}\int_{t\in I^+} \frac{q_x(t)}{\sqrt{(s-1)gd_p^3}}dt, \quad Q^*_- = \frac{1}{T_-}\int_{t\in I^-} \frac{q_x(t)}{\sqrt{(s-1)gd_p^3}}dt, \tag{4.4a,b}$$

with $I^+$ and $I^-$ the time interval for which $q_x > 0$ and $q_x < 0$ respectively and $T_+$ and $T_-$ the effective durations corresponding to intervals $I^+$ and $I^-$.

Similarly, the effective Shields number during the wave crest and the wave trough are calculated as follows:

$$\theta_+ = \frac{1}{T_+}\int_{t\in I^+} \theta(t)dt, \quad \theta_- = \frac{1}{T_-}\int_{t\in I^-} \theta(t)dt. \tag{4.5a,b}$$

Dimensionless onshore and offshore components of the dimensionless transport rate and corresponding effective Shields numbers for configurations M5010, F5010, S706015m and S706015f are presented in table 4.3.

| Configuration | $\lvert Q^*_+\rvert$ | $\lvert Q^*_-\rvert$ | $\theta_-$ | $\theta_+$ |
|---|---|---|---|---|
| $M5010$ | 28.3 | 7.3 | 1.1 | 0.5 |
| $F5010$ | 123.0 | 109.3 | 2.3 | 0.9 |
| $S706015m$ | 22.3 | 14.3 | 0.8 | 0.7 |
| $S706015f$ | 93.7 | 53.6 | 1.2 | 1 |

*Table 4.3: Onshore and offshore components of the dimensionless transport rate $|Q^*_+|$ and $|Q^*_-|$ and corresponding effective Shields numbers $\theta_+$ and $\theta_-$ for configurations F5010, M5010, S706015f and S706015m.*

As expected, because of the wave shape, the effective Shields number is larger during wave crest than during wave trough for all configurations. Furthermore, $|Q^*_+|$ is larger than $|Q^*_-|$ even for configurations F5010. Therefore, considering that the dimensionless net transport rate is given by

$$Q^* = \frac{T_+|Q^*_+| - T_-|Q^*_-|}{T} \tag{4.6}$$

it confirms that the offshore-oriented net transport rate is the result of a longer wave trough compared with the wave crest.

Dimensionless transport rates $|Q^*_\alpha|$ with $\alpha = +,-$ denoting the wave phase are plotted as a function of the excess Shields number for configurations F5010, M5010, S706015f and S706015m in figure 4.15.

For configurations M5010 and S706015m involving medium sand, phase-lag is absent and $|Q^*_\alpha|$ is well represented by a power law of the form $|Q^*_\alpha| = m(\theta_\alpha - \theta_c)^n$ with $m = 29$ and $n = 1.7$. Typical values of the power law coefficients for sediment transport under waves are $m \sim (5-10)$ and $n \sim (1.5-2)$ [22, 114]. The larger value of the coefficient $m$ predicted by the two-fluid model can be explained by two factors. First, coefficients $m$ and $n$ are often calibrated based a broad range of flow regimes for different flow conditions. As a consequence, the set of calibrated parameters may not represent perfectly a given configuration. Second, from figure 4.2, the two-phase flow model over-predicts the positive net sand flux, especially for configuration M5010 meaning that

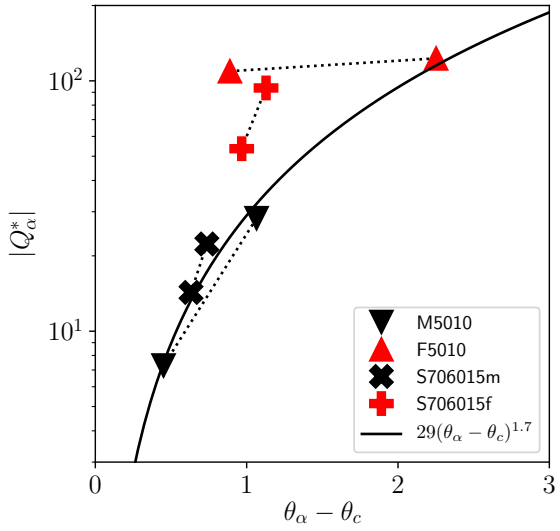


*Figure 4.15: Dimensionless onshore and offshore sediment transport rates plotted as function of the excess Shields number for configurations M5010, F5010, S706015m and S706015f.*

for a given flow forcing, the model may over-estimate the corresponding flux. Furthermore, one have to keep in mind that this scaling is obtained based on typical values of power law coefficients using four numerical points. Additional configurations should be investigated to further confirm the proposed scaling. Nevertheless, as pointed out at the beginning of the chapter, we are mainly interested in the differences between configurations involving medium and fine sand as long as the mechanisms are well reproduced by the two-fluid model rather than trying to obtain a perfect quantitative agreement.

For configurations F5010 and S706015f involving fine sand, the dimensionless transport rates are not well represented by the power law and are located above the curve. Furthermore, the effective transport rate can not be directly related to the excess Shields number using an other parameterization because of phase-lag effects. To be able to predict sand transport using a power law in configurations for which phase-lag effects are dominant, a redistribution of the sediment flux should be performed between wave crest and wave trough using adequate phase-lag modeling [114]. However, some interesting results can be discussed from the interpretation of figure 4.15.

One reason that can explain the under-estimation of the transport rates by the power law is that, due to phase-lag effects, a certain amount of sediment never settles back to the bed throughout the wave period. As a consequence, an additional flux component should be added to the total transported load to be able to parameterize sand transport using the same power law as for configurations involving medium sand.

However, the differences between transport rates for configurations involving medium and fine sand are not only the result of an additional load transported throughout the wave period for fine sand but the consequence of unsteady effects, described in chapter 3. Indeed, if the under-estimation of the sediment flux by the power law is only the consequence of an additional load, considering that all the sediment settled back to the bed at on-offshore flow reversal of configuration S706015f and that a part of the sediment load extracted during wave trough is transported during wave crest, the effective load transported during wave trough $|Q^*_-|$ should be below the curve representing the power law. However, as a result of bed instabilities and enhanced vertical mixing of particles, more particles are transported by the flow having for effect to significantly increase the horizontal sediment flux.

To further highlight this phenomenon, the time integral of the depth average Reynolds flux

$$q_y^{Re} = \int_{-\infty}^{\infty} \langle \bar{\phi}' \tilde{v}^{s'} \rangle dy \tag{4.7}$$

representing the upward particle turbulent suspension flux during wave crest and wave trough calculated as follows

$$Q_+^{Re} = \frac{1}{T_+} \int_{t \in I^+} q_y^{Re}(t) dt, \quad Q_-^{Re} = \frac{1}{T_-} \int_{t \in I^-} q_y^{Re}(t) dt, \tag{4.7a,b}$$

is represented in dimensionless form as a function of the excess Shields number in figure 4.16.

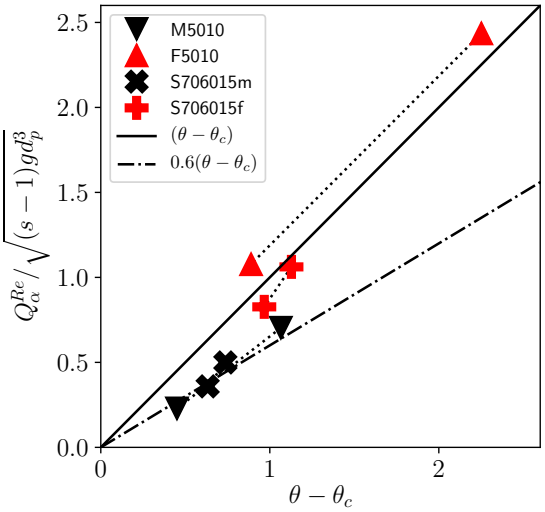


*Figure 4.16: Average upward Reynolds flux as a function of the excess Shields number for configurations M5010, F5010, S706015m and S706015f.*

Whereas the Reynolds flux increases linearly with respect to the Shields number with a factor 0.6 for configurations M5010 and S706015m involving medium sand, it increases linearly with a factor 1 for configurations F5010 and S706015f involving fine sand traducing a larger upward turbulent flux.

Considering that more particles are transported for a given flow condition, the transport rates can not be related to the excess Shields number using the same power law between fine and medium sand. Similarly to the sheet flow layer thickness, different parameterization should be used to predict the transport rates in configurations involving fine and medium sand. To be able to propose such a parameterization, phase-lag effects should be carefully integrated.

Up to now, models to take into account phase-lag effects are function of the particle fall velocity $v_s$ and the dimensionless maximum sheet flow layer thickness $\delta_m^s / d_{50}$ [30, 114]. For the phase-lag modeling to be efficient in determining phase-lag contributions, the prediction of the maximum sheet flow layer thickness should be accurate. Maximum sheet flow layer thicknesses made dimensionless by the particle diameter are plotted as a function of the maximum Shields parameter for configurations M5010, F5010, S706015m and S706015f in figure 4.17.

The sheet flow layer thickness is well predicted by the linear relation from Dohmen-Janssen *et al.* (2001) [29] for configurations M5010 and S706015m involving medium sand but a significant scatter can be observed for configurations F5010 and S706015f involving fine sand. Indeed, for configuration F5010, considering the large amount of sediment extracted during wave crest and transported during wave trough, the sheet flow layer thickness is much larger than predicted by the empirical relation. On the contrary, for configuration S706015f, particles have completely settle at

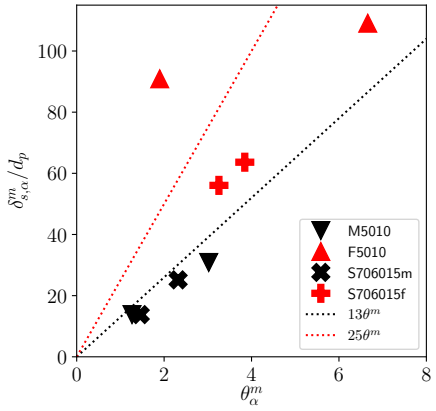


*Figure 4.17: Maximum sheet flow layer thickness made dimensionless by the particle diameter as a function of the maximum Shields number for configurations M5010, F5010, S706015m and S706015f.*

the bed during on-offshore flow reversal, phase-lag effect are absent and sheet flow layer thickness smaller than predicted by expression (E.8). However, the maximum sheet flow layer thickness is larger than the empirical relation for medium sand confirming the increase of the transport layer due to bed instabilities for fine sand.

From these observations, the prediction of phase lag effects based on the determination of the maximum sheet flow layer thickness from the empirical relation (E.8) shows some limitations. More physically-based relations should help improving model predictions for configurations involving fine sand. Suggestions on the improvement of phase-lag effects predictions are shown in the next section.

### 4.4.2 Suggestions regarding phase-lag effects modeling

As highlighted in section 3.4.2, the signature of phase-lag effects is clearly visible in the vertical sediment mass balance and vertical fluxes. Time series of depth integrated vertical total sediment fluxes

$$q_y = \int_{-\infty}^{\infty} \langle \bar{\phi} \tilde{v}^s \rangle dy \tag{4.8}$$

and its two contributions: Reynolds flux $q_y^{Re}$ given by expression (4.7) and settling flux

$$q_y^{Se} = \int_{-\infty}^{\infty} \langle \bar{\phi} \rangle \langle \tilde{v}^s \rangle dy \tag{4.9}$$

respectively are plotted in figure 4.18 for configurations M5010, F5010, S706015m and S706015f.

For configurations M5010 and S706015m involving medium sand, for which there is no phase-lag, the upward flux of sediment extracted from the bed represented by the Reynolds flux is fully compensated by the settling flux during wave crest and wave trough. The total vertical flux is first dominated by Reynolds fluxes during the acceleration phase of wave crest and wave trough, then it is dominated by settling during the deceleration phase with zero vertical flux during flow reversals. As a consequence, the time average net vertical fluxes during wave crest and wave trough are $Q_+^y = 0$ and $Q_-^y = 0$.

However, for configurations F5010 and S706015f involving fine sand, phase-lag effects are visible on the total vertical flux. The total vertical sediment flux is still settling dominated during

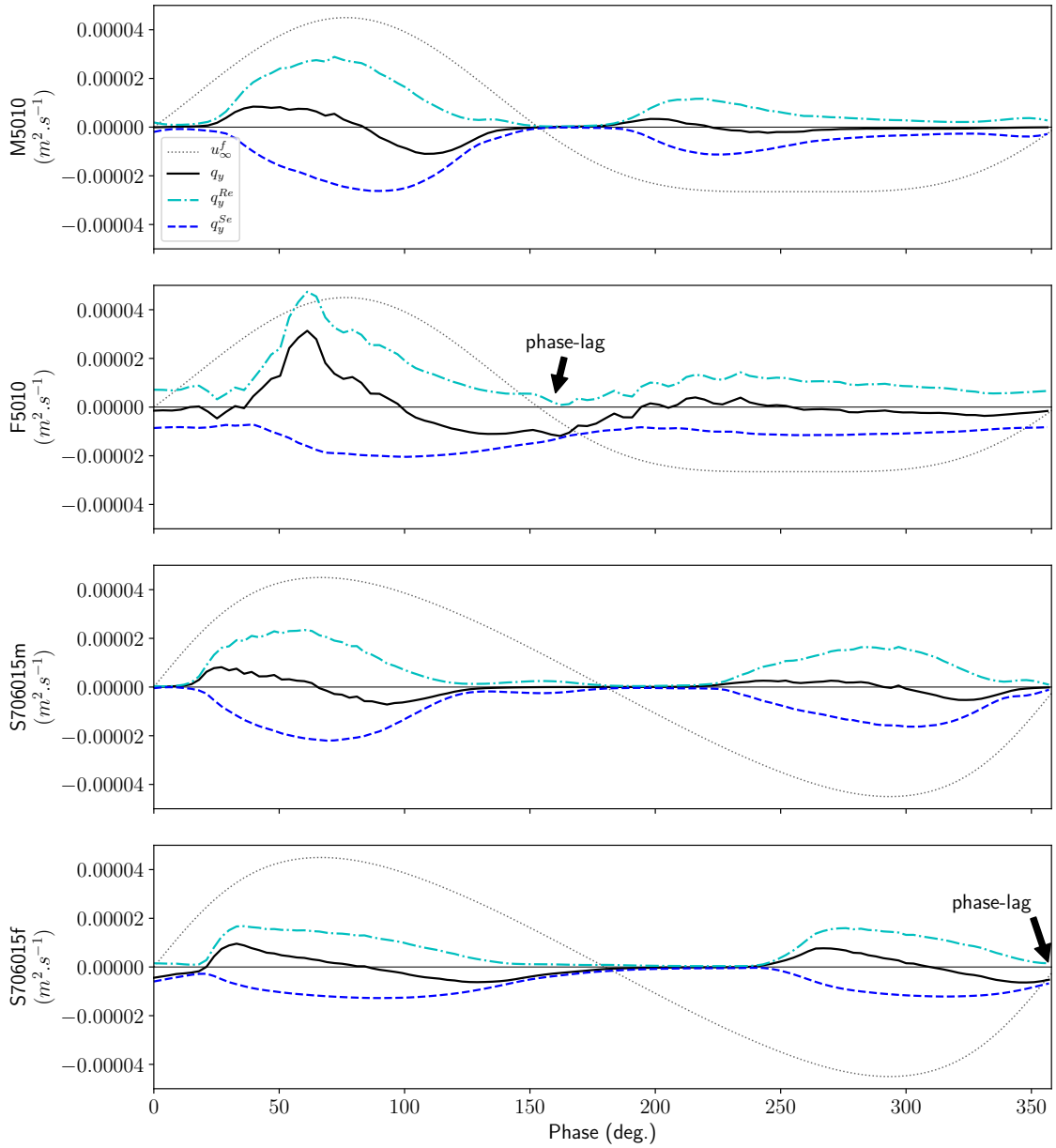


*Figure 4.18: Time series of depth integrated vertical total sediment fluxes $q_y$ and its two contributions: Reynolds and settling fluxes $q_y^{Re}$ and $q_y^{Se}$ for configurations M5010, F5010, S706015m and S706015f.*

on-offshore flow reversal for configuration F5010 and during off-onshore flow reversal for configuration S706015f. Particles that are still settling during flow reversal contribute to increase the streamwise sediment flux during the next wave phase.

For configurations without phase-lag, the ratios between the time average settling and Reynolds fluxes during wave crest and wave trough are $Q_+^{Se}/Q_+^{Re} = 1$ and $Q_-^{Se}/Q_-^{Re} = 1$. For configurations with phase-lag, the settling flux is redistributed over wave crest and wave trough yielding either $Q_+^{Se}/Q_+^{Re} > 1$ and $Q_-^{Se}/Q_-^{Re} < 1$ or $Q_+^{Se}/Q_+^{Re} < 1$ and $Q_-^{Se}/Q_-^{Re} > 1$ with a greater redistribution of fluxes for greater phase-lag effects.

The ratios $Q_+^{Se}/Q_+^{Re}$ and $Q_-^{Se}/Q_-^{Re}$, being accurate proxies for both the existence and the magnitude of phase-lag effects, should help parameterize the redistribution of sediment loads during wave crest and wave trough. However, to this point, the observations made in this section are only modeling suggestions. Indeed, the results obtained from the two configurations F5010 and S706015f investigated in this chapter are not sufficient to even try to propose accurate scaling laws based on this new set of parameters. To do so, additional configurations should be numerically investigated to explore the parameter space in term of flow intensity, wave period relative to the particle fall velocity and asymmetry/skewness factors.

## 4.5 Conclusion

The effect of wave shape on oscillatory sheet flow has been investigated using the turbulence-resolving two-fluid model sedFoam with a focus on grain size dependency and phase-lag effects.

Four configurations involving fine and medium sand subject to a asymmetric and skewed waves have been reproduced numerically. From a comparison between experimental measurements and numerical predictions of the net transport rate generated under non-sinusoidal waves, mechanisms responsible of the larger net transport rate for fine sand under asymmetric waves and negative sediment rate for fine sand under skewed waves are reproduced by the two-phase flow model.

For oscillatory sheet flow involving medium sand subjected to skewed waves, streamwise sediment flux is fully correlated to the flow forcing and the instantaneous Shields number. The sediment flux is zero at flow reversals, increases during the acceleration phase and decreases during the deceleration phase. As a result of larger bed shear stress during the wave crest, a larger amount of sediment is transported compared with wave trough. Even if the duration of the wave trough is larger, the small quantity of sediment transported offshore does not compensate the onshore contribution from wave crest and the corresponding net transport rate is directed onshore.

For fine sand, contrary to medium sand, particles eroded during the wave crest do not have the time to settle back to the bed before the on-offshore flow reversal. A significant amount of suspended sediments at flow reversal is transported offshore during the wave trough and the sediment flux is no longer correlated with the instantaneous Shields number. Even if the magnitude of the streamwise sediment flux is smaller compared with the magnitude of the sediment flux during the wave crest, the duration of wave trough is larger. As a consequence, the amount of sediment transported offshore exceeds the amount of sediment transported onshore having for effect to generate a net offshore transport rate.

The same observations can be made between configurations involving medium sand subjected to asymmetric and skewed waves. However, the larger bed shear stress observed during wave crest is the result of the stronger acceleration compared with the wave trough. Sediment flux is zero at flow reversal and the amount of sediment transported onshore exceeds the amount of sediment transported offshore generating a net onshore-oriented transport rate.

For fine sand, sediment flux returns back to zero during the on-offshore flow reversal but not at

off-onshore flow reversal. Particles remaining in suspension are transported during the wave crest having for effect to further increase the onshore-oriented net transport rate.

The same mechanisms playing a role in unsteady effects as observed in chapter 3 are present in configurations involving fine sand. The sheet flow layer thickness is increased compared with configurations involving medium sand, turbulence is attenuated at flow reversals and bed instabilities increase vertical mixing of particles. Furthermore, the increased sheet flow layer thickness during wave trough for the configuration involving fine sand subjected to asymmetric waves can only be attributed to larger bed instabilities considering that the sheet flow layer thickness was close to zero at on-offshore flow reversal.

The scaling between onshore and offshore transport rates and their corresponding representative Shields numbers revealed that the sand flux in configurations involving fine and medium sand can not be represented by a power law using the same parameterization. Indeed, for configurations involving medium sand for which there is no phase-lag effects, the sediment load are well represented by a classical power law. However, for configurations involving fine sand, the sediment load are located above the curve representing the power law meaning that, as a consequence of unsteady effects, streamwise sediment flux is increased for configurations involving fine sand.

The comparison between the predicted maximum sheet flow layer thickness during wave crest and wave trough from the two-fluid model and the empirical relation proposed by Dohmen-Janssen *et al.* (2001) [29] has shown that the maximum sheet flow layer thickness from configuration involving medium sand can be well represented by the maximum Shields number but not for configurations involving fine sand.

From the time series of the vertical sediment mass balance between upward Reynolds fluxes and downward settling fluxes, suggestions on more physically based modeling methodologies have been provided. Indeed, the imprint of phase-lag effects are clearly visible on the competition between turbulent suspension of particles and their settling. However, additional configurations involving different grain sizes, flow periods and asymmetry/skewness factors are necessary to start developing new scaling laws.

Furthermore, provide accurate scaling laws require to obtain more quantitative results in term of transport rate and concentration profiles for configurations involving medium sand. As pointed out in section 3.3.1, medium sand appears to settle back to the bed too quickly compared with the experiments. For large particles, the separation of scale between the particles and the smallest turbulent eddies is no longer verified, the particle diameter is larger than the smallest turbulent length scale $\eta$. Finite-size effects may become important and should be taken into account to accurately predict fluid-particle interactions [39].

# 5

# Finite size correction model

In this chapter, the capabilities of the turbulence-resolving Eulerian–Eulerian two-phase flow model to predict the suspension of mono-dispersed finite-sized solid particles in a turbulent boundary layer flow are investigated. For heavier-than-fluid particles, having settling velocity of the order of the bed friction velocity, the two-fluid model significantly under-estimates the turbulent dispersion of particles. It is hypothesized that finite-size effects are important and a correction model for the drag law is proposed. This model is based on the assumption that the turbulent flow scales larger than the particle diameter will contribute to the resolved relative velocity between the two phases, whereas eddies smaller than the particle diameter will have two effects: (i) they will reduce the particle response time by adding a sub-particle scale eddy viscosity to the drag coefficient, and (ii) they will contribute to increase the production of granular temperature. Integrating finite-size effects in the two-fluid model allows us to quantitatively predict the concentration profile for heavier-than-fluid particles without any tuning parameter. The proposed modification of the two-fluid model extends its range of applicability to tackle particles having a size belonging to the inertial range of turbulence. The results presented in this chapter are published in Mathieu *et al.* (2021) [67].

## Contents

## 5.1 Introduction

The two-fluid LES of unidirectional sheet flow from Cheng *et al.* (2018) [23] highlighted the under-prediction of the vertical turbulent diffusion of particles by the Eulerian model (figure 1.8). They attributed this under-prediction to the effect on the unresolved particle clusters and streamers. However, given the grid resolution of their simulation ($\Delta/d_p < 1$) and the typical size of these mesoscale structures (of the order of 10 to 100 particle diameters [1]), the observed discrepancy may certainly be due to another cause.

Indeed, the under-prediction of sediment suspension in the simulations is more probably due to the consequence of assumptions made to derive the two-fluid model that are violated in the sheet flow configuration reproduced by Cheng *et al.* (2018) [23]. First, according to Ferry and Balachandar (2001) [36], the Eulerian representation of the dispersed phase is only valid for Stokes numbers smaller than one which is not the case in the configuration from Cheng *et al.* (2018) [23]. For $St > 1$, the uniqueness of the Eulerian particle phase velocity field is no longer guaranteed. Nevertheless, uniqueness of the particle phase velocity is not crucial considering time-averaged particle phase quantities (e.g. concentration, velocity) and assuming ergodicity. More precisely, time-averaged variables are issued from multiple realization of the flow and, therefore, multiple particles trajectories. The cause of the observed discrepancies is therefore more probably related to the absence of scales separation in the flow. In the sheet flow configuration investigated in Cheng *et al.* (2018) [23], particles are finite-sized. There is no separation of scales between the dispersed phase and the turbulent flow scales associated with the carrier phase. Classical interaction laws do not hold any longer and additional sub-particle scale correction models are required to account for finite-size effects [39].

In order to extend the range of applicability of the two-fluid model to configurations involving finite-sized particles, interaction laws should be modified to include the missing physics. From the two methodologies used to model finite size effect discussed in chapter 1, the correction model proposed by Gorokhovski & Zamansky (2018) [48] taking into account finite-size effect through an effective viscosity at the particle scale included in the expression of the drag force is more suitable for volume-averaged two-phase flow models compared with the Faxén correction term which is more appropriate in a Lagrangian framework.

In this chapter, the two-fluid LES approach is applied to dilute suspension of finite-sized particles transported in a turbulent boundary layer flow. A finite-size correction model for the two-fluid approach inspired from the model proposed by Gorokhovski & Zamansky (2018) [48] is developed and tested against experimental data for particle-laden boundary layer flow configurations having $d_p/\eta > 1$. First, the finite-size correction model is presented. Then, numerical configurations used to reproduce four particle-laden flow configurations are presented as long as preliminary results without the correction model. Eventually, the performances of the correction model are discussed including the sensitivity to the correction model components, grid resolution and filter size.

## 5.2 Finite-size correction model

### 5.2.1 Model description

Compared with particles smaller than the Kolmogorov length scale, finite-size particles do not only act as a temporal filter of the turbulent flow scales through the drag force but also as a spatial filter [15, 86]. In order to take into account the finite-size effect of the particles in the Eulerian-Eulerian two-phase flow model, a distinction is made between turbulent eddies having larger or smaller length scales than the particle diameter $d_p$ (blank and hatched zones, respectively, of the

idealized turbulent spectrum represented in figure 5.1). Following observations made by Qureshi *et al.* (2007) [86] and Calzavarini *et al.* (2009) [15], turbulent eddies larger than the particle diameter will contribute to the relative velocity between the two phases in the drag force as fluid velocity "seen" by the particles whereas smaller eddies are assumed to (1) modify the particle response time by increasing the viscosity "seen" by the particles by defining an effective turbulent viscosity at the particle scale following Gorokhovski & Zamansky (2018) [48] and (2) contribute to particle agitation by increasing the production of granular temperature to be consistent with the energy transfers between correlated and uncorrelated solid phase velocity fluctuations [38,42]. The idealized turbulent spectrum presented in figure 5.1 summarizes the different contributions of the turbulent fluid flow scales to the solid phase dynamics.

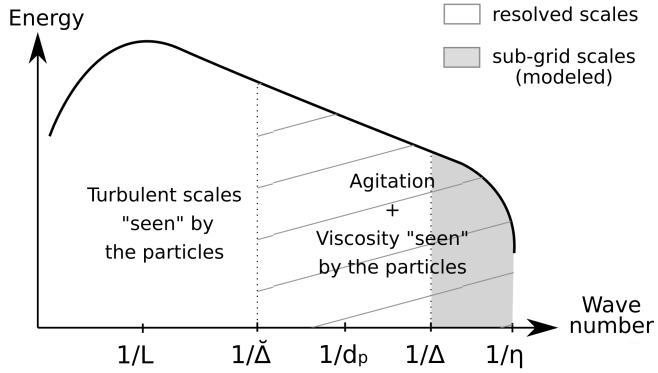


*Figure 5.1: Schematic representation of an idealized turbulent spectrum including the different flow scales and their contributions to the particles dynamics ($\eta$: Kolmogorov scale, $\Delta$: filter width, $d_p$: particle diameter, $\breve{\Delta}$: second filter width, L: integral scale of turbulence).*

To take into account finite-size effects, the filtered effective drag force is rewritten as

$$\bar{D}_i = \frac{\rho^s \bar{\phi}}{\breve{t}_s}(\breve{u}_i^f - \tilde{u}_i^s), \tag{5.1}$$

with $\breve{u}_i^f$ the fluid velocity "seen" by the particles corresponding to the resolved fluid phase velocity $\tilde{u}_i^f$ filtered at a scale $\breve{\Delta} \sim O(d_p)$. According to Kidanemariam *et al.* (2013) [60] the value of $\breve{\Delta}$ should not be too large to still be relevant to predict the particles motion but not too small to be sufficiently free from the local flow disturbances generated by the presence of the particles. To be able to determine the filter length $\breve{\Delta}$, they reported the ratio between the averaged magnitude of the flow velocity around spheres and the undisturbed flow field as a function of the distance from the center of the sphere for different particle Reynolds numbers. From their analysis, around 80% of the undisturbed mean flow velocity is recovered with a filter width taken as twice the diameter of the particle. Therefore, to compute the fluid velocity "seen" by the particles, the filter size is first chosen to be $\breve{\Delta} = 2d_p$. A sensitivity analysis to the filter size is presented in §5.4.2.

Whereas the turbulent scales smaller than the particle diameter are usually unresolved, due to the mesh refinement close to the wall, these turbulent scales are composed of both resolved and unresolved eddies in this region. In the present configuration, $\breve{\Delta} = \Delta_{x,z}$ in the streamwise and spanwise directions but $\breve{\Delta} > \Delta_y$ in the wall-normal direction. To calculate $\breve{u}_i^f$, a weighted average of the resolved fluid velocity in the wall-normal direction is performed using a Gaussian distribution function $G_w$ with standard deviation $\breve{\Delta}/2$

$$G_w = exp\left[-\frac{1}{2}\left(\frac{|y_0 - y_k|}{\breve{\Delta}/2}\right)^2\right] \tag{5.2}$$

where $y_0$ is the vertical coordinate of the cell where the avearge is computed and $y_k$ is the vertical coordinate of cell $k$ to compute the weighting coefficients.

The calculation of filtered variable imposes constraints on the parallelization of the numerical domain detailed in appendix D.

The new particle response time $\breve{t}_s$ still follows the drag law given by equation (2.39) but the relative velocity between the two phases is calculated using the filtered fluid velocity $\breve{u}_i^f$, and the expression for the particle Reynolds number is modified according to Gorokhovski & Zamansky (2018) [48] to take into account the effect of turbulent scales smaller than the particles by the mean of a turbulent eddy viscosity $\nu_p^t$ at the scale of the particles following

$$Re_p = \frac{d_p \|\breve{u}_i^f - \tilde{u}_i^s\|}{\nu^f + \nu_p^t}. \tag{5.3}$$

The turbulent viscosity at the particle scale can be calculated using Kolmogorov scaling and Prandtl's mixing length hypothesis following $\nu_p^t \sim \varepsilon_p^{1/3} d_p^{4/3}$, with $\varepsilon_p$ the dissipation of TKE at the particle scale [48]. By assuming that the turbulent scales between $\breve{\Delta}$ and $d_p$ are in the inertial range of the turbulent spectrum, the approximation $\varepsilon_{\breve{\Delta}} = \varepsilon_p$ can be made with $\varepsilon_{\breve{\Delta}}$ the dissipation rate at the filter scale.

The expression of the dissipation rate at the filter scale $\varepsilon_{\breve{\Delta}}$ is estimated following the expression from Yoshizawa and Horiuti (1985) [127] defined as a function of the filter width $\breve{\Delta}$ and the total TKE below $\breve{\Delta}$ defined as the sum of $\breve{k} = \frac{1}{2}\tilde{u}_i^{f''}\tilde{u}_i^{f''}$ the resolved TKE (from $\breve{\Delta}$ to $\Delta$), with $\tilde{u}_i^{f''} = \tilde{u}_i^f - \breve{u}_i^f$ and $\tilde{k}_{sgs}^f$ the sub-grid TKE (from $\Delta$ to $\eta$), *i.e.*

$$\varepsilon_{\breve{\Delta}} = C_\varepsilon \frac{(\breve{k} + \tilde{k}_{sgs}^f)^{3/2}}{\breve{\Delta}}. \tag{5.4}$$

Eventually, the particle response time with finite-size correction is written following Gorokhovski & Zamansky (2018) [48] as

$$\breve{t}_s = \frac{4}{3}\frac{\rho^s}{\rho^f}\frac{d_p}{C_D\|\breve{u}_i^f - \tilde{u}_i^s\|}(1-\bar{\phi})^{2.65} \quad \text{with} \quad \begin{cases} C_D = \frac{24}{Re_p}\left(1 + 0.15 Re_p^{0.687}\right) \\ Re_p = \frac{d_p\|\breve{u}_i^f - \tilde{u}_i^s\|}{\nu^f + \varepsilon_{\breve{\Delta}}^{1/3} d_p^{4/3}} \end{cases} \tag{5.5}$$

Furthermore, the turbulent flow scales smaller than $\breve{\Delta}$ contribute to increase the production of granular temperature isotropically. The fluid particle-interaction term $J_{int}$ in equation (2.29) includes the resolved sub-particle TKE, *i.e.*

$$J_{int} = \frac{\rho^s}{\breve{t}_s}\frac{\phi}{1-\phi}\left[2(\breve{k} + \tilde{k}_{sgs}^f) - 3\bar{\Theta}\right]. \tag{5.6}$$

It shall be mentioned that the proposed model tends to the two-fluid model in its traditional formulation for particles smaller than the Kolmogorov length scale ($d_p/\eta < 1$). Indeed, if $\breve{\Delta} \leq \eta$ then $\breve{u}_i^f = \tilde{u}_i^f$ and, therefore, $\breve{k} = \tilde{k}^f = 0$. The turbulent viscosity at the particle scale vanishes $\nu_p^t = 0$ and eventually $\breve{t}_s = \tilde{t}_s$. Furthermore, the proposed finite-size correction model allows us to approach the exact solution for vanishingly small mesh sizes. Indeed, the correction model allows us to decorrelate the filter width associated with the particle size in the drag law and the filter size imposed by the mesh for the LES making the solution mesh independent.

### 5.2.2 Numerical implementation

For the implementation of the finite size correction model, some changes need to be made compared with the numerical implementation presented in section 2.4. Given the fact that the expression of the fluid velocity in the drag force does no longer correspond to the resolved fluid velocity,

the fluid contribution to the drag term can not be treated implicitly. More precisely, the fluid and solid contributions of the drag force is transfered to the term $\mathbf{R}^f$ in equation (2.70) and the fluid contribution is transfered to the term $\mathbf{R}^s$ of equation (2.72). The solution procedure remains the same but with expressions $AK^s = AK^f = 0$ and the suppression of the terms involving the drag parameters in equations (2.78) and (2.79).

## 5.3 Results

### 5.3.1 Particle-laden channel flow configurations

In this section, particle-laden configurations involving spherical Glass Beads (GB) from Kiger & Pan (2002) [61], Natural Sediment (NS) particles from Muste *et al.* (2005) [75] and almost Neutrally Buoyant Sediment (NBS) particles from Muste *et al.* (2005) [75] are reproduced numerically.The flow and particles parameters are presented in table 5.1.

| Parameters | Units | GB | NS | NBS | NS* |
|---|---|---|---|---|---|
| $U_b$ | $m.s^{-1}$ | 0.51 | 0.84 | 0.84 | 0.84 |
| $u_\tau(\times 10^{-2})$ | $m.s^{-1}$ | 2.99 | 4.20 | 4.20 | 4.20 |
| $h$ | $m$ | 0.02 | 0.021 | 0.021 | 0.021 |
| $\rho^s$ | $kg.m^{-3}$ | 2600 | 2650 | 1025 | 2650 |
| $d_p$ | $\mu m$ | 195 | 230 | 230 | 230 |
| $\phi_{tot}(\times 10^{-4})$ | - | 2.31 | 4.6 | 4.6 | 16.2 |
| $v_s/u_\tau$ | - | 0.87 | 0.54 | 0.01 | 0.54 |
| $Re_p$ | - | 4.8 | 9.1 | 0.39 | 9.1 |
| $St$ | - | 3.2 | 5.7 | 6.6 | 5.7 |
| $d_p/\eta$ | - | 5.5 | 9.7 | 9.7 | 9.7 |

*Table 5.1: Flow and particles parameters for configurations GB, NS, NBS and NS*.*

In the model used to reproduce these configurations, the definitions of the viscosity and conductivity of granular temperature induced by collisions and kinetic effects are based on an earlier version of the kinetic theory from Gidapsow (1994) [46]. Compared with the model presented in section 2.1.2, the viscosity and conductivity of granular temperature are given by

$$\nu^c = d_p\sqrt{\bar{\Theta}}\left[\frac{4\bar{\phi}^2 g_0(1+e)}{\sqrt{5\pi}} + \frac{\sqrt{\pi}g_0(1+e)^2(2e-1)\bar{\phi}^2}{15(3-e)} + \frac{\sqrt{\pi}\bar{\phi}}{6(3-e)}\right] \tag{5.7}$$

and

$$\kappa_\Theta = \rho^s d_p\sqrt{\bar{\Theta}}\left[\frac{2\bar{\phi}^2 g_0(1+e)}{\sqrt{\pi}} + \frac{9\sqrt{\pi}g_0(1+e)^2(2e-1)\bar{\phi}^2}{2(49-33e)} + \frac{5\sqrt{\pi}\bar{\phi}}{2(49-33e)}\right], \tag{5.8}$$

with $g_0 = (2-\bar{\phi})/2(1-\bar{\phi})^3$ the radial distribution function for dense rigid spherical particle gases from Carnahan & Starling (1969) [17]. However, for dilute configurations, fluid-particle interaction are dominant compared with contributions from the solid phase stress. This point is further addressed in the next sections.

The targeted configurations correspond to turbulent dilute suspended sediment transport boundary layer flows. In this situation, particles are entrained into suspension by the turbulent coherent flow structures and under steady-state flow conditions, an equilibrium concentration profile across the water depth establishes as the result of an equilibrium between the gravity driven settling flux, $v_s\langle\phi\rangle$ with $v_s$ the settling velocity of the particles, and the turbulent Reynolds sediment flux $\langle v^{s'}\phi'\rangle$ [98] with $v^{s'}$ the solid phase vertical velocity fluctuations and $\phi'$ the sediment concentration fluctuations. By analogy with Fickian diffusion, this Reynolds sediment flux is modeled using a gradient diffusion model. Introducing this model in the Reynolds-averaged sediment mass balance leads to the following equation:

$$v_s\langle\phi\rangle - \frac{\nu_t^f}{S_c}\frac{d\langle\phi\rangle}{dy} = 0, \tag{5.9}$$

with $\nu_t^f$ the turbulent eddy viscosity (or turbulent momentum diffusivity) and $S_c$ the turbulent Schmidt number representing the efficiency of the sediment diffusion relative to $\nu_t^f$. For $S_c < 1$ sediment particles are dispersed more efficiently by turbulence than fluid parcels.

Given that $\nu_f^t = l_m^2 d\langle u^f\rangle/dy$ using Prandtl's mixing length $l_m = \kappa y$, with $\kappa = 0.41$ the von Karman constant and using the log-law-of-the-wall to describe the mean velocity profile, equation (5.9) can be integrated analytically to give the following expression for the Reynolds averaged particle concentration profile:

$$\frac{\langle\phi\rangle}{\phi_0} = \left(\frac{y_0}{y}\right)^{Ro}, \tag{5.10}$$

with $\phi_0$ a reference concentration at a given reference elevation $y_0$ and $Ro = S_c v_s/u_\tau\kappa$ the Rouse number. For open-channel flows, a free surface correction to the Prandtl's mixing length is introduced $l_m = \kappa y\sqrt{1-y/h}$ with $h$ representing the water depth and the Reynolds averaged particle concentration profile reads:

$$\frac{\langle\phi\rangle}{\phi_0} = \left[\frac{y}{h-y}\frac{h-y_0}{y_0}\right]^{-Ro}. \tag{5.11}$$

These two analytical solutions provide a reference with which the two-fluid LES model results can be compared. The value of $S_c$ is still debated in the sediment transport community [65], the most widely accepted model is the one from van Rijn (1984) [117] relating the turbulent Schmidt number to the suspension number as follows: $S_c = (1+2(v_s/u_\tau)^2)^{-1}$ in the limit $1/3 < S_c < 1$. Nevertheless, a lot of scatter is observed on existing experimental data and no satisfactory explanation exists to support van Rijn's empirical formula [65].

The hydrodynamic configuration, numerical domain and parameters for configuration GB are the same as the unidirectional boundary layer validation case presented in section 2.5.1. The only difference comes from the addition of a given amount of glass beads in the flow corresponding to a mean volumetric concentration of particles in the channel $\phi_{tot} = 2.31\times10^{-4}$. The particles are spherical and mono-dispersed with diameter $d_p = 195\ \mu m$ ($d_p^+ \approx 5.5$) and density $\rho^s = 2600\ kg.m^{-3}$. For such particles, the computed fall velocity in still water using the drag law from equation (2.39) is $v_s = 2.4\times10^{-2}\ m.s^{-1}$ ($v_s/u_\tau = 0.85$).

Configurations NS and NBS from Muste *et al.* (2005) [75] consist of turbulent particle-laden open-channel flows with water depth $h = 0.021m$ in which finite-sized particles with density $\rho^s = 2650\ kg.m^{-3}$ and $\rho^s = 1025\ kg.m^{-3}$, respectively, are seeded. The NS and NBS hydrodynamic conditions are the same with a bulk velocity $U_b = 0.84\ m.s^{-1}$ and a targeted friction velocity $u_\tau = 4.2\times10^{-2}\ m.s^{-1}$ corresponding to a Reynolds number based on the wall friction velocity $Re_\tau = 882$. Both type of particles have the same diameter $d_p = 230\ \mu m$ ($d_p^+ \approx 9.7$) resulting in a larger fall velocity ( *i.e.* larger suspension number) for NS $v_s = 2.4\times10^{-2}\ m.s^{-1}$ ($v_s/u_\tau = 0.57$) compared with NBS $v_s = 6\times10^{-4}\ m.s^{-1}$ ($v_s/u_\tau = 0.01$). For both configurations, the mean volumetric concentration of sediment is equal to $\phi_{tot} = 4.6\times10^{-4}$. The computational domain is a rectangular box with bi-periodic boundary conditions along $x$ and $z$ axis and no slip boundary conditions at the bottom boundary (figure 5.2).

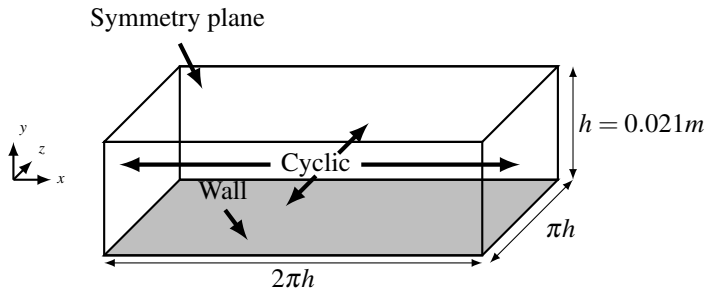


*Figure 5.2: Sketch of the geometry and boundary conditions of the numerical domain for configurations NS, NBS and NS* from Muste et al. (2005) [75].*

The mesh is decomposed into $287 \times 200 \times 147$ elements for a total of $8,323,000$ cells with uniform stream-wise and span-wise grid resolution $\Delta_x^+ = \Delta_z^+ = 19$. The mesh resolution is stretched along the $y$ axis with the first grid point located at $\Delta_y^+ \approx 1$ and $\Delta_y^+ \approx 3$ at the top. The time step is constant $\Delta t = 5 \times 10^{-5}$. Numerical parameters for configurations NS, NBS ans NS* are presented in table 5.2. $Re_p$, $St$ and $d_p/\eta$ are calculated based on the scaling analysis from Finn & Li (2016) [39]. Simulations of configuration GB lasted for about 4 to 5 days on 288 cores (n nodes) for a total of approximatively $30,000$ core-hours per simulation. For configurations NS and NBS, simulations also lasted for about 4 to 5 days but on 336 cores (n nodes) for a total of approximatively $36,000$ core-hours per simulation.

| Mesh | Number of cells | $\Delta_x^+$ | $\Delta_z^+$ | $\Delta_y^+$ (wall) | $\Delta t$ |
|---|---|---|---|---|---|
| $287 \times 200 \times 145$ | $8,323,000$ | 19 | 19 | 1 | $5 \times 10^{-5}$ |

*Table 5.2: Numerical parameters of the NS, NBS ans NS* configurations from Muste et al. (2005) [75].*

A first set of simulations for each configuration is performed in order to evaluate the predictive capability of the two-fluid model without finite-size correction. The visualization of the instantaneous turbulent coherent structures using an iso-contour of Q-criterion (figure 5.3a) and volume rendering of the concentration (figure 5.3b) from the GB configuration shows the imprint of turbulence on the sediment concentration field. The differences of sediment concentration relative to the coherent structures highlights the importance of turbulence-particle interactions. The averaged solid phase concentration profiles obtained experimentally and numerically are compared in figure 5.4. For GB (figure 5.4a), experimental and numerical concentration profiles are normalized by the reference concentration $\phi_0$ taken at $y_0 = 0.06h$. For both configurations GB and NS (figure 5.4a and 5.4b), the volume fraction of particles in suspension is significantly under-estimated compared with the experimental data. However, for the NBS configuration (figure 5.4c), the average concentration profile predicted by the two-fluid model fits perfectly well the experimental results. For $v_s/u_\tau \ll 1$, the weight of the particles is entirely supported by turbulence [10]. The two-phase flow model in its original formulation correctly reproduces the vertical balance between settling and Reynolds fluxes. For this flow and these particle parameters, finite-size effects can be considered as negligible and the two-fluid model shows very good predictive capabilities without finite-size correction model. In the following, configurations GB and NS for which the suspension number is higher are further investigated to understand the physical origin of the observed discrepancies.

The research hypothesis developed in this work is that the discrepancies observed in figure 5.4 are due to finite-size effects. One could also argue that these discrepancies are due to missing fluid-particle forces such as added mass and lift forces. A simulation including these two forces have

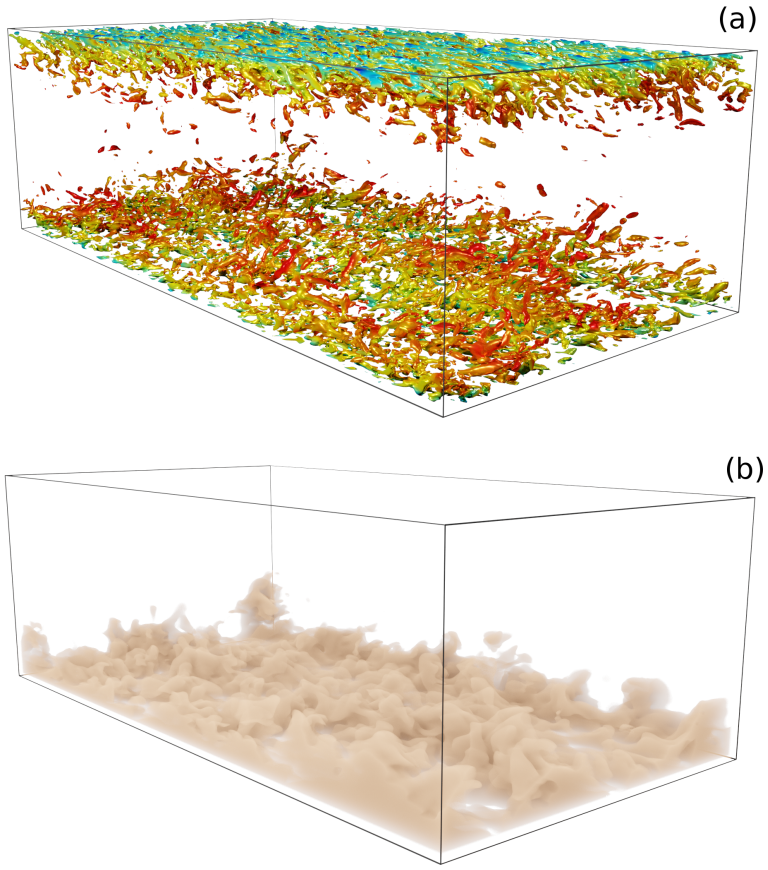


*Figure 5.3: Visualization of the instantaneous turbulent coherent structures using an iso-contour of Q-criterion colored by the velocity (panel (a)) and volume rendering of the concentration (panel (b)) from the GB configuration.*

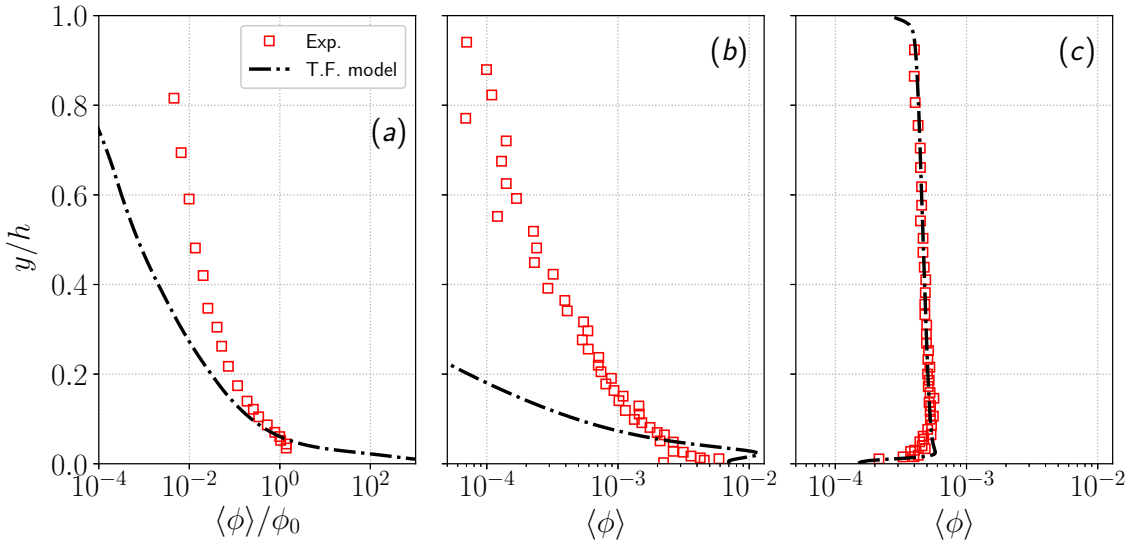


*Figure 5.4: Solid phase volumetric concentration profiles from the experiments (Exp.) and two-phase flow simulations (T.F. model) from configurations GB (panel (a)), NS (panel (b)) and NBS (panel (c)). In panel (a), experimental and numerical concentration profiles are normalized by the reference concentration $\phi_0$ taken at $y_0 = 0.06h$.*

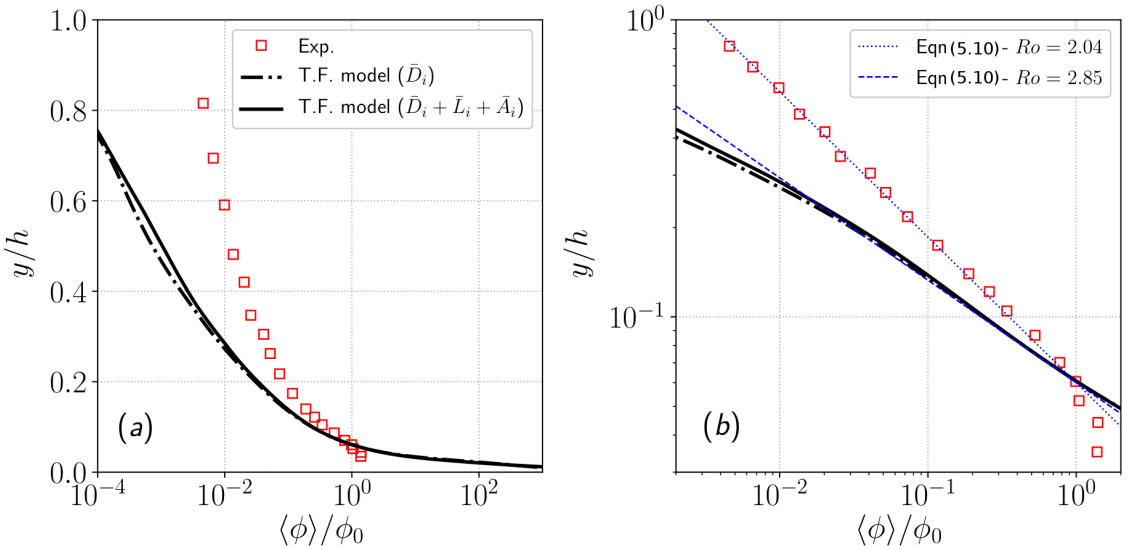


*Figure 5.5: Solid phase volumetric concentration profiles from the experiment (Exp.), two-phase flow simulation including only the drag force (T.F. model ($\bar{D}_i$)) and two-phase flow simulation including drag, lift and added mass forces (T.F. model ($\bar{D}_i + \bar{L}_i + \bar{A}_i$)) from configuration GB in semi-log scale in panel (a) and in log-log compared with analytical profiles from equation (5.10) with $Ro = 2.04$ and $Ro = 2.85$ in panel (b).*

been performed for the configuration GB and the averaged concentration profiles are compared with the experiments and the analytical concentration profile from equation (5.10) in figure 5.5. Since this expression is derived for an infinite boundary layer, one have to keep in mind that for closed channel flows, this expression could become less accurate near the centerline of the channel. The comparison between the simulation including only the drag force and the simulation including drag, lift and added mass forces indicates that the drag force is the dominant interaction force for this configuration. Lift and added-mass forces contributions are almost negligible in this problem. The concentration profiles from both simulations show a power law that fits with the equation (5.10) with $Ro = 2.85$ whereas $Ro = 2.04$ in the experiments (figure 5.5b). The Basset history force does not appear in the momentum exchange term between the two phases since it is defined from a purely Lagrangian point of view. It would therefore be very difficult to obtain a volume average expression of the history force in the Eulerian formalism. To the best of the authors knowledge, there is no references in the literature showing the Eulerian expression of the Basset history force. The authors believe that the Basset history force would be significant very near the bottom boundary where wall-particle collision occur but should not affect too much the vertical distribution of particles in the upper part of the channel where particles acceleration is weaker. It is only through a detailed comparison with Lagrangian point-particle simulations including the Basset history force that the role of this force could be investigated which is beyond the scope of the present work.

The two-phase flow model in its initial formulation, using a standard drag law, added mass and lift forces, can not reproduce the turbulent suspension of particles in this configuration. In the following, the role of unresolved turbulent length scales smaller than the particle size is investigated.

### 5.3.2 Evaluation of the finite-size correction model

From the scaling analysis proposed by Balachandar (2009) [9], the relative velocity between the fluid phase and inertial particles is mainly influenced by an eddy having the same timescale as the particles with the corresponding length scale $l^* = \varepsilon^{f1/2} t_s^{3/2}$ with $\varepsilon^f$ the dissipation rate of fluid

TKE. According to Finn & Li (2016) [39], if $l^* > \Delta > d_p$, all the relevant flow scales are resolved and the particle dynamics can be accurately predicted. The average value of $l^*$ for configuration GB is calculated in the simulation and plotted in figure 5.6. It can be seen that $l^*/d_p < 1$ and that $l^*$ decreases by one order of magnitude from the wall to the centerline of the channel. This result shows that, for this configuration, turbulent scales smaller than the particles can have a significant effect on the particle dynamics and may be responsible for the observed discrepancies.

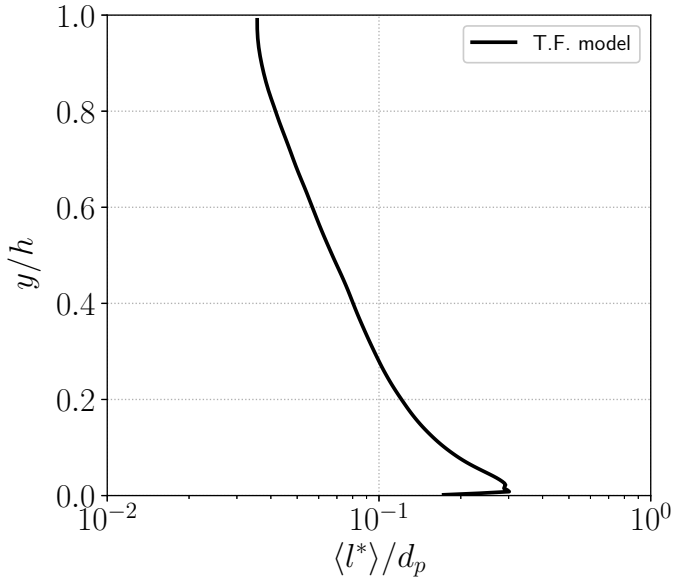


*Figure 5.6: Average profile of the length scale $l^*$ associated with the turbulent eddy having the same timescale as the particles as a fraction of $d_p$ from the two-phase simulation of configuration GB.*

Given the broad range of length and time scales involved in a particle-laden horizontal boundary layer flows, multiple types of turbulence-particle interactions occur at different locations of the boundary layer. It is therefore crucial to develop a model applicable over a wide range of turbulence-particle interaction regimes. In the following, the finite-size correction model presented in subsection 5.2 is tested for the three configurations GB, NS and NBS. The results of the simulations for the averaged concentration profile for configuration GB with and without the finite-size correction model are compared in figure 5.7. The prediction of the concentration profile by the two-phase flow model is significantly improved by the finite-size correction model without any tuning coefficient. The Rouse number predicted with the finite-size correction model is $Ro = 1.86$ which is much closer to the experimental value compared with the prediction without correction (figure 5.7b). However, in the experiment, the concentration profile is well described by the power law across the water depth whereas in the simulation, the concentration decreases more rapidly toward the centerline of the channel.

In order to further evaluate the finite-size correction model, the configurations NS and NBS are reproduced numerically using the two-phase flow model with finite-size correction. Analytical, experimental and numerical averaged concentration profiles are compared in figure 5.8 for both configurations.

For configuration NS (figure 5.8a), the same conclusions as for configuration GB can be drawn. The finite-size correction model significantly improves the prediction of the turbulent suspension of particles without any tuning coefficient. The predicted Rouse number ($Ro = 0.83$) is closer to the experimental value ($Ro = 1.00$). The modeled concentration profile obtained using finite-size correction is in very good agreement with the experimental data compared with the simulation without finite-size correction model.

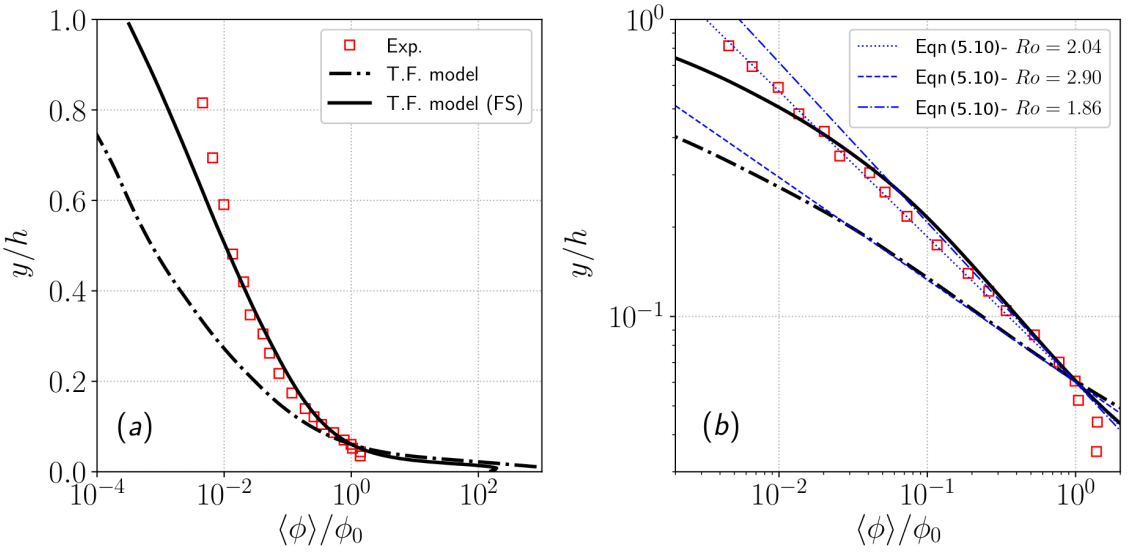


*Figure 5.7: Solid phase volumetric concentration profiles from the experiment (Exp.), two-phase flow simulation with finite-size correction model (T.F. model (FS)) and two-phase flow simulation without finite-size correction model (T.F. model) from configuration GB in semi-log scale in panel (a) and in log-log compared with analytical profiles from equation (5.10) with* $Ro = 2.04$, $Ro = 2.90$ *and* $Ro = 1.86$ *in panel (b).*

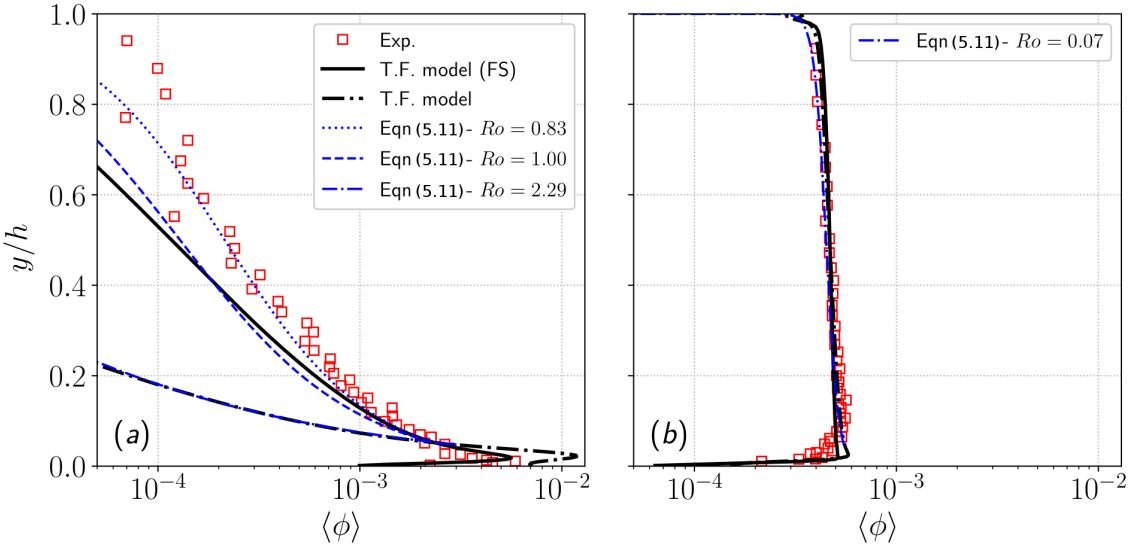


*Figure 5.8: Solid phase volumetric concentration profiles from the experiment (Exp.), two-phase flow simulation with finite-size correction model (T.F. model (FS)), two-phase flow simulation without finite-size correction model (T.F. model) and analytical profiles from equation (5.11) with* $Ro = 0.83$, $Ro = 1.00$, $Ro = 2.29$ *and* $Ro = 0.07$ *from configuration NS in panel (a) and configuration NBS in panel (b)*

For configuration NBS (figure 5.8b), the finite-size correction model does not alter the results predicted without finite-size correction. Almost no differences can be observed between the concentration profiles obtained with and without finite-size correction confirming that finite-size effects are negligible for configurations with low suspension number.

As a partial conclusion, it has been demonstrated that finite-size effects are important to predict turbulent suspension of inertial particles in a boundary layer flow when the suspension number is of the order of unity. The finite-size correction model proposed in this work significantly improves the model prediction for the average sediment concentration profile without the use of tuning parameter to fit the experimental data.

### 5.3.3 Lag velocity

Another interesting feature of turbulent suspension of inertial particles is the existence of a velocity lag between the average stream-wise velocity of the fluid and of the particles [59–61, 75, 78, 96]. Kidanemariam *et al.* (2013) [60], based on fully-resolved DNS, have been able to clearly identify the physical origin of this velocity lag as being due to the preferential concentration of suspended particles in low speed regions of the fluid flow which can be identified with ejection events. This velocity lag is not observed for particle-laden flows with low suspension number [75] such as NBS but can be as high as 20% of the bulk fluid velocity [60].

The averaged fluid and solid velocity profiles obtained numerically with or without the finite-size correction for configurations GB, NS and NBS are shown in the top panels of figure 5.9. The velocity profiles are in very good agreement with the experiments and they do not show much sensitivity to the finite-size correction model. The velocity difference is too small to be visible on these graphs, the lag velocity $u_{lag} = \langle \tilde{u}_i^f \rangle - \langle \tilde{u}_i^s \rangle$ is shown in the bottom panels of figure 5.9. For configurations GB and NS, the lag velocity is positive and of the order of 5-10% of the bulk fluid velocity. The two-fluid model predicts the correct sign and order of magnitude for the lag velocity. The major discrepancy is observed in the near-wall region $y/h < 0.2$ where the two-fluid model predict a peak that is not observed in Kiger & Pan (2002) [61] experiments. For the NS configuration, the lag velocity decreases linearly with the distance to the free surface. This is probably a free surface effect that is not fully captured by the symmetry plane boundary condition used in the present simulation, nevertheless the model predictions are very satisfactory. Given the role played by the coherent structures of the flow in the velocity lag, the fact that the flow is over-resolved near the bottom boundary could explain the observed discrepancies for the GB case. However, since this difference is not observed for the other configurations, it might also be due to the high variability of the velocity measurements of Kiger & Pan (2002) [61] near the bottom (up to 25% for $y^+ < 50$). In both GB and NS configurations the finite-size correction model has a small influence on the lag velocity. In the NBS configuration, the experimental data reveals a negligible lag velocity that can even becomes negative. The two-fluid model with and without finite-size correction model predict a zero lag velocity except very near the bottom wall. From these three configurations one can conclude that the existence of a lag velocity is not due to finite-size effects. More importantly, the fact that the model is able to recover the absence of lag velocity for NBS means that the two-fluid LES captures the physical mechanism correctly and can be used as a predictive tool to study this mechanism.

### 5.3.4 Turbulent statistics

Among the three configurations, the most accurate measurements of turbulent statistics have been obtained for configuration GB. In the following, this configuration is analyzed in details for the fluid and particle phase flow statistics.

The wall friction velocity for configuration GB predicted with and without finite-size correction is $u_\tau = 2.70 \times 10^{-2}\ m.s^{-1}$ and $u_\tau = 2.72 \times 10^{-2}\ m.s^{-1}$ respectively. Whereas the numerical

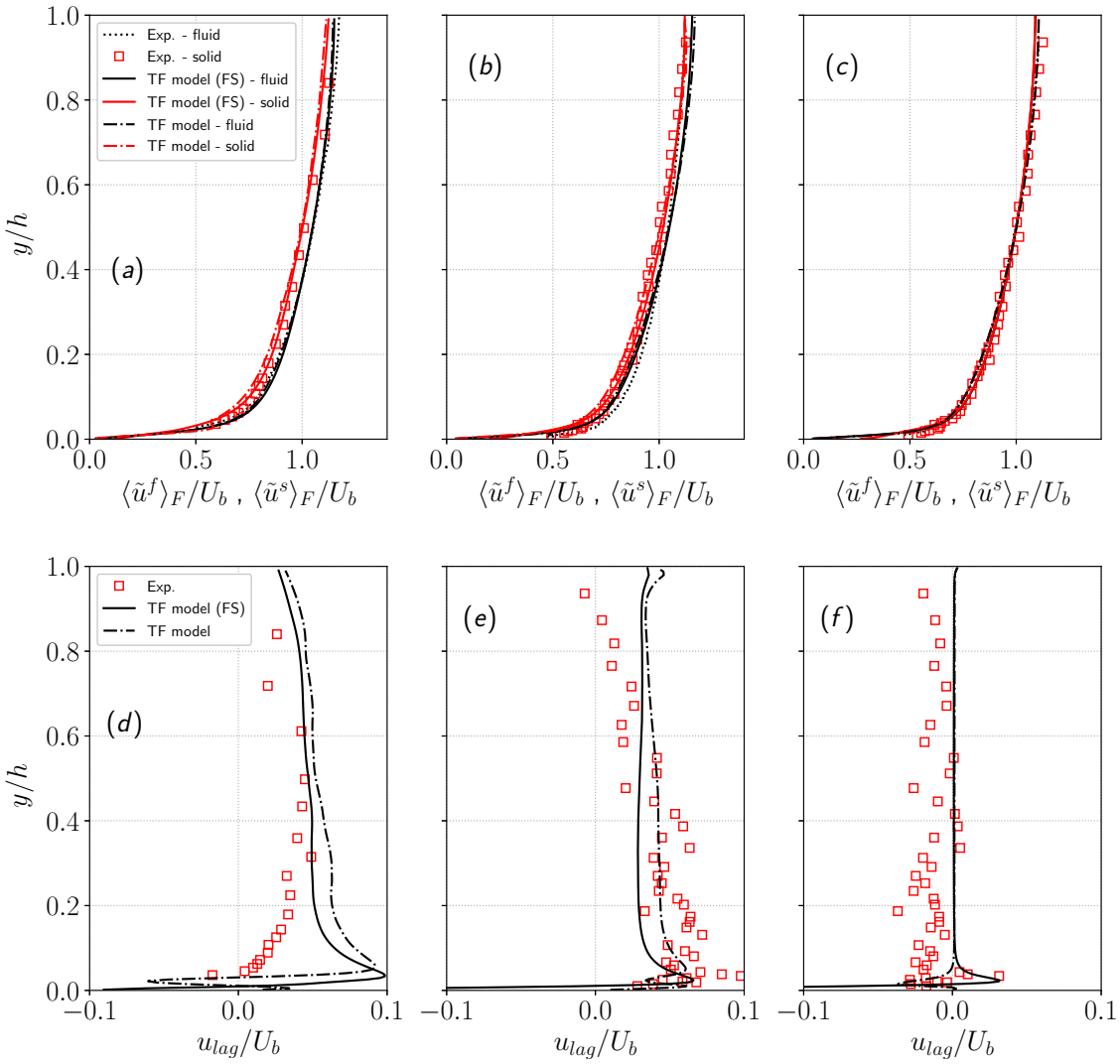


*Figure 5.9: Averaged fluid and solid velocity profiles in $(a,b,c)$ and lag velocity in $(d,e,f)$ from the two-fluid model with finite-size correction (T.F. model (FS)) and the two-fluid model without finite-size correction (T.F. model) for configurations GB (a, d), NS (b, e) and NBS (c, f) compared with experimental data (Exp.).*

wall friction velocity is similar between the clear-water and particle-laden configurations, the experiments suggest an increase of the friction velocity up to $u_\tau = 2.99 \times 10^{-2}\ m.s^{-1}$. Averaged fluid and solid Reynolds stress and Root Mean Square (RMS) of stream-wise and wall-normal velocity fluctuations profiles from configuration GB with or without finite-size correction are compared with experimental data in figure 5.10. From figure 5.10a, the two-fluid model slightly underestimates the fluid Reynolds shear stress compared with the experiments explaining the lower friction velocity in the simulations. However, experimental and numerical results are similar: the solid phase Reynolds shear stress is slightly greater than the fluid Reynolds shear stress away from the bottom wall. The maximum value for the solid Reynolds shear stress predicted by the two-fluid LES model is the same as in the experiments but the location is different. The RMS of stream-wise and wall-normal velocity fluctuations are in very good agreement with experimental results (figure 5.10b and 5.10c). As for the fluid Reynolds shear stress, the fluid phase velocity fluctuations are slightly under-estimated by the two-fluid model for $y/h > 0.1$. For both experimental and numerical profiles, the RMS of stream-wise solid phase velocity fluctuations are equal near the centerline of the channel and becomes smaller in the near bottom wall region. Similarly to the observation of Kidanemariam *et al.* (2013) [60] in their fully resolved DNS, the two-fluid model predicts stronger wall-normal solid velocity fluctuations compared with the fluid away from the wall whereas experimental solid and fluid profiles are similar close to the channel centerline. The RMS of the solid velocity fluctuations decreases more rapidly than the fluid ones towards the wall. Overall, the turbulent statistics are not significantly affected by the finite-size correction model.

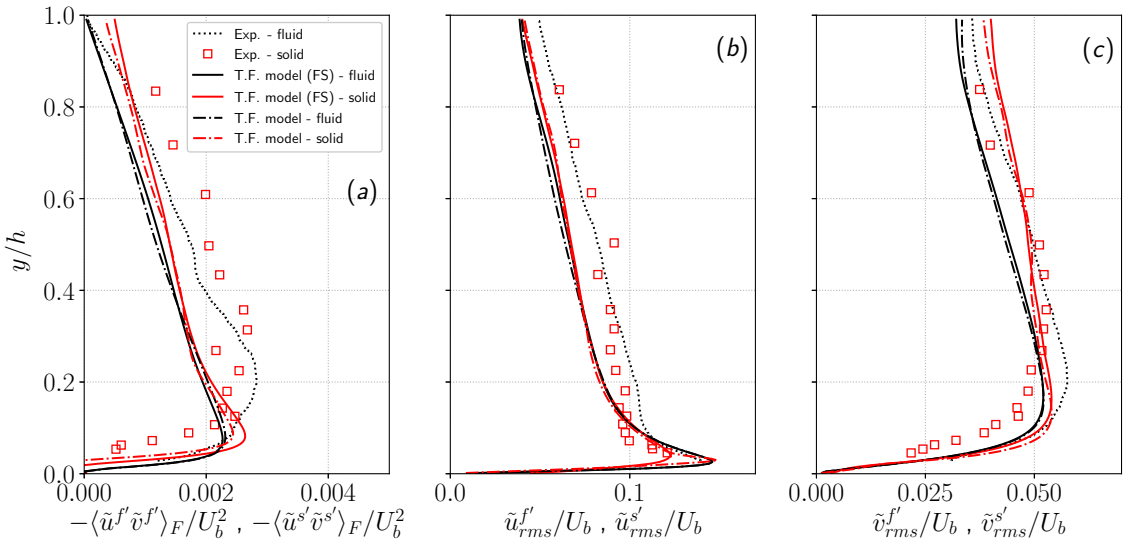


*Figure 5.10: Average profiles of fluid and solid Reynolds stress in $(a)$, r.m.s of stream-wise velocity fluctuations in $(b)$ and r.m.s of wall-normal velocity fluctuations in $(c)$ from the two-phase model with finite-size correction (T.F. model (FS)) and the two-phase model without finite-size correction (T.F. model) compared with experimental data (Exp.) from configuration GB.*

The slight differences observed between the experimental and numerical fluid phase turbulent statistics come from the modulation of the turbulence by the particles. Again, from the scaling analysis by Finn & Li (2016) [39] and given the parameters of the configuration from Kiger & Pan (2002) [61], the presence of the particles is expected to damp the fluid turbulence whereas in the experiments, a slight increase of the Reynolds stress and velocity fluctuations are observed compared with the clear water configuration. Indeed, according to Balachandar (2009) [9], the turbulence enhancement due to the presence of the particles comes from the action of the oscillating wakes behind particles having a high particle Reynolds number. The conjugate action of all the wakes of the particles participates to increase the overall fluid turbulence.

To be able to predict the turbulence enhancement, the two-fluid model should have the capacity to capture the vortex shedding behind the particles by fully resolving the fluid/solid interface which is not the case for the Eulerian-Eulerian two-phase flow model. Nevertheless, the turbulence enhancement due to the particles is not a dominant mechanism in this configuration. According to Finn & Li (2016) [39], the net production of turbulence by the particles is dominant for particle Reynolds numbers higher than Reynolds number $Re_p = 400$ even if oscillatory wakes behind particles can be observed for lower $Re_p$ depending on flow properties, particle shape or distance from the wall for example. In the present configuration, the particle Reynolds number based on the scaling relations from Finn & Li (2016) [39] is equal to $Re_p = 4.8$ and the maximum particle Reynolds number predicted in the simulation is $Re_{p,max} \approx 20$, which is significantly below the threshold value of 400.

Nevertheless, flow hydrodynamics and turbulent statistics are in good agreement with experimental data and the overall relative behavior between the fluid and solid phase is correctly captured by the two-phase flow model. The fact that the two-fluid model does not resolve the particle-fluid interface implies that the turbulence enhancement induced by the presence of the particles is not resolved. However, for such flow and particle parameters, according to the scaling analyses from Balachandar (2009) [9] and Finn & Li (2016) [39], this mechanism is not dominant. The lower fluid velocity fluctuations predicted by the two-fluid model near the channel centerline only results in a slight under-estimation of the sediment concentration in the same region compared with the experiments.

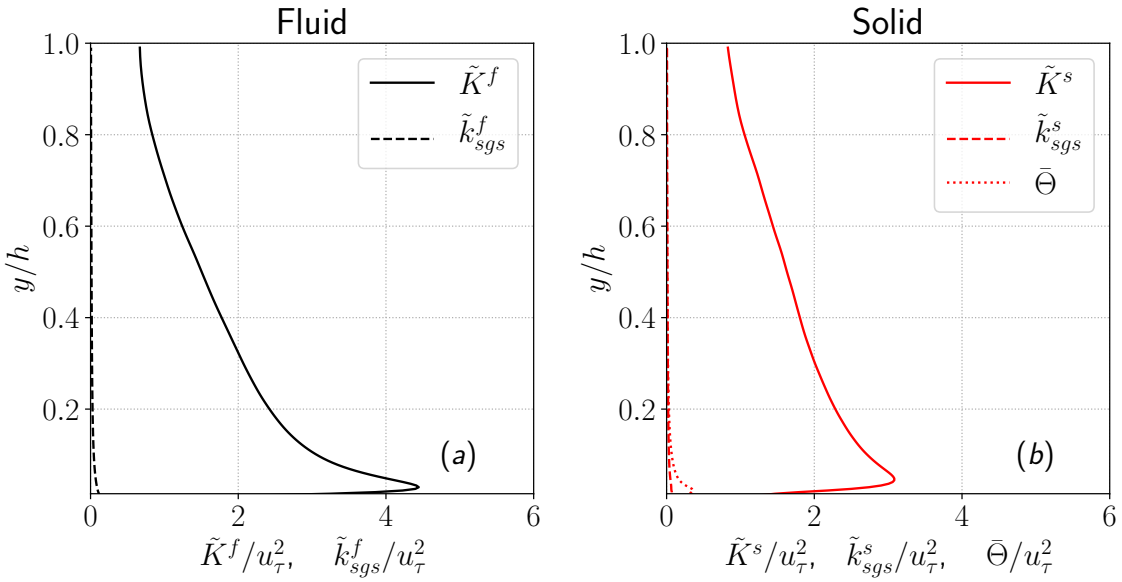


*Figure 5.11: Resolved and sub-grid fluid phase turbulent kinetic energy $\tilde{K}^f$ and $\tilde{k}^f_{sgs}$ in (a), resolved and sub-grid solid phase turbulent kinetic energy $\tilde{K}^s$ and $\tilde{k}^s_{sgs}$ and granular temperature $\Theta$ in (b) made dimensionless by the friction velocity $u_\tau$ from configuration GB.*

From the resolved and sub-grid turbulent kinetic energy profiles for the fluid and solid phases presented in figure 5.11, it appears that most of the turbulent kinetic energy is resolved ($\tilde{k}^f_{sgs}/\tilde{K}^f < 5\%$ and $\tilde{k}^s_{sgs}/\tilde{K}^s < 5\%$). The fact that the solid phase sub-grid turbulent kinetic energy is equal to zero through the channel height shows that the resolution is very close to DNS and validates the hypothesis to neglect the sub-grid terms. Furthermore, $\tilde{K}^s \gg \Theta$ in the channel except very near the solid boundary ($y/h < 0.05$) showing that kinetic and collisional dispersive forces should not be dominant compared with the drag force to suspend the solid particles for such dilute configurations. This hypothesis is further investigated in section 5.4.

### 5.3.5 Volume fraction sensitivity

An additional simulation (configuration NS*) is performed to evaluate the robustness of the proposed model to an increase of the mass loading. Experimental data from Muste *et al.* (2005) [75] using natural sediment having higher volume fractions compared with the previous NS configuration is reproduced numerically using the two-fluid model. The hydrodynamic and particle parameters are the same as for the NS configuration but the total solid phase volume fraction is multiplied by a factor 3.5 ($\phi_{tot} = 16.2 \times 10^{-4}$). The concentration can still be considered dilute and particles do not form a settled bed at the bottom of the channel.

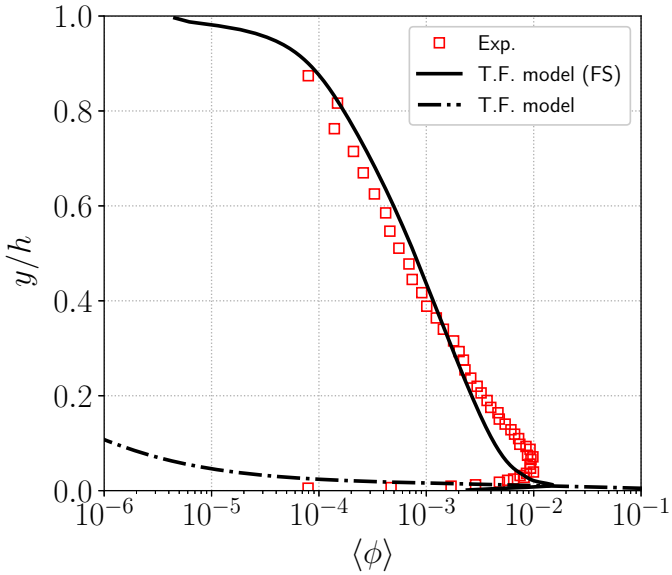


*Figure 5.12: Solid phase volumetric concentration profiles from the experiment (Exp.), two-phase flow simulation with finite-size correction model (T.F. model (FS)), two-phase flow simulation without finite-size correction model (T.F. model) from configuration NS*.*

The averaged concentration profile from the simulation of configuration NS with higher volume fraction is compared with experimental data in figure 5.12. As observed in the previous sections, the agreement with experimental data is significantly improved by the finite-size correction for natural sediments. This result is even more spectacular considering that without the correction model, the particles settle almost completely at the bottom of the channel resulting in an even larger under-estimation of the suspension of particles at higher volume fraction by the original two-fluid model.

## 5.4 Discussion

In this section, the sensitivity of the two-fluid model results to the different components of the finite-size correction model are discussed as well as the sensitivity to the grid/second filter resolution is presented.

### 5.4.1 Relative influence of the different terms of the finite-size correction model

In order to evaluate the relative influence of the modified drag law and the modified production of granular temperature, a new simulation is performed for which finite-size effects are taken into

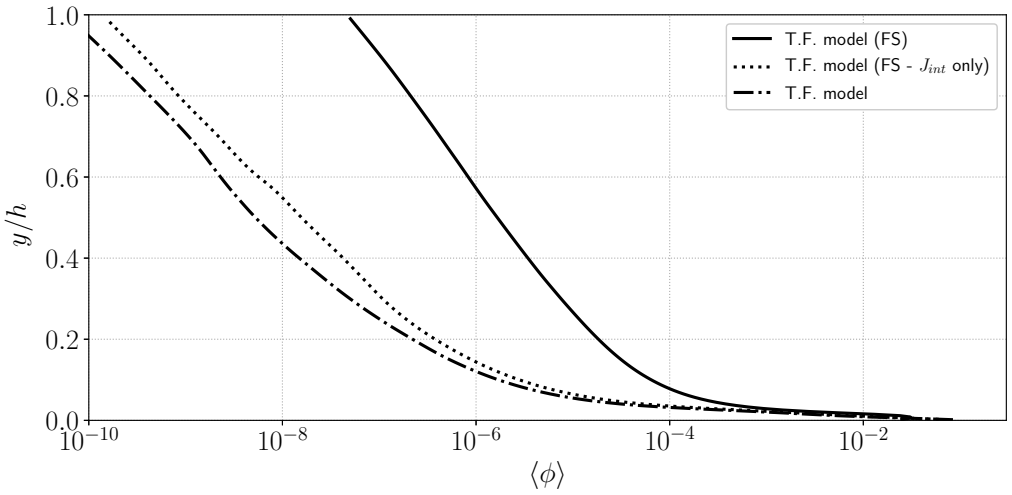


*Figure 5.13: Solid phase volumetric concentration profiles from the two-phase flow simulation with finite-size correction model (T.F. model (FS)), two-phase flow simulation with finite-size correction only in the production term of granular temperature (T.F. model (FS-$J_{int}$ only) and two-phase flow simulation without finite-size correction model (T.F. model) from configuration GB in semi-log scale.*

account only in the production term of the granular temperature transport equation. In other words, the simulation is performed using the drag law from equation (2.39) and the production of granular temperature from equation (5.6). The average concentration profile obtained from the simulation including finite-size effects only in the production of granular temperature equation is compared with the concentration profile from the simulations with or without finite-size correction in figure 5.13.

The concentration profile obtained from the two-fluid simulation including finite-size effects only in the production term of the granular temperature is similar to the profile without finite-size correction model. Indeed, for dilute suspension of particles, fluid-particle interactions are dominant compared with particle-particle interactions. The slope of the concentration profile in dilute regions of the flow is controlled by the drag force and the modification of the production term of granular temperature has almost no effect. However, the effect of the modification of the granular temperature transport equation could become dominant for higher concentrations. It should be noted that the modification of granular temperature transport equation is necessary because a simulation including finite-size effects only in the drag law and not in the production term of granular temperature was shown to be highly unstable. The observed instability is not the result of a numerical issue but rather the consequence of a physical inconsistency in the energy transfers between the two phases. Indeed, including finite-size effects only in the drag law and not in the production term of granular temperature is not physically consistent. Some of the turbulent flow scales are not taken into account in the energy budget between the phases making the simulation unstable.

The averaged wall normal momentum balance for the solid phase can be written as:

$$\underbrace{\left\langle \bar{\phi}\rho^s g \right\rangle}_{\text{Gravity}} = \underbrace{\left\langle \frac{\partial R^s_{xy}}{\partial x} + \frac{\partial R^s_{yy}}{\partial y} + \frac{\partial R^s_{zy}}{\partial z} \right\rangle}_{\text{Reynolds stresses}} + \underbrace{\left\langle \bar{\phi}\frac{\partial \bar{P}^f}{\partial y} \right\rangle}_{\text{Fluid pressure (Buoyancy)}} + \underbrace{\left\langle \frac{\partial \bar{P}^s}{\partial y} \right\rangle}_{\text{Granular pressure}} + \underbrace{\left\langle \bar{I}_y \right\rangle}_{\text{Drag}} \tag{5.12}$$

with $R_{ij} = \partial\langle\rho^s\bar{\phi}\tilde{u}_i^{s'}\tilde{u}_j^{s'}\rangle/\partial x_j$ the Reynolds shear stress coming from averaging of the non-linear

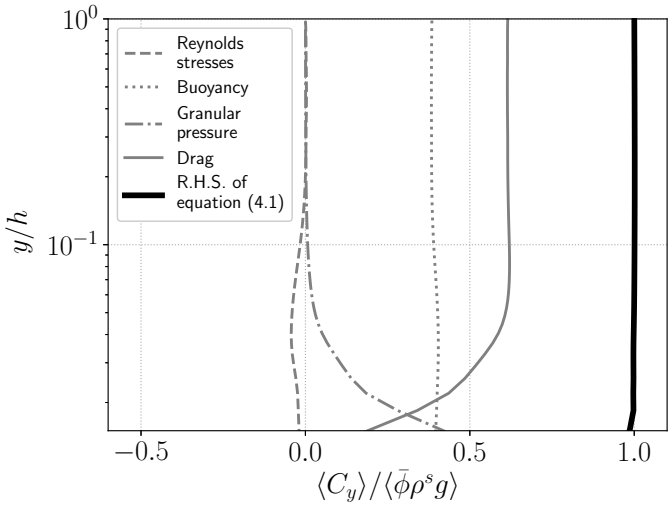


*Figure 5.14: Averaged contributions to the wall normal momentum budget $\langle C_y \rangle$ on the right hand side of the momentum balance (5.12) and their sum as a fraction of the gravity force $\langle \bar{\phi} \rho^s g \rangle$ from configuration GB.*

advection terms with $\tilde{u}_i^{s'} = \tilde{u}_i^s - \langle \tilde{u}_i^s \rangle$ the solid phase resolved velocity fluctuations. In figure 5.14, the four terms of the R.H.S. of equation (5.12) are plotted in dimensionless form, normalized by $\langle \rho^s \bar{\phi} g \rangle$, in semi-log scale for $y/h$. This figure shows that the predicted suspended particle concentration profile results from a balance between gravity, buoyancy and drag forces in the upper part of the channel. In such dilute systems, the effect of dispersive kinetic and collisional forces are not significant except very near the wall $y/h < 0.05$ ($y/d_p < 5$). This supports the hypothesis that the discrepancies observed in the original model can not be due to a flaw in the kinetic-theory formulation but are due to fluid-particle interaction forces.

### 5.4.2 Second filter size sensitivity

As mentioned in section 5.2, the width of the second filter $\breve{\Delta}$ should not be too small to be free from disturbances generated by the presence of the particles. On the other hand, the second filter size should not be too large in order to provide an accurate representation of the velocity "seen" by the particles. The minimum filter width $\breve{\Delta}_{min} = 2d_p$ has been determined from Kidanemariam *et al.* (2013) [60] but there is no clear criteria for the maximum filter width. However, for computational efficiency, since the second filter width depends on the spatial discretization in the stream-wise and span-wise direction for this configuration, it can be crucial to determine the maximum acceptable filter width to accurately predict the average concentration profile with coarser grid resolutions.

| Mesh | $N_x \times N_y \times N_z$ | $\Delta_x^+, \Delta_z^+$ | $\Delta_y^+$ (bottom) | $\breve{\Delta}$ |
|---|---|---|---|---|
| M1 | $314 \times 220 \times 160$ | 11 | 1 | $2d_p$ |
| M2 | $210 \times 147 \times 107$ | 17 | 1.5 | $3d_p$ |
| M3 | $126 \times 88 \times 63$ | 22 | 2 | $4d_p$ |
| M4 | $80 \times 56 \times 40$ | 44 | 4 | $8d_p$ |

*Table 5.3: Mesh characteristics for the second filter size sensitivity test.*

Additional simulations for configuration GB with different mesh resolutions have been performed to measure the influence of the spatial discretization and the second filter width $\breve{\Delta}$ on the

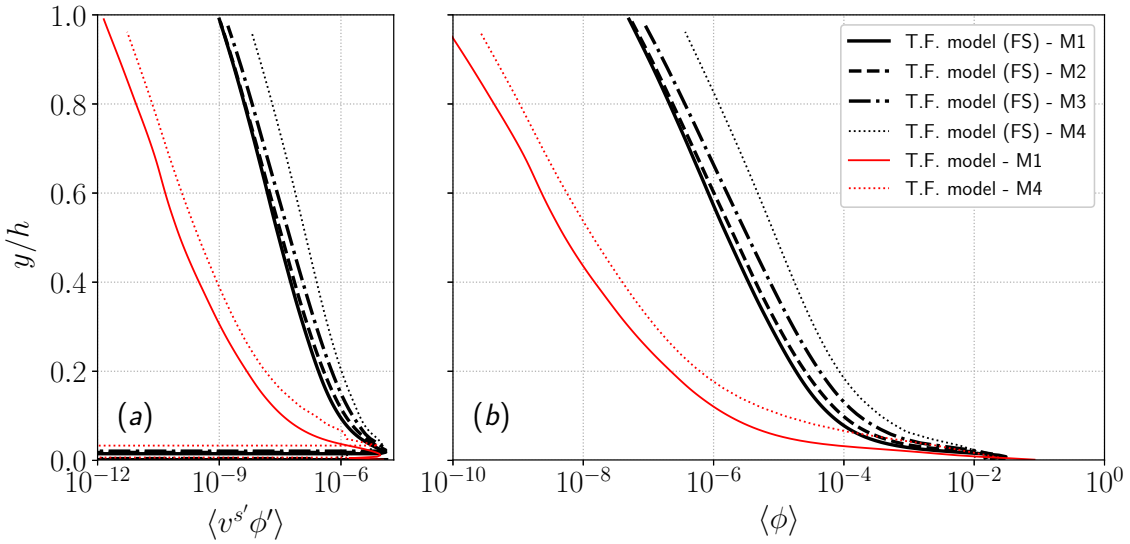


*Figure 5.15: Averaged Reynolds flux (panel (a)) and solid phase volumetric concentration (panel(b)) profiles from two-phase flow simulations with finite-size correction model (T.F. model (FS)) from configuration GB using mesh M1, M2, M3 and M4 and without finite-size correction model (T.F. model) using mesh M1 and M4.*

sediment concentration profile prediction. The mesh characteristics for the different simulations are presented in table 5.3. The comparison between Reynolds fluxes and concentration profiles with and without finite-size correction obtained with mesh M1, M2, M3 and M4 are presented in figure 5.15.

The turbulent dispersion of the particles increases for coarser resolution (figure 5.15a). As a consequence, the amount of suspended particles in the water column predicted by the two-fluid model increases with increasing filter width (figure 5.15b). The difference between the concentration profiles from simulations using the finite-size correction model with $\breve{\Delta} = 2d_p$ (mesh M1) and $\breve{\Delta} = 3d_p$ (mesh M2) is negligible and the agreement can still be considered as acceptable for a filter width of $\breve{\Delta} = 4d_p$ (mesh M3). However, discrepancies become important for larger filter width ($\breve{\Delta} = 8d_p$ with mesh M4). More quantitatively, the concentration profile converges at first order with the reference simulation results from mesh M1 for increasing vertical resolution.

Even without finite-size correction model, the Reynolds flux is increased between simulations using mesh M1 and mesh M4 (figure 5.15a) suggesting that the over-prediction of the concentration does come from the finite-size correction model only but also from the modification of the flow hydrodynamic for coarser grid resolutions.

As a conclusion, in order to accurately predict the concentration profile, the sensitivity analysis suggests that the grid resolution at the wall should not exceed 4 wall units $\Delta_y^+ < 4$. It is mandatory to have at least one grid point in the laminar sub-layer in order to resolve the turbulent coherent flow structures in the near wall region and to use a second filter smaller than $8d_p$ ($\breve{\Delta} < 8d_p$) to accurately resolve the fluid velocity "seen" by the particles.

## 5.5 Conclusion

In this chapter, the two-fluid LES method has been tested against experimental data and a finite-size correction model has been developed. The new model has been validated against avail-

able experimental data for the dilute turbulent suspension of finite-sized particles transported by a boundary layer flow. The improved model has been shown to accurately predict the suspended particle concentration profile as well as the existence of a streamwise lag velocity for heavier-than-fluid particles without the use of any tuning parameter to fit the experimental data. In the proposed correction model, a distinction is made between turbulent flow scales larger or smaller than the particle diameter. The velocity field "seen" by the particles in the drag law is filtered at a scale $\breve{\Delta} \geq 2d_p$ and smaller turbulent scales contribute to reduce the particle response time by the addition of a sub-particle scale eddy viscosity to the molecular viscosity in the particle Reynolds number definition. The second effect of the correction is to increase the production of granular temperature by a modification of the source term in the granular temperature equation. While modification of the drag law is more important for the accurate prediction of the suspended particle concentration profile in the dilute configuration investigated herein, the modification of the granular temperature equation is mandatory for the physical consistency and the numerical stability of the model. At last, the sensitivity analysis of the model results for the second filter size $\breve{\Delta}$ has shown that the grid resolution could be as high as 4 particle diameters without loss of accuracy as long as one grid point is located in the laminar sub-layer.

# Conclusion

In this thesis, sedFoam, a turbulence-resolving two-fluid model for sediment transport applications is developed and applied to oscillatory sheet flow configurations and unidirectional boundary layer flow with finite-size particles at low volume fraction.

In the model presented in chapter 2, both phases are seen as inter-penetrating continua. Fluid-particle interactions are modeled using volume-averaged formulation of the drag, lift and added mass forces. Granular stresses are modeled using the kinetic theory of granular flows [18]. The Eulerian equations of the two-fluid model are filtered to perform large-eddy simulations. The effect of unresolved sub-grid turbulent flow scales are taken into account using the dynamic Lagrangian sub-grid model from Meneveau *et al.* (1996) [72]. The model is validated using numerical and experimental data of two boundary layer flows: one unidirectional and one oscillatory.

## Unsteady effects in oscillatory sheet flow

In chapter 3, the turbulence-resolving two-fluid model sedFoam accurately reproduced oscillatory sheet flow configurations involving fine and medium sand under a symmetrical flow forcing from O'Donoghue & Wright (2004a) [81]. Quantitative predictions of concentration profiles were obtained demonstrating the predictive capabilities of the two-fluid LES model. Furthermore, two-phase flow simulations highlighted the difference of behavior that exists between oscillatory sheet flow involving medium and fine sand due to unsteady effects. Whereas turbulence-averaged models require an almost systematic tuning of empirical coefficient to model turbulence-particle interactions, the turbulence-resolving two-fluid model explicitly resolves them. The main conclusions of this chapter are:

- For medium sand, the evolution of the concentration profile shows a clockwise (resp. anti-clockwise) rotation of the concentration profile during flow acceleration (resp. deceleration) around a "pivot" of constant concentration following the classical description proposed by O'Donoghue & Wright (2004a) [81]. From a mass balance between downward settling and upward Reynolds sediment fluxes, this behavior is the result of the presence at the same location of the maximum vertical net sediment flux and the concentration profile inflexion point. The sheet flow layer characteristics such as the thickness, the erosion depth and the streamwise sand flux are in phase with the freestream velocity. The sediment bed response is relatively quick compared with the wave period and the evolution of the sheet flow layer can be considered quasi-steady.

- Sediments settle too quickly to the bed during flow deceleration leading to sharper concentration profile in the near bed region compared with the measurements. For larger particles, more complex turbulence-particle interaction regimes susceptible to affect the vertical distribution of sediment such as finite-size effects may become dominant.

- For fine sand, the presence of unsteady effects induced by the smaller particle settling velocity completely modifies the behavior of the flow compared with medium sand. As a consequence of the greater number of particles transported through the wave period, the inertia of the sheet flow layer increases, the bed response is no longer in phase with the free

stream velocity and turbulence is strongly attenuated by stable density stratification. The flow becomes almost laminar at flow reversal resulting in vanishing Reynolds fluxes and settling dominated vertical net flux. As a consequence of the nonlinear behavior of the mass conservation equation, a concentration plateau forms around flow reversal (formation of a shock). Time evolution of the concentration can no longer be represented by the classical description provided by O'Donoghue & Wright (2004a) [81] using a power law.

- Unsteady effects are the result of a chain of causes and consequences including shear instabilities and high Reynolds stress of the solid phase increasing vertical mixing of the sediment, increased boundary layer inertia, stable stratification leading to turbulence damping, and hindered settling of particles. An equilibrium between all these mechanisms is established during the wave period that controls the vertical sediment mass balance and the observed phase-lag effects.

- The mean settling velocity can be well reproduced using empirical formulation taking into account hindered settling. Therefore, to accurately predict the competition between settling and Reynolds fluxes, future research should be focused on an accurate modeling of solid phase Reynolds stresses and the vertical drift velocity.

## Wave shape effects

In chapter 4, the effect of wave shape and particle size was investigated using the two-fluid LES model sedFoam by reproducing four experimental configurations involving fine and medium sand under velocity and acceleration skewed flow forcing from O'Donoghue & Wright (2004a) [81] and van Der A *et al.* (2010) [112] respectively. The main conclusions of the chapter are:

- The mechanisms responsible for the generation of the net transport rate under non-sinusoidal waves are reproduced by the turbulence-resolving two-fluid model. Especially, the larger net transport rate for fine sand under acceleration skewed waves and negative sediment rate for fine sand under velocity skewed waves, consequences of phase-lag effects, are accurately predicted by the two-phase flow model.

- Unsteady effects highlighted in chapter 3 are also present in the configurations investigated in this chapter. Larger sheet flow layer thickness, turbulence modulation by the particles and increased vertical mixing of particles due to bed instabilities are observed for configurations involving fine sand but not for medium sand.

- As a consequence of phase-lag, the sediment flux for configurations involving fine sand can not be parameterized by the instantaneous Shields parameter. In the absence of phase-lag effects, for configurations involving medium sand, streamwise sediment flux is fully correlated with the time series of the Shields number.

- Because of unsteady effects, the onshore and offshore transport rate can not be related to the corresponding representative Shields number using a power law with the same parameterization for configurations involving fine and medium sand. Fine sand exhibits higher transport rates than medium sand, uncorrelated with the Shields number.

- The dimensionless maximum sheet flow layer thickness, used to determine the phase-lag contributions in the sand transport formula, is not accurately predicted by the scaling law proposed by Dohmen-Janssen *et al.* (2001) [29] for configurations involving fine sand.

- More physically based modeling of phase-lag effects based on the mass balance between Reynolds upward flux and downward settling flux should help improve predictions of the decomposition of the sediment loads between wave crest and wave trough. Indeed, the imprint of phase-lag effects are clearly visible on the competition between turbulent suspension of particles and their settling. However, additional configurations involving different grain sizes, flow periods and asymmetry/skewness factors and provide more quantitative results for configurations involving medium sand are necessary to start developing new scaling laws.

## Finite size correction model

In chapter 5, the two-fluid LES method was tested against experimental data for an unidirectional boundary layer flow with finite-size particles and a finite-size correction model was developed. The main conclusion of the chapter are:

- Without finite-size correction model, the suspension of particles is greatly under-estimated by the two-fluid LES model for configurations having a suspension number $v^s/u_\tau \sim \mathcal{O}(1)$. The drag force is dominant and numerical results are not sensitive to the other interaction forces.

- The implementation of a correction model, taking into account finite-size effects in the coupling between the fluid and solid phases, significantly improved the predictive capabilities of the two-fluid model without the use of any tuning parameter to fit experimental data in three different configurations.

- In the proposed correction model, a distinction is made between turbulent flow scales larger or smaller than the particle diameter. The velocity field "seen" by the particles in the drag law is filtered at a scale $\breve{\Delta} \geq 2d_p$ and smaller turbulent scales contribute to reduce the particle response time by the addition of a sub-particle scale eddy viscosity to the molecular viscosity in the particle Reynolds number definition. The second effect of the correction is to increase the production of granular temperature by a modification of the source term in the granular temperature equation.

- In dilute conditions, the effect of the drag law modification is dominant compared with the modification of the granular temperature. However, from our experience, this modification is mandatory for physical consistency and numerical stability of the model.

- Model results are not very sensitive to the grid resolution as long as the condition that the filter size is smaller than four times the particle diameter ($\breve{\Delta} \leq 4d_p$) is respected and that one grid point is located in the laminar sub-layer near the wall.

The Eulerian model has a very high potential considering its predictive capabilities, the significant insight that it provides into turbulent mechanisms occurring in the transport layer and its capacity to avoid the limitations in term of number of particles compared with Lagrangian modeling methodologies.

This work represents one of the first steps toward exploiting the full capabilities of the two-fluid LES model sedFoam for sediment transport applications. It opens the way to investigate many scientific topics related to sediment transport in the coastal, estuarine or river environments. Some of these perspectives are presented in the next section.

# Perspectives

Recent development of the two-fluid model for sediment transport applications should help provide answers to scientific questions for which experiments, turbulence-averaged and Lagrangian modeling methodologies are not appropriate or not the best option. Two main perspectives related to the two-fluid model are detailed in the next sections. The first one, more fundamental, deals with the improvement of the finite-size correction model. The second one, more applied, is related to the parameterization of a practical sand transport formula.

## Extended finite-size correction model

In a prospect of providing more physically based parameterization for turbulence-averaged and larger-scale models, the turbulence-resolving two-fluid model should be applied to a wide range of flow and particle parameters. However, given the great diversity of turbulence-particle interaction regimes present in sediment transport conditions typical of the coastal and river environments, the two-fluid model and especially the finite size correction model should be further improved to extend its range of applicability to larger size ratios $d_p/\eta$.

Indeed, using the finite size correction model introduced in chapter 5 for oscillatory sheet flow configurations of chapters 3 and 4 and unidirectional sheet flow configuration from Revil-Baudard *et al.* (2015) [88] investigated by Cheng *et al.* (2018) [23] resulted in a over-estimation of the particle suspension.

In configurations investigated in chapter 5, Stokes number is on the order of unity. As a consequence, the length scale associated with turbulent eddies having the same timescale as the particle $l^*$ is of the order of the Kolmogorov length scale $\eta$ justifying taking into account the effect of the full range of the turbulent flow scales below the particle diameter in the coupling between the fluid and solid phase. However, more inertial particles act as a temporal filter of the turbulent spectrum. In that case, $l^* > \eta$ and taking into account the effect of turbulent flow scales between $l^*$ and $\eta$ has for effect to overestimate the effective viscosity in the finite-size correction model and turbulent suspension of particles.

In this section, the development of an extended finite-size correction model for inertial particles is proposed. This improvement is still at the early stage of development and should be regarded as a possible way to include the Stokes number dependency in the finite size correction model.

Contrary to the finite-size correction model presented in chapter 5, the definition of the effective viscosity in the momentum coupling and the sub-particle TKE in the granular temperature transport equation should only include the effect of turbulent flow scales between $l^*$ and $\eta$. The effective viscosity is now function of the dissipation rate of TKE between scales $d_p$ and $l^*$ $\varepsilon_{d_p-l^*}$. Making the assumption that $d_p$ and $l^*$ are in the inertial range of turbulence, following Kolmogorov's theory, $\varepsilon_{d_p-l^*}$ can be calculated by integrating the dissipation rate of TKE spectrum between $d_p$ and $l^*$ following:

$$\begin{aligned}\varepsilon_{d_p-l^*} &= 2\nu^f \int_{\frac{2\pi}{d_p}}^{\frac{2\pi}{l^*}} (K^f)^2 E(K^f) dK^f \\ &= \frac{2}{3} C_k \nu^f \langle\varepsilon\rangle^{\frac{2}{3}} (2\pi)^{\frac{4}{3}} \left[ l^{*-\frac{4}{3}} - d_p^{\frac{4}{3}} \right]\end{aligned} \tag{5.13}$$

with $E(K^f) = (K^f)^{-4/3}$ the expression of the TKE spectrum in the inertial range of turbulence, $C_k = 0.5$ an empirical constant. Similarly, sub-particle TKE between $d_p$ and $l^*$ is obtained by integrating the TKE spectrum as follows:

$$\begin{aligned} k^f_{d_p-l^*} &= \int_{\frac{2\pi}{d_p}}^{\frac{2\pi}{l^*}} E(K^f) dK^f \\ &= \frac{3}{2} C_k \langle \varepsilon \rangle^{\frac{2}{3}} (2\pi)^{-\frac{2}{3}} \left[ d_p^{\frac{2}{3}} - l^{*\frac{2}{3}} \right]. \end{aligned} \tag{5.14}$$

Eventually, the expression of the effective viscosity and sub-particle TKE are given by:

$$\nu^t_{d_p-l^*} = min\left(\varepsilon^{1/3}_{d_p-l^*} d_p^{4/3}, \quad \nu^t_p\right), \quad k^f_{d_p-l^*} = min\left(\frac{3}{2} C_k \langle \varepsilon \rangle^{\frac{2}{3}} (2\pi)^{-\frac{2}{3}} \left[ d_p^{\frac{2}{3}} - l^{*\frac{2}{3}} \right], \quad \breve{k}^f + k^f\right) \tag{5.15a,b}$$

taking the minimum between the values calculated using new version and the values calculated using the previous version presented in chapter 5. Indeed, values calculated using the new version can not be larger than the values calculated using the previous finite-size correction model given that it already includes the effect of the full the turbulent spectrum between $d_p$ and $\eta$.

To assess the extended finite-size correction model, a configuration involving large plastic particles taken from new experiments carried out during the Ph.D thesis of Hélder Guta in the LEGI tilting flume [49, 50] are reproduced numerically using the TF model. Particles having a mean diameter $d_p = 3mm$, and density $\rho^s = 1192$ ($v_s = 0.056m.s^{-1}$) are transported by an unidirectional flow having a bulk velocity $U_b = 0.75m.s^{-1}$, water depth $h = 0.1m$ and bottom friction velocity $u_\tau = 0.042m.s^{-1}$. Such particles and flow conditions yields $d_p/\eta \approx 120$, $St \approx 160$ and $v_s/u_\tau = 1.3$.

Similarly to configurations investigated in chapter 5, volume fractions is very low ($\phi_{tot} = 3 \times 10^{-3}$) to isolate the effect of turbulence-particle interactions and avoid interactions with a deposited bed. However, unlike in previous configurations, the bottom is composed of roughness elements having the same size as the particles.

To take into account bottom roughness in LES, a canopy model presented in appendix F is developed and tested against clear water configurations carried out in the same flume. This model allows to recover mean flow and second order turbulent statistical features typical of rough boundary layer flows.

Given the large channel dimensions, the resolution of the numerical domain is coarser compared with previous configurations. Nevertheless, high numerical resolution is not yet an objective considering that simulations are performed for first evaluation of a model under development. Furthermore, in rough boundary layers, the near wall resolution constraint can be relaxed given that the laminar sub-layer is no longer present and does not need to be resolved. For the numerical configuration presented in this section, the dimensionless cell size in the streamwise and spanwise directions are $\Delta x^+ \approx 240$ and $\Delta z^+ \approx 200$. Cells in the wall normal directions are non-uniform with a first cell size $\Delta y^+ \approx 30$.

Averaged concentration profiles from simulations with the TF model using the finite size correction presented in chapter 5, extended finite size correction and no correction are compared with the experimental profile in figure 3.

As for configurations presented in chapter 5, the absence of finite-size correction leads to a great under-estimation of particle suspension. However, as experienced in unidirectional and oscillatory sheet flow configurations, using the original finite-size correction model greatly over-estimate particle suspension. The concentration profile is almost vertical across the water depth justifying the inclusion of a Stokes number dependency. The early development of the extended finite-size correction model is extremely promising given the significant improvement of the model predictions without the use of tuning coefficients. However, particle suspension is still slightly over-estimated especially in the outer region.

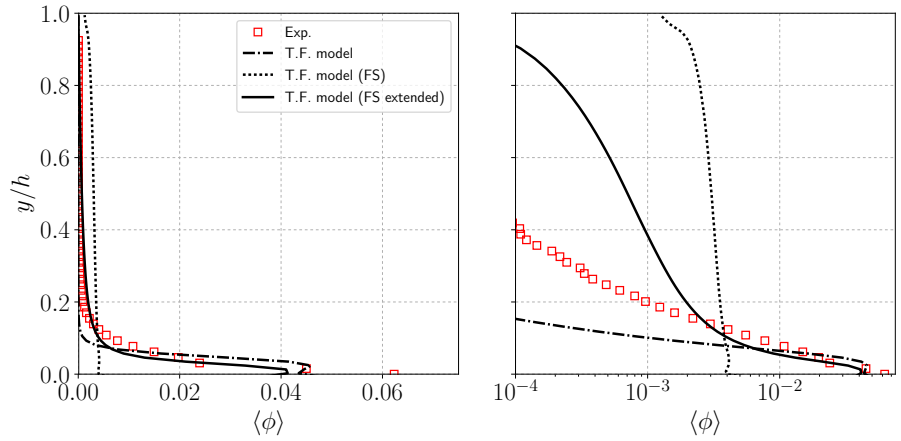


*Figure 3: Average concentration profiles from experiments (Exp.) and two-phase flow simulations without finite size correction (T.F. model), with the original finite-size correction model (T.F. model (FS)) and with the extended finite size correction model (T.F. model (FS extended)) using conventional axis scaling in the left panel and in semi-log scaling in the right panel.*

Considering the strong assumptions made to derive the model, the coarse mesh resolution and the difficulty to represent rough boundary layer features in the LES framework, we believe that the quality of the simulation results using the TF model together with the extended finite-size correction is very good.

We believe that this vision on the inclusion of turbulence-particle interactions into the momentum coupling between the two phases represent a great opportunity to extend the range of applicability of the TF model. However, additional development are required to further improve the model predictions to be able to apply it to more complex configurations involving a greater volume fraction and larger range of particle and flow parameters.

An accurate prediction of the concentration profiles using the finite-size correction model should help providing more physically-based parameterization for the vertical turbulent diffusion of particles. As pointed out in chapter 5, the value of the Schmidt number $S_c$ representing the efficiency of sediment mass diffusion relative to the turbulent momentum diffusion or eddy viscosity is highly debated [65]. The most widely accepted model is the one from van Rijn (1984) [117] relating the turbulent Schmidt number to the suspension number as follows: $S_c = (1+2(v_s/u_\tau)^2)^{-1}$. Nevertheless, a lot of scatter is observed on existing experimental data and no satisfactory explanation exists to support van Rijn's empirical formula [65].

From two-phase flow simulations, detailed information on the concentration profiles, turbulent statistics ($\nu_t^f$) and Reynolds fluxes can be obtained to study the relative mass and momentum diffusion processes in particle-laden boundary layer flows. Covering a large number of flow and particle parameters should help improving $S_c$ predictions by proposing more physically based relationships.

Furthermore, as observed in chapters 3 and 4, the presence of particles can significantly damp the fluid turbulence. Accurately modeling the momentum exchange between the two phases offers the opportunity to investigate energy transfers between the fluid and the solid phase and between resolved and unresolved scales of the flow based on the two-phase energy balance equations (see figure 2.1).

The complete set of balance equations for the total and turbulent kinetic energy in term of filtered and unfiltered flow variables are presented for the fluid phase in appendix B. The same methodology can be followed to derive balance equations for the solid phase total and turbulent kinetic energy.

Considering the great importance of energy transfers between both phases, having an energy-

based approach with a turbulence-resolving two-phase flow model should help improving the coupling between fluid and solid phases in turbulence models and in particle phase stress models.

## Comparison between simulation results and a practical sand transport formula

Results presented in chapter 4 showed that high resolution simulations using the two-fluid model are a powerful tool to investigate the relationships between sand transport and hydrodynamic conditions in oscillatory sheet flow. In the future, two-phase flow simulation results should help providing more physically based relationships between the net transport rate and a given wave condition in practical sand transport formulas.

One of the most accurate and advanced modeling approach to model the net sediment flux under velocity and acceleration skewed waves is the practical sand transport formula from van Der A *et al.* (2013) [114]. This approach is based on the semi-unsteady half-cycle concept introduced by Dibajnia and Watanabe (1992) [26]. The net sediment flux is calculated based on the difference between the onshore transport rate generated during wave crest and offshore transport rate generated during wave trough. Contributions due to phase-lag are taken into account by calculating the amount of sediment entrained during the previous wave phase and transported during the current wave phase. More details on the sand transport formula are proposed in appendix E.

In the next sections, we discuss the scaling and empirical relations used to compute the net sediment flux based on the two-phase flow simulations. The accuracy of the model relies on a good prediction of the duration of the wave crest and wave trough $T_c$ and $T_t$, the representative Shields numbers during the wave crest and the wave trough $\theta_c$ and $\theta_t$, the corresponding sediment loads $\Omega_c^*$ and $\Omega_t^*$ and their distribution over wave crest and trough using the phase-lag parameters $P_c$ and $P_t$. All these modeling aspects are investigated in the following sections.

### Duration of the wave phases

In the formula from van Der A *et al.* (2013) [114], the respective durations of wave crest and wave trough are calculated using the time series of the free stream velocity. However, the corresponding durations of onshore and offshore flow velocities inside the boundary layer can be different. In the numerical simulations, the effective durations of wave crest and trough is retrieved from durations of positive (onshore) and negative (offshore) sediment fluxes $T_+$ and $T_-$.

The ratio between durations of wave crest and wave trough determined from time series of freestream velocity and effective durations of wave crest and trough from positive/negative sediment fluxes are presented in figure 4. For all configurations, duration of wave crest determined from free stream velocity is greater than the effective duration of positive sediment flux. Symmetrically, duration of wave trough is smaller.

For velocity skewed waves (configurations M5010 and F5010), the effect of velocity asymmetry is increased inside the boundary layer with $T_+/T_- < T_c/T_t$. Furthermore, flow asymmetry is even greater for configurations F5010 for which phase-lag has a significant effect.

More strikingly, for configurations S706015m and S706015f, even if there is no velocity asymmetry in the flow forcing, the effective duration of wave crest and wave trough are not equal. From experimental observations of flow hydrodynamics under skewed waves by van Der A *et al.* (2011) [113], onshore/offshore flow reversal occurs sooner towards the bottom leading to a smaller ratio of onshore/offshore wave phase duration. As a consequence, the effective flow asymmetry is greater for configuration S706015m for which the transport layer is very thin close to the bed in comparison with the thicker transport layer from configuration S706015f.

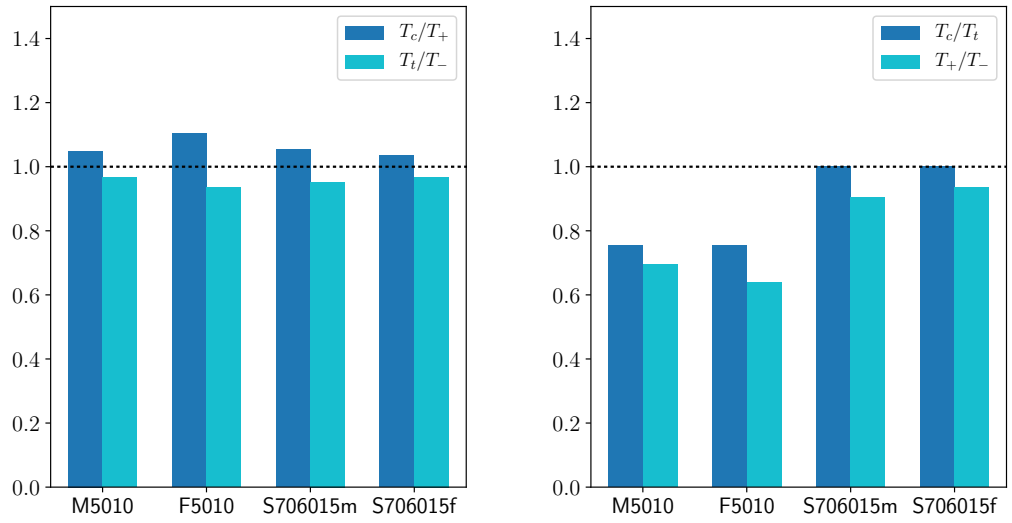


*Figure 4: Ratio between duration of wave phases determined from time series of freestream velocity and effective durations from positive/negative sediment fluxes $T_c/T_+$ and $T_t/T_-$ (left panel) and $T_c/T_t$ and $T_+/T_-$ (right panel) for configurations M5010, F5010, S706015m and S706015f.*

There is a significant difference between flow asymmetry far from the bed and inside the bottom boundary layer. To a smaller extent, as the flow asymmetry is not constant in the wall normal direction, the effective flow asymmetry is function of the sheet flow layer thickness. Asymmetry is increased for larger sheet flow layer thickness subject to a velocity skewed flow forcing and decreased for larger sheet flow layer thickness subject to an acceleration skewed flow forcing.

### Shields number determination

In the model proposed by van Der A *et al.* (2013) [114], the representative Shields number during wave crest and wave trough are calculated as a function of the representative velocities during the corresponding wave phase $u^f_{c,r} = \frac{\sqrt{2}}{2}U^f_m$ and $u^f_{t,r} = \frac{\sqrt{2}}{2}u^f_m$ following:

$$\theta_c = \frac{\frac{1}{2}f_c|u^f_{c,r}|^2}{(s-1)gd_p}, \quad \theta_t = \frac{\frac{1}{2}f_t|u^f_{t,r}|^2}{(s-1)gd_p} \tag{5.16a,b}$$

with $f_c$ and $f_t$ the friction factor during wave crest and wave trough respectively.

Following van Der A *et al.* (2013) [114], the friction factor for phase $\alpha$ is calculated based on Swart (1974) [110] modified by Silva *et al.* (2006) [106] to include acceleration effects yielding:

$$f_\alpha = \begin{cases} 0.00251exp\left(5.21\left[\left(\frac{2T_{\alpha u}}{T_\alpha}\right)^{2.6}\frac{a_r}{k_s}\right]^{-0.19}\right), & \frac{a_r}{k_s} > 1.587 \\ 0.3, & \frac{a_r}{k_s} \leq 1.587 \end{cases} \tag{5.17}$$

with $k_s$ the bed roughness and $a_r = u^f_r T/2\pi$ the representative excursion length function of the representative orbital velocity amplitude defined as:

$$u^f_r = \sqrt{\frac{2}{T}\int_0^T u^f_\infty(t)^2 dt}. \tag{5.18}$$

The bed roughness $k_s$ is calculated based on Ribberink (1998) [91]:

$$k_s = max\Big(d_p, \quad d_p\big[\mu + 6(\theta_{av} - 1)\big]\Big) \tag{5.19}$$

with $\mu$ a coefficient taking into account the increased bed roughness for increased sheet flow layer thickness for fine sand ($\mu = 6$ for fine sand and $\mu = 1$ for medium sand) and $\theta_{av}$ the wave-averaged Shields number calculated as

$$\theta_{av} = \frac{\frac{1}{4} f_w u_r^{f2}}{(s-1) g d_p}. \tag{5.20}$$

with $f_w$ the wave friction factor given by the expression

$$f_w = \begin{cases} 0.00251 exp\left[5.21 \left(\frac{a_r}{k_s}\right)^{-0.19}\right], & \frac{a_r}{k_s} > 1.587 \\ 0.3, & \frac{a_r}{k_s} \leq 1.587 \end{cases}. \tag{5.21}$$

Considering that the expression of the wave averaged Shields number is also function of $k_s$, it is calculated iteratively.

| Configuration | $\theta_c$ | $\theta_+$ | $\theta_t$ | $\theta_-$ |
|---|---|---|---|---|
| $M5010$ | 0.93 | 1.11 | 0.32 | 0.45 |
| $F5010$ | 2.68 | 2.31 | 0.93 | 0.95 |
| $S706015m$ | 0.78 | 0.71 | 0.59 | 0.59 |
| $S706015f$ | 2.40 | 1.19 | 1.59 | 1.03 |

*Table 2: Representative Shields numbers calculated using the methodology proposed in van Der A et al. (2013) [114] and from two-phase flow simulations for configurations M5010, F5010, S706015m and S706015f.*

Representative Shields numbers calculated using the methodology proposed by van Der A *et al.* (2013) [114] and from two-phase flow simulations using expression 4.5 are listed in table 2 and compared in figure 5. In the left panel of figure 5, the ratio between representative Shields numbers $\theta_c/\theta_+$ and $\theta_t/\theta_-$ are represented for configurations M5010, F5010, S706015m and S706015f. For configuration M5010, the representative Shields number ratios for wave crest and trough are both below unity. For this configuration, the empirical determination of the Shields number leads to a slight under-estimation compared with the predictions made with the two-fluid model. For configurations F5010 and S706015m, Shields number predictions using the two-fluid model and empirical relation are very close. However, for configuration S706015f, differences between the empirical relation and the two-fluid model are more important with a factor two.

In the right panel of figure 5, ratios between representative Shields numbers during wave crest and wave trough $\theta_c/\theta_t$ and $\theta_+/\theta_-$ are presented. As expected, for velocity skewed waves (configurations M5010 and F5010), the Shields number during wave crest is much larger, by a factor 2.5, than during wave trough because of largest onshore near bed velocities. From the empirical relation, the ratio between onshore and offshore representative Shields number is independent of the particle size. For acceleration skewed waves, strongest acceleration generates larger bed shear stress resulting in larger Shields numbers during wave crest. The same dynamics is observed for all configurations but with greater ratios from the empirical predictions compared with numerical results.

### Sediment load calculation

The accurate prediction of the sediment loads $\Omega^*_{cc}$, $\Omega^*_{tt}$, $\Omega^*_{ct}$ and $\Omega^*_{tc}$ relies on the representation of the sediment load $\omega^*_\alpha$ by a power law and an accurate decomposition between sediment extracted during one half wave phase and transported during the other. As presented in chapter 4, for

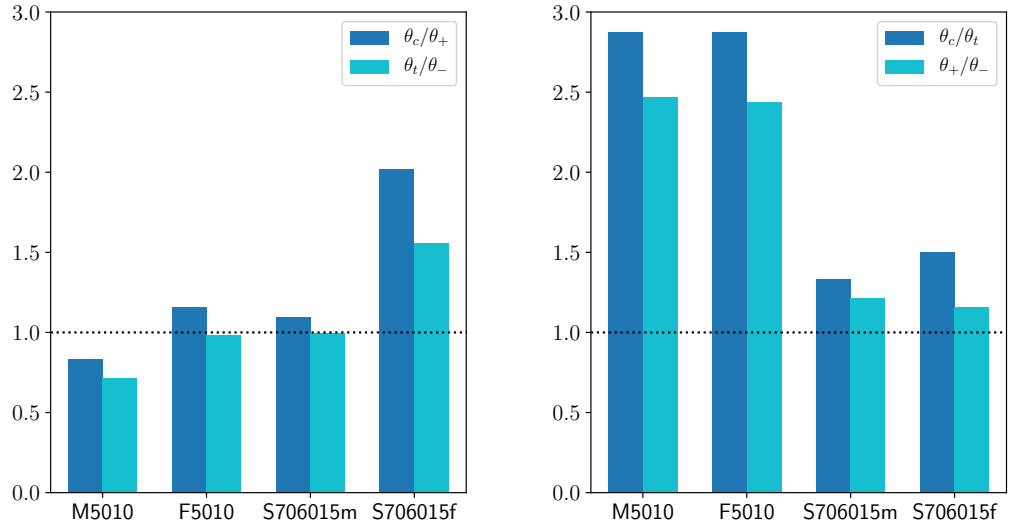


*Figure 5: Ratio between representative Shields numbers during wave crest and wave trough determined from the methodology proposed in van Der A et al. (2013) [114] and from two-phase flow simulations $\theta_c/\theta_+$ and $\theta_t/\theta_-$ (left panel) and $\theta_c/\theta_t$ and $\theta_+/\theta_-$ (right panel) for configurations M5010, F5010, S706015m and S706015f.*

medium sand, the dimensionless transport rate is well represented by a power law of the excess Shields number. Considering that, in the sheet flow regime, $\theta_\alpha \gg \theta_{cr}$, the sediment load defined as the transport rate divided by the square root of the representative Shields number should also be well represented by a power law.

Nevertheless, from the results presented in chapter 4, the presence of unsteady effects play an important role in streamwise sediment transport. As a consequence, the dimensionless transport rate can not be related to the excess Shields number using the same parameterization between fine and medium sand. However, in van Der A *et al.* (2013) [114], the same power law is used to determine the sediment loads for fine and medium sand.

### Phase-lag contribution

In the practical sand transport formula from van Der A *et al.* (2013) [114], phase-lag is taken into account through a redistribution of the sediment load extracted during a given wave phase between the current and the next wave phase following equations (E.4)-(E.7). The parameters controlling this re-distributions are the phase-lag parameters $P_c$ and $P_t$ function of the particle fall velocity $v_s$ and the dimensionless sheet flow layer thickness. As observed in figure 4.17, the dimensionless sheet flow layer thickness as a function of the maximum Shields number shows a significant scatter for configurations involving fine sand and can not be parameterized using the relation proposed by Dohmen-Janssen *et al.* (2001) [29]. As a consequence, the redistribution of the sediment loads during wave crest and wave trough based on the determination of the maximum sheet flow layer thickness to take into account phase-lag effects is not accurate.

In order to provide better parameterizations and more physically-based scaling laws for practical sand transport formulas as suggested in section 4.4.2, additional configurations should be investigated to cover a wider range of flow and particle parameters. Furthermore, finite-size effects should be carefully integrated to obtain quantitative results for configurations involving medium sand.

# Bibliography


[1] K. Agrawal, P. N. Loezos, M. Syamlal, and S. Sundaresan. The role of meso-scale structures in rapid gas-solid flows. *Journal of Fluid Mechanics*, 445:151–185, 2001.

[2] L. Amoudry, T.-J. Hsu, and P. L.-F. Liu. Two-phase model for sand transport in sheet flow regime. *Journal of Geophysical Research: Oceans*, 113(C3):1–15, 2008.

[3] L. O. Amoudry. Assessing sediment stress closures in two-phase sheet flow models. *Advances in Water Resources*, 48:92–101, 2012.

[4] L. O. Amoudry. Extension of k- turbulence closure to two-phase sediment transport modelling: Application to oscillatory sheet flows. *Advances in Water Resources*, 72:110–121, 2014.

[5] M. N. Ardekani and L. Brandt. Turbulence modulation in channel flow of finite-size spheroidal particles. *Journal of Fluid Mechanics*, 859:887–901, 2019.

[6] M. N. Ardekani, P. Costa, W.-P. Breugem, F. Picano, and L. Brandt. Drag reduction in turbulent channel flow laden with finite-size oblate spheroids. *Journal of Fluid Mechanics*, 816:43–70, 2017.

[7] S. K. Arolla and O. Desjardins. Transport modeling of sedimenting particles in a turbulent pipe flow using euler–lagrange large eddy simulation. *International Journal of Multiphase Flow*, 75:1–11, 2015.

[8] S. Arshad, E. Gonzalez-Juez, A. Dasgupta, S. Menon, and M. Oevermann. Subgrid reaction-diffusion closure for large eddy simulations using the linear-eddy model. *Flow, Turbulence and Combustion*, 04 2019.

[9] S. Balachandar. A scaling analysis for point-particle approaches to turbulent multiphase flows. *International Journal of Multiphase Flow*, 35:801–810, 2009.

[10] D. Berzi and L. Fraccarollo. Intense sediment transport: Collisional to turbulent suspension. *Physics of Fluids*, 28(2):023302, 2016.

[11] W.-P. Breugem. A second-order accurate immersed boundary method for fully resolved simulations of particle-laden flows. *Journal of Computational Physics*, 231(13):4469–4498, 2012.

[12] M. Bustos and F. Concha. On the construction of global weak solutions in the kynch theory of sedimentation. *Mathematical Methods in the Applied Sciences*, 10:245 – 264, 1988.

[13] M. Bustos and F. Concha. Settling velocities of particulate systems: 10. a numerical method for solving kynch sedimentation processes. *International Journal of Mineral Processing*, 57(3):185–203, 1999.

[14] R. Bürger and E. Tory. On upper rarefaction waves in batch settling. *Powder Technology*, 108(1):74–87, 2000.

[15] E. Calzavarini, R. Volk, M. Bourgoin, E. Lévêque, J.-F. Pinton, and F. Toschi. Acceleration statistics of finite-sized particles in turbulent flow: the role of faxén forces. *Journal of Fluid Mechanics*, 630:179–189, 2009.

[16] M. I. Cantero, S. Balachandar, A. Cantelli, C. Pirmez, and G. Parker. Turbidity current with a roof: Direct numerical simulation of self-stratified turbulent channel flow driven by suspended sediment. *Journal of Geophysical Research: Oceans*, 114(C3):C03008, 2009.

[17] N. F. Carnahan and K. E. Starling. Equation of state for nonattracting rigid spheres. *The Journal of Chemical Physics*, 51(2):635–636, 1969.

[18] R. Chassagne, J. Chauchat, and C. Bonamy. A modified kinetic theory for frictional-collisional bedload transport valid from dense to dilute regime. *Submitted to Physical Review Fluids*, 2021.

[19] A. Chatzimichailidis, C. Argyropoulos, M. Assael, and K. Kakosimos. Qualitative and quantitative investigation of multiple large eddy simulation aspects for pollutant dispersion in street canyons using openfoam. *Atmosphere*, 10:17, 01 2019.

[20] J. Chauchat, Z. Cheng, T. Nagel, C. Bonamy, and T.-J. Hsu. Sedfoam-2.0: a 3-d two-phase flow numerical model for sediment transport. *Geoscientific Model Development*, 10(12):4367–4392, 2017.

[21] Z. Cheng. *A multi-dimensional two-phase flow modeling Framework for sediment transport applications*. PhD thesis, University of Delaware, 2016.

[22] Z. Cheng, T.-J. Hsu, and J. Calantoni. Sedfoam: A multi-dimensional eulerian two-phase model for sediment transport and its application to momentary bed failure. *Coastal Engineering*, 119:32 – 50, 2017.

[23] Z. Cheng, T.-J. Hsu, and J. Chauchat. An eulerian two-phase model for steady sheet flow using large-eddy simulation methodology. *Advances in Water Resources*, 111:205 – 223, 2018.

[24] Z. Cheng, X. Yu, T.-J. Hsu, C. E. Ozdemir, and S. Balachandar. On the transport modes of fine sediment in the wave boundary layer due to resuspension/deposition: A turbulence-resolving numerical investigation. *Journal of Geophysical Research: Oceans*, 120(3):1918–1936, 2015.

[25] E. De Villiers. *The Potential of Large Eddy Simulation for the Modeling of Wall Bounded Flows Eugene de Villiers*. PhD thesis, Imperial College, 2006.

[26] M. Dibajnia and A. Watanabe. *Sheet Flow Under Nonlinear Waves and Currents*, chapter 155, pages 2015–2028.

[27] J. Ding and D. Gidaspow. A bubbling fluidization model using kinetic theory of granular flow. *AIChE Journal*, 36(4):523–538, 1990.

[28] C. M. Dohmen-Janssen and D. M. Hanes. Sheet flow dynamics under monochromatic nonbreaking waves. *Journal of Geophysical Research: Oceans*, 107(C10):13–1–13–21, 2002.

[29] C. M. Dohmen-Janssen, W. N. Hassan, and J. S. Ribberink. Mobile-bed effects in oscillatory sheet flow. *Journal of Geophysical Research: Oceans*, 106(C11):27103–27115, 2001.

[30] C. M. Dohmen-Janssen, D. F. Kroekenstoel, W. N. Hassan, and J. S. Ribberink. Phase lags in oscillatory sheet flow: experiments and bed load modelling. *Coastal Engineering*, 46(1):61–87, 2002.

[31] P. Dong and K. Zhang. Intense near-bed sediment motions in waves and currents. *Coastal Engineering*, 45(2):75–87, 2002.

[32] S. Elghobashi. Particle-laden turbulent flows: direct simulation and closure models. *Applied Scientific Research*, 48:301–314, 1991.

[33] S. Elghobashi. On predicting particle-laden turbulent flows. *Applied Scientific Research*, 52:309–329, 1994.

[34] S. Elghobashi. An updated classification map of particle-laden turbulent flows. In *IUTAM Symposium on Computational Approaches to Multiphase Flow. Fluid Mechanics and Its Applications*, volume 81, pages 3–10, 2006.

[35] A. Eshghinejadfard, S. A. Hosseini, and D. Thévenin. Fully-resolved prolate spheroids in turbulent channel flows: A lattice boltzmann study. *AIP Advances*, 7(9):095007, 2017.

[36] J. Ferry and S. Balachandar. A fast eulerian method for disperse two-phase flow. *International Journal of Multiphase Flow*, 27(7):1199 – 1226, 2001.

[37] J. Ferry and S. Balachandar. Equilibrium eulerian approach for predicting the thermal field of a dispersion of small particles. *International Journal of Heat and Mass Transfer*, 48(3):681 – 689, 2005.

[38] P. Février, O. Simonin, and K. D. Squires. Partitioning of particle velocities in gas-solid turbulent flows into a continuous field and a spatially uncorrelated random distribution: theoretical formalism and numerical study. *Journal of Fluid Mechanics*, 533:1–46, 2005.

[39] J. R. Finn and M. Li. Regimes of sediment-turbulence interaction and guidelines for simulating the multiphase bottom boundary layer. *International Journal of Multiphase Flow*, 85:278 – 283, 2016.

[40] J. R. Finn, M. Li, and S. V. Apte. Particle based modelling and simulation of natural sand dynamics in the wave bottom boundary layer. *Journal of Fluid Mechanics*, 796:340–385, 2016.

[41] D. L. Foster, A. J. Bowen, R. A. Holman, and P. Natoo. Field evidence of pressure gradient induced incipient motion. *Journal of Geophysical Research: Oceans*, 111(C5), 2006.

[42] R. O. Fox. On multiphase turbulence models for collisional fluid-particle flows. *Journal of Fluid Mechanics*, 742:368–424, 2014.

[43] E. L. Gallagher, S. Elgar, and R. T. Guza. Observations of sand bar evolution on a natural beach. *Journal of Geophysical Research: Oceans*, 103(C2):3203–3215, 1998.

[44] R. Gatignol. The faxén formulae for a rigid particle in an unsteady non-uniform stokes flow. *Journal de Mécanique Théorique et Appliquée*, 1:143–160, 1983.

[45] M. Germano, U. Piomelli, P. Moin, and W. H. Cabot. A dynamic subgrid-scale eddy viscosity model. *Physics of Fluids A: Fluid Dynamics*, 3(7):1760–1765, 1991.

[46] D. Gidaspow. *Multiphase Flow and Fluidization*. Academic Press, San Diego, 1994.

[47] J. M. Gonzalez-Ondina, L. Fraccarollo, and P. L.-F. Liu. Two-level, two-phase model for intense, turbulent sediment transport. *Journal of Fluid Mechanics*, 839:198–238, 2018.

[48] M. Gorokhovski and R. Zamansky. Modeling the effects of small turbulent scales on the drag force for particles below and above the kolmogorov scale. *Phys. Rev. Fluids*, 3:034602, 2018.

[49] H. Guta, J. Chauchat, and D. Hurther. Bed-load effects on turbulent suspension properties in heavy particle sheet-flows. *Journal of Hydraulic Engineering*, Submitted.

[50] H. Guta, D. Hurther, and J. Chauchat. Turbulent sediment transport processes in energetic sediment-laden open-channel flows. In *Proceedings of the 10th Conference on Fluvial Hydraulics, Delft, The Netherlands*, page 227–235, 2020.

[51] H. Homann and J. Bec. Finite-size effects in the dynamics of neutrally buoyant particles in turbulent flow. *Journal of Fluid Mechanics*, 651:81–91, 2010.

[52] T.-J. Hsu and D. M. Hanes. Effects of wave shape on sheet flow sediment transport. *Journal of Geophysical Research: Oceans*, 109(C5):1–15, 2004b.

[53] T.-J. Hsu, J. T. Jenkins, and P. L.-F. Liu. On two-phase sediment transport: sheet flow of massive particles. *Proceedings of the Royal Society of London. Series A: Mathematical, Physical and Engineering Sciences*, 460(2048):2223–2250, 2004a.

[54] D. Hurther, P. D. Thorne, M. Bricault, U. Lemmin, and J.-M. Barnoud. A multi-frequency acoustic concentration and velocity profiler (acvp) for boundary layer measurements of fine-scale flow and sediment transport processes. *Coastal Engineering*, 58(7):594–605, 2011.

[55] R. Jackson. *The Dynamics of Fluidized Particles*. Cambridge University Press, 2000.

[56] H. Jasak and T. Uroić. *Practical Computational Fluid Dynamics with the Finite Volume Method*, pages 103–161. 2020.

[57] B. L. Jensen, B. M. Sumer, and J. Fredsøe. Turbulent oscillatory boundary layers at high reynolds numbers. *Journal of Fluid Mechanics*, 206:265–297, 1989.

[58] P. C. Johnson and R. Jackson. Frictional–collisional constitutive relations for granular materials, with application to plane shearing. *Journal of Fluid Mechanics*, 176:67–93, 1987.

[59] D. Kaftori, G. Hetsroni, and S. Banerjee. Particle behavior in the turbulent boundary layer. ii. velocity and distribution profiles. *Physics of Fluids*, 7(5):1107–1121, 1995.

[60] A. G. Kidanemariam, C. Chan-Braun, T. Doychev, and M. Uhlmann. Dns of horizontal open channel flow with finite-size, heavy particles at low solid volume fraction. *New Journal of Physics*, 15(2):25–31, 2013.

[61] K. Kiger and C. Pan. Suspension and turbulence modification effects of solid particulates on a horizontal turbulent channel flow. *Journal of Turbulence*, 3:27–29, 04 2002.

[62] W. M. Kranenburg, T.-J. Hsu, and J. S. Ribberink. Two-phase modeling of sheet-flow beneath waves and its dependence on grain size and streaming. *Advances in Water Resources*, 72:57 – 70, 2014.

[63] D. K. Lilly. A proposed modification of the germano subgrid-scale closure method. *Physics of Fluids A: Fluid Dynamics*, 4(3):633–635, 1992.

[64] H. Liu and S. Sato. A two-phase flow model for asymmetric sheetflow conditions. *Coastal Engineering*, 53(10):825–843, 2006.

[65] D. A. Lyn. *Turbulence Models for Sediment Transport Engineering*, chapter Chapter 16. ASCE, 2008.

[66] D. Marquez. *An extended mixture model for the simultaneous treatment of short and long scale interfaces*. PhD thesis, 11 2013.

[67] A. Mathieu, J. Chauchat, C. Bonamy, G. Balarac, and T.-J. Hsu. A finite-size correction model for two-fluid large-eddy simulation of particle-laden boundary layer flow. *Journal of Fluid Mechanics*, 913:A26, 2021.

[68] M. R. Maxey and J. J. Riley. Equation of motion for a small rigid sphere in a nonuniform flow. *The Physics of Fluids*, 26(4):883–889, 1983.

[69] M. Mazzuoli, P. Blondeaux, G. Vittori, M. Uhlmann, J. Simeonov, and J. Calantoni. Interface-resolved direct numerical simulations of sediment transport in a turbulent oscillatory boundary layer. *Journal of Fluid Mechanics*, 885:A28, 2020.

[70] M. Mazzuoli, A. G. Kidanemariam, and M. Uhlmann. Direct numerical simulations of ripples in an oscillatory flow. *Journal of Fluid Mechanics*, 863:572–600, 2019.

[71] R. Mei. Effect of turbulence on the particle settling velocity in the nonlinear drag range. *International Journal of Multiphase Flow*, 20(2):273–284, 1994.

[72] C. Meneveau, T. S. Lund, and W. H. Cabot. A lagrangian dynamic subgrid-scale model of turbulence. *Journal of Fluid Mechanics*, 319:353–385, 1996.

[73] M. Montecchia, G. Brethouwer, S. Wallin, A. V. Johansson, and T. Knacke. Improving les with openfoam by minimising numerical dissipation and use of explicit algebraic sgs stress model. *Journal of Turbulence*, 20(11-12):697–722, 2019.

[74] R. D. Moser, J. Kim, and N. N. Mansour. Direct numerical simulation of turbulent channel flow up to $re_\tau = 590$. *Physics of Fluids*, 11(4):943–945, 1999.

[75] M. Muste, K. Yu, I. Fujita, and R. Ettema. Two-phase versus mixed-flow perspective on suspended sediment transport in turbulent channel flows. *Water Resources Research*, 41:1–22.

[76] T. Nagel, J. Chauchat, C. Bonamy, X. Liu, Z. Cheng, and T.-J. Hsu. Three-dimensional scour simulations with a two-phase flow model. *Advances in Water Resources*, 138:103544, 2020.

[77] I. Nezu and H. Nakagawa. *Turbulence in Open Channel Flows*. IAHR Monograph, 1993.

[78] Y. Niño and M. H. Garcia. Experiments on particle-turbulence interactions in the near-wall region of an open channel flow: implications for sediment transport. *Journal of Fluid Mechanics*, 326:285–319, 1996.

[79] P. Nielsen. On the motion of suspended sand particles. *Journal of Geophysical Research: Oceans*, 89(C1):616–626, 1984.

[80] P. Nielsen. Turbulence effects on the settling of suspended particles. *Journal of Sedimentary Research*, 63(5):835–838, 09 1993.

[81] T. O'Donoghue and S. Wright. Concentrations in oscillatory sheet flow for well sorted and graded sands. *Coastal Engineering*, 50(3):117 – 138, 2004.

[82] T. O'Donoghue and S. Wright. Flow tunnel measurements of velocities and sand flux in oscillatory sheet flow for well-sorted and graded sands. *Coastal Engineering*, 51(11):1163–1184, 2004.

[83] C. E. Ozdemir, T.-J. Hsu, and S. Balachandar. A numerical investigation of fine particle laden flow in an oscillatory channel: the role of particle-induced density stratification. *Journal of Fluid Mechanics*, 665:1–45, 2010.

[84] C. E. Ozdemir, T.-J. Hsu, and S. Balachandar. A numerical investigation of lutocline dynamics and saturation of fine sediment in the oscillatory boundary layer. *Journal of Geophysical Research: Oceans*, 116(C9):C09012, 2011.

[85] A. Ozel, P. Fede, and O. Simonin. Development of filtered euler-euler two-phase model for circulating fluidised bed: High resolution simulation, formulation and a priori analyses. *International Journal of Multiphase Flow*, 55:43 – 63, 2013.

[86] N. M. Qureshi, M. Bourgoin, C. Baudet, A. Cartellier, and Y. Gagne. Turbulent transport of material particles: An experimental study of finite size effects. *Phys. Rev. Lett.*, 99:184502, 2007.

[87] T. Revil-Baudard and J. Chauchat. A two-phase model for sheet flow regime based on dense granular flow rheology. *Journal of Geophysical Research: Oceans*, 118(2):619–634, 2013.

[88] T. Revil-Baudard, J. Chauchat, D. Hurther, and P.-A. Barraud. Investigation of sheet-flow processes based on novel acoustic high-resolution velocity and concentration measurements. *Journal of Fluid Mechanics*, 769:723–724, 2015.

[89] T. Revil-Baudard, J. Chauchat, D. Hurther, and O. Eiff. Turbulence modifications induced by the bed mobility in intense sediment-laden flows. *Journal of Fluid Mechanics*, 808:469–484, 2016.

[90] C. M. Rhie and W. L. Chow. Numerical study of the turbulent flow past an airfoil with trailing edge separation. *AIAA Journal*, 21(11):1525–1532, 1983.

[91] J. S. Ribberink. Bed-load transport for steady flows and unsteady oscillatory flows. *Coastal Engineering*, 34(1):59–82, 1998.

[92] J. S. Ribberink and A. A. Al-Salem. Sheet flow and suspension of sand in oscillatory boundary layers. *Coastal Engineering*, 25(3):205–225, 1995.

[93] J. S. Ribberink, J. J. van der Werf, T. O'Donoghue, and W. N. Hassan. Sand motion induced by oscillatory flows: Sheet flow and vortex ripples. *Journal of Turbulence*, 9:N20, 2008.

[94] J. Richardson and W. Zaki. Sedimentation and fluidisation: Part i. *Chemical Engineering Research and Design*, 75:S82–S100, 1997.

[95] F. Ries, Y. Li, K. Nishad, L. Dressler, M. Ziefuss, A. Mehdizadeh, C. Hasse, and A. Sadiki. A wall-adapted anisotropic heat flux model for large eddy simulations of complex turbulent thermal flows. *Flow, Turbulence and Combustion*, 08 2020.

[96] M. Righetti and G. P. Romano. Particle-fluid interactions in a plane near-wall turbulent flow. *Journal of Fluid Mechanics*, 505:93–121, 2004.

[97] L. C. V. Rijn, J. S. Ribberink, J. V. D. Werf, and D. J. Walstra. Coastal sediment dynamics: recent advances and future research needs. *Journal of Hydraulic Research*, 51(5):475–493, 2013.

[98] H. Rouse. Experiments on the mechanics of sediment suspension. In *ICTAM*, pages 550–554, 1938.

[99] H. Rusche. *Computational Fluid Dynamics of Dispersed Two-Phase Flows at High Phase Fractions*. PhD thesis, 01 2002.

[100] E. S. Fluid flow through packed columns. *Chemical Engineering Progress*, 48:89–94, 1952.

[101] J. Salinas, S. Balachandar, M. Shringarpure, J. Fedele, D. Hoyal, S. Zuniga, and M. I. Cantero. Anatomy of subcritical submarine flows with a lutocline and an intermediate destruction layer. *Nature Communications*, 12(1649), 2021.

[102] D. G. Schaeffer. Instability in the evolution equations describing incompressible granular flow. *Journal of Differential Equations*, 66(1):19–50, 1987.

[103] M. Scherer, A. G. Kidanemariam, and M. Uhlmann. On the scaling of the instability of a flat sediment bed with respect to ripple-like patterns. *Journal of Fluid Mechanics*, 900:A1, 2020.

[104] M. W. Schmeeckle. Numerical simulation of turbulence and sediment transport of medium sand. *Journal of Geophysical Research: Earth Surface*, 119(6):1240–1262, 2014.

[105] P. Silva, T. Abreu, D. Van Der A, F. Sancho, B. Ruessink, J. van der Werf, and J. Ribberink. Sediment transport in non-linear skewed oscillatory flows: the transkew experiments. *Journal of Hydraulic Research*, 49(S1):72–80, 2011.

[106] P. Silva, A. Temperville, and F. Seabra Santos. Sand transport under combined current and wave conditions: A semi-unsteady, practical model. *Coastal Engineering*, 53(11):897–913, 2006.

[107] J. Sleath. Conditions for plug formation in oscillatory flow. *Continental Shelf Research*, 19(13):1643 – 1664, 1999.

[108] R. Soulsby. *Dynamics of marine sands*. Thomas Telford Publishing, 1997.

[109] B. M. Sumer, A. Kozakiewicz, J. Fredsøe, and R. Deigaard. Velocity and concentration profiles in sheet-flow layer of movable bed. *Journal of Hydraulic Engineering*, 122(10):549–558, 1996.

[110] D. H. Swart. Offshore sediment transport and equilibrium beach profiles. *Delft Hydrolics Laboratory Publication*, 131, 1974.

[111] M. Uhlmann. An immersed boundary method with direct forcing for the simulation of particulate flows. *Journal of Computational Physics*, 209(2):448–476, 2005.

[112] D. A. van der A, T. O'Donoghue, and J. S. Ribberink. Measurements of sheet flow transport in acceleration-skewed oscillatory flow and comparison with practical formulations. *Coastal Engineering*, 57(3):331–342, 2010.

[113] D. A. van der A, T. O'Donoghue, A. G. Davies, and J. S. Ribberink. Experimental study of the turbulent boundary layer in acceleration-skewed oscillatory flow. *Journal of Fluid Mechanics*, 684:251–283, 2011.

[114] D. A. van der A, J. S. Ribberink, J. J. van der Werf, T. O'Donoghue, R. H. Buijsrogge, and W. M. Kranenburg. Practical sand transport formula for non-breaking waves and currents. *Coastal Engineering*, 76:26–42, 2013.

[115] J. J. van der Werf, J. S. Doucette, T. O'Donoghue, and J. S. Ribberink. Detailed measurements of velocities and suspended sand concentrations over full-scale ripples in regular oscillatory flow. *Journal of Geophysical Research: Earth Surface*, 112(F2):1–18, 2007.

[116] L. van Rijn, D. Walstra, B. Grasmeijer, J. Sutherland, S. Pan, and J. Sierra. The predictability of cross-shore bed evolution of sandy beaches at the time scale of storms and seasons using process-based profile models. *Coastal Engineering*, 47(3):295–327, 2003.

[117] L. C. van Rijn. Sediment transport, part ii: Suspended load transport. *Journal of Hydraulic Engineering*, 110(11):1613–1641, 1984.

[118] G. Vittori, P. Blondeaux, M. Mazzuoli, J. Simeonov, and J. Calantoni. Sediment transport under oscillatory flows. *International Journal of Multiphase Flow*, 133:103454, 2020.

[119] G. A. Voth, A. La Porta, A. M. Crawford, J. Alexander, and E. Bodenschatz. Measurement of particle accelerations in fully developed turbulence. *Journal of Fluid Mechanics*, 469:121–160, 2002.

[120] B. Vowinckel. Incorporating grain-scale processes in macroscopic sediment transport models. *Acta Mechanica*, 232:2023–2050, 2021.

[121] A. Vreman. A staggered overset grid method for resolved simulation of incompressible flow around moving spheres. *Journal of Computational Physics*, 333:269–296, 2017.

[122] C. Y. Wen and Y. H. Yu. A generalized method for predicting the minimum fluidization velocity. *AIChE Journal*, 12(3):610–612, 1966.

[123] C. K. Wentworth. A scale of grade and class terms for clastic sediments. *The Journal of Geology*, 30(5):377–392, 1922.

[124] K. Wilson, J. Andersen, and J. Shaw. Effects of wave asymmetry on sheet flow. *Coastal Engineering*, 25(3):191–204, 1995.

[125] K. C. Wilson. Analysis of bed-load motion at high shear stress. *Journal of Hydraulic Engineering*, 113(1):97–103, 1987.

[126] H. Xu and E. Bodenschatz. Motion of inertial particles with size larger than kolmogorov scale in turbulent flows. *Physica D: Nonlinear Phenomena*, 237(14):2095 – 2100, 2008.

[127] A. Yoshizawa and K. Horiuti. A statistically-derived subgrid-scale kinetic energy model for the large-eddy simulation of turbulent flows. *Journal of the Physical Society of Japan*, 54(8):2834–2839, 1985.

[128] W. Yu, I. Vinkovic, and M. Buffat. Acceleration statistics of finite-size particles in turbulent channel flow in the absence of gravity. *Flow, Turbulence and Combustion*, 96:183–205, 2016.

[129] W. Yu, I. Vinkovic, and M. Buffat. Finite-size particles in turbulent channel flow: quadrant analysis and acceleration statistics. *Journal of Turbulence*, 17(11):1048–1071, 2016.

[130] X. Yu, C. E. Ozdemir, T.-J. Hsu, and S. Balachandar. Numerical investigation of turbulence modulation by sediment-induced stratification and enhanced viscosity in oscillatory flows. *Journal of Waterway, Port, Coastal, and Ocean Engineering*, 140(2):160–172, 2014.

[131] N. Zala-Flores and J. F. A. Sleath. Mobile layer in oscillatory sheet flow. *Journal of Geophysical Research: Oceans*, 103(C6):12783–12793, 1998.

[132] D. Z. Zhang and A. Prosperetti. Momentum and energy equations for disperse two-phase flows and their closure for dilute suspensions. *International Journal of Multiphase Flow*, 23(3):425–453, 1997.

# List of Figures

# List of Tables

# A

# Résumé de la thèse en français

*Un résumé en français comprenant le contexte, les motivations et les principaux résultats obtenus au cours de cette thèse est présenté dans cette annexe.*

La compréhension des processus physiques impliqués dans le transport intense de sédiments est de la plus haute importance. Lors d'événements météorologiques extrêmes, comme les tempêtes par exemple, l'évolution morphologique des plages de sable est fortement influencée par le transport de sédiment en régime de charriage intense induit par les vagues. Dans le contexte du changement climatique, pour lequel on s'attend à ce que la fréquence et l'intensité des événements extrêmes augmentent, il est fondamental de pouvoir comprendre les mécanismes impliqués dans le transport par charriage intense pour des écoulements oscillants typiques de l'environnement côtier afin de modéliser et de prévoir la morphologie des plages sableuse à grande échelle [97].

Il existe dans la littérature un grand nombre de publications présentant des expériences menées dans des tunnels hydrodynamiques (voir figure 1.9) pour étudier le transport de sable en régime de charriage intense dans la couche limite oscillante. Cette configuration représente une idéalisation de la couche limite générée par les vagues réelles en milieu côtier et présente l'avantage d'être plus facile à reproduire numériquement en évitant la résolution de la surface libre. Les données expérimentales ont servis à développer des modèles de transport de sédiments que ce soit des formules de transport net par vague [114] ou des modèles diphasiques à phases résolues [2, 53]. Ces dernières décennies, des progrès significatifs ont été obtenus par la modélisation empirique et numérique. Cependant, certains phénomènes ne sont pas encore bien compris et modélisés, c'est le cas par exemple des effets instationnaires pour les sables fins comme le déphasage entre le flux de transport de sables et la contrainte de cisaillement au fond ou l'effet de l'asymétrie des vagues sur le flux net de sable.

De plus, étant donné que l'érosion, le transport et le dépôt des sédiments dans les écoulements oscillants sont principalement contrôlés par des processus liés à la turbulence, les capacités de prédiction des modèles basés sur une vision moyennée de la turbulence souffrent de limitations majeures, en particulier pour les sables fins pour lesquels les interactions entre particules et turbulence sont dominantes.

Pour étudier les processus fins jouant un rôle dans le transport de sédiment, différentes approches de simulation numérique à turbulence résolue existent. Ces approches peuvent être regroupées en deux familles : les approches Lagrangiennes et Eulériennes. Dans les approches

Lagrangiennes, la trajectoire de chaque particule est résolue. Au contraire, dans les approches Eulériennes, des équations de conservation de la masse et de quantité de mouvement sont obtenue par la réalisation d'une moyenne spatiale sur l'ensemble des particules contenu dans un volume de contrôle. L'écoulement peut alors être défini en fonction de la concentration volumique de particules et des valeurs moyennes des quantités (vitesse, pression, ...) de la phase porteuse fluide et de la phase dispersée composée de l'ensemble des particules.

Dans les régimes d'écoulement intenses, typiques de l'environnement côtier, un très grand nombre de particules est transporté dans l'écoulement. Suivre la trajectoire des particules individuelles est impossible compte tenu des ressources informatiques disponibles actuellement. Dans ce contexte, le développement des approches Eulériennes à turbulence résolue représente un enjeu majeur pour la compréhension des processus physiques impliqués dans le transport de sable en régime de charriage intense. Néanmoins, les hypothèses émises pour obtenir les équations du modèle diphasique Eulérien restreignent son champ d'applicabilité en terme de régimes d'interaction turbulence-particule. En effet, lorsque les particules sont plus grosses que plus petites échelles spatiales de la turbulence, les particules sont dites de taille finie, il n'y a plus séparation d'échelle entre l'écoulement et les particules et les lois d'interactions entre la phase fluide et la phase solide ne sont plus valides. Il est alors nécessaire de développer de nouveaux modèles prenant en compte les interactions complexes existant entre turbulence et particules.

Dans ce contexte, un modèle diphasique Eulérien (ou modèle bi-fluide) à turbulence résolue pour des applications de transport de sédiments a été développé au cours de cette thèse.

Le chapitre 2 expose les développements nécessaires à l'obtention du modèle bi-fluide tels que les opérations de moyenne spatiale, les différents modèles de fermeture. Pour les contraintes de la phase solide, la théorie cinétique pour les écoulements granulaires de Chassagne *et al.* (submitted) [18] est utilisée. Les interactions fluides-particules sont modélisées en prenant en compte la poussée d'Archimède, la force de traînée, de portance et de masse ajoutée. Enfin, les équations sont filtrées pour pouvoir réaliser des simulations des grandes échelles de la turbulence. L'effet des contributions sous-mailles non résolues est pris en compte par le modèle de turbulence de type Smagorinsky avec une procédure dynamique dite Lagrangienne proposée par Meneveau *et al.* (1996) [72] pour calculer les coefficients du modèle. Deux configurations sans particules sont reproduites numériquement afin de valider l'implémentation du modèle.

Dans le chapitre 3, le modèle bi-fluide a été appliqué dans un premier temps aux configurations d'écoulement en régime de charriage intense pour deux types de sable (sable fin de diamètre $d_p = 150\ \mu m$ et moyen de diamètre $d_p = 280\ \mu m$) soumis à un forçage hydrodynamique oscillant sinusoïdal afin de rendre compte des différences de comportement de la couche limite oscillante en fonction de la taille des particules. L'effet de la forme des vagues est investigué dans le chapitre 4 en appliquant le modèle bi-fluide à des configurations impliquant les mêmes types de sable, mais des forçage hydrodynamiques asymétriques en vitesse et en accélération. Enfin, un modèle de correction prenant en compte les effets de taille finie des particules est développé et validé sur des configurations d'écoulements unidirectionnels chargés en particules à faible fraction volumique dans le chapitre 5.

## Effets instationnaires dans un écoulement oscillant en régime de charriage intense

Le modèle bi-fluide à turbulence résolue a été appliqué avec succès à des configurations d'écoulements oscillants en régime de charriage intense impliquant des sables fins et moyens sous un forçage d'écoulement symétrique (configurations F512 et M512 de O'Donoghue & Wright

(2004a) [81]). Un aperçu des simulations montrant les interactions entre concentration de particules et la turbulence du fluide ainsi que les différences de comportement de la couche limite oscillante est présenté sur la figure 3.9.

Un accord quantitatif des profils de concentration moyens $\langle\bar{\phi}\rangle$ est obtenu par rapport aux profils expérimentaux (figure A.1), démontrant les capacités de prédiction du modèle. Cependant, de petites divergences peuvent être observées pour la configuration impliquant des sables moyens. Les sédiments se déposent trop rapidement sur le lit pendant la phase de décélération de l'écoulement, ce qui entraîne un profil de concentration plus plat dans la région proche du lit par rapport aux mesures. D'après l'étude des régimes d'interactions turbulence-particules présentée dans le chapitre 1, pour des particules plus grandes, des régimes d'interaction plus complexes apparaissent et des processus physiques tels que les effets de taille finie peuvent devenir importants. Dans ce cas, des modifications du terme d'interaction fluide-particule, susceptibles d'affecter la distribution verticale des sédiments, sont nécessaires [39].

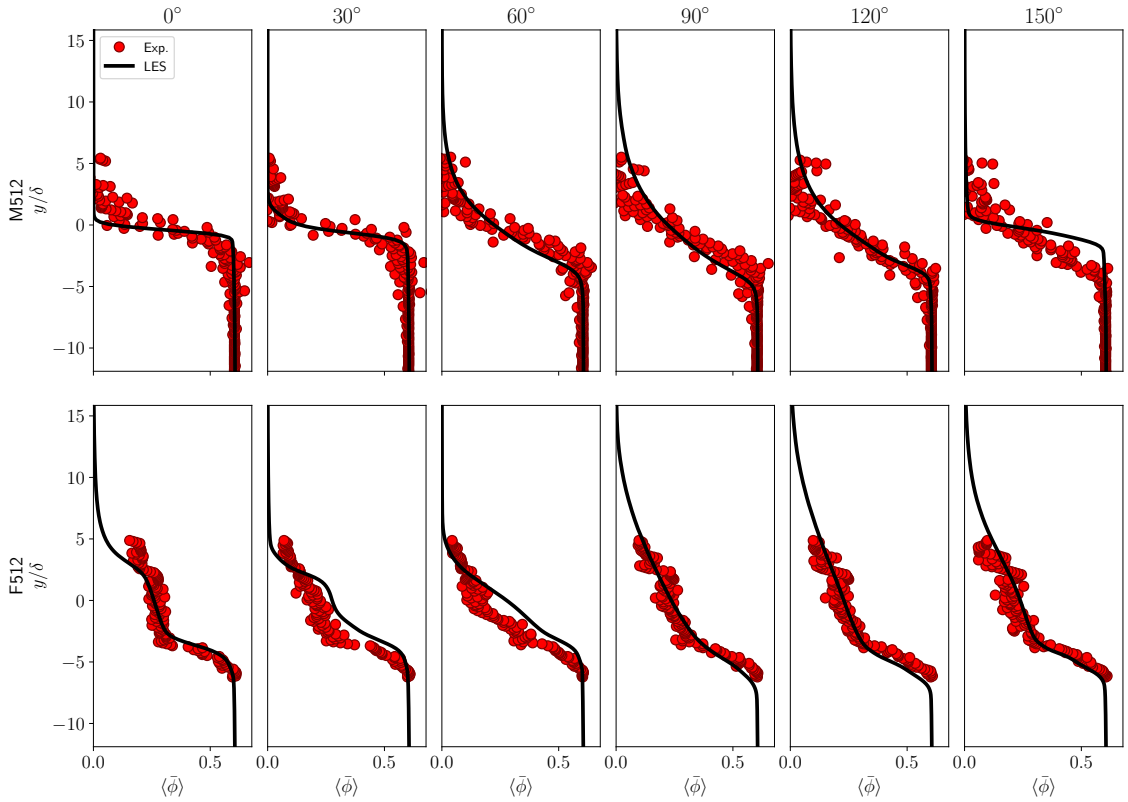


*Figure A.1: Profils de concentration moyenne des configurations M512 et F512 présentées dans le chapitre 3 prédits par le modèle bi-fluide (LES) comparés aux données expérimentales d'O'Donoghue & Wright (2004a) [81] (Exp.)*

Néanmoins, le bon accord entre les résultats de simulation et les expériences valide le modèle bi-fluide. Il est remarquable que le modèle bi-fluide à turbulence résolue reproduise de manière satisfaisante les différences de comportement observées entre sables moyens et sables fins alors que les modèles bi-fluides à turbulence moyennée nécessite un ajustement des paramètres empiriques pour les modèles d'interactions turbulence-particules [4, 64]. Ce résultat important démontre que le modèle bi-fluide à Simulation des Grandes Échelles résout explicitement ces interactions et il peut donc être utilisé pour analyser en détails les bilan de masse et les statistiques turbulentes pour expliquer les différences observées expérimentalement.

Pour un écoulement oscillant en régime de charriage intense impliquant des sables moyens, l'évolution du profil de concentration à travers la période de la vague suit la description bien

documentée proposée par O'Donoghue & Wright (2004a) [81] avec une rotation dans le sens des aiguilles d'une montre (resp. dans le sens inverse) du profil de concentration pendant l'accélération (resp. la décélération) de l'écoulement autour d'un "pivot" de concentration constante (voir figure 1.12). Ce comportement est le résultat d'une compétition entre les flux de sédimentation et de suspension turbulente pendant le cycle de la vague. L'épaisseur de la couche de transport, la profondeur d'érosion et le flux horizontal de sédiments sont parfaitement en phase avec la vitesse de l'écoulement externe *i.e.* en dehors de la couche limite, ce qui suggère que la réponse du lit de sédiments aux changements de l'écoulement est très rapide. Ce résultat confirme qu'une vision quasi-stationnaire de l'évolution de la couche de transport est pertinente.

Pour le sable fin, des effets instationnaires sont présents entraînant un comportement complètement différent de l'écoulement et du transport. En raison des instabilités hydrodynamiques observées pendant la phase d'accélération, la contrainte de Reynolds de la phase solide devient importante et l'épaisseur de la couche de transport est considérablement augmentée pendant toute la période de la vague. Par conséquent, une grande quantité de sédiments est transportée dans la couche limite, ce qui augmente l'inertie de la couche de transport. La réponse du lit de sédiments n'est plus en phase avec la vitesse de l'écoulement loin du lit. Pendant la phase de décélération, la présence de particules en suspension induit une stratification de l'écoulement qui amortit fortement la turbulence et conduit à des flux de suspension turbulente verticaux presque nuls. La couche limite passe d'un comportement turbulent à un comportement laminaire et la dynamique des sédiments est de plus en plus dominée par la sédimentation. Par rapport aux sables moyens, le flux net vertical maximal est situé plus haut dans l'écoulement, ce qui conduit à la formation d'un plateau de concentration dû à un comportement non-linéaire dans le bilan de masse (formation d'un choc). L'évolution temporelle de la concentration ne peut plus être représentée par la description classique fournie par O'Donoghue & Wright (2004a) [81]. Le plateau de concentration "glisse" presque librement au-dessus du lit immobile avec un profil de vitesse constant présentant des similitudes avec les écoulements en bouchon observés par Sleath (1999) [107].

Par rapport aux sables moyens, la turbulence de la phase solide joue un rôle plus important dans l'écoulement en régime de charriage intense pour des sables fins. Habituellement non prise en compte dans les modèles à turbulence moyennée, elle contribue à expliquer leurs incapacités à prédire les configurations impliquant des sables fins. Les effets instationnaires sont le résultat d'une chaîne de causes et de conséquences comprenant des instabilités de cisaillement et une forte contrainte de Reynolds de la phase solide augmentant le mélange vertical des sédiments, une inertie accrue de la couche limite, une stratification stable conduisant un amortissement de la turbulence et la chute entravée des particules à forte concentration. Un équilibre entre tous ces mécanismes s'établit pendant la période des vagues qui contrôle le bilan de masse vertical des sédiments et les effets de déphasage observés.

En conclusion, la prédiction précise de l'évolution temporelle du profil de concentration dépend d'une modélisation fiable de la compétition entre le flux de sédimentation et le flux de suspension turbulente. Les résultats de la simulation utilisant le modèle bi-fluide montrent que la vitesse moyenne de sédimentation peut être bien reproduite en utilisant une formulation empirique prenant en compte la chute entravée des particules. Les recherches futures devraient donc se concentrer sur une modélisation précise des contraintes de Reynolds particulaire et de la vitesse de glissement turbulent entre le fluide et les particules.

## Effets de la forme des vagues

Dans un deuxième temps, l'effet de la forme des vagues sur l'écoulement oscillant en régime de charriage intense a été étudié en mettant l'accent sur la dépendance à la taille des grains et aux

effets de déphasage.

Quatre configurations impliquant des sables fins et moyens soumis à des vagues asymétriques en vitesse (panneau du milieu sur la figure 2) et en accélération (panneau du bas sur la figure 2) provenant de O'Donoghue & Wright (2004a) [81] et de van der A *et al.* (2010) [112] ont été reproduites numériquement.

Contrairement aux vagues symétriques, le flux de sédiments net moyenné sur une période complète de vague non nul. Il est positif *i.e.* dirigé vers la côte, ou négatif *i.e.* dirigé vers le large suivant les cas. À partir d'une comparaison entre les mesures expérimentales et les prédictions numériques, les mécanismes physiques responsables du flux net de sédiments plus important pour les sables fins sous des vagues asymétriques en accélération et du flux net de sédiments négatif pour les sables fins sous des vagues asymétriques en vitesse sont reproduits par le modèle bi-fluide.

La comparaison entre le flux net prédit par le modèle bi-fluide et celui mesuré expérimentalement et présentée sur la figure A.2 avec M5010 la configuration impliquant des sables moyens et des vague asymétriques en vitesse, F5010 la configuration sables fins pour les mêmes vagues, S706015m la configuration sables moyens et des vagues asymétriques en accélération et S706015f la configuration sables fins pour les mêmes vagues.

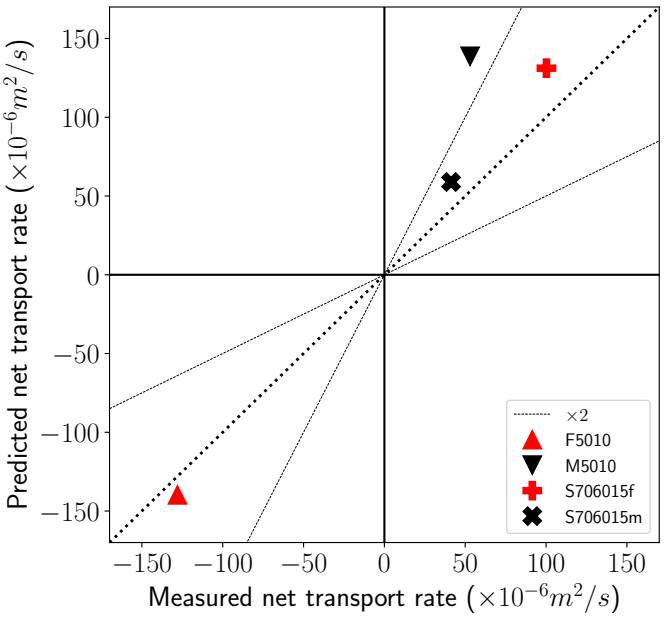


*Figure A.2: comparaison entre le taux de transport net prédit par le modèle bi-fluide et mesuré expérimentalement pour les configurations F5010, M5010, S706015f and S706015m.*

Pour la configuration M5010, le flux de sédiments est corrélé avec le nombre de Shields instantané traduisant la contrainte de cisaillement appliquée sur le lit. Le flux de sédiments est nul lors des phases de renverses de la vague, il augmente pendant la phase d'accélération et diminue pendant la phase de décélération. En raison de la plus grande contrainte de cisaillement du lit pendant la crête de la vague, une plus grande quantité de sédiments est transportée par rapport à la phase de creux. Bien que la durée du creux soit plus longue, la quantité de sédiments transportée vers le large ne compense pas la contribution dirigée vers la côte pendant la crête et le flux net sur le cycle de vague est dirigé vers la côte.

Pour la configuration F5010, au contraire, les particules érodées pendant la crête de la vague n'ont pas le temps de se redéposer avant la phase de renverse (de la côte vers le large). Une quantité importante de sédiments restée en suspension lors de la phase de renverse est transportée vers le large pendant le creux de la vague et le flux de sédiments n'est plus corrélé avec le nombre

de Shields instantané. Même si le flux de sédiments instantané est plus faible pendant le creux que pendant la crête de la vague, la plus longue durée du creux générer un flux net vers le large.

Les mêmes observations peuvent être faites entre les configurations M5010 et S706015m impliquant des sables moyens soumis à des vagues asymétriques en vitesse et en accélération. Cependant, la plus forte contrainte de cisaillement du lit observée pendant la crête de la vague est le résultat de la plus forte accélération par rapport au creux de la vague. Le flux de sédiments est nul lors de la phase de renverse et la quantité de sédiments transportés vers la côte dépasse la quantité de sédiments transportés vers le large pendant le creux conduisant à un flux net orienté vers la côte.

Pour la configuration S706015f, le flux de sédiments revient à zéro pendant la phase de renverse de la côte vers le large, mais pas lors de la phase de renverse du large vers la côte. Les particules restant en suspension sont transportées pendant la crête de la vague ayant pour effet d'augmenter encore le taux de transport net orienté vers la côte.

Les mêmes mécanismes jouant un rôle dans les effets instationnaires observés au chapitre 3 sont présents dans les configurations impliquant des sables fins. L'épaisseur de la couche de transport est augmentée par rapport aux configurations impliquant des sables moyens, la turbulence est atténuée lors des phases de renverses et les instabilités du lit augmentent le mélange vertical des particules. En outre, l'augmentation de l'épaisseur de la couche de transport pendant le creux de la vague pour la configuration impliquant de sables fins soumis à des vagues asymétriques en accélération ne peut être attribuée qu'à des instabilités du lit plus importantes, étant donné que l'épaisseur de la couche de transport était proche de zéro lors de la phase de renverse de la côte vers le large.

La relation entre les taux de transport durant les demi-phases de la vague et leurs nombres de Shields représentatifs a révélé que le flux de sable dans les configurations impliquant des sables fins et moyens ne peut pas être représenté par une loi puissance en utilisant les mêmes paramètres pour les deux tailles de sédiments. En effet, pour les sables moyens, il n'y a pas d'effets de déphasage et le flux sédimentaire est bien représenté par une loi de puissance classique *i.e.* comme en écoulement unidirectionnel. Cependant, pour les sables fins, le flux sédimentaire est plus important ce qui signifie que les effets instationnaires contribuent à augmenter le flux sédimentaire dans le sens du courant.

La comparaison entre l'épaisseur maximale de la couche de transport prédite pendant la crête et pendant le creux des vagues à partir du modèle bi-fluide et la relation empirique proposée par Dohmen-Janssen *et al.* (2001) [29] a montré que l'épaisseur maximale de la couche de transport d'une configuration impliquant des sables moyens peut être bien représentée par le nombre maximal de Shields, mais pas pour les configurations impliquant des sables fins.

À partir des séries temporelles du bilan de masse vertical des sédiments entre les flux ascendants de suspension turbulente et les flux descendants de sédimentation, des suggestions sur la méthodologie de modélisation des effets de décalage de phase basées sur la physique ont été fournies. En effet, l'empreinte des effets de déphasage est clairement visible sur la compétition entre la suspension turbulente des particules et leur sédimentation. Cependant, des configurations supplémentaires impliquant différentes tailles de grains, différentes périodes d'écoulement et différents facteurs d'asymétrie sont nécessaires pour commencer à développer de nouvelles lois d'échelle.

En outre, pour fournir des lois d'échelle précises, il est nécessaire d'obtenir des résultats plus quantitatifs en termes de taux de transport et de profils de concentration pour les configurations impliquant des sables moyens. Comme souligné dans la section 3.3.1, les sables moyens semblent se déposer sur le lit trop rapidement par rapport aux expériences. Pour les grosses particules, la séparation d'échelle entre les particules et les plus petits tourbillons turbulents n'est plus vérifiée, le diamètre des particules est plus grand que la plus petite échelle de longueur turbulente $\eta$. Les effets de taille finie peuvent devenir importants et doivent être pris en compte pour prédire avec précision les interactions fluide-particules [39].

## Modèle de correction de taille finie

Afin de mesurer les capacités prédictives du modèle bi-fluide pour des configurations impliquant des particules de taille finie, il a été appliqué à des configurations expérimentales de couches limites unidirectionnelles chargées en particules ayant un rapport de taille $d_p/\eta \sim \mathcal{O}(1-10)$. Dans le but d'éliminer un niveau de complexité supplémentaire induit par la présence d'un lit de particules déposées et d'isoler la contribution des interactions turbulence-particules, les configurations présentées impliquent des suspension diluées.

Comme observé dans les simulations de la configuration d'écoulement unidirectionnel en régime de charriage intense par Cheng *et al.* (2018) [23], la suspension des particules de taille finie est sous-estimées pour les configurations impliquant un nombre de suspension $S = u_\tau/v_s \sim \mathcal{O}(1)$ avec $u_\tau$ la vitesse de frottement au fond et $v_s$ la vitesse de chute d'une particule isolée.

Afin d'obtenir un accord quantitatif entre les profils de concentration moyens prédits par le modèle bi-fluide et les données expérimentales, un modèle de correction de taille finie basé sur le modèle de Gorokhovski & Zamansky (2018) [48] a été proposé. Dans ce modèle, une distinction est faite entre les échelles d'écoulement turbulent plus grandes ou plus petites que le diamètre de la particule. Le champ de vitesse "vu" par les particules dans la loi de traînée est filtré à une échelle $\breve{\Delta} \geq 2d_p$ et les échelles turbulentes plus petites contribuent à réduire le temps de réponse des particules par l'ajout d'une viscosité turbulente à la viscosité moléculaire dans la définition du nombre de Reynolds particulaire et à augmenter la production de température granulaire.

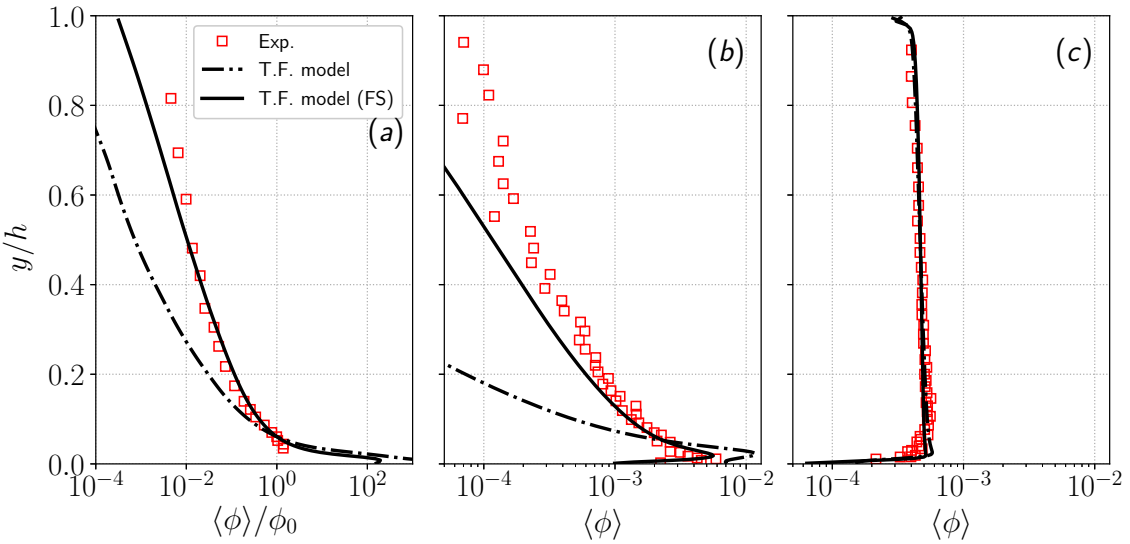


*Figure A.3: Profils de concentration moyens des configurations GB (panneau (a)) NS (panneau (b)) et NBS (panneau (c)) obtenus avec et sans modèle de correction de taille finie (T.F. model et T.F. model (FS) respectivement) comparés aux données expérimentales (Exp.).*

Les profils de concentration moyens des configurations impliquant des billes de verre de densité $\rho^s = 2600\ kg.m^{-3}$ de Kiger & Pan (2002) [61] (configuration GB) et des sédiments naturels de densité $rho^s = 2650\ kg.m^{-3}$ (configuration NB) et de densité $\rho^s = 1025\ kg.m^{-3}$ (configuration NBS) de Muste *et al.* (2005) [75] obtenus avec et sans modèle de correction de taille finie sont comparés aux données expérimentales dans la figure A.3. Pour les configurations GB et NS, l'ajout du modèle de correction de taille finie permet d'améliorer significativement la prédiction de la suspension turbulente des particules sans aucun paramètre de réglage. Pour la configuration NBS, l'accord est quantitatif entre les profils de concentration avec et sans modèle de correction de taille finie. De plus, l'étude d'une configuration supplémentaire impliquant une concentration en sédiments plus élevée (configuration NS*) a montré que la différence entre les profils de

concentration prédits avec et sans modèle de taille finie et plus importante pour des plus fortes concentrations en sédiments.

D'après l'évaluation du modèle de correction de taille finie, alors que la modification de la loi de traînée est plus importante pour la prédiction du profil de concentration des particules en suspension dans les configurations étudiée ici, la modification de l'équation de température granulaire est obligatoire pour la cohérence physique et la stabilité numérique du modèle. Enfin, l'analyse de sensibilité des résultats du modèle pour la taille de filtre $\breve{\Delta}$ a montré que la résolution de la grille pouvait atteindre 4 diamètres de particules sans perte de précision, tant qu'un point de grille est situé dans la sous-couche visqueuse.

Dans la perspective de fournir une paramétrisation plus physique pour les modèles à turbulence moyennée, le modèle bi-fluide à turbulence résolue devrait être appliqué à une large gamme de paramètres d'écoulement et de particules. Cependant, étant donné la grande diversité des régimes d'interaction turbulence-particules présents dans les conditions de transport de sédiments typiques des environnements côtiers et fluviaux, le modèle à deux fluides et en particulier le modèle de correction de la taille finie devrait être encore amélioré pour étendre son champ d'application à des rapports de taille $d_p/\eta$ plus grands.

En effet, en utilisant le modèle de correction de taille finie pour les configurations d'écoulement oscillant en régime de charriage intense des chapitres 3 et 4 et la configuration d'écoulement unidirectionnel de Revil-Baudard *et al.* (2015) [88] étudiée par Cheng *et al.* (2018) [23] a entraîné une surestimation de la suspension des particules.

Dans les configurations étudiées dans le chapitre 5, le nombre de Stokes défini comme étant le rapport entre les échelles de temps associées aux particules et aux plus petites échelles turbulentes (échelles de Kolmogorov $\eta$) est de l'ordre de l'unité. En conséquence, l'échelle de longueur $l^*$ associée aux tourbillons ayant la même échelle de temps que la particule est de l'ordre de $\eta$ justifiant la prise en compte de l'effet de toute la gamme des échelles de l'écoulement turbulent en dessous du diamètre de la particule dans le couplage entre le fluide et la phase solide. Cependant, les particules plus inertielles agissent comme un filtre temporel du spectre turbulent. Dans ce cas, $l^* > \eta$ et la prise en compte de l'effet des échelles d'écoulement turbulent entre $l^*$ et $\eta$ a pour effet de surestimer la viscosité effective dans le modèle de correction de taille finie et de suspension turbulente de particules.

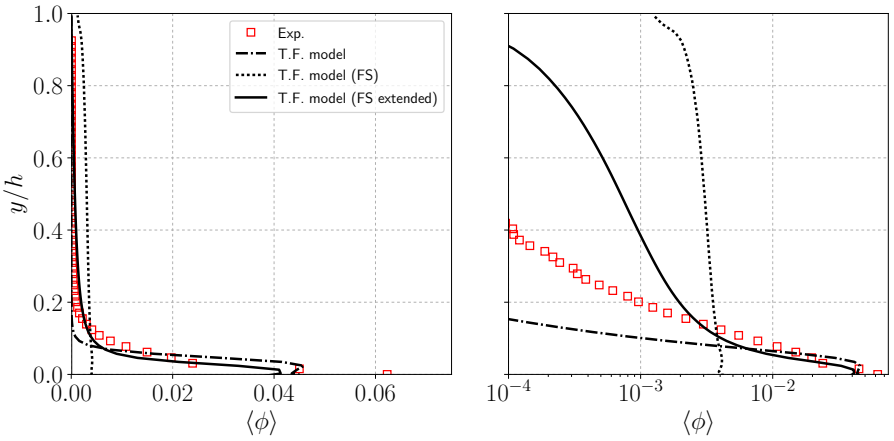


*Figure A.4: Profils de concentration moyens provenant des expériences (Exp.) et des simulations sans modèle de taille finie (T.F. model), avec le modèle de taille finie présenté dans le chapitre 5 (T.F. model (FS)) et avec le modèle de taille finie étendu (T.F. model (FS extended)) en utilisant une échelle conventionnelle dans le panneau de gauche et en utilisant une échelle semi-logarithmique dans le panneau de droite.*

Le développement d'un modèle de correction de taille finie étendu pour les particules iner-

tielles, encore à un stade précoce de développement, est proposé dans les perspectives de la thèse. Appliqué à une configuration expérimentale impliquant des particules de taille finie ayant un rapport de taille $d_p/\eta \approx 120$ et un nombre de Stokes $St \approx 160$, le nouveau modèle améliore sensiblement la prédiction du profil de concentration moyen. D'après les profils de concentration présentés sur la figure A.4, sans le modèle de correction de taille finie, la concentration est très largement sous-estimées dans les parties supérieures de l'écoulement. Avec le modèle de correction de taille finie présenté dans le chapitre 5, la suspension est sur-estimée avec un profil de concentration presque vertical. Enfin, avec le modèle de correction de taille finie étendu, la prédiction du profil de concentration est améliorée dans la partie basse de l'écoulement. Le développement précoce du modèle de correction de taille finie étendu est extrêmement prometteur étant donné l'amélioration significative des prédictions du modèle sans l'utilisation de coefficients de réglage. Cependant, la suspension des particules est encore surestimée, surtout dans la région supérieure de l'écoulement.

Cette vision sur l'inclusion des interactions turbulence-particules dans le couplage de la quantité de mouvement entre les deux phases représente une grande opportunité d'étendre la gamme d'applicabilité du modèle bi-fluide. Cependant, des développements supplémentaires sont nécessaires pour améliorer davantage les prédictions du modèle afin de pouvoir l'appliquer à des configurations plus complexes impliquant une plus grande fraction volumique et une plus grande gamme de paramètres de particules et d'écoulement.

En conclusion, le modèle bi-fluide détient un potentiel très élevé compte tenu de ses capacités de prédiction, des informations qu'il fournit sur les mécanismes turbulents se produisant dans la couche de transport et de sa capacité à s'affranchir les limitations en termes de nombre de particules par rapport aux méthodologies de modélisation Lagrangienne. Le travail réalisé au cours de cette thèse représente l'une des premières étapes vers l'exploitation de toutes les capacités du modèle bi-fluide pour les applications de transport de sédiments. Il ouvre la voie à l'étude de nombreux enjeux scientifiques liés au transport de sédiments dans l'environnement côtier, estuarien ou fluvial.

# B

# Derivation of kinetic energy equations for the fluid phase in the Eulerian two-fluid formalism

*The derivation of the kinetic energy equations in the Eulerian two-fluid formalism are presented in this appendix. It includes equations for the total, main field and turbulent kinetic energy equations. Furthermore, equations are presented in term of filtered variables in the LES framework.*

## B.1 Mean total kinetic energy

Starting from the momentum equation (2.16) and multiplying it by the fluid velocity $u_i^f$ gives:

$$u_i^f \frac{\partial (1-\phi) u_i^f}{\partial t} + u_i^f \frac{\partial (1-\phi) u_j^f u_i^f}{\partial x_j} = -u_i^f \frac{(1-\phi)}{\rho^f} \frac{\partial P^f}{\partial x_i} + u_i^f \frac{\partial T_{ij}^f}{\partial x_j} - u_i^f I_i + u_i^f (1-\phi) g_i. \tag{B.1}$$

Using the expression for the derivation of a product

$$\frac{\partial a \cdot b}{\partial \eta} = b \frac{\partial a}{\partial \eta} + a \frac{\partial b}{\partial \eta}, \tag{B.2}$$

and taking the ensemble average (operator $\langle \cdot \rangle$) allows to write equation (B.1):

$$\frac{\partial \left\langle (1-\phi) u_i^f u_i^f /2 \right\rangle}{\partial t} + \frac{\partial \left\langle (1-\phi) u_j^f u_i^f u_i^f /2 \right\rangle}{\partial x_j} = -\left\langle u_i^f \frac{(1-\phi)}{\rho^f} \frac{\partial P^f}{\partial x_i} \right\rangle + \left\langle u_i^f \frac{\partial T_{ij}^f}{\partial x_j} \right\rangle - \left\langle u_i^f I_i \right\rangle + \left\langle u_i^f (1-\phi) g_i \right\rangle. \tag{B.3}$$

Developing the stress term on the right hand side of equation (B.3) and using Favre averaged

variables (operator $\langle\cdot\rangle_F$) gives:

$$\frac{\partial(1-\langle\phi\rangle)\langle u_i^f u_i^f/2\rangle_F}{\partial t}+\frac{\partial(1-\langle\phi\rangle)\langle u_j^f u_i^f u_i^f/2\rangle_F}{\partial x_j}=-\left\langle u_i^f\frac{(1-\phi)}{\rho^f}\frac{\partial P^f}{\partial x_i}\right\rangle +\left\langle\frac{\partial u_i^f T_{ij}^f}{\partial x_j}\right\rangle-\left\langle T_{ij}^f\frac{\partial u_i^f}{\partial x_j}\right\rangle-\left\langle u_i^f I_i\right\rangle+(1-\langle\phi\rangle)\langle u_i^f\rangle_F g_i. \tag{B.4}$$

Introducing now the mean total kinetic energy $K^f=\langle u_i^f u_i^f\rangle_F/2$ gives the final form of $K^f$ equation:

$$\underbrace{\frac{\partial(1-\langle\phi\rangle)K^f}{\partial t}}_{\substack{I\\ \text{rate of change}}}+\underbrace{\frac{\partial(1-\langle\phi\rangle)\langle u_j^f u_i^f u_i^f/2\rangle_F}{\partial x_j}}_{\substack{II\\ \text{convection}}}=\underbrace{-\left\langle u_i^f\frac{(1-\phi)}{\rho^f}\frac{\partial P^f}{\partial x_i}\right\rangle}_{\substack{III\\ \text{pressure contribution}}}+\underbrace{\left\langle\frac{\partial u_i^f T_{ij}^f}{\partial x_j}\right\rangle}_{\substack{IV\\ \text{viscous diffusion}}}-\underbrace{\left\langle T_{ij}^f\frac{\partial u_i^f}{\partial x_j}\right\rangle}_{\substack{V\\ \text{viscous dissipation}}}-\underbrace{\left\langle u_i^f I_i\right\rangle}_{\substack{VI\\ \text{coupling contribution}}}+\underbrace{(1-\langle\phi\rangle)\langle u_i^f\rangle_F g_i}_{\substack{VII\\ \text{gravity contribution}}}. \tag{B.5}$$

## B.2 Main field and turbulent kinetic energy

The Mean total kinetic energy can be decomposed into a main field and turbulent kinetic energy $\langle K^f\rangle_F$ and $k^f$ respectively following:

$$K^f=\frac{\langle u_i^f u_i^f\rangle_F}{2}=\frac{\langle u_i^f\rangle_F\langle u_i^f\rangle_F}{2}+\underbrace{\left\langle\langle u_i^f\rangle_F u_i^{f'}\right\rangle_F}_{=0}+\frac{\langle u_i^{f'}u_i^{f'}\rangle_F}{2}=\langle K^f\rangle_F+k^f \tag{B.6}$$

with $u_i^{f'}$ the fluid velocity fluctuations.

Each term of equation (B.5) is decomposed into main field and fluctuating part.

Term $I$:

$$\frac{\partial(1-\langle\phi\rangle)K^f}{\partial t}=\frac{\partial(1-\langle\phi\rangle)\langle K^f\rangle_F}{\partial t}+\frac{\partial(1-\langle\phi\rangle)k^f}{\partial t} \tag{B.7}$$

Term *II*:

$$\begin{aligned}\frac{\partial(1-\langle\phi\rangle)\langle u_j^f u_i^f u_i^f/2\rangle_F}{\partial x_j} &= \frac{\partial(1-\langle\phi\rangle)\langle u_j^f\rangle_F\langle u_i^f\rangle_F\langle u_i^f\rangle_F/2}{\partial x_j} + \underbrace{\frac{\partial(1-\langle\phi\rangle)\langle u_j^{f'}\rangle_F\langle u_i^f\rangle_F\langle u_i^f\rangle_F/2}{\partial x_j}}_{=0} \\ &+ \underbrace{\frac{\partial(1-\langle\phi\rangle)\langle u_j^f\rangle_F\langle u_i^{f'}\rangle_F\langle u_i^f\rangle_F}{\partial x_j}}_{=0} + \frac{\partial(1-\langle\phi\rangle)\langle u_j^{f'}u_i^{f'}\rangle_F\langle u_i^f\rangle_F}{\partial x_j} \\ &+ \frac{\partial(1-\langle\phi\rangle)\langle u_j^f\rangle_F\langle u_i^{f'}u_i^{f'}\rangle_F/2}{\partial x_j} + \frac{\partial(1-\langle\phi\rangle)\langle u_j^{f'}u_i^{f'}u_i^{f'}\rangle_F/2}{\partial x_j} \\ &= \frac{\partial(1-\langle\phi\rangle)\langle u_j^f\rangle_F\langle K\rangle_F}{\partial x_j} + \frac{\partial(1-\langle\phi\rangle)\langle u_j^f\rangle_F k}{\partial x_j} + \frac{\partial(1-\langle\phi\rangle)\langle u_j^{f'}u_i^{f'}u_i^{f'}\rangle_F/2}{\partial x_j} \\ &+ (1-\langle\phi\rangle)\langle u_j^{f'}u_i^{f'}\rangle_F\frac{\partial\langle u_i^f\rangle_F}{\partial x_j} + \langle u_i^f\rangle_F\frac{\partial(1-\langle\phi\rangle)\langle u_j^{f'}u_i^{f'}\rangle_F}{\partial x_j}\end{aligned} \tag{B.8}$$

Term *III*:

$$\left\langle u_i^f\frac{(1-\phi)}{\rho^f}\frac{\partial P^f}{\partial x_i}\right\rangle = \langle u_i^f\rangle_F\left\langle\frac{(1-\phi)}{\rho^f}\frac{\partial P^f}{\partial x_i}\right\rangle + \left\langle u_i^{f'}\frac{(1-\phi)}{\rho^f}\frac{\partial P^f}{\partial x_i}\right\rangle \tag{B.9}$$

Term *IV*:

$$\left\langle\frac{\partial u_i^f T_{ij}^f}{\partial x_j}\right\rangle = \left\langle\frac{\partial\langle u_i^f\rangle_F T_{ij}^f}{\partial x_j}\right\rangle + \left\langle\frac{\partial u_i^{f'}T_{ij}^f}{\partial x_j}\right\rangle \tag{B.10}$$

Term *V*:

$$\left\langle T_{ij}^f\frac{\partial u_i^f}{\partial x_j}\right\rangle = \left\langle T_{ij}^f\frac{\partial\langle u_i^f\rangle_F}{\partial x_j}\right\rangle + \left\langle T_{ij}^f\frac{\partial u_i^{f'}}{\partial x_j}\right\rangle \tag{B.11}$$

Term *VI*:

$$\langle u_i^f I_i\rangle = \langle u_i^f\rangle_F\langle I_i\rangle + \langle u_i^{f'}I_i\rangle \tag{B.12}$$

Term *VII*:

$$(1-\langle\phi\rangle)\langle u_i^f\rangle_F g_i = (1-\langle\phi\rangle)\big\langle\langle u_i^f\rangle_F\big\rangle_F g_i + \underbrace{(1-\langle\phi\rangle)\langle u_i^{f'}\rangle_F g_i}_{=0} = (1-\langle\phi\rangle)\langle u_i^f\rangle_F g_i \tag{B.13}$$

Two equations for the main field and turbulent kinetic energy can be extracted from this decomposition:

$$\begin{aligned}&\underbrace{\frac{\partial(1-\langle\phi\rangle)\langle K^f\rangle_F}{\partial t}}_{\substack{\text{rate}\\ \text{of change}}} + \underbrace{\frac{\partial(1-\langle\phi\rangle)\langle u_j^f\rangle_F\langle K^f\rangle_F}{\partial x_j}}_{\text{convection}} = -\underbrace{\langle u_i^f\rangle_F\left\langle\frac{(1-\phi)}{\rho^f}\frac{\partial P^f}{\partial x_i}\right\rangle}_{\substack{\text{pressure}\\ \text{contribution}}} + \underbrace{\left\langle\frac{\partial\langle u_i^f\rangle_F T_{ij}^f}{\partial x_j}\right\rangle}_{\substack{\text{viscouss}\\ \text{diffusion}}} \\ &- \underbrace{\left\langle T_{ij}^f\frac{\partial\langle u_i^f\rangle_F}{\partial x_j}\right\rangle}_{\substack{\text{viscouss}\\ \text{dissipation}}} - \underbrace{\langle u_i^f\rangle_F\frac{\partial(1-\langle\phi\rangle)\langle u_j^{f'}u_i^{f'}\rangle_F}{\partial x_j}}_{\substack{\text{Reynolds-like}\\ \text{contribution}}} - \underbrace{\langle u_i^f\rangle_F\langle I_i\rangle}_{\substack{\text{coupling}\\ \text{contribution}}} + \underbrace{(1-\langle\phi\rangle)\langle u_i^f\rangle_F g_i}_{\substack{\text{gravity}\\ \text{contribution}}}\end{aligned} \tag{B.14}$$

$$\underbrace{\frac{\partial(1-\langle\phi\rangle)k^f}{\partial t}}_{\substack{\text{rate}\\ \text{of change}}}+\underbrace{\frac{\partial(1-\langle\phi\rangle)\langle u_j^f\rangle_F k^f}{\partial x_j}}_{\text{convection}}=\underbrace{-(1-\langle\phi\rangle)\langle u_j^{f'}u_i^{f'}\rangle_F\frac{\partial\langle u_i^f\rangle_F}{\partial x_j}}_{\text{production}}\underbrace{-\left\langle u_i^{f'}\frac{(1-\phi)}{\rho^f}\frac{\partial P^f}{\partial x_i}\right\rangle}_{\substack{\text{pressure}\\ \text{contribution}}}$$
$$+\underbrace{\left\langle\frac{\partial u_i^{f'}T_{ij}^f}{\partial x_j}\right\rangle}_{\substack{\text{viscouss}\\ \text{diffusion}}}-\underbrace{\left\langle T_{ij}^f\frac{\partial u_i^{f'}}{\partial x_j}\right\rangle}_{\substack{\text{viscouss}\\ \text{dissipation}}}-\underbrace{\frac{\partial(1-\langle\phi\rangle)\langle u_j^{f'}u_i^{f'}u_i^{f'}\rangle_F/2}{\partial x_j}}_{\substack{\text{turbulent}\\ \text{transport}}}-\underbrace{\langle u_i^{f'}I_i\rangle}_{\substack{\text{coupling}\\ \text{contribution}}} \tag{B.15}$$

## B.3 Kinetic energy equations for filtered two-phase flow equations

Applying the same procedure as in section B.1 to the filtered fluid momentum equation (2.45) gives the mean resolved kinetic energy $\tilde{K}^f=\langle\tilde{u}_i^f\tilde{u}_i^f\rangle_F/2$ equation (B.16):

$$\underbrace{\frac{\partial(1-\langle\overline{\phi}\rangle)\tilde{K}^f}{\partial t}}_{\substack{\text{rate of}\\ \text{change}}}+\underbrace{\frac{\partial(1-\langle\overline{\phi}\rangle)\langle\tilde{u}_j^f\tilde{u}_i^f\tilde{u}_i^f/2\rangle_F}{\partial x_j}}_{\substack{II\\ \text{convection}}}=\underbrace{-\left\langle\tilde{u}_i^f\frac{(1-\overline{\phi})}{\rho^f}\frac{\partial\overline{P}^f}{\partial x_i}\right\rangle}_{\substack{\text{pressure}\\ \text{contribution}}}+\underbrace{\left\langle\frac{\partial\tilde{u}_i^f\tilde{T}_{ij}^f}{\partial x_j}\right\rangle}_{\substack{\text{viscous}\\ \text{diffusion}}}-\underbrace{\left\langle\tilde{T}_{ij}^f\frac{\partial\tilde{u}_i^f}{\partial x_j}\right\rangle}_{\substack{\text{viscous}\\ \text{dissipation}}}$$
$$-\underbrace{\langle\tilde{u}_i^f\bar{I}_i\rangle}_{\substack{\text{coupling}\\ \text{contribution}}}+\underbrace{(1-\langle\overline{\phi}\rangle)\langle\tilde{u}_i^f\rangle_F g_i}_{\substack{\text{gravity}\\ \text{contribution}}}+\underbrace{\left\langle\frac{\partial\tilde{u}_i^f\sigma_{ij}^{f,sgs}}{\partial x_j}\right\rangle}_{\substack{\text{sub-grid}\\ \text{diffusion}}}-\underbrace{\left\langle\sigma_{ij}^{f,sgs}\frac{\partial\tilde{u}_i^f}{\partial x_j}\right\rangle}_{\substack{\text{sub-grid}\\ \text{dissipation}}}+\underbrace{\left\langle\tilde{u}_i^f(\Phi_i^{f,sgs}+I_i^{sgs})\right\rangle}_{\substack{\text{other}\\ \text{sub-grid}\\ \text{contributions}}}. \tag{B.16}$$

The mean resolved total kinetic energy can also be decomposed into a mean field and a turbulent kinetic energy following :

$$\tilde{K}^f=\frac{\langle\tilde{u}_i^f\tilde{u}_i^f\rangle_F}{2}=\frac{\langle\tilde{u}_i^f\rangle_F\langle\tilde{u}_i^f\rangle_F}{2}+\underbrace{\langle\langle\tilde{u}_i^f\rangle_F\tilde{u}_i^{f'}\rangle_F}_{=0}+\frac{\langle\tilde{u}_i^{f'}\tilde{u}_i^{f'}\rangle_F}{2}=\langle\tilde{K}^f\rangle_F+\tilde{k}^f. \tag{B.17}$$

As in section B.2, the equations for the filtered main field and turbulent kinetic energy can be extracted from equation (B.16) with the filtered velocity decomposition:

$$\underbrace{\frac{\partial(1-\langle\overline{\phi}\rangle)\langle\tilde{K}^f\rangle_F}{\partial t}}_{\substack{\text{rate}\\ \text{of change}}}+\underbrace{\frac{\partial(1-\langle\overline{\phi}\rangle)\langle\tilde{u}_j^f\rangle_F\langle\tilde{K}^f\rangle_F}{\partial x_j}}_{\text{convection}}=\underbrace{-\langle\tilde{u}_i^f\rangle_F\left\langle\frac{(1-\overline{\phi})}{\rho^f}\frac{\partial\overline{P}^f}{\partial x_i}\right\rangle}_{\substack{\text{pressure}\\ \text{contribution}}}+\underbrace{\left\langle\frac{\partial\langle\tilde{u}_i^f\rangle_F\tilde{T}_{ij}^f}{\partial x_j}\right\rangle}_{\substack{\text{viscouss}\\ \text{diffusion}}}$$
$$\underbrace{-\left\langle\tilde{T}_{ij}^f\frac{\partial\langle\tilde{u}_i^f\rangle_F}{\partial x_j}\right\rangle}_{\substack{\text{viscouss}\\ \text{dissipation}}}\underbrace{-\langle\tilde{u}_i^f\rangle_F\frac{\partial(1-\langle\overline{\phi}\rangle)\langle\tilde{u}_j^{f'}\tilde{u}_i^{f'}\rangle_F}{\partial x_j}}_{\substack{\text{Reynolds-like}\\ \text{contribution}}}\underbrace{-\langle\tilde{u}_i^f\rangle_F\langle\overline{I}_i\rangle}_{\substack{\text{coupling}\\ \text{contribution}}}\underbrace{+(1-\langle\overline{\phi}\rangle)\langle\tilde{u}_i^f\rangle_F g_i}_{\substack{\text{gravity}\\ \text{contribution}}} \tag{B.18}$$
$$\underbrace{+\left\langle\frac{\partial\langle\tilde{u}_i^f\rangle_F\sigma_{ij}^{f,sgs}}{\partial x_j}\right\rangle}_{\substack{\text{sub-grid}\\ \text{diffusion}}}\underbrace{-\left\langle\sigma_{ij}^{f,sgs}\frac{\partial\langle\tilde{u}_i^f\rangle_F}{\partial x_j}\right\rangle}_{\substack{\text{sub-grid}\\ \text{dissipation}}}\underbrace{+\langle\tilde{u}_i^f\rangle_F\left\langle(\Phi_i^{f,sgs}+I_i^{sgs})\right\rangle}_{\substack{\text{other}\\ \text{sub-grid}\\ \text{contributions}}}$$

$$\underbrace{\frac{\partial(1-\langle\overline{\phi}\rangle)\tilde{k}^f}{\partial t}}_{\substack{\text{rate}\\ \text{of change}}}+\underbrace{\frac{\partial(1-\langle\overline{\phi}\rangle)\langle\tilde{u}_j^f\rangle_F\tilde{k}^f}{\partial x_j}}_{\text{convection}}=\underbrace{-(1-\langle\overline{\phi}\rangle)\langle\tilde{u}_j^{f'}\tilde{u}_i^{f'}\rangle_F\frac{\partial\langle\tilde{u}_i^f\rangle_F}{\partial x_j}}_{\text{production}}\underbrace{-\left\langle\tilde{u}_i^{f'}\frac{(1-\overline{\phi})}{\rho^f}\frac{\partial\overline{P}^f}{\partial x_i}\right\rangle}_{\substack{\text{pressure}\\ \text{contribution}}}$$
$$\underbrace{+\left\langle\frac{\partial\tilde{u}_i^{f'}\tilde{T}_{ij}^f}{\partial x_j}\right\rangle}_{\substack{\text{viscouss}\\ \text{diffusion}}}\underbrace{-\left\langle\tilde{T}_{ij}^f\frac{\partial\tilde{u}_i^{f'}}{\partial x_j}\right\rangle}_{\substack{\text{viscouss}\\ \text{dissipation}}}\underbrace{-\frac{\partial(1-\langle\overline{\phi}\rangle)\langle\tilde{u}_j^{f'}\tilde{u}_i^{f'}\tilde{u}_i^{f'}\rangle_F/2}{\partial x_j}}_{\substack{\text{turbulent}\\ \text{transport}}}\underbrace{-\langle\tilde{u}_i^{f'}\overline{I}_i\rangle}_{\substack{\text{coupling}\\ \text{contribution}}}$$
$$\underbrace{+\left\langle\frac{\partial\tilde{u}_i^{f'}\sigma_{ij}^{f,sgs}}{\partial x_j}\right\rangle}_{\substack{\text{sub-grid}\\ \text{diffusion}}}\underbrace{-\left\langle\sigma_{ij}^{f,sgs}\frac{\partial\tilde{u}_i^{f'}}{\partial x_j}\right\rangle}_{\substack{\text{sub-grid}\\ \text{dissipation}}}\underbrace{+\left\langle\tilde{u}_i^{f'}(\Phi_i^{f,sgs}+I_i^{sgs})\right\rangle}_{\substack{\text{other}\\ \text{sub-grid}\\ \text{contributions}}} \tag{B.19}$$

# C

# Favre averaging procedure

*This appendix aims at presenting the Favre-averaging procedure used to compute Favre-averaged variable for the undirectional flow configurations.*

The given variable $\psi$ can be decomposed into the sum of the Favre-averaged variable $\langle\psi\rangle_F$ and the associated fluctuation $\psi'$. Favre-averaging operations on the variables $\psi^f$ or $\psi^s$ correspond to perform an ensemble average (operator $\langle\cdot\rangle$) of the variables weighted by the ensemble-averaged phase concentration $\langle 1-\phi\rangle$ or $\langle\phi\rangle$ following

$$\langle\psi^f\rangle_F = \frac{\langle(1-\phi)\psi^f\rangle}{\langle 1-\bar{\phi}\rangle}, \quad \langle\psi^s\rangle_F = \frac{\langle\phi\,\psi^f\rangle}{\langle\phi\rangle}. \tag{C.1a,b}$$

Numerically, averaged variables are calculated by performing a spatial averaging operation in the streamwise and spanwise directions of a temporally averaged variable $\langle\psi\rangle_t$ following

$$\langle\psi\rangle = \frac{1}{L_x L_z}\int_0^{L_x}\int_0^{L_z}\langle\psi\rangle_t dxdz, \tag{C.2}$$

with $L_x$ and $L_z$ the lengths of the numerical domain in the streamwise and spanwise directions respectively.

The temporal averaging operation is performed using an iterative procedure at each time step with the temporal average value of the variable $\psi$ at time $t_{n+1}$ given by

$$\langle\psi(t_{n+1})\rangle_t = \frac{\psi(t_{n+1}) + n\langle\psi(t_n)\rangle_t}{n+1}. \tag{C.3}$$

Second-order statistical moments such as r.m.s. of the velocity fluctuations or Reynolds stresses are obtained by calculating the fluid or solid Favre-averaged covariance tensor $\langle\psi_i'\psi_j'\rangle_F$ following

$$\langle\psi_i'\psi_j'\rangle_F = \langle\psi_i\psi_j\rangle_F - \langle\psi_i\rangle_F\langle\psi_j\rangle_F \tag{C.4}$$

One can notice that in clear water conditions (without solid phase), fluid phase Favre averaging is equivalent to ensemble averaging.

# D

# Numerical domain parallelization constraints for filtering operation in the finite-size correction model

*In this appendix, constraints on the numerical domain parallelization imposed by the filtering operation in the finite-size correction model are presented.*

To compute filtered variables using the methodology developed in chapter 5, the value of the quantity to be filtered at a distance $\breve{\Delta}$ of the location where the filtered variable is calculated has to be known. In sequential, from a simple exploration algorithm, all the values from the cells located at a distance inferior to $\breve{\Delta}$ together with their relative distance can be stored to compute the filtered variables.

In parallel computations, the numerical domain is decomposed into blocks that are treated independently by multiple processors. One block is allocated to a given processor and information is transmitted from a block to its neighbor through their shared interface following a communication protocol. In that case, the exploration algorithm, executed by a given processor, can only explore cells located in its own block. Gathering information of neighboring cells from an other block is not trivial, especially for unstructured meshes. As a consequence, in order to use the filtering operation in configurations requiring parallelization, some constraints on the domain decomposition have to be respected.

In all the configurations investigated in this manuscript and, more generally, in channel flow configurations, the mesh is uniform in the streamwise and spanwise directions ($x$ direction and $z$ direction in this manuscript), and non-uniform in the wall normal direction ($y$-direction). In the most simple case, corresponding to the configurations presented in chapter 5, the filter size $\breve{\Delta}$ is equal to the grid spacing in the $x$ and $z-$ directions. In that case, the filtering operation is performed only using information from cells in the wall normal direction. The exploration algorithm can find the neighboring cells only if the numerical domain is decomposed into blocks in the $x$ and $z$ directions as presented in figure D.1. Furthermore, in order to ensure coincidence between the block's frontier and cell faces, the number of cells in the $x$ and $z$ directions should be a multiple of the number of blocks in the same direction.

For more complicated configurations for which $\breve{\Delta}$ is larger than the grid size in the $x$ and $z$ directions, a methodology developed to communicate information from neighboring cells located

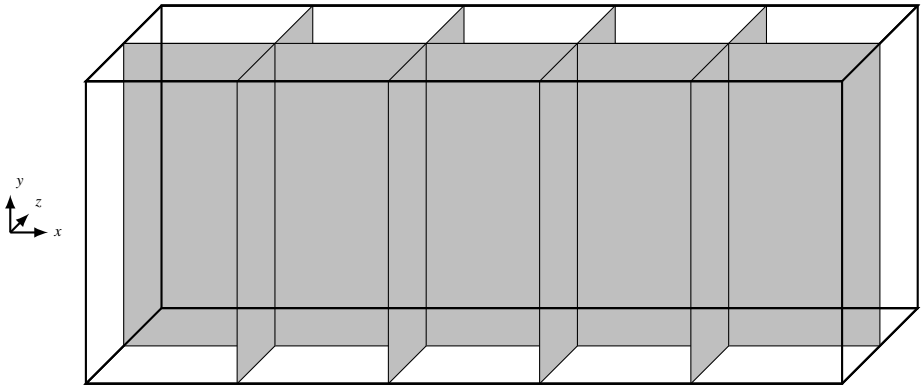


*Figure D.1: Sketch of the numerical domain decomposed into 5 blocks in the x−direction and 2 blocks in the z−direction.*

in an other block has been implemented. This methodology is only valid if the grid spacing is uniform in the $x$ and $z$ directions. Besides constraints relative to the simplest case described above, additional constraints on the relation between grid spacing, filter size and domain decomposition need to be respected to be able to compute the filtered variables.

All the constraints are listed below:

- Uniform grid spacing in the $x$ and $z$ directions
- Numerical domain is divided into blocks only in the $x$ and $z$ directions
- Filter size $\breve{\Delta}$ smaller than the block size
- Half of the filter size $\breve{\Delta}/2$ not a multiple of the grid spacing in the $x$ and $y$ directions.

Removing the constraints on the discretization is technically possible but would require an important development time.

# E

# Practical sand transport formula

*The practical sand transport formula from van Der A et al. (2013) [114] based on the semi-unsteady half-cycle concept introduced by Dibajnia and Watanabe (1992) [26] is presented in this appendix.*

One of the most accurate and advanced modeling approach to determine the net sediment flux under velocity and acceleration skewed waves is the practical sand transport formula from van Der A *et al.* (2013) [114]. This approach is based on the semi-unsteady half-cycle concept introduced by Dibajnia and Watanabe (1992) [26]. The net sediment flux is calculated based on the difference between the onshore transport rate generated during wave crest and offshore transport rate generated during wave trough. Contributions due to phase-lag are taken into account by calculating the amount of sediment entrained during the previous wave phase and transported during current phase. The model is applicable to configurations involving sediment transport in the ripple or sheet flow regime subject to an oscillatory flow, under real waves and in currents for different grain sizes but in this appendix, we present a simplified version of the sand transport formula for oscillatory flow in the sheet flow regime involving monodispersed particles.

In the model proposed by van Der A *et al.* (2013) [114], the dimensionless net sediment flux $Q^*$ is defined as the difference between the dimensionless onshore and offshore sediment fluxes $Q_c^*$ and $Q_t^*$ respectively weighted by the corresponding duration of the wave crest $T_c$ and wave trough $T_t$ (see figure E.1):

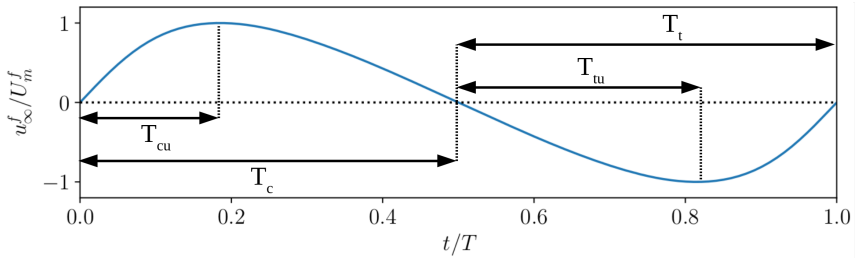


*Figure E.1: Time series of free stream velocity with durations of wave crest $T_c$, accelerating phase of the wave crest $T_{cu}$, wave trough $T_t$ and accelerating phase of the wave trough $T_{tu}$.*

$$Q^* = \frac{Q}{\sqrt{(s-1)gd_p^3}} = \frac{T_c Q_c^* - T_t Q_t^*}{T} \tag{E.1}$$

with $Q_c^*$ and $Q_t^*$ calculated as the product of a sediment load transported during the wave phase and the dimensionless velocity represented by the square root of the representative Shields number of the corresponding wave phase $\theta_c$ and $\theta_t$ following:

$$Q_c^* = \sqrt{\theta_c}\left(\Omega_{cc}^* + \frac{T_c}{2T_{cu}}\Omega_{tc}^*\right), \quad Q_t^* = \sqrt{\theta_t}\left(\Omega_{tt}^* + \frac{T_t}{2T_{tu}}\Omega_{ct}^*\right) \tag{E.2a,b}$$

with $T_{cu}$ and $T_{tu}$ the durations of wave crest and trough acceleration (see figure E.1). The total sediment load transported during wave crest and trough is decomposed into the sediment load entrained and transported during the corresponding wave phase $\Omega_{cc}^*$ and $\Omega_{tt}^*$ respectively and the sediment load entrained during the crest or trough and transported during the next wave phase $\Omega_{ct}^*$ and $\Omega_{tc}^*$ respectively. The coefficients $T_c/2T_{cu}$ and $T_t/2T_{tu}$ take into account acceleration skewness on the phase-lag contribution of the sediment load.

The total sediment load entrained during wave crest $\Omega_c^* = \Omega_{cc}^* + \Omega_{ct}^*$ and wave trough $\Omega_t^* = \Omega_{tt}^* + \Omega_{tc}^*$ are calculated as follows:

$$\Omega_\alpha^* = \begin{cases} 0, & \theta_\alpha \leq \theta_{cr} \\ m(\theta_\alpha - \theta_{cr})^n, & \theta_\alpha > \theta_{cr} \end{cases} \tag{E.3}$$

with subscript $\alpha = c,t$ denoting either wave crest or wave trough, $\theta_{cr}$ the critical Shields number for initiation of motion function of the particle diameter calculated using empirical relation from Soulsby (1997) [108], $m = 12$ and $n = 1.2$ model coefficients determined empirically by van Der A *et al.* (2013) [114] based on the SANTOSS database containing 226 net transport rates measurements in water tunnels or under real waves, in the ripple or sheet flow regime, under acceleration or velocity skewed waves and with or without superimposed current.

To determine the ratio of the sediment load $\Omega_\alpha^*$ transported during the corresponding and the next wave phase, a phase-lag parameter for each wave phase $P_\alpha$ is proposed. Corresponding sediment loads are then given by:

$$\Omega_{cc}^* = \begin{cases} \Omega_c^*, & P_c \leq 1 \\ \dfrac{1}{P_c}\Omega_c^*, & P_c > 1 \end{cases} \tag{E.4}$$

$$\Omega_{tt}^* = \begin{cases} \Omega_t^*, & P_t \leq 1 \\ \dfrac{1}{P_t}\Omega_t^*, & P_t > 1 \end{cases} \tag{E.5}$$

$$\Omega_{ct}^* = \begin{cases} 0, & P_c \leq 1 \\ \left(1 - \dfrac{1}{P_c}\right)\Omega_c^*, & P_c > 1 \end{cases} \tag{E.6}$$

$$\Omega_{tc}^* = \begin{cases} 0, & P_t \leq 1 \\ \left(1 - \dfrac{1}{P_t}\right)\Omega_t^*, & P_t > 1 \end{cases} \tag{E.7}$$

The phase-lag parameters are calculated as:

$$P_c = \frac{\beta\delta_{s,c}^m}{2(T_c - T_{cu})v_s}, \quad P_t = \frac{\beta\delta_{s,t}^m}{2(T_t - T_{tu})v_s}, \tag{E.7a,b}$$

with $\beta = 8.2$ a tuning coefficient calibrated using the SANTOSS database, $v_s$ the particle fall velocity and $\delta^m_{s,c}$ and $\delta^m_{s,t}$ the maximum sheet flow layer thickness during wave crest and wave trough estimated based on the scaling law proposed by Dohmen-Janssen *et al.* (2001) [29]:

$$\frac{\delta^m_{s,\alpha}}{d_p} = \begin{cases} 13\theta^m_\alpha, & d_p \geq 200\mu m \\ \left[25 - \dfrac{12(d_p - 150)}{200 - 150}\right]\theta^m_\alpha, & 150\mu m < d_p < 200\mu m \\ 25\theta^m_\alpha, & d_p \leq 150\mu m \end{cases} \tag{E.8}$$

where the maximum Shields number $\theta^m_\alpha$ is calculated using expression (5.17) using the maximum free stream velocity during phase $\alpha$.

# F

# Development of a bottom roughness model for large-eddy simulation

*The development of a canopy model to represent bottom roughness is presented in this appendix. The model is validated by numerically reproducing an experimental configuration of an unidirectional open channel flow with bottom roughness.*

In the model proposed in this manuscript, the increased flow resistance induced by the presence of roughness elements at the bottom of a channel is represented by the addition of a drag term in the fluid and solid phase momentum equations (2.16) and (2.17).

Assuming that roughness elements are immobile particles of diameter $d_p$, the drag force has the same expression as $D_i$ in the momentum coupling between the solid and fluid phase in the two-fluid model shown in equation (2.38). However, in the expression of the drag force, $u_i^s = 0$ and $\phi$ is replaced by the concentration of roughness elements at the bottom of the channel $\phi^r$. For an accurate prediction of the bottom roughness, the modeling challenge is to determine the concentration $\phi_r$.

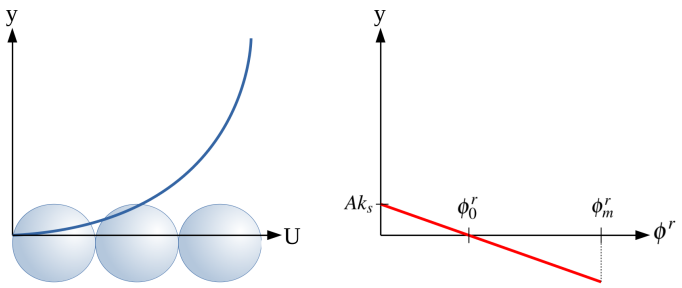


*Figure F.1: Schematic representation of a flow over a rough bed.*

For rough bottom boundaries in horizontal channel flows constituted of packed particles, concentration $\phi^r$ is assumed to decrease linearly from the maximum volume fraction at the wall $\phi_m^r$ to $\phi^r = 0$ over a distance equal to $k_s = 2.5d_p$ the Nikuradse roughness length. However, the level of fluid zero velocity, corresponding of the mesh bottom boundary of the numerical domain in the simulation, is not coincident with the location of maximum volume fraction $\phi_m^r$. Following Nezu

& Nakagawa (1993) [77], the distance from the top of the roughness elements to the bed level with zero velocity is defined as a fraction of the roughness length $Ak_s$ with typical values of $A$ between 0.15 and 0.3 (see figure F.1). As a consequence, taking the level of zero fluid velocity coincident with the mesh boundary, the concentration $\phi^r$ increases linearly from the concentration at $y = 0$ in the numerical domain $\phi_0^r = \phi_m^r(1-A)$ to $\phi^r = 0$ at the top of the roughness elements. The concentration of roughness elements is therefore defined everywhere in the numerical domain following the expression:

$$\phi^r = max\left(\phi_0^r - \frac{\phi_m^r}{k_s}y, \quad 0\right). \tag{F.1}$$

To test and validate the model, a clear water experimental configuration carried out in the LEGI tilting flume during the Ph.D thesis of Hélder Guta is reproduced numerically. The configuration corresponds to an unidirectional boundary layer flow over a rough bed composed of glued plastic particles of diameter $d_p = 3mm$. Water flows with a bulk velocity $U_b = 0.75m.s^{-1}$ and a depth $h = 0.1m$. The bottom friction velocity determined experimentally is $u_\tau = 0.042m.s^{-1}$. Flow parameters are presented in table F.1.

| $U_b\ (m.s^{-1})$ | $h\ (m)$ | $u_\tau\ (m.s^{-1})$ | $Re_\tau$ |
|---|---|---|---|
| 0.75 | 0.1 | $4.2 \times 10^{-2}$ | 4200 |

*Table F.1: Flow parameters of the clear water configuration from the Ph.D thesis of Hélder Guta.*

Similarly to the open channel flow configurations presented in chapter 5, the numerical domain is a bi-periodic rectangular box with cyclic boundary conditions in $x$ and $z$ directions, no slip boundary condition at the bottom and a symmetry boundary condition a the top. The volume force driving the flow is adjusted at each time step to match the bulk velocity. The mesh is composed of $320 \times 200 \times 192$ elements corresponding to a total of $12,288,000$ cells. The span-wise and stream-wise resolution is constant with $\Delta_x^+ \approx 82$ and $\Delta_z^+ \approx 70$. The mesh is stretched along the $y$-axis with $\Delta_y^+ \approx 4$ at the wall and $\Delta_y^+ \approx 60$ at the top. The time step is set to the constant value of $\Delta t = 2 \times 10^{-4}s$ to ensure the condition $CFL < 0.3$ Numerical parameters are presented in table F.2.

| Mesh | Number of cells | $\Delta_x^+$ | $\Delta_z^+$ | $\Delta_y^+$ (wall) | $\Delta t\ (s)$ |
|---|---|---|---|---|---|
| $320 \times 200 \times 192$ | $12,288,000$ | 82 | 70 | 4 | $2 \times 10^{-4}$ |

*Table F.2: Numerical parameters of the clear water configuration from the Ph.D thesis of Hélder Guta.*

Considering the strong gradient of $\phi^r$ close to the bottom, the model is very sensitive to the near wall resolution. In this configuration, fifteen grid points are located between the wall and the position where $\phi^r = 0$. The maximum roughness elements concentration is set to $\phi_m^r = 0.55$ and the value of $A = 0.2$ have shown the best predictions.

Profiles of averaged velocity and Reynolds stresses from simulations using the two-fluid model with and without roughness model are compared with experimental measurements in figure F.2. Without roughness, the two-fluid model predicts much "flatter" velocity profile compared with experiments. Furthermore, the slope of Reynolds stress is significantly under-predicted resulting in lower bed shear stress. However, prediction made using the roughness model agree very well with experimental measurements. This result demonstrates the importance of including the effect of bed roughness in the simulation and the capacity of the proposed model to accurately predict the flow hydrodynamics.

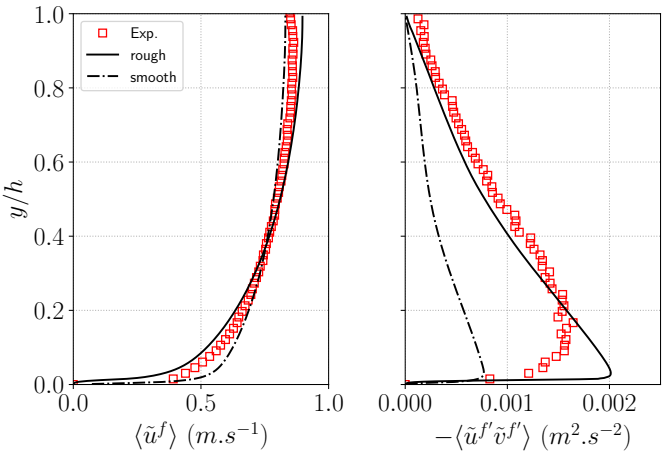


*Figure F.2: Average velocity (left panel) and Reynolds stress (right panel) profiles from simulations of the clear water configuration the Ph.D thesis of Hélder Guta using the roughness model (rough), without roughness model (smooth) compared with experimental measurements (Exp.)*

## Résumé

Compte tenu de l'importance du transport de sable dans des conditions d'écoulement intense sur l'évolution de la morphologie des plages, la compréhension des mécanismes physiques à petite échelle tels que les interactions particule-turbulence impliquées dans le transport de sédiments sous les vagues est une étape importante vers des prédictions des modifications du littoral à grande échelle. Dans ce contexte, le développement de modèles à turbulence résolue est un sujet extrêmement actif au sein de la communauté scientifique. Cependant, les simulations utilisant les méthodes classiques de modélisation lagrangienne, où les trajectoires des particules individuelles sont suivies, sont irréalisables du point de vue des capacités de calcul étant donné la grande quantité de particules transportées dans l'écoulement. Dans cette thèse, un modèle eulérien d'écoulement diphasique (ou modèle bi-fluide) à turbulence résolue est développé. Dans ce modèle, la phase porteuse et la phase dispersée sont considérées comme des continuums s'affranchissant des limitations en terme de nombre de particules. Le modèle est appliqué avec succès à des configurations de charriage intense oscillant sous un écoulement sinusoïdal. les résultats de simulation ont permis de confirmer que des instabilités du lit sédimentaire et la modulation de la turbulence par les particules contribuent aux effets instationnaires, à savoir l'effet de décalage de phase et l'augmentation de l'épaisseur de la couche limite pour le sable fin.
Le modèle bi-fluide est ensuite appliqué à des configurations de charriage intense oscillant impliquant un écoulement asymétrique en vitesse et en accélération pour étudier les effets liés à la forme des vagues. La comparaison entre les mesures et les prédictions numériques du flux net de sédiments au cours de la vague a montré que le modèle bi-fluide est capable de capturer la dynamique de l'écoulement, en particulier le changement de signe du flux net pour le sable fin sous des vagues asymétriques en vitesse. Ces résultats ont permis de confirmer les observations faites à partir de configurations impliquant un écoulement sinusoïdal.
A partir des simulations impliquant du sable moyen, certaines divergences concernant la concentration lors de la phase de renverse de la vague sont observées. L'hypothèse est que ces divergences sont le résultat d'une absence de séparation d'échelles entre les particules et les plus petites échelles de l'écoulement turbulent. Pour de telles conditions d'écoulement, les lois d'interaction classiques entre les deux phases ne sont plus valables et doivent être modifiées pour prendre en compte les effets de taille finie.
Afin d'étendre le champ d'application du modèle bi-fluide à des configurations impliquant des particules plus grandes que les plus petites échelles d'écoulement turbulent, un modèle de correction de taille finie est proposé et validé par rapport à des configurations impliquant un écoulement de couche limite unidirectionnel chargé de particules dans le régime dilué. Ce modèle est basé sur l'hypothèse que les échelles turbulentes plus grandes que le diamètre de la particule contribueront à la vitesse relative résolue entre les deux phases, alors que les tourbillons plus petits que le diamètre de la particule auront deux effets : (i) ils réduiront le temps de réponse des particules en ajoutant une viscosité turbulente à l'échelle sub-particulaire au coefficient de traînée, et (ii) ils contribueront à augmenter la production de température granulaire. L'intégration des effets de taille finie dans le modèle bi-fluide nous permet de prédire quantitativement le profil de concentration sans aucune paramétrisation.



**Mots-clés :** Transport de sédiments, simulation des grandes échelles de la turbulence, modélisation diphasique, intéractions turbulence-particules



## Abstract

Considering the importance of the cross-shore sand transport under intense flow conditions on the evolution of beaches' morphology, understanding physical mechanisms at small scales such as particle-turbulence interactions involved in sediment transport under waves is an important step toward accurate predictions of the coastline modifications at large scales. In this context, development of turbulence resolving modeling approaches is an extremely active topic among the scientific community. However, simulations using classical Lagrangian modeling methodologies, for which the trajectories of individual particles are tracked, are computationally unfeasible given the large amount of particles transported in the flow.
In this thesis, an Eulerian turbulence-resolving two-phase flow model (or two-fluid model) is developed. In this modeling approach, both the carrier phase and the dispersed phase are seen as continua avoiding the limitations in term of number of particles. The model is successfully applied to oscillatory sheet flow configurations under a symmetric sinusoidal flow forcing. Numerical results allowed to confirm that bed instabilities and turbulence modulation by the presence of the particles contributes to unsteady effects, namely phase-lag effect and enhanced boundary layer thickness for fine sand.
The two-fluid model is then applied to oscillatory sheet flow configurations involving velocity skewed and acceleration skewed flow forcing to study wave shape effects. Comparison between experimental measurements and numerical predictions of the wave averaged net sediment flux showed that the two-fluid model is able to accurately capture the flow dynamics, especially the change of sign of the net flux for fine sand under velocity skewed waves. These results allowed to further confirm the observations made from configurations involving a symmetric sinusoidal flow forcing.
From simulations of configurations involving medium sand, some discrepancies regarding the concentration at flow reversal are observed. It is hypothesized that these discrepancies are the result of an absence of separation of scales between the particles and the smallest turbulent flow scales. For such particle and flow conditions, the classical interaction laws between the two phases do no longer hold and should be modified to take into account finite-size effects.
To extend the range of applicability of the two-fluid model to configurations involving particles larger than the smallest turbulent flow scales, a finite-size correction model is proposed and validated against experimental configurations involving particle-laden unidirectional boundary layer flow in the dilute regime. This model is based on the assumption that the turbulent flow scales larger than the particle diameter will contribute to the resolved relative velocity between the two phases, whereas eddies smaller than the particle diameter will have two effects: (i) they will reduce the particle response time by adding a sub-particle scale eddy viscosity to the drag coefficient, and (ii) they will contribute to increase the production of granular temperature. Integrating finite-size effects in the two-fluid model allows us to quantitatively predict the concentration profile for heavier-than-fluid particles without any tuning parameter.



**Keywords :** Sediment transport, large-eddy simulation, two-phase flow modeling, turbulence-particle interactions